Assessing the Mechanical Microstructure of Shale by Nanoindentation: The Link Between Mineral Composition and Mechanical Properties

by

Christopher P. Bobko

B.S.E., Princeton University (2003)
M.S., Massachusetts Institute of Technology (2005)

V. 1

Submitted to the Department of Civil and Environmental Engineering
in partial fulfillment of the requirements for the Degree of

Doctor of Philosophy in Structures and Materials

at the

MASSACHUSETTS INSTITUTE OF TECHNOLOGY

September 2008

Signature of Author .....
Department of Civil and Environmental Engineering
August 4, 2008

Certified by .....
Franz-Josef Ulm
Professor of Civil and Environmental Engineering
Thesis Supervisor

Accepted by .....
Daniele Veneziano
Chairman, Departmental Committee for Graduate Students

Assessing the Mechanical Microstructure of Shale by Nanoindentation: The Link Between Mineral Composition and Mechanical Properties

by

Christopher P. Bobko

Submitted to the Department of Civil and Environmental Engineering
on August 4, 2008, in partial fulfillment of the
requirements for the Degree of
Doctor of Philosophy in Structures and Materials

Abstract

Shale is a multi-phase, multi-scale sedimentary rock that makes up 75% of the earth's sedimentary basins and is especially critical in petroleum engineering applications. At macroscopic scales, shales possess a diverse set of possible compositions, resulting in a diverse set of mechanical properties. This thesis assesses microstructure and material invariant properties of shale as the link between engineering performance and composition.

A comprehensive experimental microporomechanics approach, employing advanced experimental and analytical nanoindentation techniques, provides the basis for assessment of microstructure and material invariant properties. Nanoindentation experiments and analysis tools are designed to probe and infer the elastic and strength properties of the porous clay composite in shale.

The results of this investigation show that properties of the porous clay composite scale with the clay packing density in the material, but otherwise do not depend on mineral composition. These scaling relationships are representative of a granular composite of spherical particles, and lead to identification of intrinsically anisotropic material invariant elastic properties and intrinsically isotropic material invariant hardness properties. The material invariant hardness represents a combination of cohesive and frictional behavior that is seen to scale with the average clay packing density in the sample. Nanoindentation results also provide evidence of packing density distributions that are analogous to pore size distributions.

These observations are combined to define a model of the elementary building block of shale. Exploring the physical origin of this building block suggests that it represents an agglomerated polycrystal group of individual clay minerals. Particles in the porous clay composite exhibit fractal packings, which suggest a quantitative link between contemporary theories about the origin of friction and the experimental scaling of friction in shale.

The new understanding provided by this thesis represents a leap forward for predictive models of shale behavior. The model of the elementary building block can be used as a basis for micromechanical homogenization models which predict poroelastic properties and strength behavior of shale at the lab-bench scale based on only two volume fraction parameters. The success of these models validates the elementary building block model and illustrates its engineering significance.

Thesis Supervisor: Franz-Josef Ulm
Title: Professor of Civil and Environmental Engineering

Contents

List of Tables

List of Figures

Acknowledgements

The work presented in this dissertation would truly have not been possible without the support of many wonderful people. Their recognition here is only a small token of my appreciation.

First, thanks must go to my advisor, Franz-Josef Ulm, who has often simultaneously challenged, frustrated, enlightenened, and championed me and my work for the past five years. Always pushing for the next idea or further improvement has, in the end, led to great work. Likewise, I recognize the efforts and support of my thesis committee, including Dr. Christine Ortiz for her perspective on nanoindentation issues and the materials science approach, and Dr. Brian Evans for his perspective on rock physics and mechanics. In particular, I would like to thank Dr. John Germaine for his assistance in the Civil Engineering Laboratory and for his support throughout. Thank you as well to Alan Schwartzman and the Nanomechanical Testing Laboratory at MIT.

The financial and technial support of the MIT-OU GeoGenome Industrial Consortium is gratefully acknowledged. Dr. Younane Abousleiman at Oklahoma University has been a great supporter, and I also appreciate the work of his team at OU. Special thanks also go to Dr. Greg Perez for his helpful comments and industrial perspective throughout the project.

My student colleagues represent the best of the best, and I treasure your friendship and your scholarly collaborations. J. Alberto Ortega, Dr. Matthieu Vandamme, Benjamin Gathier, Sophie Cariou, Mahalia Miller, Naomi Stein, Naeem Abdulhadi, Antoine Delafargue, and Dr. Georgios Constantinides have all made direct contributions to the work presented in this dissertation. Other students in the research group, including Rouzbeh Shah, Zenzile Brooks, James Vanzo, Jong-Min Shim and Emilo Silva, also deserve recognition.

Finally, I thank some very special people whom I love dearly. To my parents, thank you for your everlasting love and support (as well as last-minute proofreading help!) - I love you. To my dearest Kelly, thank you for your love, your patience, and your joy - I love you.

THANK YOU!

Part I

GENERAL PRESENTATION

Chapter 1

Introduction

Shale is a multi-phase, multi-scale, compositionally diverse sedimentary rock. It is composed primarily of sedimented clay particles, and some quantities of larger, silt-sized inclusions, and is especially critical for the oil industry in both exploration and exploitation applications. The complex nature of shale materials, however, has challenged researchers to understand how shales behave mechanically, and how their elasticity and strength behavior may be predicted. The widely documented diversity of shale materials currently demands detailed localized testing in engineering applications. An improved understanding of the mechanical behavior of shale will lead to a leap forward in the accuracy and usefulness of predictive models.

1.1 Industrial Context & Research Motivation

Shales account for approximately 75% of the earth's sedimentary basins and are commonly encountered by the petroleum industry. In particular, the low permeability of shale means that it is very often a sealing formation, covering hydrocarbon reservoirs (Fig. 1-1, top). In addition, shale can also be a source rock, as organic material trapped during sedimentation evolves into hydrocarbon deposits.

As shale is so commonly associated with the presence of hydrocarbon reservoirs, understanding the mechanical behavior of the material is important in both of the primary aspects of petroleum geoengineering; exploration and exploitation. The elastic behavior of shale is of particular importance during seismic exploration, where the well-documented elastic anisotropy

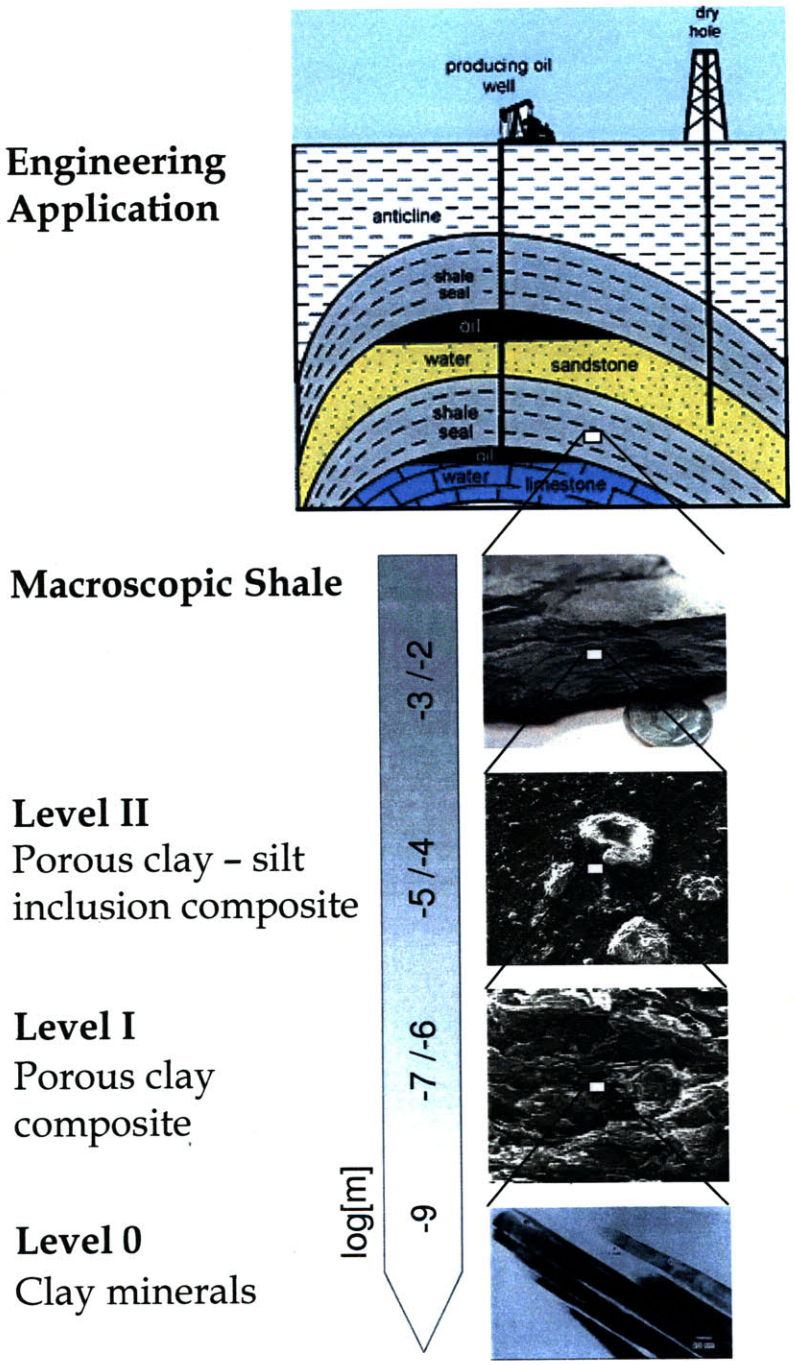

Figure 1-1: The multiscale thought model for shale in the context of Petroleum Engineering Applications. Top drawing: Schematic of shale as a sealing formation for oil reservoirs. From the Illinois State Geological Survey (http://http://www.isgs.uiuc.edu/maps-data-pub/publications/geobits/geobit9.shtml). Bottom set of images: The multiscale thought model for the stucture of shale, adapted from [172]. Level '0' image from [119].

of shale poses problems in interpretation of field data. The strength behavior of shale is of critical importance during drilling operations. Borehole failures and wellbore stability problems are most frequently encountered when dealing with shale materials, and these issues may easily be viewed as plastic failure problems [68]. As of 2003, wellbore stability problems were estimated to cost the industry at least one billion dollars per year [1].

A new approach to solving these problems has been undertaken by the MIT-OU GeoGenome Industry Consortium. The approach aims to identify a fundamental unit of material invariant mechanical behavior in sedimentary rocks. Once these units have been identified and characterized, it is possible to upscale the intrinsic material behavior to the macroscopic scale of engineering application. The work presented in this thesis provides an experimental basis on which the fundamental unit of mechanical behavior in shale is identified and characterized.

1.2 Problem Statement and Approach

The ultimate goal of this study is to implement the materials science paradigm for shale materials; that is, to link material composition and microstructure to engineering performance of the composite material. Such an implementation requires fundamental understanding of the microstructure of the constituent material phases, as well as their mechanical properties. Thus, the challenge to be addressed in this thesis, through the use of experimental microporomechanics, is:

> *Can the macroscopic diversity of shale be understood by assessing microstructure and material invariant mechanical properties as the link between composition and engineering performance?*

Experimental microporomechanics provides the framework for assessing the microstructure and mechanical behavior of complex porous composite materials. This framework combines theoretical work in microporomechanics, which relates the macroscopic response of a porous composite to the microscopic behavior of its constituent material phases, with advanced experimental techniques which permit assessment of that microscopic behavior. Responding to the challenge of understanding shale materials presents a prime opportunity for application of experimental micromechanics.

1.3 Research Objectives

A comprehensive experimental approach is presented to address the scientific challenge. Four primary research objectives guide the overall approach:

Objective 1 *Review the multi-scale nature of shale, identify the length scales where experimental microporomechanics is useful, and adapt nanoindentation tools for use with shale materials.* Shale is a multi-scale material, with levels ranging from the scale of individual clay minerals to macroscopic specimens of rock (Fig. 1-1). Because of the small size of individual clay minerals, their mechanical properties are difficult to assess. Moreover, when such an assessment is possible, it may not capture well the interactions between individual clay minerals. Nanoindentation provides a possibility of assessing the mechanical behavior of shale at the appropriate scale, but while nanoindentation is a robust technique for testing homogenous materials, its application to shale presents some unique challenges. Existing experimental techniques and analysis methods must be reviewed and adapted to shale materials.

Objective 2 *Perform nanoindentation experiments on a wide variety of shale materials.* Many different samples need to be tested in order to represent the great diversity of shale materials. This extensive database can then be mined to identify trends, links, and relationships between properties.

Objective 3 *Define an elementary building block for shale by determining the mechanical microstructure and material invariant stiffness and strength properties of the porous clay phase.* Predictive modeling of shale materials depends on an understanding of the mechanical microstructure and the material invariant properties of the porous clay phase in shale. Analysis of nanoindentation results can provide these ingredients, which are combined in a model of the elementary building block of shale.

Objective 4 *Explore the origins of the elementary building block and demonstrate its usefulness for modeling the mechanical behavior of shale.* The existence of an elementary building block for shale is remarkable, as are many of its properties. To better understand the model, a variety of approaches are considered to deduce the physical origin of the ele-

mentary building block model. Reviewing and extending predictive modeling based on the elementary building block, and comparing model results with macroscopic data, will demonstrate the relevance of the elementary building block model.

1.4 Outline of Thesis

The first part of this thesis contains this introductory material. Part II, Materials and Methods, is divided into three chapters which address the first Research Objective. Chapter 2 uses the context of a multiscale thought model for the structure of shale, which highlights important length scales for the material, to present detailed information about the considered shale materials. This understanding and information guides the experimental and theoretical investigation. Chapter 3 reviews the nanoindentation technique as applied to homogeneous materials. Chapter 4 reviews and adapts recent research that allows nanoindentation to be applied to heterogeneous materials. These experimental and analytical techniques are required when testing a complex natural composite such as shale.

Part III of the thesis, Results - Mechanical Behavior of Porous Clay in Shale, addresses the second Research Objective by presenting the results of a nanoindentation campaign on a wide variety of shale samples. The results are structured in two chapters. The first, Chapter 5, presents results on the mechanical behavior of porous clay in shale by statistical analysis of nanoindentation tests at two different scales. Chapter 6 continues the presentation of results, using the recently developed scaling analysis approach to provide packing density distributions and quantitative information about the strength behavior of the porous clay in shale. In particular, remarkable results are obtained regarding scaling relationships for the cohesive frictional strength properties of the material.

Part IV of the thesis contains a discussion centering on the elementary building block of shale. The first chapter in this part, Chapter 7, satisifies the third Research Objective by defining the model of the elementary building block, based on the results from nanoindentation as presented in Part III. Chapter 8 strives to provide a deeper understanding of the elementary building block model by exploring the physical origins of its morphology, elastic content, and strength properties. The relevance of the elementary building block model is demonstrated in

Chapter 9 by reviewing micromechanical models that make use of the elementary building block. Physically-based model predictions are seen to compare favorably to experimental data. These last two chapters fulfill the fourth Research Objective, to better understand the elementary building block.

Finally, Part V of the thesis contains a chapter presenting some concluding remarks, summarizing the results of this study and providing perspectives for future research endeavors.

1.5 Industrial and Scientific Benefits

Achievement of the proposed research objectives leads to several industrial and scientific benefits. Among these benefits are:

- Tools for assessing mechanical properties of shale from nanoindentation experiments, which require small sample sizes and alleviate the need for lengthy triaxial tests.
- Understanding of the material invariant elastic and strength properties of shales.
- Assessment of the nanogranular morphology of the porous clay in shale, and its effect on the mechanical properties of shale.
- A relevant model which enables physics-based predictions of the macroscopic mechanical behavior of shale.

Part II

MATERIALS AND METHODS

Chapter 2

The Multi-Scale Nature of Shale

Shale is a diverse class of sedimentary rock composed of sedimented clay particles, and some quantities of larger inclusions. Small scale layering, associated with the bedding direction of a slow sedimentation process, is a hallmark of shale – similar rocks without an apparent layering may be called mudstones or siltstones, depending on the quantities of inclusions. For the purpose of this study, all such materials are considered as "shale." Any or all of the primary clay minerals (kaolinite, illite, and smectite) may be present in shale, while the inclusions are typically quartz or feldspars. This chapter introduces the considered materials and investigates both common features and differences from one material to another.

The multiscale thought model for the structure of shale, originally presented by Ulm et al. [172], provides the framework for investigation in this chapter and throughout this thesis. The model, which suggests the important length scales for shale materials, is reviewed and illustrated through thin section and scanning electron micrographs. Detailed information about each of the samples, including mineralogy and porosity data, is presented in the context of the multi-scale model. A quantitative deconvolution analysis of pore-size distributions adds to the characterization of the materials and their length scales. Finally, two important volume fraction parameters associated with the multi-scale model, inclusion volume fraction and clay packing density, are identified as a common means of characterizing each shale.

2.1 Introduction to the Studied Materials

Three primary categories of samples were studied in detail for this project. First are a group of shales known as the GeoGenome shales, as they were the initial materials selected for consideration in the GeoGenome Industrial Consortium. Next is a series of samples from the Woodford formation; these samples are from a "source rock," meaning that they contain a significant fraction of organic material. The final category of samples are not natural shale materials, but a series of highly compressed resedimented Boston Blue Clay samples.

2.1.1 GeoGenome Shales

The nine GeoGenome shales were selected for initial study because they represent a good cross-section of the diverse possibilities of shale composition and mechanical properties for shales in sealing formations. Sealing formations, with low permeability, act to trap hydrocarbons in reservoirs (see Fig. 1-1 (top)). The samples were provided from drill cuttings by Chevron, Norsk Hydro (now StatOilHydro), and Oklahoma University. Information about the geological origin of these samples was generally not provided, although detailed mineralogy and porosity information was disclosed (and is presented below). Only one shale, the Pierre shale, was identified by geological origin. The others are identified by names corresponding to their physical appearance (the "Light" and "Dark" and "Low-Clay" shales) or by a reference number (S1, S2, S3, S4, and S7).

2.1.2 Woodford Shales

The Woodford shales provide an interesting addition to the GeoGenome shales. While the GeoGenome shales represent the wide view of diversity of shale materials (their mineralogies and porosities, and likely their geological origins, are vastly different), the six Woodford shale samples come from one single core, over a sampling distance of less than 100 feet [3]. And, while the GeoGenome shale samples were taken from sealing formations, the Woodford formation contains shales which are source rocks, and contain a significant volume fraction of kerogen, an organic antecedent to exploitable hydrocarbons [181]. An investigation of these shales permits an understanding of the effect of kerogen, as well as the variation of properties within a relatively

small range of burial depths. Detailed mineralogy and porosity was obtained by researchers at Oklahoma University for these samples, as were a full set of downhole logs. The Woodford Shale samples are identified by number associated with the burial depth, in feet, of the sample (i.e. Woodford 110, 131, 154, 166, 175, and 185).

2.1.3 Highly Consolidated Resedimented Boston Blue Clay

The final material considered in this study is a "synthetic" sedimentary material which can be seen as an analogue to shale. The raw material is Resedimented Boston Blue Clay (RBBC), a geomaterial that has been well-studied at MIT for more than four decades [11], [114], [79], [155]. Among the many advantages of such a material is that samples are derived from a natural material, so while the behavior of RBBC is similar to what is expected for materials encountered in nature, inherent variations between samples are largely eliminated. As a result, many different kinds of tests may be performed on nearly identical samples, or the effects of various sedimentation and consolidation processes may be studied.

To synthesize rock-like samples from RBBC, the samples of RBBC considered here experienced consolidation pressures of up to 10 MPa. The experimental procedure may be briefly summarized [2]:

1. Batched Boston Blue Clay powder is mixed with water, in equal quantities, by mass (100% water content).
2. A vacuum is applied to the slurry to remove air bubbles.
3. The material is loaded in an oedometer consisting of a Plexiglas cylinder, with porous stones above and below the soil.
4. Vertical load is applied incrementally and the height change is measured, until the required consolidation stress is achieved (this process may take 4 to 6 weeks depending on the final stress level).
5. The sample is unloaded in the oedometer to an over-consolidation ratio [1] (OCR) of 4.

[1] Overconsolidation ratio (OCR) is a soil mechanics term, referring to ratio of maximum compressive effective stress to the current compressive effective stress a certain soil deposit has experienced. In the case of OCR = 4

6. The sample is removed from the Plexiglas cylinder. End trimmings were delivered for nanoindentation testing, while the main sample is used for conventional triaxial testing or hollow cylinder testing.

The RBBC sample is subject to top and bottom drainage during loading and unloading in the oedometer, so water is expelled during consolidation, while a small amount of swelling occurs during the unloading to OCR of 4. Results of the consolidation process are presented later, when considering overall porosity. The Boston Blue Clay samples are identified by their final consolidation pressure (i.e. 4 MPa, 6.5 MPa, and 10 MPa).

2.1.4 Sample Storage

As shales contain clay minerals which can be sensitive to water content and other environmental factors, sample storage is a key concern for the shale materials. The basic idea is to keep the shale samples as close as possible to their natural relative humidity levels. For Shale 1, Shale 2, Shale 3, Shale 4, and Shale 7, this was acheived by storing the samples above specially designed saturated salt solutions in dessicator jars. For Shale 1, a relative humidty of 96% was maintained with a solution of potassium sulfate. For Shale 2 and Shale 4, a relative humidity of 80% was maintained with a solution of potassium chloride. Finally, for Shale 3 and Shale 7, a relative humidity of 75% was maintained with a solution of sodium chloride. For the other shale samples, a slightly simpler solution was employed; the samples were stored in tightly sealed jars filled with n-decane to prevent the exhange of water between the shale sample and the laboratory environment.

2.2 The Multi-Scale Model for Shale

Shale, when present either as a sealing formation, a source rock, or even synthetically formed, is a highly heterogeneous geo-composite, with heterogeneities which manifest themselves at various scales. An intact, macroscopic rock sample is considered at the scale of 10^{-3} m and above. These are the scales typically encountered for intact rock samples in the laboratory. At these

described here, the soil is unloaded in the oedometer to a compressive stress 1/4 of the maximum consolidation stress.

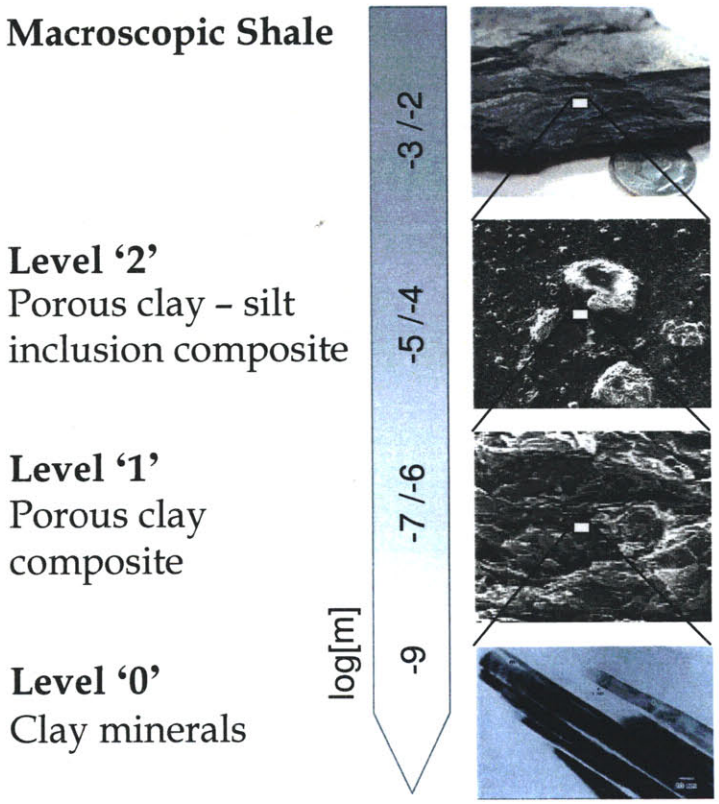

Figure 2-1: The multiscale thought model for shale. Adapted from [172]. Level '0' image from [119].

scales, the rock can be considered homogeneous, without containing large-scale heterogeneities that might be associated with fracture, stratigraphic layering, or other larger-scale geological features. The samples appear homogeneous to the naked eye.

Below the scale of macroscopic rock, a multi-scale thought model for shale, originally proposed by Ulm et al. [172], organizes and describes the different scales and different components of shale. Three levels are considered; Level '2' is the level of a porous clay and silt/sand inclusion composite, Level '1' is the level of the porous clay composite, and Level '0' is the level containing a composite of clay minerals. The model is summarized in Figure 2-1, and discussed in more detail with images from thin section and scanning electron microscopy in the remainder of this section.

2.2.1 Level '2' - Porous Clay and Silt/Sand Inclusion Composite

In Level '2', at the scale of 10^{-5} to 10^{-4} m, shale is clearly seen as a composite of a porous clay phase and a silt or sand inclusion phase. Figure 2-2 shows examples of thin-section optical micrographs and Figure 2-3 shows examples of Environmental Scanning Electron Microscope (ESEM) micrographs of shale samples. Both sets of images display evidence of silt- or sand-sized inclusions distributed randomly throughout the composite. Mineralogy information, presented in the next section, suggests that these inclusions are typically quartz or feldspar minerals.

2.2.2 Level '1' - Porous Clay Composite

Level '1' refers to a scale on the order of 10^{-7} to 10^{-6} m, and focuses on the properties of the porous clay, which is seen as a composite of clay particles and porosity. Figure 2-4 displays three representative ESEM images at this scale. All are taken parallel to the bedding direction, the $x1$-direction, and the apparent tendency for particles and pore space to possess some alignment associated with the bedding direction is clear in these images.

2.2.3 Level '0' - Clay Mineral Composite

Figure 2-5 displays Transmission Electron Microscope (TEM) images of clay minerals. Note that these images are from published literature on clays and shales, rather than the shale samples considered in this study, but a similar structure is expected at this scale [28], [119]. In

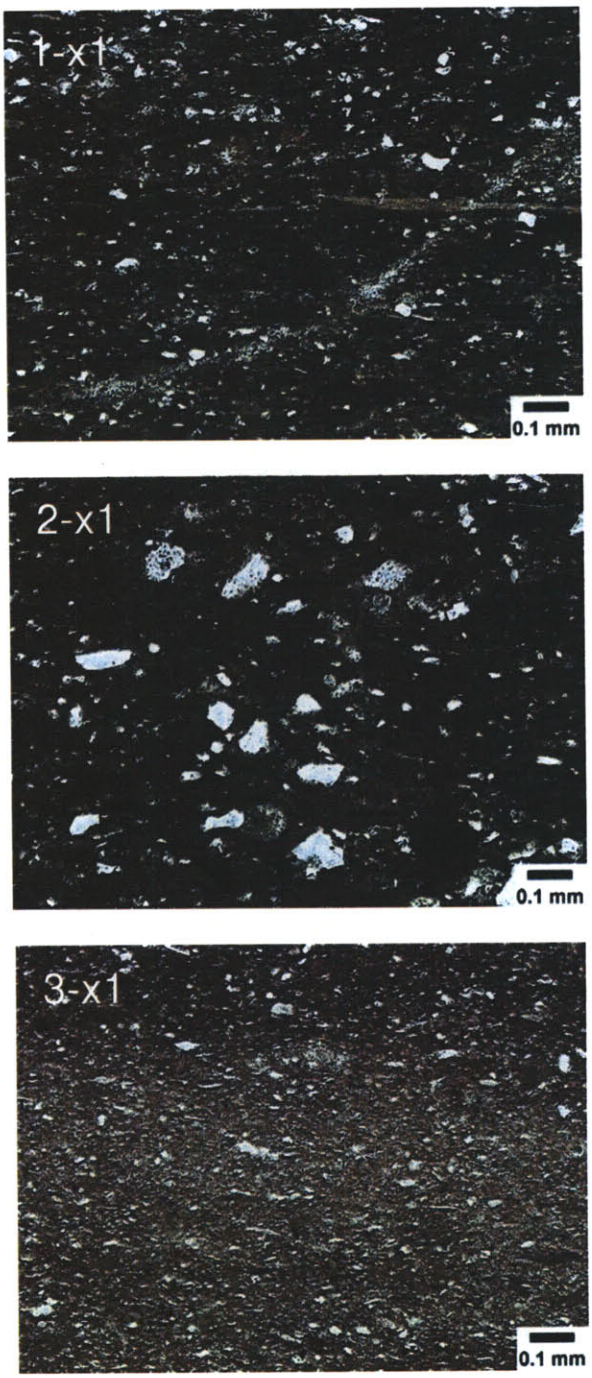

Figure 2-2: Thin section optical micrographs provided by Chevron for GeoGenome samples Shale 1, Shale 2, and Shale 3 taken in the parallel-to-bedding ($x1$) direction. The light objects, about 100 microns or less in typical size, are silt inclusions. They are randomly distributed throughout the composite. Adapted from [51].

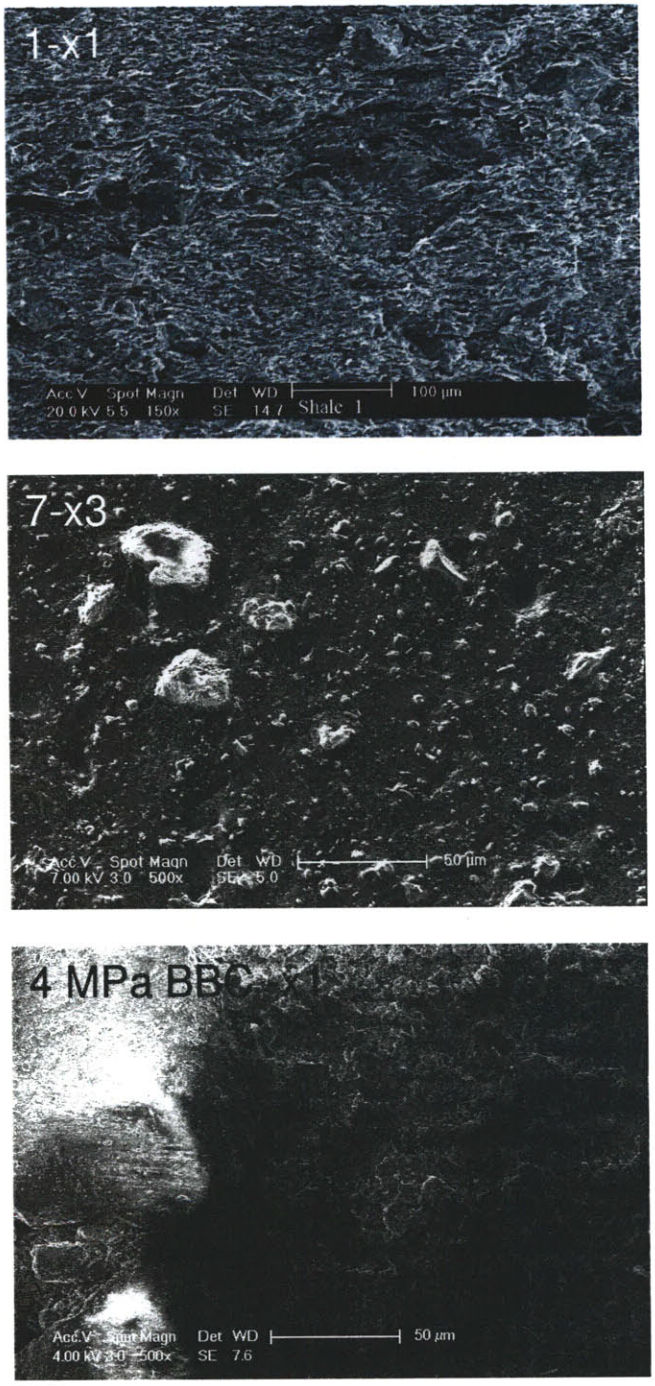

Figure 2-3: ESEM micrographs (Secondary Electron imaging) of GeoGenome Shale 1 in the $x1$-direction, GeoGenome Shale 7 in the $x3$-direction, and the 4 MPa compressed resedimented Boston Blue Clay sample in the $x1$-direction. The images clearly show silt- and sand-sized inclusions randomly distributed throughout the composite. Top figure (Shale 1-1) from [51].

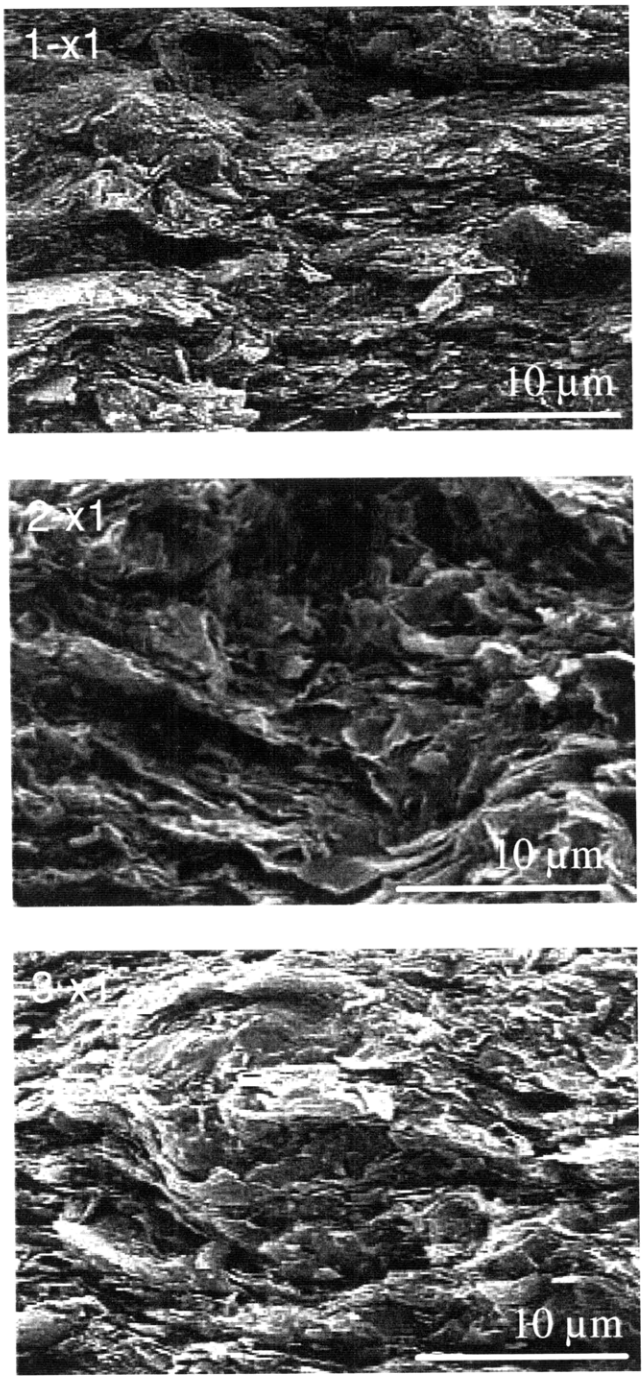

Figure 2-4: ESEM images (Secondary Electron) of GeoGenome Shale 1, Shale 2, and Shale 3, taken parallel to the bedding direction ($x1$-direction). The images display the scale of the porous clay composite at Level '1.' Adapted from [51].

Figure 2-5 (top), a TEM cross-section demonstrates that thin platelets of clay minerals align and aggregate to form roughly equidimensional particles, about 1 micron in diameter. In Figure 2-5 (bottom), a TEM cross section shows the individual clay mineral platelets, with thicknesses on the order of 20 nm. If kerogen is present, it is also considered at this scale.

2.3 Shale Mineralogy and Porosity

With the multi-scale model for shale in mind, this section introduces quantitative information about the shale materials. Mineralogy information is used to understand the proportions of clay and silt minerals, and knowledge of the density of each mineral permits an understanding of the volume fractions. Porosity and bulk density information is also presented, including pore size distributions. The mineralogy and porosity data is summarized in the key parameters for Level '1' and Level '2,' the clay packing density and the inclusion volume fraction, respectively.

2.3.1 Common Shale Minerals

Following the multiscale thought model for shale, as well as a preliminary understanding of mineralogy, the mineral composition of shales is divided into two categories, clay minerals, which enter at the scale of Level '0', and non-clay minerals, which enter at the scale of Level '2.' In addition, shales can also contain organic matter, which enters at the scale of Level '0.'

Clay Minerals

Clay minerals are phyllosilicates, meaning they are silicate materials occurring in the form of sheets. Two structural units form the basis for clay minerals, the silicon tetrahedron and the aluminum or magnesium octahedron. The most common clay minerals are composed of these structural units, linked together in sheets, in stacking arrangements. How the layers are stacked, and what other cations or water layers are in place, distinguish between the different minerals, as depicted in Figure 2-6 [138]. Three clay minerals, kaolinite, smectite, and illite, are particularly common in shale materials.

Kaolinite is known as a 1:1 mineral because its layer structure consists of one tetrahedral sheet for every octahedral sheet, fixing the atomic ratio between silicon and aluminum. Kaolin-

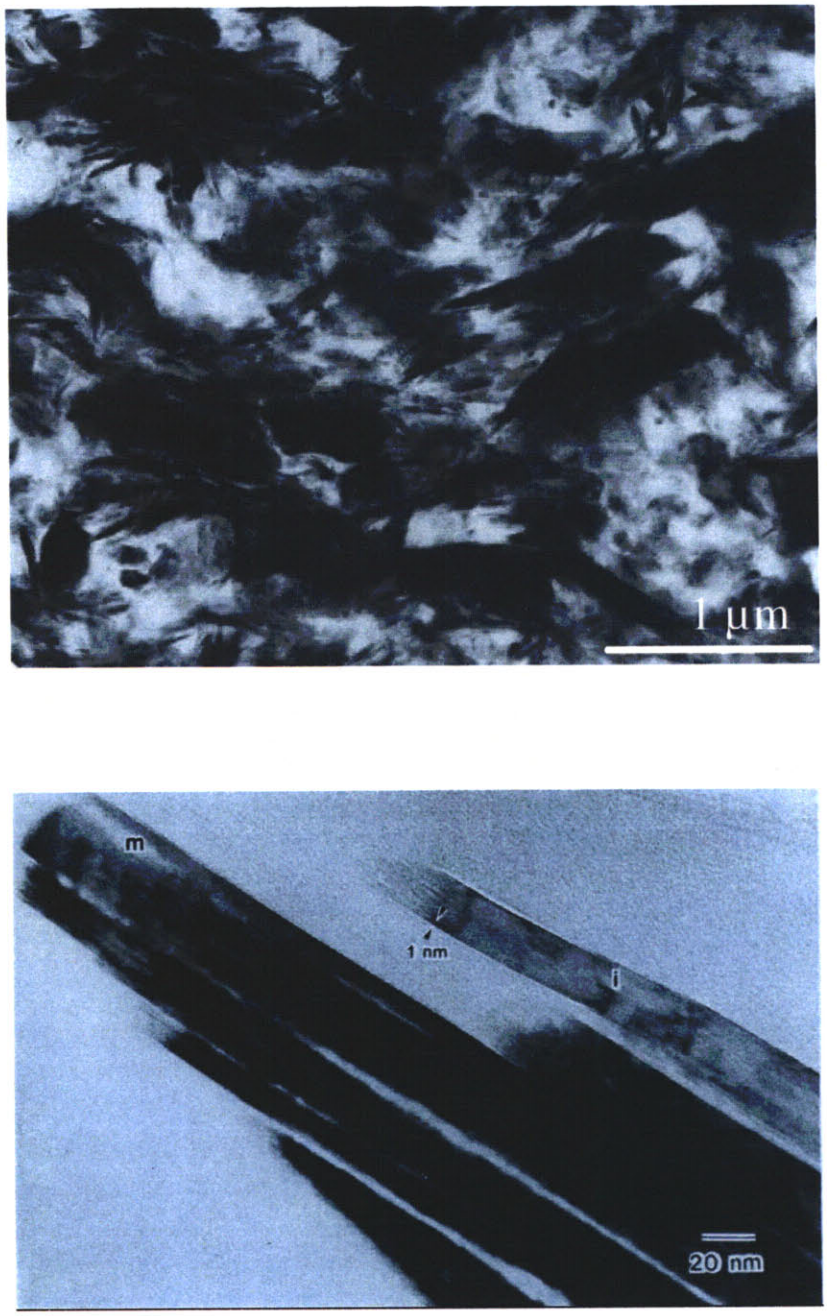

Figure 2-5: TEM images displaying cross-sections of (top) a consolidated natural clay deposit [28] and (bottom) individual clay platelet particles in shale [119].

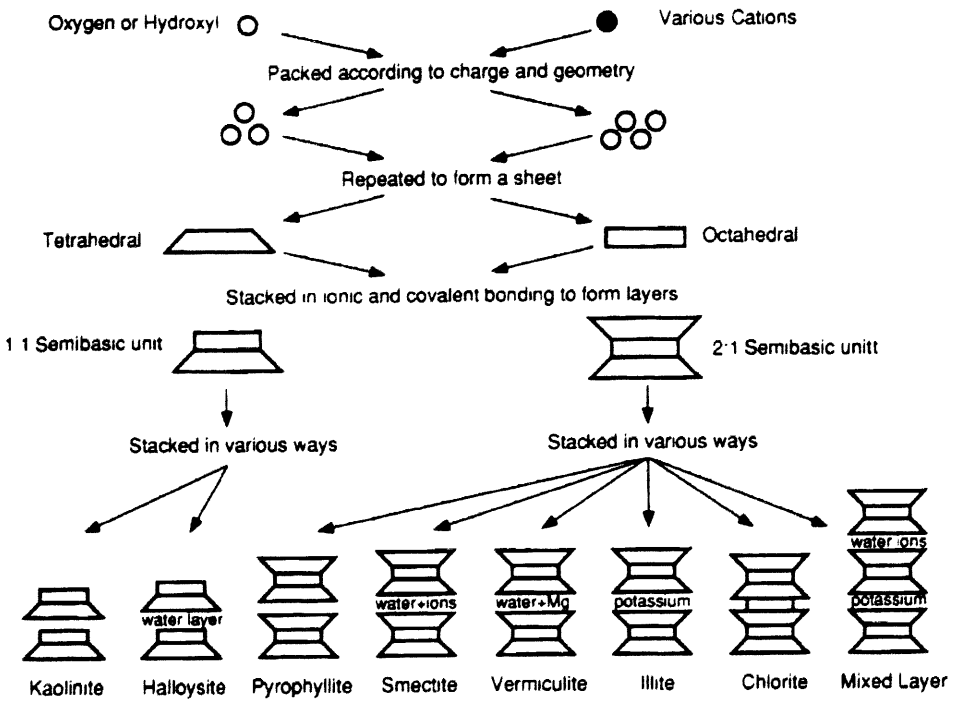

Figure 2-6: Synthesis patterns of clay minerals. Reproduced from [138].

ite particles can be well or poorly crystallized as six-sided platelets, resulting in a wide variation of typical particle sizes: from 0.1 μm up to 4 μm length, and forming books with thicknesses of 0.05 to 2 μm in thickness [138].

Smectite is a 2:1 mineral with a layer structure consisting of one octahedral sheet sandwiched between two tetrahedral sheets. Between each tetrahedral sheet, interlayer water molecules and ions form relatively weak van der Waals and electrostatic bonds. A common form of smectite, montmorillonite, consists of very thin platelets, with particle sizes 1 to 2 μm in length but only 1 to 10 nm in thickness [138].

Related to smectite is illite, another 2:1 mineral with a similar layered structure. The difference between the two minerals is that illite contains potassium ions that fit well into the atomic structure of the tetrahedral sheets and balance charge differences. The result is that electrostatic bonds between layers are stronger in illite than in smectite [138]. It is hypothesized that during chemical lithification processes in shales, smectite is converted into illite [16]. Illite particles are typically small platelets, with sizes between 0.1 μm to 2 μm in length, and thicknesses as small as 3 nm [138].

As each clay mineral is composed of similar constituents, various clay minerals often occur together in natural deposits [138]. The typical length scales for all the considered clay minerals range between 0.1 and 4 μm in length, with much smaller thicknesses.

Non-Clay Minerals

Shale materials also include various non-clay minerals, with quartz and K-feldspar (also known as orthoclase) being the two most common non-clay minerals in shale, as well as the most abundant minerals in the continental crust. Quartz and K-feldspar form denser crystal structures than the clay minerals, so they are expected to be much stronger and stiffer. From visual observations, it is clear that these minerals exist in shale with particle diameters on the order of 30 to 100 microns, much larger than the scale of the clay minerals.

Kerogen

A final possible solid component of shale materials is Kerogen. SEM and TEM image observations have suggested that the kerogen in shales can have lamellar structures with nanometer

Mineral	Bulk Density	Mineral	Bulk Density	Mineral	Bulk Density
Quartz	2.650	Halite	2.160	Chlorite	2.950
K-Feldspar	2.572	Pyrite	4.990	2:1 Fe clay	2.673
Plagioclase	2.680	Barite	4.500	Illite	2.795
Calcite	2.710	Anhydrite	2.950	Montmoril.	2.500
Dolomite	2.895	Gypsum	2.335	Kaolinite	2.645
Ankerite	3.015	Alunite	2.700	Kerogen	1.300

Table 2.1: Bulk density data for minerals present in shales. [145]

X-ray Diffraction Mineralogy
X-ray diffraction (XRD) is commonly used to study the structure of crystalline materials by studying the wavelengths of diffracted X-rays. These wavelengths are related to the spacing of interatomic layers in the material, and as a result are characteristic of each material. The layered structure of clay minerals is particularly suitable for X-ray diffraction. To make the diffraction experiment with small particles of various mineralogies, a small powdered sample is used. The use powder ensures that some impinging X-rays are properly aligned with the atomic layers to create measurable diffracted X-rays. For a composite powder, a intensity spectrum is obtained, with different peaks associated with particular minerals. Kaolinite, for example, exhibits a peak associated with 7 Å, while illite and dried smectite have peaks associated with 10 Å. Quartz and K-feldspar materials are also easily identified.

Table 2.2: Background: X-ray Diffraction Mineralogy (adapted from [138])

thicknesses [81], possess amorphous granular structures [55], or be dispersed as microlayers between clay phases [181]. The length scales identified by these studies justify the choice of including kerogen with clay minerals.

Table 2.1 provides bulk density information for the minerals (and kerogen) reviewed here, as well as other less-common minerals that may be present in the considered shale materials. This information will prove useful later in this chapter.

2.3.2 Mineralogy Data

Mineralogy data for the GeoGenome and Woodford shales was obtained by X-ray diffraction (XRD), described in Table 2.2. This technique "is the most widely used method for identification of fine-grained soil minerals" [138]. Quantitative analysis by XRD can be difficult, however, because of absorption and differing sample preparation techniques. Good, repeat-

able laboratory techniques and comparison studies can still provide an excellent quantitative estimate of composition [138].[2]

Mineralogy data, in terms of mass fractions, for the GeoGenome shales, Woodford Shales, and Highly Compressed Resedimented Boston Blue Clay is given in Table 2.3. The tested shales demonstrate and represent the diversity of possible mineralogies, and confirm the assertion that the clay minerals are often mixed together in a single deposit. Still, some materials feature a large mass fraction of kaolinite, while others are dominated by illite and smectite. Some materials have larger quantities of quartz and feldspar, while others are predominantly composed of clay minerals. The Woodford shale samples have a significant kerogen volume fraction. Detailed mineralogy was unavailable for the Boston Blue Clay, although it is typically considered as an illitic marine material [110]. Grain size distributions for the Boston Blue Clay suggest that particles which are silt-sized and larger occupy 20% of the solid mass of the material in powder form [155]. It is assumed that these silt-sized and larger particles are all quartz and feldspar particles, and that the remaining solid mass consists of some kind of clay particles.

2.3.3 Overall Porosity and Bulk Density

The remaining component of shale materials is porosity, the space not taken up by solid minerals. Porosity of the materials was measured in various ways. The results are presented in Table 2.4. Mercury intrusion consists of forcing mercury, at high pressures, into an evacuated pore space [8]. This technique is used to measure the pore size distributions (discussed in more detail in Sec. 2.3.4 below), as well as the total porosity, although it is well known that the technique tends to underestimate the actual porosity [57]. Porosity may also be estimated in the field by means of the Neutron Porosity log [102].

Drying Porosity

Drying porosity is determined by comparing the density of a saturated and dried sample:

$$\phi_{dry.} = \frac{\rho_{sat} - \rho_{dry}}{\rho_{fl}} \tag{2.1}$$

[2] A round-robin study performed in concert with the GeoGenome project found that the Chevron lab, which provided the mineralogy data reported here, gave reliable estimates for mineralogy from XRD [4].

Sample	Quartz/ Feldspar	Kaolinite	Illite/ Smectite	Other Clay	Total Clay	Kerogen
GeoGenome Shales						
S1	22	36	38	2	76	-
S2	28	21	42	9	72	-
S3	30	9	54	7	70	-
S4	40	7	44	6	57	-
S7	31	37	21	9	67	-
Light	80	3	11	6	20	-
Dark	66	1	23	10	34	-
Pierre	64	0	30	6	36	-
Low-Clay	n.a.	n.a.	n.a.	n.a.	n.a.	-
Woodford Shales						
110	62	0	20	0	20	18
131	54	1	26	3	29	17
154	55	0	25	3	28	18
166	51	0	27	4	31	18
175	52	0	31	5	36	12
185	49	3	29	4	33	14
Boston Blue Clay						
4 MPa	20	n.a.	n.a.	n.a.	80	-
6.5 MPa	20	n.a.	n.a.	n.a.	80	-
10 MPa	20	n.a.	n.a.	n.a.	80	-

Table 2.3: Mineralogy data (in mass percent) for the tested samples.

where ρ_{sat} and ρ_{dry} are the mass densities of the fully saturated and oven-dried ($T = 135\,^{\circ}\mathrm{C}$) samples, and ρ_{fl} is the density of the saturating fluid (either water or a brine).

Bulk Density and Porosity

Another method used to estimate the porosity of the shale materials is a calculation based on the measured bulk density, a typically reported characteristic of rock materials. The bulk density is measured by:

$$\rho_{sat} = \frac{M_{sat}}{V_{total}} \tag{2.2}$$

where M_{sat} is the total mass of a fully saturated sample and V_{total} is the total volume of a sample. Well logging tools, i.e. the gamma ray log, are also available to estimate the bulk density of materials in the earth [102]. Table 2.4 includes a report of the measured bulk density of the tested shale samples. Porosity is inferred by considering the bulk density as an average density of all the constituents of the porous rock:

$$\rho_{sat} = (1-\phi)\sum_{i=1}^{N}\left(\frac{m_i}{\rho_i}\right) + \phi\rho_{fl} \tag{2.3a}$$

$$\Downarrow$$

$$\phi_\rho = \frac{\rho_{sat} - \left(\sum_{i=1}^{N}\left(\frac{m_i}{\rho_i}\right)\right)^{-1}}{\left(\sum_{i=1}^{N}\left(\frac{m_i}{\rho_i}\right)\right)^{-1} - \rho_{fl}} \tag{2.3b}$$

where m_i stands for the mass fractions of the N solid constituents of shale provided by XRD with corresponding bulk densities ρ_i, provided in Table 2.1, and ρ_{fl} is the density of the saturating fluid phase. For the considered shales, water is assumed as the saturating fluid. The results of this porosity estimation are shown in Table 2.4

Consolidation Porosity for BBC

Finally, for the Highly Compressed Resedimented Boston Blue Clay samples, the porosity is estimated by monitoring the volume change during the consolidation process. Consolidation curves for the three samples are shown in Figure 2-7 [2] where void ratio, e, is defined as

$$e = \frac{V_{\text{voids}}}{V_{\text{solids}}} \tag{2.4}$$

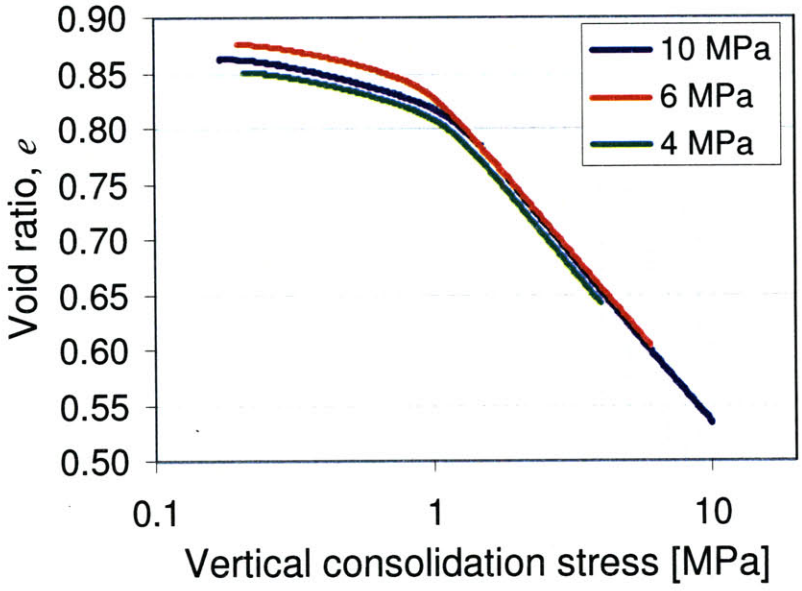

Figure 2-7: Consolidation curves, displayed as void ratio vs. the effective vertical consolidation stress, for Resedimented Boston Blue Clay consolidated to 4, 6, and 10 MPa. The repeatability of the consolidation curve highlights the uniformity of the material. Void ratio information can be translated into porosity. Data provided by N. Abdulhadi [2]

which may be related to porosity by:

$$\phi = \frac{e}{1+e} \tag{2.5}$$

There is a small amount of swelling during the unloading to an overconsolidation ratio of 4, i.e. a reduction by a factor of 4 from the maximum consolidation stress. This swelling increases the void ratio with respect to the maximum void ratio obtained during loading, but it is assumed that no further changes to void ratio or porosity occur after the sample is removed from the oedometer. The void ratios before and after swelling give the range of porosities for the Boston Blue Clay samples.

Summary

Overall, the various samples have porosities spanning an order of magnitude, from 4% to 40%. This wide range of porosities gives another demonstration of the diversity of materials that can be called shale. The different techniques for measuring porosity give relatively similar results. Typically, the bulk density gives higher porosity estimates than mercury porosity, as expected. The average difference is less than 5% of the total volume.

2.3.4 Pore Size Distributions - Deconvolution

The overall porosity data is useful, but as of yet gives no clue as to the length scales involved with porosity. Mercury intrusion porosimetry gives access to distributions of pore throat radius [8], and a quantitative understanding of these distributions can give this length scale information. In the porosimetry experiment, intrusion of mercury proceeds at higher and higher pressures, and the volume of mercury intruded per pressure increment is recorded. A cylindrical pore model is used in conjunction with an understanding of the capillary behavior of a non-wetting fluid, such as mercury. This model and understanding permit a relationship between the pressure applied to the mercury and the pore throat radius at that sampling point. Two primary limitations of the technique are the assumption of a cylindrical pore model, and the assumption that all the volume associated with a particular pressure increment is associated with that pore throat radius. A case where a large pore is only accessible by a small pore throat radius does not match the latter assumption [57]. Despite the limitations of the technique and its analysis,

Sample	Mercury Porosity	Drying Porosity	Neut. Log Porosity	Consolid. Porosity	Bulk Density	Bulk Den. Porosity
GeoGenome Shales						
S1	26	26	-	-	2.20	30
S2	13	17	-	-	2.43	17
S3	7	13	-	-	2.55	7
S4	20	21	-	-	2.33	22
S7	7	12	-	-	2.51	11
Light	6	-	-	-	2.48	10
Dark	4	-	-	-	2.57	9
Pierre	-	-	-	-	2.25-2.40(*)	-
Low-Clay	29	-	-	-	-	-
Woodford Shales						
110	14	-	23	-	2.11	21
131	13	-	16	-	2.21	19
154	12	-	21	-	2.18	23
166	16	-	16	-	2.18	21
175	19	-	19	-	2.26	19
185	15	-	21	-	2.11	26
Boston Blue Clay						
4 MPa	-	-	-	40 - 42	-	-
6.5 MPa	-	-	-	38 - 39	-	-
10 MPa	-	-	-	35 - 37	-	-

Table 2.4: Porosity and bulk density data for the tested shale samples.
(*) from Savage and Braddock [156].

it has been shown that for similarly structured geo-materials, comparisons between pore-size distributions are reliable [151].

To reach a quantitative understanding of the pore size distributions, a fitting deconvolution procedure was used to determine the mean and standard deviation of each pore size family in a given distribution. These pore size families are characterized by distinct peaks in the pore size distrubition. This deconvolution procedure was motivated by the one introduced by Constantinides, Ulm, and co-workers [43], [45], [46], [53] for understanding the results of nanoindentation measurements, which will be further reviewed in the context of nanoindentation in Chapter 4. The technique as adapted for quantitative analysis of pore size distributions is presented in some detail here.

Choice of Phase Distribution Functions

The first point that needs to be addressed is the best *a priori* choice of distribution function for each peak in the frequency plot. A distribution function is uniquely defined by its statistical moments [136]. The first moment about the origin is the mean, while the second moment around the mean is the variance and is usually denoted by σ^2, where σ is the standard deviation. Higher order moments serve to continue refining the definition of a given distribution, including a definition of the skewness, or asymmetry of the distribution. If there was only one pore throat radius associated with each material, one would expect a single infinitely sharp peak in the probability distribution function (PDF) of the pore size distribution, while for two distinct pore throat radii, two infinitely sharp peaks would be expected. In this case, each peak would be characterized by its first moment (mean value) only. In a natural material like shale, however, variation around a mean value is expected.

Two relatively simple distributions emerge as possible candidates, the normal or Gaussian distribution and the log-normal distribution. The normal distribution is a special distribution which arises as a consequence of the limit sum of any set of independent, identically distributed random variables. This explains why the normal distribution is commonly used to describe experimental results – regardless of whatever probability distribution describes an individual experimental result, the distribution of a large number of experiments (which should theoretically measure one single property) will converge to a normal distribution [6].

The probability density function (PDF) of the normal distribution is given by

$$f_X(x) = \frac{1}{\sqrt{2\pi}s} \exp\left(-\frac{(x-\mu)^2}{2s^2}\right) \tag{2.6}$$

where μ is the mean and s^2 is the variance of the data set. As a two-parameter distribution, the normal distribution maybe notated in statistical shorthand by:

$$x \sim N\left(\mu,\ s^2\right) \tag{2.7}$$

The Cumulative Distribution Function (CDF) of the normal distribution is not determined analytically (although it is well-known and well-tabulated).

The log-normal distribution arises from the limit *product* of any set of independent, identically distributed random variables. It is mathematically intuitive that the log of a quantity or function dealing with products corresponds to a quantity or function dealing with sums, as the log-space is dealing with exponents (and exponents add when they are multiplied). The lognormal distribution is similar to the normal distribution [6]. It is also natural to consider a lognormal distribution for pore size distributions as pore sizes within a given material can span many orders of magnitude. Indeed, the results of porosimetry measurements are typically plotted in semi-log space. The lognormal distribution has been shown to apply to a large range of natural applications [122]. It has been shown, for example, that pore size distributions in cementitious materials, which may have similar pore structures as shale materials, tend to follow lognormal distributions [58], [164].

The PDF of the log-normal distribution is given by

$$f_X(x) = \frac{1}{X}\frac{1}{\sqrt{2\pi}s_{\ln x}} \exp\left(-\frac{(\ln x - \mu_{\ln x})^2}{2s_{\ln x}^2}\right) \tag{2.8}$$

where $\mu_{\ln x}$ is the mean of the "logged" data and $s_{\ln x}^2$ is the variance of the "logged" data. As a two-parameter distribution, the log-normal distribution maybe notated in statistical shorthand by

$$x \sim LN\left(\mu_{\ln x},\ s_{\ln x}^2\right) \tag{2.9}$$

A study of the transformation of variables between the normal and log-normal distributions gives a set of relationships between the mean and variance of normal and log-normal distributions [6]. If $X \sim N\left(\mu_X,\ s_X^2\right)$, then $Y = e^x \sim LN\left(\mu_Y,\ s_Y^2\right)$, with mean value and variance given by

$$\begin{aligned} \mu_Y &= \exp\left(\mu_X + \frac{1}{2}s_X^2\right) \\ s_Y^2 &= \exp\left(2\mu_X + s_X^2\right)\left(e^{s_X^2} - 1\right) \end{aligned} \tag{2.10}$$

To work backwards, $X = \ln Y$, and μ_X and s_X^2 may be found from μ_Y and s_Y^2 by

$$\begin{aligned} \mu_X &= 2\ln\left(\mu_Y\right) - \frac{1}{2}\ln\left(s_Y^2 + \mu_Y^2\right) \\ s_X^2 &= -2\ln\left(\mu_Y\right) + \ln\left(s_Y^2 + \mu_Y^2\right) \end{aligned} \tag{2.11}$$

Implementation of Deconvolution Technique

The deconvolution technique operates on the experimental CDF because it does not require the use of bin sizes that would be necessary to generate an experimental histogram or frequency plot of a PDF. The experimental CDF is defined in a discrete manner, such that $D_r\left(r_i\right)$ is defined as the percentage of pore volume that exists in pores with pore throat radii smaller than r_i sampled at N different points.

The overall distribution is considered as the weighted sum of distributions for n material phases with sufficient contrast in pore throat radii. The j-th pore family occupies a volume fraction f_j of the total porosity. Considering first the Gaussian distribution to describe the distribution of pore size families, identified by mean value μ_j^r and standard deviation s_j^r. The CDF of the j-th Gaussian distributed family of pore throat radii, r, is given by:

$$D(r_i; \mu_j^r, s_j^r) = \frac{1}{s_j^r\sqrt{2\pi}} \int_{-\infty}^{r_i} \exp\left(\frac{-(u-\mu_j^r)^2}{2(s_j^r)^2}\right) du \tag{2.12}$$

The unknowns $\{f_j, \mu_j^r, s_j^r\}$ for $j \in [1, n]$ are determined by minimizing the difference between

the experimental CDFs and the weighted model-phase CDFs at each of the N sampling points:

$$\min \sum_{i=1}^{N} \sum_{r} \left(\sum_{j=1}^{n} f_j D(r_i; \mu_j^r, s_j^r) - D_r(r_i) \right)^2$$
$$s.t. \tag{2.13}$$
$$\sum_{j=1}^{n} f_j = 1$$

where the constraint of the minimization problem requires that the volume fractions of the different pore size families sum to one. To ensure that pore size families have sufficient contrast, and thus to avoid that two neighboring Gaussians overlap, the optimization problem is additionally constrained by:

$$\mu_j^r + s_j^r \leq \mu_{j+1}^r - s_{j+1}^r \tag{2.14}$$

A similar operation is applied when considering log-normal distributions rather than Gaussian distributions. The CDF of the j-th lognormal distributed family of pore throat radii, r, is given by:

$$D_{LN}(r_i; \mu_{\ln r,j}, s_{\ln r,j}) = \frac{1}{r} \frac{1}{s_{\ln r,j}\sqrt{2\pi}} \int_{-\infty}^{r_i} \exp\left(-\frac{(\ln u - \mu_{\ln r,j})^2}{2 s_{\ln r,j})^2} \right) du \tag{2.15}$$

As before, the unknowns $\{f_j, \mu_j^{\ln r}, s_j^{\ln r}\}$ for $j \in [1, n]$ are determined by minimizing the difference between the experimental CDFs and the weighted model-phase CDFs at each of the N sampling points:

$$\min \sum_{i=1}^{N} \sum_{r} \left(\sum_{j=1}^{n} f_j D_{LN}(r_i; \mu_{\ln r,j}, s_{\ln r,j}) - D_r(r_i) \right)^2$$
$$s.t. \tag{2.16}$$
$$\sum_{j=1}^{n} f_j = 1$$

where the constraint of the minimization problem requires that the volume fractions of the different pore size families sum to one. Again, it is important to ensure that the pore size

families have sufficient contrast, adding the constraint:

$$\mu_{\ln r,j} + s_{\ln r,j} \leq \mu_{\ln r,j+1} - s_{\ln r,j+1} \tag{2.17}$$

The deconvolution procedure, implemented as an optimization problem, is automated except for two choices. First, the model distribution (Gaussian or log-normal) must be chosen, and second, the number of pore size families, n, to consider must be identified. Fortunately, it has been demonstrated for many natural phenomena that many distributions may be equally well modeled by a normal distribution and a lognormal distribution [122]. In addition, visual inspection of the fitted model distributions can give qualitative preference to one form or another. Visual inspection of experimental distributions also provides a straight-forward way to determine the number of pore size families to consider. For the shales studied here, most are best fitted by a single Gaussian distribution. When two pore size families are evident, the experimental distribution is best fit by two lognormal distributions. These results are presented next.

Results of pore size deconvolution

Although the deconvolution technique operates on the experimental CDF, the PDF is more visually intuitive, so presentation of results is in terms of frequency plots. Mercury intrusion porosimetry was performed by Chevron for most of the GeoGenome shale samples as well as for the Woodford shale samples. These results, along with fitted distributions, are presented in Figures 2-8 to 2-10. For the first four GeoGenome Shales, a single normal distribution provides the best fit to experimental data, as shown in Figure 2-8. For the Light and Dark GeoGenome shales, two log-normal distributions provide the best fit, as seen in Figure 2-9. Finally, a single normal distribution provided the best fit to experimental data for the Woodford Shales, as seen in Figure 2-10. Table 2.5 presents the results of these fittings.

Porosity and the Multi-Scale Thought Model for Shale

The results from porosimetry, including the detailed quantitative information obtained from deconvolution and fitting of model distributions, give information about the length scale of

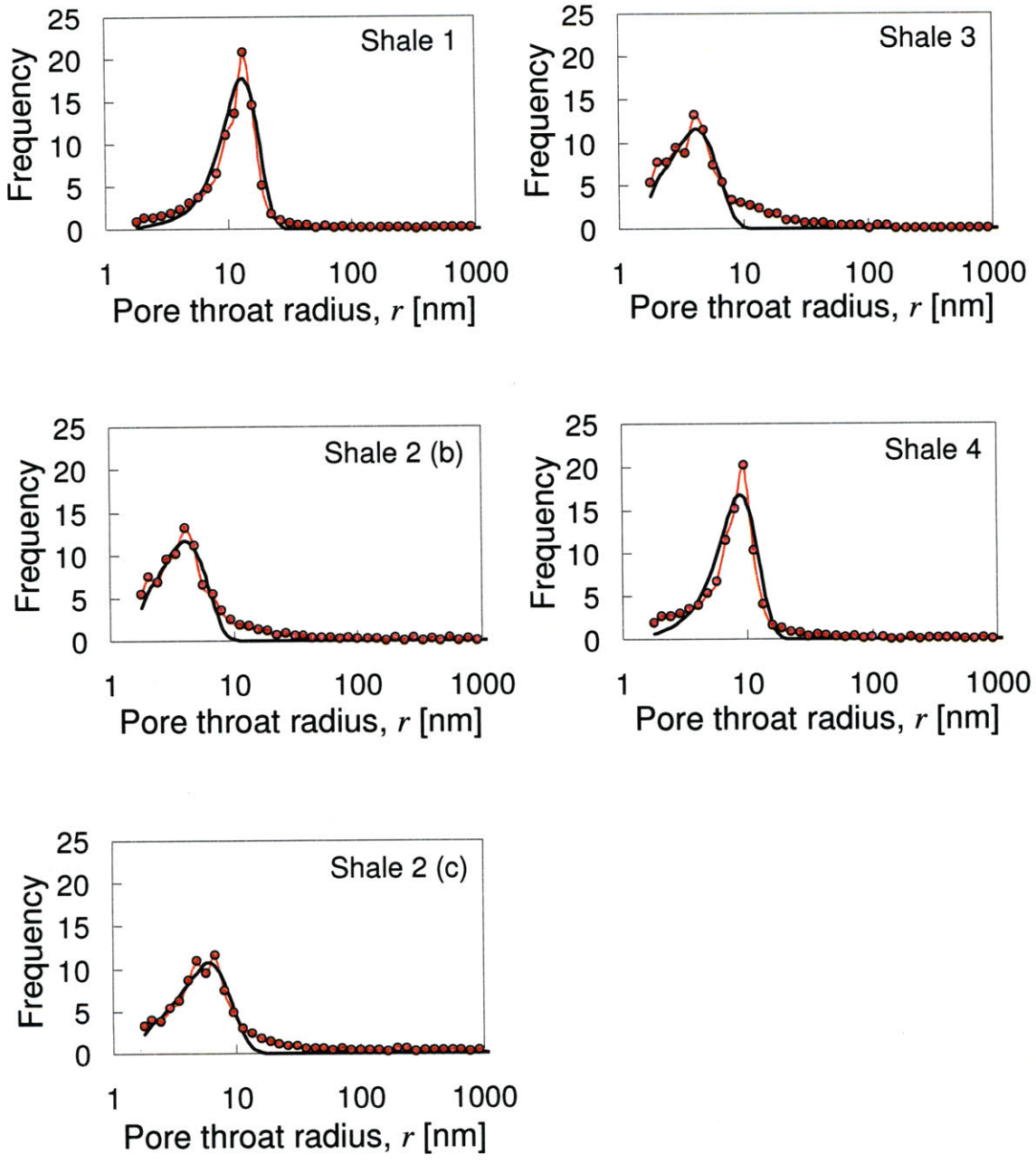

Figure 2-8: Fitted pore size distributions, displayed as PDFs, for 4 of the GeoGenome shales (2 samples of Shale 2 were tested). The experimental distributions (connected red dots) were fitted using a single Gaussian distribution (solid black line).

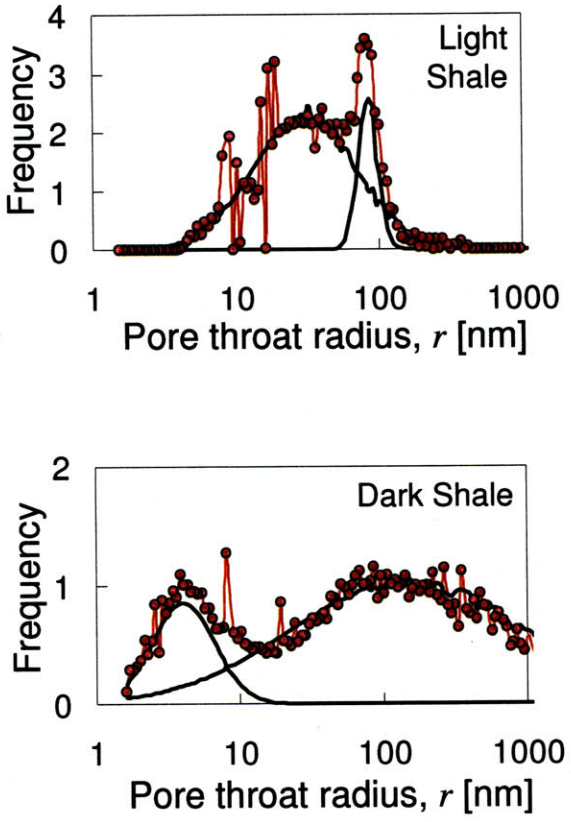

Figure 2-9: Fitted experimental pore size distributions (connected red dots), displayed as PDFs, for 2 of the GeoGenome shales. Two lognormal distributions (solid black lines) were used in the deconvolution fitting.

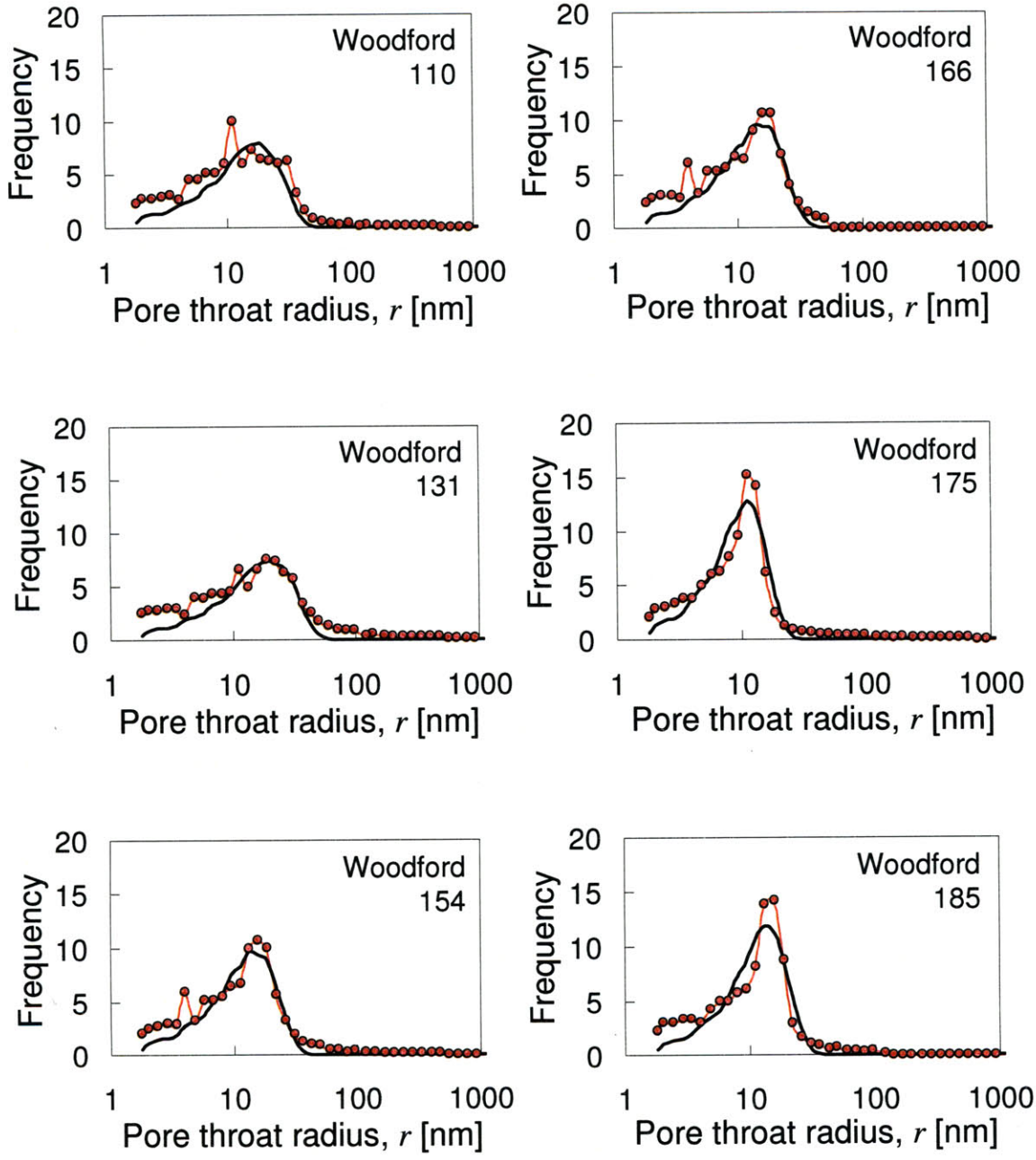

Figure 2-10: Fitted pore size distributions, displayed as PDFs, for the 6 tested Woodford shale samples. The experimental distributions (connected red dots) were fitted using a single Gaussian distribution (solid black line).

Sample	r, First Peak mean	S.D.	f	r, Second Peak mean	S.D.	f
GeoGenome Shales						
S1	12.5	5.0	100	-	-	-
S2	4.6	3.6	100	-	-	-
S3	3.4	2.3	100	-	-	-
S4	8.3	3.6	100	-	-	-
Light	39.2	30.2	82	85.5	2.2	18
Dark	5.6	3.8	34	238	560	66
Woodford Shales						
110	10.6	13.0	100	-	-	-
131	11.2	15.3	100	-	-	-
154	10.7	9.5	100	-	-	-
166	11.1	9.9	100	-	-	-
175	9.3	5.8	100	-	-	-
185	11.2	7.7	100	-	-	-

Table 2.5: Mean pore throat radius for the tested shale samples. Mean and standard deviation values in nm. Volume fraction, f, is expressed as a percentage of pore volume. For the Light and Dark shales where lognormal distributions were used, the actual mean and standard deviation are reported.

porosity. The results show that a typical pore throat radius is on the order of tens of nanometers, with the possibility of pore sizes as large as about 1 micron. Even for the shale samples with two pore families, both mean porosities are at the scale of Level '1' in the multiscale model for shale, implying that porosity should be considered as an integral feature of Level '1.'

Some shale researchers suggest that shales possess microcracks [181], [169], which would enter the multiscale thought model for shale at the scale of Level '2.' Neither the mercury intrusion porosimetry results nor the microscopy images provide any evidence of microcracking or other larger scale porosity in any of the considered materials, which are representative of a wide variety of shale materials. As a result, all porosity in the shale materials studied here is considered at the scale of Level '1.'

2.4 The Multiscale Model and Volume Fraction Parameters

The mineralogy and porosimetry investigation of the considered set of shale materials bolsters the definition of the different levels in the multiscale thought model for shale. In particular,

this analysis adds to consideration of key volume fraction parameters for each level, which are important for micromechanical experimentation and modeling [3].

Detailed mineralogy measurements in terms of mass fractions may be translated into volume fractions with a knowledge of the densities of individual minerals. The volume fraction V_i of each constituent is given by:

$$V_i = (1-\phi)\frac{m_i/\rho_i}{\sum_{i=1}^{N}(m_i/\rho_i)} \tag{2.18}$$

where m_i is the mass fraction of each constituent with bulk density ρ_i. The volume fractions differ based on the method used to calculate the porosity of the material.

2.4.1 Inclusion Volume Fraction at Level '2'

The microscope images presented in Section 2.2 provided the first clues that the silt and sand sized particles were the dominant heterogeneity at the scale of Level '2.' A consideration of the particle sizes of typical clay minerals in shale, and of the average pore sizes demonstrates that these constituents enter at much smaller scales. As a result, they may be considered to be homogeneous at the scale of Level '2.'

The inclusion volume fraction, f_{inc}, is identified as the key volume fraction parameter for Level '2.' To obtain this parameter, the solids with volume fractions of $V_s = 1-\phi$ are categorized as clay minerals (CM), non-clay minerals (NC), and kerogen (K), such that $V_s = V_{CM} + V_{NC} + V_K$. The non-clay minerals are predominantly quartz and feldspar, but also can include smaller amounts of plagioclase, calcite, dolomite, ankerite, halite, pyrite, barite, anhydrite, gypsum, and alunite. The inclusion volume fraction is calculated as:

$$f_{inc} = \frac{V_{NC}}{V_{total}} = (1-\phi)\frac{\sum_{i=1}^{NC} m_i/\rho_i}{\sum_{i=1}^{N}(m_i/\rho_i)} \tag{2.19}$$

The value of f_{inc} depends on the method for estimating the porosity of the sample. Maximum values for porosity, such as those obtained from mineralogy and bulk density measurements, give a minimum for inclusion volume fraction. Conversely, minimum values for porosity, such as those obtained by mercury intrusion, give a maximum for inclusion volume fraction. Figure 2-11 (top) compares the minimum and maximum estimates for inclusion volume frac-

[3] The presentation of this section is inspired by the presentation of Ortega et al. [145]

Sample	$f^{inc}_{\min}$	$f^{inc}_{\max}$	$\overline{f}^{inc}$	$\phi_{\min}$	$\phi_{\max}$	$\overline{\phi}$	$\eta_{\min}$	$\eta_{\max}$	$\overline{\eta}$	f_k
GeoGenome Shales										
S1	0.155	0.164	0.159	0.260	0.299	0.279	0.647	0.689	0.668	-
S2	0.225	0.235	0.230	0.133	0.169	0.151	0.782	0.827	0.804	-
S3	0.275	0.276	0.275	0.075	0.076	0.075	0.896	0.897	0.896	-
S4	0.321	0.331	0.326	0.196	0.221	0.208	0.675	0.708	0.691	-
S7	0.269	0.279	0.274	0.075	0.108	0.091	0.853	0.897	0.875	-
Light	0.615	0.643	0.629	0.065	0.098	0.081	0.746	0.819	0.783	-
Dark	0.588	0.620	0.604	0.036	0.087	0.062	0.790	0.904	0.847	-
Pierre	0.466	0.524	0.495	0.168	0.257	0.213	0.517	0.647	0.582	-
Low-Clay	-	0.560	0.560	0.290	-	0.145	-	0.341	0.341	-
Woodford Shales										
110	0.433	0.470	0.451	0.143	0.210	0.176	0.630	0.730	0.680	0.598
131	0.372	0.401	0.386	0.127	0.189	0.158	0.700	0.788	0.744	0.487
154	0.349	0.399	0.374	0.119	0.230	0.174	0.647	0.724	0.686	0.518
166	0.343	0.365	0.354	0.156	0.208	0.182	0.684	0.719	0.702	0.494
175	0.378	0.378	0.378	0.190	0.189	0.190	0.696	0.695	0.695	0.359
185	0.326	0.376	0.351	0.145	0.260	0.202	0.615	0.691	0.653	0.394
Boston Blue Clay										
4 MPa	0.116	0.120	0.118	0.399	0.419	0.409	0.526	0.546	0.536	-
6.5 MPa	0.121	0.125	0.123	0.376	0.394	0.385	0.552	0.571	0.561	-
10 MPa	0.125	0.129	0.127	0.355	0.375	0.365	0.571	0.593	0.582	-

Table 2.6: Volume fraction data for the tested shales.

tion, and Table 2.6 presents the values $f^{inc}_{\min}$ and $f^{inc}_{\max}$. The comparisons between minimum and maximum are relatively close, with a mean difference of 2% of total volume. Rather than continuing to report a minimum and maximum value, instead consider the mean value (denoted by the overbar) and an uncertainty associated with the porosity calculation:

$$\overline{f}^{inc} = \frac{1}{2}\left(f^{inc}_{\min} + f^{inc}_{\max}\right) \pm \frac{1}{2}\left(f^{inc}_{\max} - f^{inc}_{\min}\right) \tag{2.20}$$

This mean value is also reported in Table 2.6. In future plots, the ($\pm$) uncertainty is displayed as an error bar on both sides of the mean value.

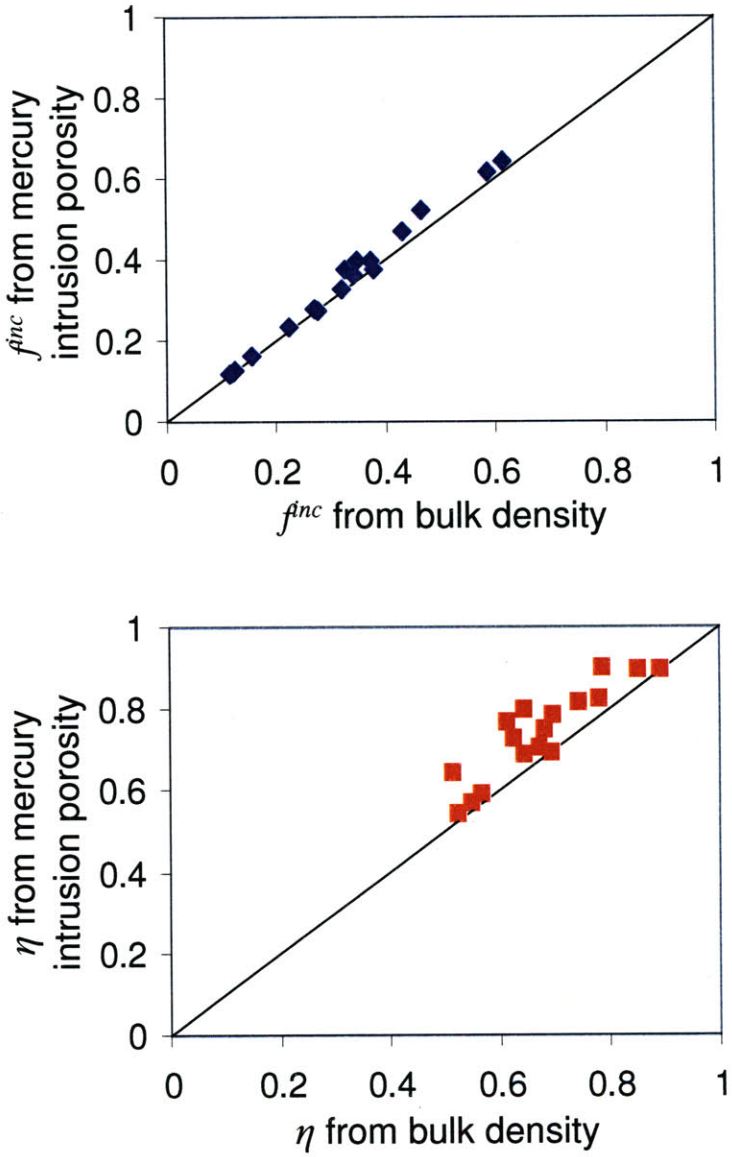

Figure 2-11: Comparisons of inclusion volume fraction (top) and clay packing density (bottom) estimates, based on mineralogy and on porosity estimated by bulk density and mineralogy (which gives minimum results) or on porosity estimated by mercury intrusion (which gives maximum results).

2.4.2 Clay Packing Density at Level '1'

The microscope images presented in Section 2.2 provided the first clues that heterogeneities in Level '1' were associated with clay minerals and pores. Typical clay mineral sizes on the order of tens of nanometers to 2 microns, and pore throat radii of similar scales, give further evidence for this observation. Although shale materials are comprised of many different clay minerals, as evidenced by the mineralogy data reported in Table 2.3, these minerals coexist at the same length scale in shale. From this perspective, there is no difference between illite, smectite, kaolinite, and other clay minerals.

As a result, the volume fraction parameter associated with Level '1' is the clay packing density, η. The clay packing density can be expressed in terms of the total porosity, ϕ, and the inclusion volume fraction, f_{inc}, by:

$$\eta = 1 - n = 1 - \frac{\phi}{1 - f_{inc}} \tag{2.21}$$

where n is the clay porosity.

As before, the method of porosity estimation plays an important role in the calculation of clay packing density. Maximum values for porosity, such as those obtained from mineralogy and bulk density measurements, give a minimum for clay packing density, while the minimum values for porosity, such as those obtained by mercury intrusion, give a maximum for clay packing density. Figure 2-11 (bottom) compares the minimum and maximum estimates for clay packing density, and Table 2.6 presents the values $\eta_{\min}$ and $\eta_{\max}$. The comparisons between minimum and maximum are not as good as the inclusion volume fraction, but are still relatively close, with a mean difference of 6.5% of total volume. Rather than continuing to report a minimum and maximum value, instead consider the mean value and an uncertainty associated with the porosity calculation:

$$\overline{\eta} = \frac{1}{2}\left(\eta_{\min} + \eta_{\max}\right) \pm \frac{1}{2}\left(\eta_{\max} - \eta_{\min}\right) \tag{2.22}$$

This mean value is also reported in Table 2.6. In future plots, the ($\pm$) uncertainty is displayed as an error bar on both sides of the mean value.

For shales with kerogen, such as the Woodford shale, the clay packing density includes kerogen as a "clay" because of the length scales associated with kerogen. Nonetheless, kerogen is expected to have mechanical properties which differ from those of clay minerals. As a result, another volume fraction parameter is needed for kerogen-rich shales. The kerogen volume fraction is expressed as a fraction of solid materials at Level '1':

$$f_k = \frac{V_{\text{kerogen}}}{1 - f_{inc} - \phi} \tag{2.23}$$

For the Woodford shale, this volume fraction parameter is also reported in Table 2.6.

2.5 Chapter Summary

This chapter began by introducing the multiscale thought model for the structure of shale. This model provided a framework for exploring the mineralogy and porosity of shale. A detailed quantitative understanding of the pore sizes in the considered materials was provided by applying a statistical deconvolution analysis to the experimental pore size distributions. Mineralogy and porosity information demonstrated a wide diversity of material composition in various shales, which provides a likely starting point for explaining the wide diversity in shale's mechanical properties.

Key volume fraction parameters, motivated by the multiscale model, were identified to summarize the compositional diversity of shale. In particular, at the scale of Level '2', the inclusion volume fraction, f_{inc}, was identified as the controlling parameter. At the scale of Level '1', clay packing density η is the key parameter, and additionally the kerogen fraction f_k is needed to fully describe kerogen-rich shales. Some variation exists in the experimental determination of these parameters, based on different methods for assessing the porosity of the shale materials. These three parameters focus entirely on volume fractions, and do not transmit any information about the clay mineralogy or about the shapes of particles and pores.

The focus of this thesis is to link the composition of shale with its engineering performance by assessing its microstructure and material invariant properties. This chapter has confirmed the compositional diversity of shale materials, but the multiscale thought model for the structure of shale provides a framework for understanding three key parameters that summarize this

diversity. In particular, we wish to assess the microstructure and material invariant properties of the porous clay composite at the scale of Level '1,' associated with the clay packing density, η. The next two chapters review the nanoindentation technique that is designed to measure the sought properties at the scale of Level '1,' and to assess how these properties relate to the clay packing density.

Chapter 3

Nanoindentation Methods and Indentation Analysis for a Homogeneous Solid

This chapter provides an introduction to general concepts of nanoindentation. The experimental nanoindentation technique, including a description of the equipment employed for this study, opens the chapter. The remainder of the chapter presents a review of analysis techniques that aim to link quantities measured by nanoindentation to properties describing the mechanical behavior of a homogeneous solid. Included are a discussion of the importance of self-similarity in indentation, development of the indentation modulus measurement, and development of the hardness measurement. The next chapter will review ways of extending this analysis to natural, heterogeneous, porous composite materials such as shale.

3.1 Nanoindentation Technique

An indentation test is a surface test that gives access to bulk properties using the tools of continuum indentation analysis. Indentation tests have been used to measure hardness for over a century (for a review see [24] and references cited therein). More recently, thanks to progress in hardware and software control, depth sensing techniques were introduced. This new generation of equipment allows a continuous monitoring of the load on the indenter and

the displacement of the indenter into the specimen surface during both loading and unloading. The idea of depth sensing techniques and its implementation down to the nanoscale appears to have developed first in the former Soviet Union from the mid 1950s on throughout the 1970s. These ideas have received considerable attention world-wide since Doerner and Nix [61] and Oliver and Pharr [142], in the late 1980s and early 1990s, identified indentation techniques for analysis and estimation of mechanical properties of materials.

3.1.1 Equipment

Nanoindentation experiments for this study were performed on two different test platforms. The platforms are similar in principle, but have slight variations in the methods of surface detection, load application, and displacement sensing. The first test platform is a Hysitron Triboindenter ("Hysitron") located in the Nanomechanical Technology Laboratory in the Materials Science and Engineering Department at MIT. An overall view of the apparatus is shown in Figure 3-1 (top). Force is applied to the indenter tip electrostatically by means of a three-plate capacitor system. This system is also employed to measure the displacement of the indenter tip. A schematic diagram of the transducer and indenter tip system is shown in Figure 3-1 (bottom). The indenter is also equipped with an optical microscope for selecting the areas to be indented and a piezoelectric crystal that allows the indenter to map the surface topography of the sample with the indenter tip. The Hysitron is also equipped with an Atomic Force Microscope (AFM) that permits, after careful calibration, a more precise mapping of the surface topography of the sample after an indentation. The samples and indenter heads are located on a platform which rests on an anti-vibration table and is housed inside a sealed box to minimize temperature drifts and acoustic noise. The system is managed via a personal computer for experimental control, data acquisition, and initial analysis work. All measurements are taken electronically and high precision may be achieved. The apparatus is capable of applying and measuring loads between 0 and 30 mN with a resolution of less than one nN. The maximum displacement is 5 μm, with a resolution of 0.2 nm [98].

The second test platform is a CSM Instruments Nano Hardness Tester ("CSM") located in the Department of Civil and Environmental Engineering at MIT. An overall view of the apparatus is shown in Figure 3-2 (top). Force is applied to the indenter tip electrodynamically

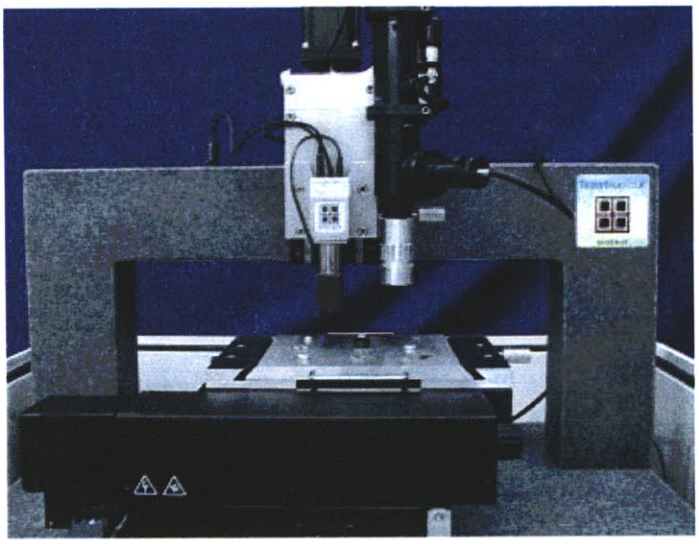

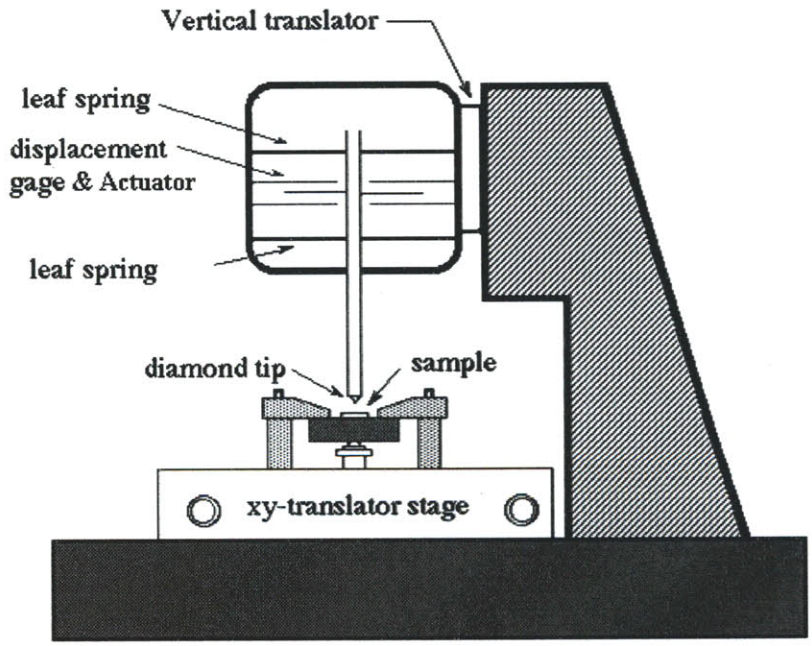

Figure 3-1: Top: Hysitron Triboindenter (from http://www.hysitron.com/) Bottom: A schematic diagram of the nanoindenter (adapted from an image from the Nix Group, mse.stanford.edu).

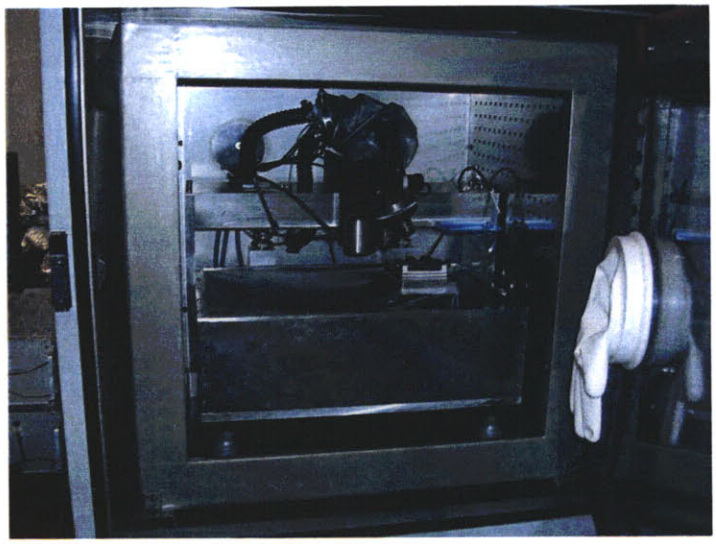

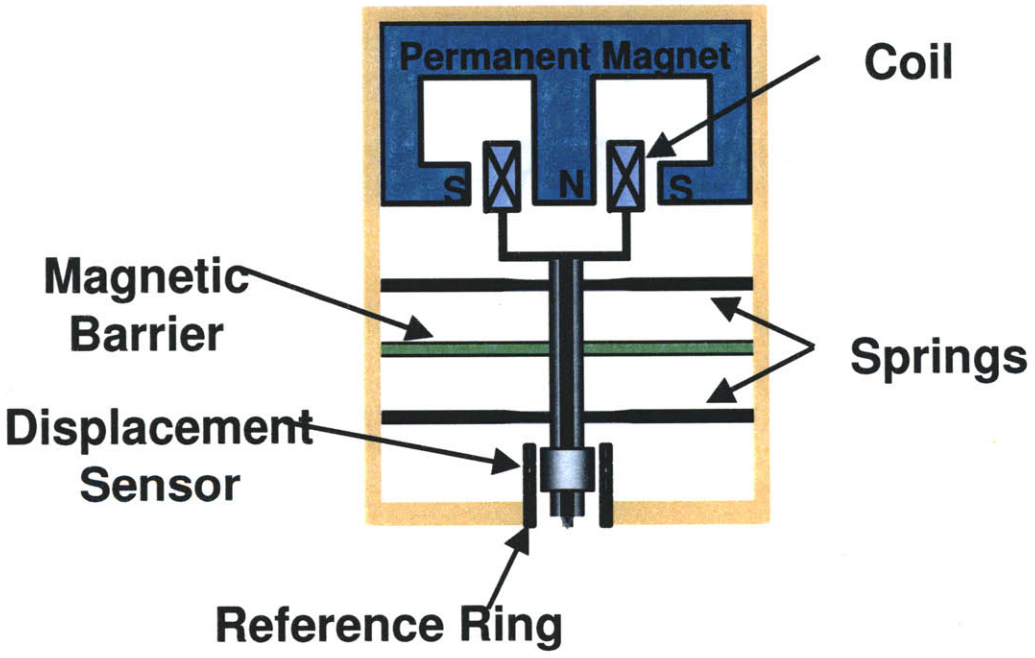

Figure 3-2: Top: Overview of the CSM Nano-Hardness tester (in an environmentally controlled chamber). Bottom: Schematic of the measurement head of the the CSM Nano-Hardness tester (courtesy N. Randall, CSM Instruments).

by means of a speaker coil, and displacement of the indenter tip is measured by a capacitance gage. A schematic diagram of the transducer and indenter tip system is shown in Figure 3-2 (bottom). The indentation depth measurements are taken with respect to the position of the reference ring, which rests on the surface of the sample. The indenter is also equipped with an optical microscope for selecting the areas to be indented. The samples and indenter heads are housed inside a sealed box to minimize temperature drifts and acoustic noise, and the entire apparatus rests on an anti-vibration table. The system is managed via a personal computer for experimental control, data acquisition, and initial analysis work. All measurements are taken electronically and high precision may be achieved. The apparatus is capable of applying and measuring loads between 0 and 62.5 mN with a resolution of one μN. The maximum displacement is 20 μm, with a resolution of 0.3 nm [50].

3.1.2 Calibrations

A series of calibrations were performed on the nanoindenters before data collection could begin. The Hysitron requires that force and displacement transducer constants are calibrated daily by performing an indent in the air in the Triboindenter chamber. The force-displacement curve comes from the stiffness of the leaf springs whose properties are known; the software adjusts the transducer constants to match the experimental data with the predicted curve. The CSM requires biannual calibration of similar constants, but requires little daily maintenance.

Other calibrations are performed only when required by variations in equipment conditions, such as changing transducers or indenter tips. The first of these calibrations is a stage calibration that applies to both test platforms. This calibration finds the match between the optical location and the indenter tip location by creating a known pattern of indents. The user then selects the center of this pattern and the eventual position of the indenter tip is known. This technique is also used in the Hysitron to calibrate the location of the AFM tip with the indenter tip by selecting the center of the pattern from an AFM scan.

Another calibration is the determination of machine compliance. Machine compliance in the Hysitron is evaluated through an analysis of a series of 100 indents on a known sample, typically fused silica. The maximum load is increased by 100 μN for each indent, and the machine compliance is extracted from a relationship between the results of each indent. Machine

compliance of the CSM is fixed, based on the reference design of the CSM measurement head. With all calibrations complete, the equipment is ready for use.

3.1.3 Typical Procedures

The general procedure for an indentation test consists of several steps, irrespective of the equipment used. For this study, a Berkovich indenter probe, a three sided pyramid, is used. First, the indenter probe makes contact with the sample surface. Next, the indenter probe is pressed into the sample surface to a prescribed load over a prescribed time, held for another prescribed time, and unloaded to zero load for a third prescribed time. The indenter tip is then retracted further from the material surface. The details of this procedure are slightly different for the Hysitron and CSM.

Hysitron

Each indentation in the Hysitron consists of several steps [98]. First, the overall height of the sample surface is calibrated as the indenter tip slowly approaches, and then makes contact with, the surface of the sample. Once indentations begin, the indenter tip returns to a slightly higher position. Then the indenter tip again slowly approaches, and makes contact with, the sample surface. Next, the software records baseline data for at least 6 seconds to determine the appropriate drift correction. Once the drift correction is calculated, this data is discarded, and data collection commences as a prescribed load function is executed. Figure 3-3 shows a plot of the loading function versus time and the measured load response versus depth. In the first segment, the tip remains on the surface for 10 seconds to allow the tip and transducer to settle. Load is applied at a constant rate through open loop control for 15 seconds, when the maximum load is achieved. This load is held for 10 seconds to allow the sample to undergo time dependent deformation before the load decreases at a constant rate for 15 seconds. The tip is then retracted and the stage moved to the next position for indentation.

CSM

The typical procedure in the CSM [50] follows the same basic steps as for the Hysitron, with minor differences. In the CSM, the sample is raised until contact is made with an outer

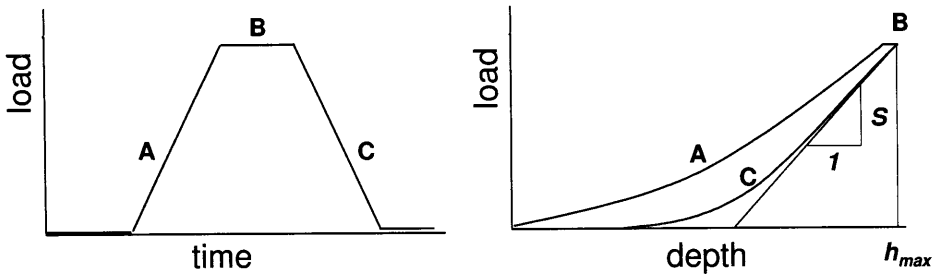

Figure 3-3: Indentation loading function and typical response. (A) is the loading branch, (B) is the holding branch, and (C) is the unloading branch. The initial unloading slope, S, and the maximum depth, $h_{\max}$, are also highlighted.

reference ring. Then, the indenter tip slowly moves through the reference ring and approaches the surface of the sample. When the indenter tip makes contact with the sample surface, a calibration, giving the position of the indenter tip at sample contact relative to the reference ring, is stored. This relative position is used throughout an array of tests. The sample is then lowered from contact with the reference ring. To begin a single test, the stage is moved to a selected position and the sample is raised until contact is made with the reference ring. The indenter tip then slowly approaches and makes contact with the sample surface. Once contact is made, data collection commences as a prescribed load function is executed; the CSM does not require a thermal drift correction because the displacement is measured relative to the reference ring. The same loading function (Fig. 3-3) as in the Hysitron is used. After loading, the tip is retracted, the sample is lowered from contact with the reference ring, and the stage is moved to the next position for indentation.

3.1.4 Typical Indentation Response

The indentation response consists of (at least) three phases; a loading phase, a holding phase, and an unloading phase (Fig. 3-3), during which the force, P, is prescribed. The rigid displacement of the indenter, h, is not necessarily the contact depth, h_c, corresponding to the maximum projected contact surface of the indenter with the deformed half-space surface. The main difficulty of the analysis is that the projected contact area, A_c, is not known *a priori*, but is a solution of a boundary value problem. These dimensions are shown in Figure 3-4.

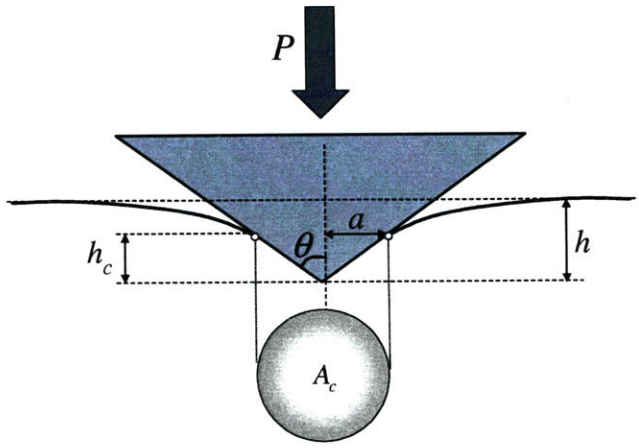

Figure 3-4: Diagram of a typical indentation showing the depth, h, the contact depth, h_c, the contact area, A_c and the (equivalent) cone angle, θ.

Although the typical procedures for indentation with the Hysitron and the CSM vary slightly, the final result of testing with both platforms is an accurately measured report of load and depth versus time, translated into a typical $P - h$ indentation load vs. depth curve (Fig. 3-3). Studies have been made on various materials to check the comparability and repeatability of nanoindentation results between the two test platforms. As the two platforms give practically identical results, no further distinction is made between tests performed on the Hysitron and tests performed on the CSM.

3.1.5 Potential Sources of Measurement Error

Mechanical vibrations are the limiting factor for depth resolution in nanoindentation, which explains the use of vibration-damping tables in both the Hysitron and CSM equipment. Vibrations that cannot be damped contribute to measurement error.

Thermal drift, whether it is actually temperature related or it is a surrogate for electronic drift, can be another potential source of measurement error. Drift can be corrected by analyzing the hold periods at the beginning or end of a test. Such a correction is applied for the Hysitron equipment, although the effect is negligible as long as tests are run at least an hour after the chamber door has been closed, allowing the temperature in the chamber to equilibrate. The reference ring design of the CSM equipment makes thermal drift much less of a concern.

Another potential source of error lies in determining the point at which the indenter probe actually makes contact with the sample surface. This is a particular problem for sharp indenter tips because the contact area at the point of first contact is, in theory, infinitesimally small. Mechanical vibrations and surface roughness can each add to the difficulty of determining the contact point. Uncertainty on the initial contact point can propagate through the rest of the analysis, although it usually on the order of a few nanometers of indentation depth. This error, therefore, is not so significant unless maximum indentation depths are particularly small.

3.2 Self-Similarity of the Indentation Test

While one of the key difficulties in analysis of indentation tests is the determination of the contact area, a key feature of sharp pyramidal (Berkovich) indentation is that the contact problem possesses self-similarity. Self-similarity of indentations depends on three criteria [24]. First, the constitutive relations must be homogeneous functions of stress or strain. Second, the indenter shape must be able to be described by a homogeneous function with degree greater than or equal to one. Finally, the load is assumed to be increasing as the contact is made. The result of self-similarity is that given known homogeneous functions, an initial contact area or contact depth, and a corresponding initial load, the contact area or contact depth at any other load may be calculated using relatively simple scaling formulas. That is, for a given indenter described by a homogeneous function, the average pressure below the indenter is independent of the indentation load and the true contact area. This section reviews these concepts in some more detail. [1]

3.2.1 Geometric Similarity of the Berkovich Indenter

The Berkovich indenter tip, one of the most commonly used indenters, is a three-sided pyramidal tip. The sharp geometry allows for the testing of volumes of materials smaller than is the case with probes of other geometries. However, this sharp geometry generates stress concentrations at the probe tip, so that the indented material is solicited plastically even at low load magnitudes. During indentation with the Berkovich tip, the contact surface between the probe

[1] This Section is inspired by the presentation of the topic by M. Vandamme [177].

and the indenter probe is constantly changing.

For any given probe, within a Cartesian coordinate system $Ox_1x_2x_3$ whose origin is at the tip of the probe, with x_3 going into the depth of the probe (Figure 3-5), the height z of the surface of the probe verifies:

$$z(\lambda x_1, \lambda x_2) = \lambda^d z(x_1, x_2) \text{ with } \lambda > 0 \tag{3.1}$$

where d is the degree of the homogeneous function. For axisymmetric probes, Eq. (3.1) can be condensed into:

$$z(r) = Br^d \tag{3.2}$$

where r is the radius of the probe at a given height z, and B is a proportionality factor that represents the radius at unit radius (Figure 3-5). The degree is $d = 1$ and the proportionality factor is $B = \cot(\theta^{eq})$ for the Berkovich probe, where θ^{eq} is an equivalent cone angle to be developed next.

Two objects which can be transformed into each other by dilation or contraction are 'geometrically similar'. Applied to the considered indenter geometries, all flat punch indenter probes are geometrically similar. In contrast, pyramidal indenters are invariant when contracted or dilated. That is, pyramidal and conical indenters are similar to themselves and are said to be 'geometrically self-similar'. Making use of this geometric self-similarity, the non-axisymmetric pyramidal probes are often approximated, for the purpose of indentation analysis, by axisymmetric cones of same degree $d = 1$, which greatly simplifies the indentation analysis as shown later on (Section 3.3.1). This is achieved by means of an equivalent half-cone angle (or cone opening angle) θ^{eq}, whose associated cone gives the same projected contact area for a given depth as the original pyramidal indenter. The contact area function for a perfect Berkovich indenter is [142]:

$$A_c(h) = 24.56h^2 \tag{3.3}$$

and for a conical indenter is:

$$A_c(h) = \pi(h\tan\theta)^2 \tag{3.4}$$

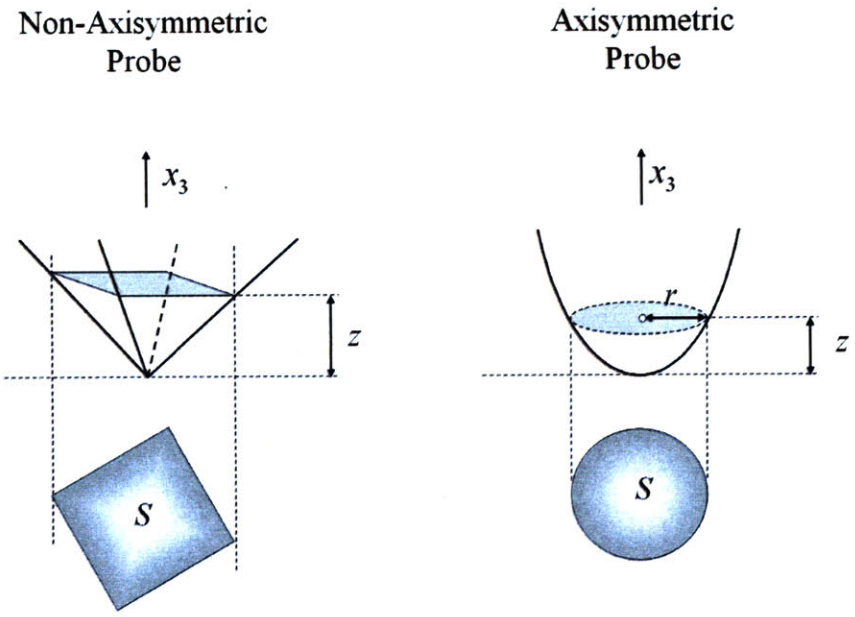

Figure 3-5: Parameters defining the geometry of an indenter probe. z is the height, S the cross-sectional area. For an axisymmetric probe, r is the radius.

which leads to the equivalent half-cone angle of the Berkovich probe:

$$\theta^{eq} = \tan^{-1}\sqrt{\frac{24.56}{\pi}} \approx 70.32^{\circ} \tag{3.5}$$

3.2.2 Material Behavior

For the indentation problem to be self-similar, the constitutive relationships of the indented material need to be homogeneous with respect to the strains (or strain rates) or stresses; which means that the operator of constitutive relations F (and thus the stress tensor $\boldsymbol{\sigma}(\boldsymbol{\varepsilon})$) must scale as:

$$F(\lambda\boldsymbol{\varepsilon}) = \lambda^{\kappa}F(\boldsymbol{\varepsilon}) \tag{3.6}$$

where $\boldsymbol{\varepsilon}$ is the strain tensor, and κ is the degree of the homogeneous constitutive function F. Linear and non-linear elasticity satisfy this requirement, provided that [22]:

$$\boldsymbol{\sigma} = \mathbb{C}(\boldsymbol{\varepsilon}) : \boldsymbol{\varepsilon};\ \mathbb{C}(\lambda\boldsymbol{\varepsilon}) = \lambda^{\kappa-1}\mathbb{C}(\boldsymbol{\varepsilon}) \tag{3.7}$$

where $\mathbb{C}(\boldsymbol{\varepsilon})$ is the secant stiffness tensor; and $\kappa = 1$ in the case of linear elasticity. The condition is also satisfied for a rigid plastic limit behavior, for which the stress derives from the dissipation function (or support function) $\boldsymbol{\sigma} : \mathbf{d} = \pi(\mathbf{d})$; [66]:

$$\boldsymbol{\sigma} = \frac{\partial \pi}{\partial \mathbf{d}}(\mathbf{d}) \tag{3.8}$$

where $\pi(\mathbf{d})$ is a homogeneous function of degree 1 with respect to the strain rate tensor $\mathbf{d}$, such that:

$$\pi(\lambda\mathbf{d}) = \lambda\,\pi(\mathbf{d}) \tag{3.9}$$

In this case, which will be considered in more detail in Section 3.4, it is readily understood that yield design solutions applied to indentation analysis satisfy the self-similarity condition, Eq. (3.6), with $\kappa = 0$.

But not all materials satisfy Eq. (3.6). An instance of such a material is a linear–elastic perfectly–plastic material, for which $\kappa = 1$ within the elastic domain, while $\kappa = 0$ at the limit of the elastic domain corresponding to the strength limit. That is, there is no unique value of κ for which Eq. (3.6) holds for all strain levels eventually present in the indentation test, and indentations performed on linear–elastic perfectly–plastic materials are, therefore, not self-similar. More generally, whenever the material response of the indented half-space is not uniformly governed by the same class of material behavior identified by the constituent coefficient κ, the non-homogeneous stress distribution within the indented half-space may entail a loss of self-similarity of the indentation test. We keep this in mind for later developments.

3.2.3 Self-Similar Scaling Relations

Provided that Eq. (3.1) and Eq. (3.6) are satisfied, the loading phase of an indentation test possesses self-similarity. That is, given a known indentation response, represented by load P_0, indentation depth h_0, contact depth $(h_c)_0$ and projected area of contact $(A_c)_0$ (see Figure 3-4),

the indentation response (P, h, h_c, A_c) is obtained from a similarity transformation [21]:

$$\frac{P}{P_0} = \left(\frac{h}{h_0}\right)^{\frac{2+\kappa(d-1)}{d}} \tag{3.10}$$

For a conical or pyramidal indenter probe ($d = 1$), $P \propto h^2$ irrespective of the material behavior. This provides a strong argument in favor of using the Berkovich indenter, as self-similarity will prevail irrespective of the constitutive relations.

Another relation obtained from the self-similarity of the indentation test is [21]:

$$\frac{h}{h_0} = \left(\frac{A_c}{(A_c)_0}\right)^{\frac{d}{2}} \tag{3.11}$$

which depends only on indenter geometry, and not material behavior.

A combination of the previous two scaling relations readily shows that the average pressure below the indenter —that is the hardness $H = P/A_c$— scales as:

$$\frac{H}{H_0} = \left(\frac{h}{h_0}\right)^{\frac{\kappa(d-1)}{d}} \tag{3.12}$$

Hence, for any rigid plastic behavior ($\kappa = 0$) or for any pyramidal or conical indenter shape, the hardness is constant throughout the loading process, and does not depend on the applied load.

Finally, noting that $A_c = \pi a^2$, where a is the contact radius, Eq. (3.11) can be rewritten as:

$$\frac{a^d}{h} = \text{constant} \tag{3.13}$$

or equivalently, for axisymmetric probes, for which the contact radius a and the contact depth h_c are linked by $h_c = Ba^d$ from Eq. (3.2):

$$\frac{h_c}{h} = \text{constant} \tag{3.14}$$

Thus, provided self-similarity of the indentation test, the contact height –to– indentation depth ratio h_c/h does not depend on the load P. This result is of critical importance for indentation

analysis and forms much of the basis of indirect methods of determination of the projected area of contact A_c in the contact problem.

3.3 Indentation Analysis of Elastic Properties: Indentation Modulus

This section introduces analysis of elastic properties as measured in nanoindentation by indentation modulus. Indentation modulus, with hardness, is one of the two most commonly extracted parameters of an instrumented indentation test. To relate the quantities measured by nanoindentation to material properties, contact mechanics solutions are required. Two approaches are considered, the Galin-Sneddon solution and one based on Green's functions. As shales are known to possess transversely isotropic behavior in elasticity, estimated analytical solutions for related indentation moduli are reviewed.

3.3.1 The Galin-Sneddon Solution

Indentation problems are contact mechanics problems: Two bodies (an indenter and a material half-space) interact mechanically through an area of contact (which is not known a priori except for the specific case of flat punch indentation).[2] Because of the unknown area of contact, the governing equations of a contact mechanics problem are non–linear by nature even if the material behavior is linear. Hertz in 1881 was the first to analytically solve a contact mechanics problem, namely the contact of two elastic spheres [91]. The indentation of an elastic half-space by a rigid indenter was first solved by Love for a flat punch [125] and for a conical punch [126]. The general solution for a rigid axisymmetric indenter of arbitrary shape was given by Galin [73] in 1953 in the former USSR. His solution was presented in the USA by Sneddon [165], and is now known as the Galin-Sneddon solution.

The Galin-Sneddon solution is derived under the assumption of small perturbations, i.e., under the assumptions of both small displacements and small deformations. The geometry of the problem is defined in Figure 3-4. The boundary conditions on the infinite half space to be indented are specified both outside and inside the area of contact. Outside the area of contact,

[2] This Section is inspired by the presentation of the topic by G. Constantinides [44] and M. Vandamme [177].

the surface of the indented material is stress-free. Inside the area of contact, the contact between the indenter tip and the surface of the indented material is frictionless. Therefore, everywhere on the surface of the indented material, the stress vector can only have a z-component. Inside the area of contact, the z-component of the displacement of the surface of the indented material is imposed by the shape of the indenter.

Several methods can be used to solve this problem, one being the use of Hankel transforms (two-dimensional Fourier transforms for circular symmetric functions) on the polar coordinates ρ and ω. As a result of the derivation, for an indenter of monomial shape $z = Br^d$ (Sec. 3.2.1), the indentation load is linked to the indentation depth by:

$$P = \frac{2}{(\sqrt{\pi}B)^{1/d} M_0 \frac{d}{d+1}} \left[\frac{\Gamma\left(\frac{d}{2}+\frac{1}{2}\right)}{\Gamma\left(\frac{d}{2}+1\right)} \right]^{1/d} h^{1+1/d} \tag{3.15}$$

where $\Gamma(x)$ is the Euler Gamma function, $\Gamma(x) = \int_0^\infty t^{x-1} \exp(-t)\, dt$, d is the degree of the homogeneous function describing the shape of the indenter, and M_0 is the plane stress modulus in the case of elastic isotropy:

$$M_0 = \frac{E_0}{1-\nu^2} = 4G_0 \frac{3K_0 + G_0}{3K_0 + 4G_0} \tag{3.16}$$

where the Young's modulus E_0 and Poisson's ratio ν are the isotropic elastic constants, which may also be expressed in terms of bulk modulus K_0 and shear modulus G_0.

For conical indentation, the Galin-Sneddon solution provides the displacement field $\underline{u}$ and the stress field $\boldsymbol{\sigma}$ in the elastic half space. This solution reads in cylindrical coordinates at the surface where the contact area has radius a [165]:

$$u_\rho(\rho < a, 0) = \frac{1-2\nu}{4(1-\nu)} \frac{\rho}{\tan\theta} \left[\ln\left(\frac{\rho/a}{1+\sqrt{1-(\rho/a)^2}} \right) - \frac{1-\sqrt{1-(\rho/a)^2}}{(\rho/a)^2} \right] \tag{3.17}$$

$$u_z(\rho < a, 0) = \frac{1}{\tan\theta} \left[a \sin^{-1}\left(\frac{a}{\rho}\right) + \sqrt{\rho^2 - a^2} - \rho \right] \tag{3.18}$$

$$\sigma_{zz}(\rho < a, 0) = \frac{M_0}{2\tan\theta} \cosh^{-1}\left(\frac{a}{\rho}\right) \tag{3.19}$$

Note that there is a stress singularity for $\rho = 0$ below the tip of an infinitely sharp conical probe.

The solution also yields the contact depth –to– indentation depth ratio h_c/h:

$$\frac{h_c}{h} = \frac{1}{\sqrt{\pi}} \frac{\Gamma\left(\frac{d}{2} + \frac{1}{2}\right)}{\Gamma\left(\frac{d}{2} + 1\right)} \tag{3.20}$$

As expected from the self-similarity of the indentation test (Sec. 3.2.3), h_c/h for a given indenter probe is found to be constant. A differentiation of Eq. (3.15) with respect to the indentation depth h combined with Eq. (3.20) yields the BASh formula, a definition first proposed by Bulychev, Alekhin, and Shorshorov [31]:

$$S = \frac{2}{\sqrt{\pi}} M_0 \sqrt{A_c} \tag{3.21}$$

Since h_c/h is known, the contact depth h_c, and consequently the projected area of contact A_c, can be calculated from the measured indentation depth h. Thus, all variables in the BASh formula, Eq. (3.21), are obtained from the indentation test, and the plane stress modulus M_0 of the indented material can be calculated. Regardless of the actual material behavior (i.e. elastic content or plasticity behavior), M is essentially a measured property and, dropping the subscript, is known as the indentation modulus.

Relevance of Assumption of Small Perturbations

The Galin-Sneddon solution assumes small perturbations, that is small displacements and small deformations. Given that infinite stresses (and therefore infinite strains) occur at the tip of a sharp conical indenter, the assumption of small deformations is surely not valid. Furthermore, by assuming small displacements, the initial and actual configurations are merged, and the boundary conditions are expressed in the initial configuration for the derivation of the Galin-Sneddon solution. With an indenter of half-cone angle θ, the surface of the indented material rotates by $\pi/2 - \theta$ inside the area of contact, which translates to about 20° for a Berkovich probe. Thus the assumption of small displacements is not valid either, and the assumption of small

perturbations has true theoretical restrictions when it comes to indentation analysis. On the other hand, the question of interest for day-to-day indentation analysis is the deviation of the Galin-Sneddon solution from the actual finite strain and large displacement elastic indentation solution.

Researchers have considered corrections for the BASh formula for conical indentation:

$$S = \beta(\nu, \theta)\frac{2}{\sqrt{\pi}} M_0 \sqrt{A_c} \tag{3.22}$$

where the β-factor captures all deviations from the Galin-Sneddon solution. The β-factor for elastic indentation was studied numerically by Hay et al. [85], who found that the β-factor is always greater than unity because the displacement of the surface below the indenter has a non-zero radial component for any compressible material. The Galin-Sneddon solution, which is first-order in nature, disregards this radial displacement. Taking into account the radial displacement and performing a new analytical derivation, Hay et al. proposed an expression for β:

$$\beta(\nu, \theta) = \pi \frac{\frac{\pi}{4} + 0.1548\frac{1-2\nu}{4(1-\nu)}\cot\theta}{\left[\frac{\pi}{2} - 0.8312\frac{1-2\nu}{4(1-\nu)}\right]^2} \tag{3.23}$$

The correction factor depends on both the half-cone angle θ and the Poisson's ratio ν of the indented material. $\beta(\nu = 0.5, \theta) = 1$ for any half-cone angle θ. For an incompressible material, the displacement of the surface has no radial component and the BASh formula, Eq. (3.21), requires no correction.

Finite Elasticity of Indenter Probe

The Galin-Sneddon solution was derived under the assumption of a rigid indenter probe. From a practical point of view, the probe is never rigid. Although stiffer than many materials, probes are often made of diamond, which has a finite Young's modulus, $E_{in} \simeq 1,141$ GPa [50], and Poisson's ratio $\nu_{in} = 0.07$ [50]. Hertz's original contact solution between two elastic spheres already accounted for the different elasticity of the two bodies; from which:

$$\frac{1}{M_0} = \frac{1-\nu_{in}^2}{E_{in}} + \frac{1-\nu^2}{E_0} \tag{3.24}$$

The finite elasticity of the indenter tip is accounted for by approximating the tip-material system as two springs in series with respective plane-stress stiffnesses $E_{in}/(1-\nu_{in}^2)$ and $E_0/(1-\nu^2)$ [142]. In practice, this correction is rather small.

3.3.2 Green's Function Solutions

Solutions for a point indentation can also be derived, employing the Green's function.[3] The solution method for the finite contact problem consists of using the principle of superposition and integrating the contributions of all point indentations over the contact area. This approach has two advantages over the Galin-Sneddon approach:

1. Once the fundamental solution for a point indentation is known, it can be easily applied to various situations without having to reconsider the set of governing equations.

2. The approach can be used to obtain estimates of stress and displacement fields if the problem has no analytical solution. In this case, one needs to assume a stress field in the area of contact, as well as the shape and size of the projected contact surface. The accuracy of the chosen field is checked by comparing the resulting displacements in the contact region with the actual indenter shape. An eventual mismatch can help to quantify the accuracy of the stress field assumption.

Consider conical indentation (with half cone angle θ) into a linear elastic isotropic half-space, defined by polar coordinates ρ and ω. The Green's surface function reads [182]:

$$\mathcal{G} = \frac{\mathcal{H}}{\rho} \tag{3.25}$$

where $\mathcal{H}$ is a constant depending on the elastic properties of the solid. In the case of an isotropic solid, it reads:

$$\mathcal{H} = \frac{1-\nu^2}{\pi E} \tag{3.26}$$

[3] The presentation of this subsection is inspired by that of A. Delafargue [51].

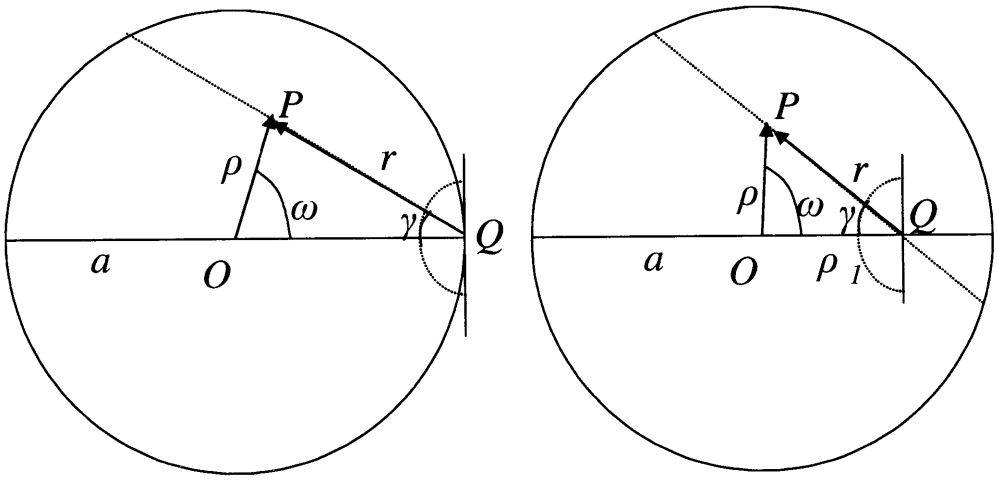

Figure 3-6: Change of variables for the Green's function solutions (from [51]).

The contact area is a circle of radius a, and the pressure distribution is assumed of the form, as in Eq. (3.19):

$$p(\rho) = p_0 \cosh^{-1}\left(\frac{a}{\rho}\right) \tag{3.27}$$

where $p_0 = P/(\pi a^2)$ is the average pressure with respect to the projected contact area. The displacement at any point $Q(\rho, \omega)$ situated on the projected contact surface is given by:

$$u_1(\rho_1, \omega) = \int\int_S p(\rho)\, \mathcal{G}(\rho_1 - \rho)\, \rho d\rho d\omega \tag{3.28}$$

The indentation depth h is equal to the displacement u_1 at the cone tip. Evaluating Eq. (3.28) for $r = 0$ gives:

$$h = u_1(\rho_1 = 0) = 2\pi\mathcal{H}p_0 \int_0^a \cosh^{-1}\left(\frac{a}{\rho}\right) d\rho = \pi\mathcal{H}\frac{P}{a} \tag{3.29}$$

The vertical displacements at the contact edges are found using a change of variables $(\rho, \omega) \rightarrow (r, \gamma)$ as defined on Figure 3-6:

$$h - h_c = u_1(\rho_1 = a) = \mathcal{H}p_0 \int_{-\pi/2}^{\pi/2} \int_{r=0}^{2a\cos\gamma} \cosh^{-1}\left(\frac{a}{\rho}\right) dr d\gamma \tag{3.30}$$

where $\rho^2 = (a - r\cos\gamma)^2 + (r\sin\gamma)^2$. After integrating with respect to r, Eq. (3.30) yields:

$$\begin{aligned} h - h_c &= \mathcal{H}p_0 a\pi \int_{\gamma=-\pi/2}^{\pi/2} \int (1 - |\sin\gamma|)\, d\gamma \\ &= \mathcal{H}\frac{P}{a}(\pi - 2) \end{aligned} \tag{3.31}$$

Finally, combining Eq. (3.31) and (3.30), the ratio h_c/h already given by Eq. (3.20) is obtained:

$$h_c = \frac{2}{\pi} h$$

So far, the assumed stress field, Eq. (3.27), has not been proven to agree with the displacement boundary conditions under the cone. To do so, one needs to calculate the displacement $u_1(\rho_1)$ and show that it is indeed linear in ρ_1 so that it matches the actual conical indenter shape:

$$u_1(0 < \rho_1 < a) = \mathcal{H}p_0 \int_{\gamma=-\pi/2}^{\pi/2} \int_{r=r_-}^{r=r_+} \cosh^{-1}\left(\frac{a}{\rho}\right) dr d\gamma \tag{3.32}$$

where r_- and r_+ are obtained from the change of variables into the coordinates (r, γ):

$$r_- = \rho_1\cos\gamma - \sqrt{a - (r\sin\gamma)^2} \tag{3.33}$$

$$r_+ = \rho_1\cos\gamma + \sqrt{a - (r\sin\gamma)^2} \tag{3.34}$$

and $\rho^2 = (r - \rho_1\cos\gamma)^2 + (\rho_1\sin\gamma)^2$.

After rearrangement, integration with respect to r yields:

$$u_1(0 < \rho_1 < a) = \mathcal{H}p_0 a\pi \int_{\gamma=-\pi/2}^{\pi/2} \int \left(1 - \frac{\rho_1}{a}|\sin\gamma|\right) d\gamma \tag{3.35}$$

$$= \mathcal{H}\frac{P}{a}\left(\pi - 2\frac{\rho_1}{a}\right) \tag{3.36}$$

which shows that the displacement field is linear in ρ_1, confirming that the assumed pressure field is the exact one. Further rearrangement and derivation recovers the BASh formula:

$$P = \frac{2}{\pi}\frac{h^2\tan\theta}{\pi\mathcal{H}} \tag{3.37}$$

$$S = \frac{dP}{dh} = \frac{2}{\sqrt{\pi}}\sqrt{A_c}\frac{1}{\pi\mathcal{H}} \tag{3.38}$$

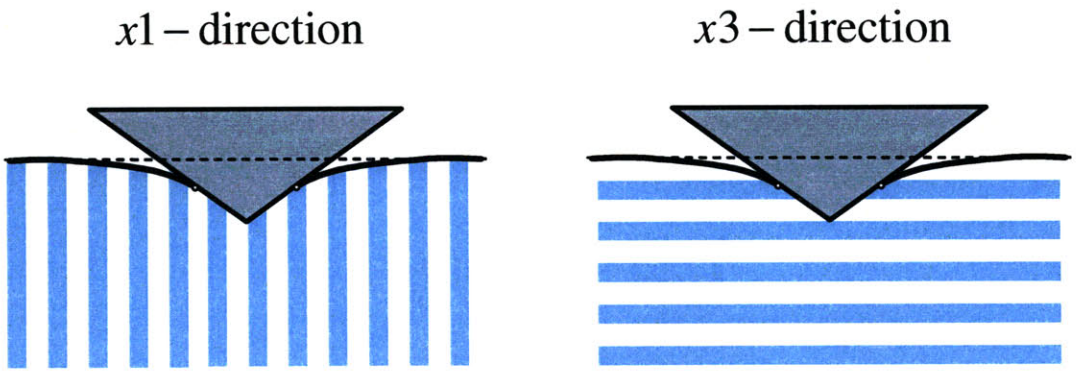

Figure 3-7: Cartoon depicting possibilities for indentation on a transversely isotropic material. Indentation in the $x1$-direction is normal to the axis of symmetry and indenation in the $x3$-direction is parallel to the axis of symmetry.

with the indentation modulus:

$$M_0 = \frac{1}{\pi \mathcal{H}} \tag{3.39}$$

which, with $\mathcal{H}$ defined as in Eq. (3.26), corresponds to the solution obtained in the Galin-Sneddon solution, i.e. Eq. (3.16).

3.3.3 Indentation Modulus and Elastic Anisotropy

Shales exhibit transversely isotropic elasticity behavior, which is typically understood to be associated with the sedimentation process. The full stiffness tensor, in Voigt notation, of such a material is given by

$$\mathbb{C} = \begin{bmatrix} C_{11} & C_{12} & C_{13} & & & \\ C_{12} & C_{22} & C_{13} & & (0) & \\ C_{13} & C_{13} & C_{33} & & & \\ & & & 2C_{44} & 0 & 0 \\ & (0) & & 0 & 2C_{44} & 0 \\ & & & 0 & 0 & 2C_{66} \end{bmatrix} \tag{3.40}$$

where $2C_{66} = C_{11} - C_{12}$, meaning that five independent stiffness components characterize the three dimensional elasticity content.

How to assess the transversely isotropic nature of a material by nanoindentation is a challenge. All five components of the material may be measured macroscopically by careful applications of wave propagation techniques [9]. Nanoindentation, on the other hand, is essentially a one-dimensional test, so the options are limited. The solution is to indent in two perpendicular directions - one which is parallel to the axis of symmetry (termed the $x3$-direction) and one which is normal to the axis of symmetry (termed the $x1$-direction), as shown in Figure 3-7. The axis of symmetry is assumed to be associated with the bedding direction of the shale materials. This is achieved by trimming and mounting shale samples to expose the desired surface for nanoindentation.

Analysis of the nanoindentation $P-h$ curves can then proceed as with an isotropic material. This analysis results in an indentation modulus, M_i, where $i = 1, 3$ correspond to the direction of indentation. Based on the Green's function approach, Delafargue and Ulm [52] developed explicit approximations of the indentation moduli M_1 and M_3 as functions of the components of the stiffness tensor.

Considering first indentation in the $x3$-direction, the problem remains axisymmetric, and the elastic constant $\mathcal{H}$ in the Green's function can be calculated from the components of the stiffness tensor:

$$\mathcal{H} = \frac{1}{2\pi}\sqrt{\frac{C_{11}}{C_{11}C_{33}-C_{13}^2}\left(\frac{1}{C_{44}}+\frac{2}{\sqrt{C_{11}C_{33}}+C_{13}}\right)} \tag{3.41}$$

Indentation in the $x1$-direction is much more complicated, as the problem is no longer axisymmetric, and the projected contact area is no longer circular. Delafargue and Ulm [52] suggested an interpolation between solutions parallel and normal to isotropy planes (i.e. $\mathcal{H}_2 = \mathcal{H}(\omega = 0)$ and $\mathcal{H}_3 = \mathcal{H}(\omega = \pi/2)$):

$$\mathcal{H}_2 = \mathcal{H}(\omega = 0) = \frac{1}{2\pi}\sqrt{\frac{C_{33}}{C_{11}C_{33}-C_{13}^2}\left(\frac{1}{C_{44}}+\frac{2}{\sqrt{C_{11}C_{33}}+C_{13}}\right)} = \sqrt{\frac{C_{33}}{C_{11}}}\mathcal{H} \tag{3.42}$$

$$\mathcal{H}_3 = \mathcal{H}(\omega = \pi/2) = \frac{1}{\pi}\frac{C_{11}}{C_{11}^2-C_{12}^2} \tag{3.43}$$

and the interpolation reads:

$$\widetilde{\mathcal{H}}(\omega) = \frac{\mathcal{H}_2+\mathcal{H}_3}{2} + \frac{\mathcal{H}_2-\mathcal{H}_3}{2}\cos(2\omega) \tag{3.44}$$

Delafargue and Ulm [52] then demonstrated that the projected contact area can be represented by a circle if the actual contact area is an ellipse with elliptical ratio less than 1.25. Derivation of the superposition problem with the circular assumption yields

$$\mathcal{H}_1 = \sqrt{\mathcal{H}_2\mathcal{H}_3} = \sqrt{\frac{1}{\pi}\sqrt{\frac{C_{33}}{C_{11}}}\frac{C_{11}}{C_{11}^2 - C_{12}^2}\mathcal{H}} \tag{3.45}$$

Finally, employing the obtained expressions for the elastic constants $\mathcal{H}$ and $\mathcal{H}_1$ in Eq. (3.37) and deriving with respect to h results in the sought expressions for the indentation moduli [52]:

$$M_3 = 2\sqrt{\frac{C_{11}C_{33} - C_{13}^2}{C_{11}}\left(\frac{1}{C_{44}} + \frac{2}{\sqrt{C_{11}C_{33}} + C_{13}}\right)^{-1}} \tag{3.46a}$$

$$M_1 \approx \sqrt{\sqrt{\frac{C_{11}}{C_{33}}}\frac{C_{11}^2 - C_{12}^2}{C_{11}}M_3} \tag{3.46b}$$

where M_1 is an approximation due to the assumption of circular contact area. Together, these two expressions are a function of all five independent components of the stiffness tensor.

Delafargue and Ulm [52] also generated explict approximations for indentation moduli on orthotropic solids, with nine independent stiffness constants, as given by:

$$\mathbb{C} = \begin{bmatrix} C_{11} & C_{12} & C_{13} & & & \\ C_{12} & C_{22} & C_{23} & & (0) & \\ C_{23} & C_{13} & C_{33} & & & \\ & & & 2C_{44} & 0 & 0 \\ & (0) & & 0 & 2C_{55} & 0 \\ & & & 0 & 0 & 2C_{66} \end{bmatrix} \tag{3.47}$$

For this case, the indentation moduli are different in all three orthogonal directions (i.e. the

$x1$-, $x2$-, and $x3$-directions.). The approximations for indentation moduli M_1, M_2, and M_3 are:

$$\begin{aligned} M_1 &\approx \sqrt{M_{12}M_{13}} \\ M_2 &\approx \sqrt{M_{21}M_{23}} \\ M_3 &\approx \sqrt{M_{31}M_{32}} \end{aligned} \tag{3.48}$$

where

$$\begin{aligned} M_{21} &= 2\sqrt{\frac{C_{21}^2 - C_{12}^2}{C_{11}}\left(\frac{1}{C_{66}} + \frac{2}{C_{21}+C_{12}}\right)^{-1}} \\ M_{31} &= 2\sqrt{\frac{C_{31}^2 - C_{13}^2}{C_{11}}\left(\frac{1}{C_{55}} + \frac{2}{C_{31}+C_{13}}\right)^{-1}} \\ M_{32} &= 2\sqrt{\frac{C_{32}^2 - C_{23}^2}{C_{22}}\left(\frac{1}{C_{44}} + \frac{2}{C_{32}+C_{23}}\right)^{-1}} \end{aligned} \tag{3.49}$$

and

$$\begin{aligned} M_{12} &= M_{21}\sqrt{\frac{C_{11}}{C_{22}}} \\ M_{13} &= M_{31}\sqrt{\frac{C_{11}}{C_{33}}} \\ M_{23} &= M_{32}\sqrt{\frac{C_{22}}{C_{33}}} \end{aligned} \tag{3.50}$$

For either anisotropic case, either transverse isotropy or orthotropy, the indentation moduli obtained from indentations in the primary directions can be seen as 'snapshots' of the elastic behavior. They summarize the elastic material response, characterized by 5 independent stiffness coefficients for transverse isotropy and 9 independent stiffness coefficients for orthotropy into 2 or 3 values, respectively.

3.4 Indentation Analysis of Strength Properties: Indentation Hardness

Attention is now turned to hardness, which is the other parameter most commonly reported from an indentation test. In fact, 'hardness' has been associated with indentation testing for hundreds of years, although early researchers like Mohs (1773-1893) were interested in hardness as a classifying term (i.e. the Mohs scale of mineral hardness) rather than a means to assess material properties. The association between hardness and strength can be traced back to the work of Brinnell, who in 1900 correlated the strength of metal alloy with the shape of the permanent impression left by a small ball of hardened steel or tungsten carbide on the material surface [26].

The focus of this section is to understand indentation hardness as measured by instrumented indentation, in terms of material strength properties. Hardness is the value traditionally obtained from indentation tests, and the classical definition of hardness, H, which can be determined at any point along the $P-h$ curve for which the contact area is known is:

$$H = \frac{P_1}{A_1} = \frac{P_2}{A_2} = ... = \frac{P}{A} \tag{3.51}$$

where $A_c = \pi a^2$ is the projected contact area (which for self-similar indentation is proportional to the true contact area), and $a = h_c \tan\theta$ is the contact radius for a conical indenter (θ is the cone half angle, see Fig. 3-4). With an eye towards an application to shale materials, cohesive-frictional strength behavior is considered (see Tab. 3.1).

3.4.1 Dimensional Analysis for Hardness of a Cohesive-Frictional Material

Dimensional analysis is a powerful tool very often used in sciences to understand physical situations involving several quantities. The fundamental idea is that physical laws do not depend on arbitrarily chosen basic units of measurement. This basic idea leads to the so-called Π-theorem proposed by Buckingham [30], which allows identification of key ratios in the problem, reducing the number of arguments in the different mathematical expressions.

Dimensional analysis has proven useful for understanding the analysis of indentation testing (for a recent review, see [38]). Consider an indentation test where a rigid conical indenter

Friction and Cohesive-Frictional Strength
The concept of friction was first studied by Leonardo Da Vinci (1452-1519). He stated the two basic laws of friction: (i) the area of contact has no effect on friction, and (ii) if the load of an object is doubled, its friction will also be doubled. Guillaume Amontons (1663-1705) also developed an original set of theories. He believed that friction was predominantly a result of the work done to lift one surface over the roughness of another, or from the deforming or the wearing of the other surface. The work of Charles Coulomb (1736-1806) completed Amontons' work, leading to the "Amontons-Coulomb Law" for the contact between two solids: $$F_t = \mu F_n$$ where the frictional force, F_t, is proportional to the normal force, F_n, but independent of the area of the sliding bodies, and their relative velocity. The coefficient μ is commonly known as the coefficient of friction, with friction angle φ defined as $\varphi = \tan^{-1}\mu$. Since the discovery and statement of these laws, researchers have struggled to understand their physical origin, with ever more advanced experimental tools enabling additional research. Determining the actual origin of frictional behavior is still a subject of active research. In the context of strength behavior, cohesive-frictional models capture a pressure sensitivity in strength, meaning that shear strength increases with increasing confining pressure. The coefficient of friction μ can be seen as a measure of pressure sensitivity, with the cohesion c relating to the strength of a material under zero confinment.

Table 3.1: Background: Friction and Amontons-Coulomb Laws (based on [76] and [77])

(half-cone angle θ, indentation depth h) penetrates into an infinite half-space consisting of a cohesive-frictional material, defined by cohesion c and coefficient of friction, μ. The elastic behavior of the solid phase is defined by the plane strain modulus, M_0 (see Eq. (3.16)), and Poisson's ratio ν for the isotropic case, which is considered for the purposes of the dimensional analysis. Dimensional analysis will be employed to understand the effect of these physical quantities on the measured properties from nanoindentation.

The question addressed by dimensional analysis is how those parameters affect the experimentally measurable indentation hardness. To begin, consider the two dependent variables in the loading portion of the contact problem [38] that define the hardness, namely indentation force P and projected contact area A_c:

$$P = f(h, \theta, M_0, \nu, c, \mu) \tag{3.52a}$$

$$A_c = f(h, \theta, M_0, \nu, c, \mu) \tag{3.52b}$$

Indentation load P has dimension of force, projected contact area A_c has dimension of length squared, indentation depth h has dimension of length, and stiffness M_0 and cohesion c have dimensions of force divided by length squared. The other parameters, θ and μ, are dimensionless. As a result, application of the Π-theorem [30] to Eq. (3.52) yields the dimensionless relations:

$$\frac{P}{ch^2} = \Pi_{P,\,\text{load}}\left(\theta, \frac{M_0}{c}, \nu, \mu\right) \tag{3.53a}$$

$$\frac{A_c}{h^2} = \Pi_{A_c}\left(\theta, \frac{M_0}{c}, \nu, \mu\right) \tag{3.53b}$$

A substitution of Eq. (3.53) in Eq. (3.51) readily yields a new invariant, the hardness–to–cohesion ratio:

$$\frac{H}{c} = \frac{\Pi_P}{\Pi_{A_c}} = \Pi_H\left(\theta, \frac{M_0}{c}, \nu, \mu\right) \tag{3.54}$$

The dimensionless relation Π_H confirms that the hardness does not depend on the indentation depth. This is due to the absence of any other length scale in the infinite half-space cohesive-frictional model, including characteristic material lengths, such as the Burgess vector that characterizes dislocations.

3.4.2 Linking Hardness and Strength

Linking indentation hardness to strength properties has been a recent focus of research, as well a traditional practice. It is worthwhile to consider this kind of relationship in terms of the dimensional analysis. Tabor's relationship between hardness, H, and yield strength, Y, of the form $H/Y = 3$ [168] already suggests a dimensionless parameter. This type of relationship has been more recently examined for elastoplastic cohesive solids, where comprehensive finite element simulations of conical indentation with $\theta = 68°$ have shown that as $(M_0/Y)^{-1} \to 0$, the $H/Y-$ratio comes close to Tabor's 1948 suggestion, with the result $H/Y \simeq 2.8$ [38].

Noting that the yield strength Y relates to the cohesion c of the Von-Mises (frictionless) solid by $Y = \sqrt{3}c$, the dimensionless equation (Eq. 3.54) reads:

$$\frac{H}{Y} = \frac{1}{\sqrt{3}}\Pi_H\left(\theta = 68°, \frac{M_0}{Y} \to \infty, \nu, \mu = 0\right) \simeq 2.8 \tag{3.55}$$

The assumption $M_0/Y \to \infty$ comes close to the rigid-plastic assumption of yield design approaches which can be found early on in the indentation literature. For instance, Lockett [123] and Chitkara and Butt [39] developed yield design solutions for conical indentations in cohesive rigid-plastic solids (without and with friction at the indenter-material interface).

More recent analysis has employed the upper bound theorem of yield design. Using this approach, Ganneau et al. [74], [75], [173] developed a dual indentation approach which allows the determination of cohesion and coefficient of friction from the dependence of the hardness-to-cohesion ratio on the cone angle:

$$\frac{M_0}{c} \to \infty;\ \frac{H}{c} = \Pi'_H(\theta, \nu, \mu) \tag{3.56}$$

Figure 3-8 displays the results for a Berkovich indenter ($\theta^{eq} = 70.32°$) and a cube corner indenter ($\theta^{eq} = 42.28°$) in terms of the H/c ratio vs. friction angle φ. More generally, the application of yield design solutions to indentation hardness analysis is based on the premise that the material half-space, in response to the application of the indentation load P, has exhausted its capacity to store externally supplied work into recoverable energy, which is equivalent to assuming a rigid plastic behavior.

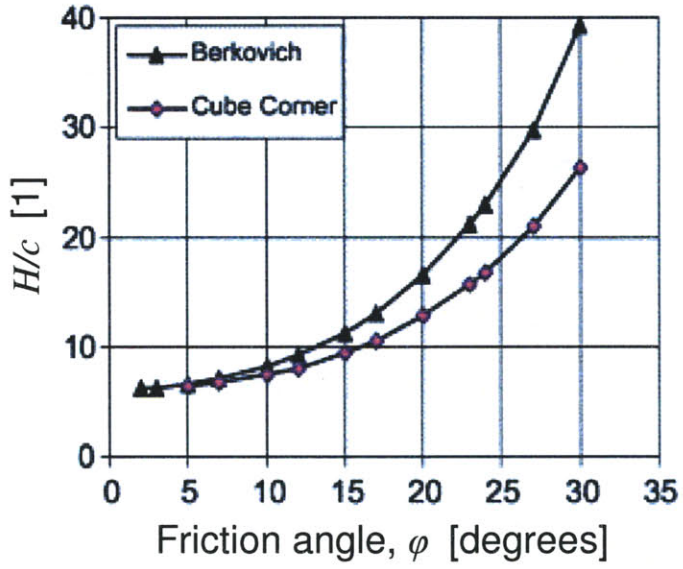

Figure 3-8: Hardness cohesion ratios, obtained from an upper bound analysis, vary with friction angle for two different indenter geometries, the Berkovich probe and the cube corner probe. From [75].

3.5 Elasto-Plastic Materials: The Oliver & Pharr Method

So far, the cases of purely elastic or perfectly plastic materials have been treated, and in each of these cases, self-similarity is preserved. As mentioned in the section on material behavior in self-similarity (Sec. 3.2.2), however, the self-similarity is broken for an elasto-plastic material. Nonetheless, developments around this problem have permitted the BASh formula, Eq. (3.21), derived for the case of purely elastic indentation, to be applied to the unloading branch of the elasto-plastic material reponse. As a result, elasticity content can be obtained from indentations on elasto-plastic materials.

3.5.1 Dimensional Analysis

First, consider application of dimensional analysis to indentation modulus measurements in an elasto-plastic material. In such a material, indentation modulus is determined from quantities measured during the unloading portion of the indentation. Considering the unloading portion requires an additional parameter with dimensions of length, the maximum indentation depth,

$h_{\max}$, which defines the point where unloading begins. Application of the Π-theorem revises Eq. (3.53a):

$$\frac{P}{M_0 h^2} = \Pi_{P,\,\text{unload}}\left(\theta, \frac{c}{M_0}, \nu, \mu, \frac{h}{h_{\max}}\right) \tag{3.57}$$

In the typical indentation test, the unloading slope $S = \frac{dP}{dh}$ is measured at the initial unloading point, such that $h/h_{\max} = 1$. To make the comparison, the unloading response, Eq. (3.57), is derived with respect to the indentation depth, h, and evaluated at $h/h_{\max} = 1$ to obtain:

$$\begin{aligned}
\frac{S}{M_0 h_{\max}} &= \frac{1}{M_0 h_{\max}} \left.\frac{dP}{dh}\right|_{h/h_{\max}=1} \\
&= 2\Pi_{P,\,\text{unload}}\left(\theta, \frac{c}{M_0}, \nu, \mu, \frac{h}{h_{\max}} = 1\right) + \Pi'_{P,\,\text{unload}}\left(\theta, \frac{c}{M_0}, \nu, \mu, \frac{h}{h_{\max}} = 1\right) \\
&\equiv \Pi_S\left(\theta, \frac{c}{M_0}, \nu, \mu\right)
\end{aligned} \tag{3.58}$$

where:

$$\begin{aligned}
\Pi'_{P,\,\text{unload}}\left(\theta, \frac{c}{M_0}, \nu, \mu, \frac{h}{h_{\max}} = 1\right) &= \frac{d\Pi_{P,\,\text{unload}}}{dh} \\
&= \frac{1}{h_{\max}} \frac{d\Pi_{P,\,\text{unload}}}{d\left(\frac{h}{h_{\max}}\right)}
\end{aligned} \tag{3.59}$$

Eq. (3.58) reveals that the contact stiffness S increases with indentation depth during the indentation experiment if all other parameters are held constant. Considering evaluation at $h = h_{\max}$, the dimensionless expression for the projected contact area A_c, given by Eq. (3.53b), is still valid. Combining Eq. (3.53b) and Eq. (3.58) at $h = h_{\max}$ yields a new invariant:

$$\frac{S}{M_0\sqrt{A_c}} = \frac{\Pi_S\left(\theta, \frac{c}{M_0}, \mu\right)}{\sqrt{\Pi_{A_c}\left(\theta, \frac{M_0}{c}, \mu\right)}} \tag{3.60}$$

These manipulations have been made in order to obtain a relation of dimensionless quantities that resembles the BASh equation, Eq. (3.21). A comparison with Eq. (3.60) yields:

$$\frac{S}{M_0\sqrt{A_c}} = \frac{2}{\sqrt{\pi}}\frac{M}{M_0} = \Pi_M\left(\theta, \frac{c}{M_0}, \nu, \mu\right) \tag{3.61}$$

This result suggests that the measured indentation modulus M is a function of both the elastic and plastic properties of the material, for a given indenter geometry. Experimental and numerical observations, however, are in favor of applying elasticity solutions to the unloading portion of the indentation response:

- Stillwell and Tabor provided experimental observations from large-scale conical indentations that suggest the initial unloading portions of indentation responses are purely elastic [167]. They demonstrated, for cohesive materials, that cyclic loading cycles at the beginning of unloading tend to trace the same path. This suggests that reverse plasticity effects are negligible and that it can be reasonably assumed that the initial unloading portion of the $P-h$ curve represents an elastic response.

- Cheng and Cheng [38] and Dao et al. [59] performed large series of elastoplastic finite element simulations (with and without plastic hardening) which demonstrated that the measured indentation modulus is insensitive to plastic properties, including the yield strength-to-stiffness ratio and the power law exponent for the case of strain hardening materials.

While the experimental and numerical results were obtained for cohesive materials, it is reasonable to assume that similar results hold for cohesive-frictional materials. The dimensional analysis thus can be simplified:

$$\frac{S}{M\sqrt{A_c}} = \frac{2}{\sqrt{\pi}} = \Pi_M(\theta) \tag{3.62}$$

The dimensional analysis, in concert with the experimental and numerical observations, demonstrates that the unloading response is purely elastic and any plasticity effects during loading are incorporated in the evolution of the projected contact area during loading. This finding justifies the use of elastic contact solutions to obtain elastic properties of the material based on measurements during indentation. An anisotropic elastic reponse would add complexity, but the previous relationships would still hold for the anisotropic case, provided that appropriate anisotropic ratios are included in the analysis.

3.5.2 Oliver and Pharr Method - Contact Depth

While we may use elastic contact solutions to work with elasto-plastic indentations, implementation of these solutions is not so straightforward. In the purely elastic case, the projected contact area, A_c, required for use in the BASh formula, Eq. (3.21), was obtained from the ratio h_c/h as provided by the Galin-Sneddon solution in Eq. (3.20). This information, however, is *a priori* unknown for the elasto-plastic problem, where the material may have flowed around the indenter tip. Traditionally, the contact area could be estimated by the area of the residual imprint, measured optically after indentation. This approach is impractical, however, at the small length scales employed in nanoindentation, as post-indentation imaging is both difficult and time-consuming. To overcome this problem, a variety of indirect methods to determine the projected area of contact at maximum load have been proposed [61], [80], with the Oliver and Pharr method being by far the most popular [142].

The Oliver and Pharr method is based on the assumption that the elastic contact depth - indentation depth ratio $h_c/h = 1/2$ for parabolic probes applies also to the elastic unloading of the elasto-plastic indentation of a conical probe:

$$h_c - h_f = \frac{1}{2}(h_{\max} - h_f) \tag{3.63}$$

where h_f is the residual indentation depth (Fig. 3-9).

Both $h_{\max}$ and h_f are data available from the test, so that Eq. (3.63) provides an indirect means to determine the contact depth h_c, and thus the projected area of contact A_c. Furthermore, since the measurement of the residual depth h_f is sensitive to surface roughness, an expression is sought in which h_f does not appear. The effective indenter being close to a paraboloid, the load-depth relation during unloading is:

$$P \simeq c(h - h_f)^{3/2} \tag{3.64}$$

which, after differentiation with respect to h and evaluation at $h = h_{\max}$, yields:

$$h_{\max} - h_f = 2\frac{P}{S} \tag{3.65}$$

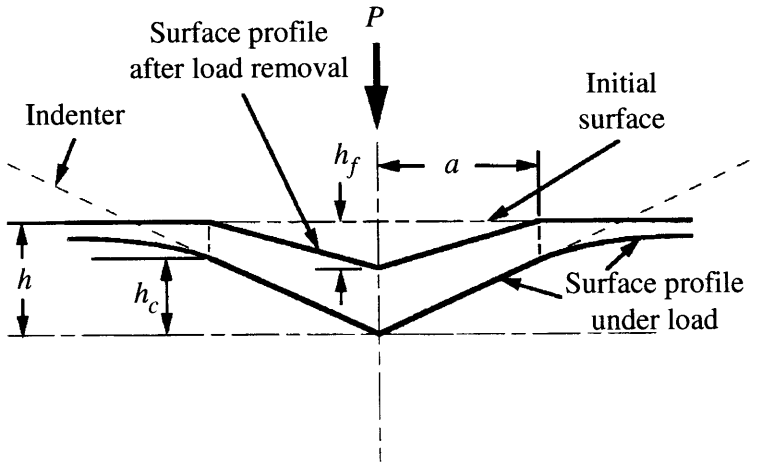

Figure 3-9: Determination of the projected contact area with the Oliver and Pharr method (from [142]).

Combining Eqs. (3.63) and (3.65) yields:

$$\frac{h_c}{h_{\max}} = 1 - \varepsilon \frac{P_{\max}}{S h_{\max}} \tag{3.66}$$

where $\varepsilon = 3/4$. Since the maximum indentation load $P_{\max}$, the contact stiffness S, and the maximum indentation depth $h_{\max}$ are all available from the test, Eq. (3.66) provides a convenient way to estimate the contact depth h_c, and thus the projected area of contact A_c.

Though a powerful tool in indentation analysis, the Oliver and Pharr method has one limitation. It can only capture 'sink-in' phenomena, for which $h_c/h < 1$, but not 'pile-up', for which the contact depth is greater than the indentation depth, and which has been observed experimentally, especially in sharp indentation for some plastically dilating materials. Despite this limitation, for Berkovich indentation on cementitious materials, Constantinides verified experimentally that the Oliver and Pharr method provides a good estimate of the projected area of contact [44]. It is assumed that this verification holds for shale materials, as well.

3.5.3 Oliver and Pharr Method: Contact Area

Oliver and Pharr also developed a convenient way to link the contact depth h_c to the projected contact area A_c for non-ideal indenter shapes. For a perfectly sharp Berkovich indenter, the projected contact area, A_c, should be related to the contact depth, h_c, by the relation:

$$A = 24.56h_c^2 \tag{3.67}$$

Many researchers [23], [61] have noted, however, that a perfectly sharp indenter tip is impossible to achieve. Furthermore, at small loads and small displacements, the scale of the displacement may approach the scale of the imperfection. In this regime, there can be a significant deviation between the contact area predicted by formulas for perfect indenters and the contact area experienced experimentally. Oliver and Pharr suggested that the projected contact area function could be represented by a series of terms:

$$A\left(h_c\right) = c_0h_c^2 + c_1h_c^1 + c_2h_c^{\frac{1}{2}} + c_3h_c^{\frac{1}{4}} + c_4h_c^{\frac{1}{8}} + c_5h_c^{\frac{1}{16}} + ... \tag{3.68}$$

where the coefficients c_i must be calibrated for a given indenter tip.

As a result, to use the Oliver and Pharr method for assessing contact area, another series of calibration indents are run on a sample material (as in the machine compliance calibration, this is typically fused silica) whose mechanical properties are known in advance. The indentation depths of the calibration indents are varied over the range of interest, and the coefficients c_i are found through an iterative fitting procedure such that the experimental properties match the predicted values, with c_0 the original coefficient for the perfectly sharp indenter (i.e. $c_0 = 24.56$ for the Berkovich probe).

3.6 Chapter Summary

This chapter introduced general techniques and concepts relating to nanoindentation on a homogeneous solid. Experimental equipment, including procedures, calibrations, and limitations were discussed. Self similarity theory and contact mechanics solutions relating to the indentation problem were reviewed. Detailed dimensional analyses of the commonly reported

indentation parameters, hardness and indentation modulus, gave a framework for relationships between elastic content, cohesive-frictional plastic properties, and the measured quantities.

So far, the treatment of nanoindentation has assumed that indentation occurs on a perfectly smooth, homogeneous solid material. These assumptions are not strictly applicable to nanoindentation experiments on natural materials such as shale. A review and extension of work that permits repeatable, quantitative nanoindentation on a highly heterogeneous composite material like shale is discussed in the next chapter.

Chapter 4

Nanoindentation Methods and Statistical Indentation Analysis for a Heterogeneous Composite - Grid Indentation, Deconvolution, and Surface Preparation

While the use of instrumented nanoindentation has been extensively studied in the past two decades, the tools have been limited, until recently, to either homogeneous samples or to layered samples (thin films) whose thicknesses are previously known (see e.g. [147]). Recently developed and refined techniques, however, have extended the application of nanoindentation to heterogeneous, composite materials [43], [45], [46]. This chapter reviews that work, which is needed for an application of nanoindentation to shale materials.

As discussed in Chapter 2, shale is a highly heterogeneous composite material, with heterogeneities entering at various scales. The goal of this chapter is to review nanoindentation methods and analysis techniques required to measure the properties of the porous clay composite, the scale of Level '1' in the multiscale thought model for shale. Heterogeneities exist at and above this scale in the form of silt (quartz and feldspar) inclusions. The grid indentation

technique with deconvolution analysis, is a tool which can provide indentation properties for each phase in a material.

Additionally, the porous clay composite is heterogeneous at a scale below, consisting of clay minerals at Level '0' and porosity. The next chapter reviews a recently developed tool that relies on an inverse approach to scaling of porous composite behavior to assess heterogeneous behavior at the scale below the application of nanoindentation.

Finally, this chapter introduces sample preparation and surface roughness issues that must be considered when dealing with a heterogeneous porous composite material such as shale. An acceptable roughness is difficult to achieve in a natural composite, and what is 'acceptable' also needs to be defined. This section develops surface roughness criteria for nanoindentation on a heterogeneous composite, and demonstrates its application to shale materials.

4.1 Grid Indentation Technique for Heterogeneous Materials

In theory, it could be possible to choose to indent on specific material phases (such an approach has been taken by Donnely et al. [65] for an indentation study of bone). Recognizing the high heterogeneity of shale at the nano- and micro-scale, however, this approach quickly becomes infeasible for a large array of samples, as it is difficult to choose to indent on a specific material phase with sufficient repeatability. To address this issue, Ulm and co-workers [43], [45], [46], [53] realized the advantage of performing large grids of indentations on heterogeneous samples. They proposed that if the grid size and indentation depth are chosen properly, each indentation test may be treated as an independent statistical event. Then statistical techniques may be applied to the results.

4.1.1 Grid Indentation Principle

To introduce the grid indentation technique, consider an indentation test on an infinite half-space composed of two materials of different mechanical properties. Provided that the indentation depth is much smaller than the characteristic size of the two phases, a random indentation on the sample surface should provide access to either of the phase properties, with a probability that equals the surface fraction the two phases occupy on the sample surface. By contrast,

an indentation to a depth much larger than the characteristic size of the two phases should mechanically sample the composite response via "mechanical homogenization" [45]. If the individual phase properties are sought, the indentation depth must be chosen according to the characteristic length scale, as discussed in the next subsection.

On a heterogeneous composite, a single random indentation test does not provide enough information about the properties of each material phase in the composite. The grid indentation technique is designed to overcome this problem, by performing a large array of indentations tests on a sample surface and analyzing the results statistically.

To introduce the quantities that are measured by the technique, reconsider indentation on a two-phase composite. A large number of indentations is performed at random locations on the surface of the two-phase material (Fig. 4-1 (a)). The indentations are shallow enough to ensure that scale separability is respected. Although a few indentations may measure a composite response, scale separability ensures that a large majority of the indentations will probe the intrinsic properties of the two phases. It is intuitively appealing to display the experimental results as histograms (or frequency plots) of the measured indentation properties (indentation modulus M, indentation hardness H, etc.), which in the case of the two-phase composite material display two peaks (Fig. 4-1 (c)). The mean value of each peak represents the mean phase property.

The area below each curve of the histogram is a measure of the percentage of all indentations performed on the corresponding phase, and is therefore a measure of the surface fraction of each phase. For a perfectly disordered material, surface fractions and volume fractions are identical, which is known at the Delesse principle [54]. Therefore, the volume fraction of each phase of the heterogeneous material can also be obtained by an analysis of the experimental frequency plot.

The randomness of the location of the indentations ensures that the measured properties are not correlated from indentation to indentation. If the indented material is perfectly disordered, this zero correlation can also be ensured by performing the indentations on a grid, as long as the size of the grid is greater than the characteristic size D of the phases (Fig. 4-1 (b)). Since it is easier to program an indenter to perform indentations on a grid, the approach is referred to as the 'grid–indentation technique' [45].

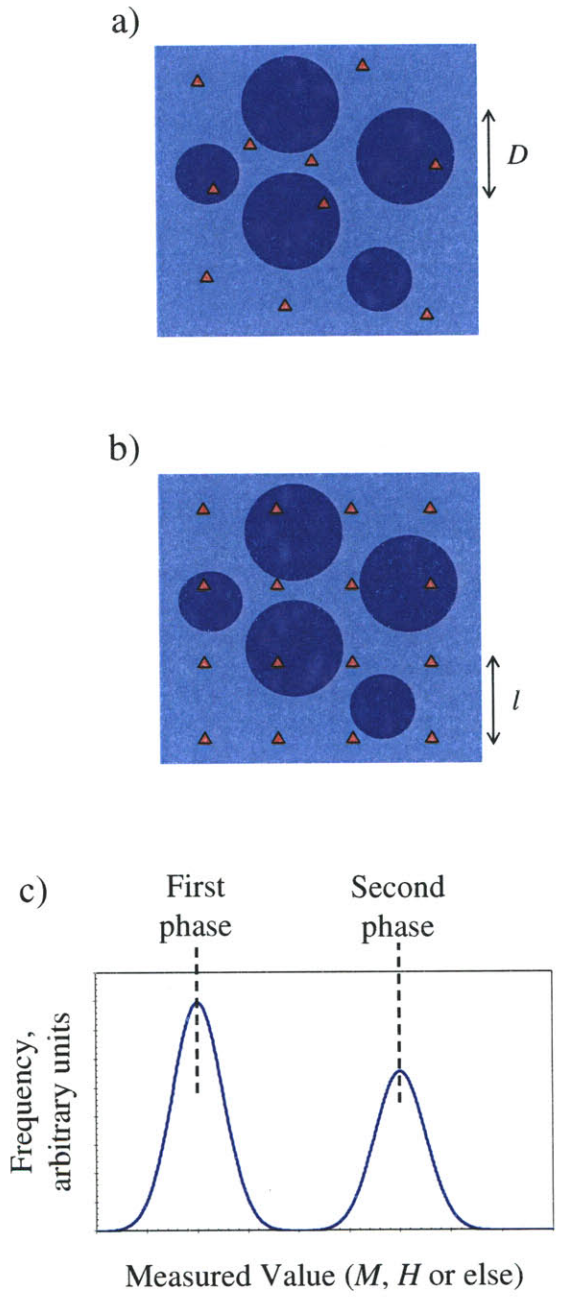

Figure 4-1: Indentations performed on a heterogeneous two-phase material. Each indentation (represented by a red triangle reminiscent of Berkovich indents) provides the mechanical properties of one of the two phases. (a) Indentations are performed at random locations. (b) Indentations are performed on a grid. (c) Resulting histogram (frequency plot). From [177].

The principle of the grid-indentation technique is described for a two-phase composite, but it obviously applies to more phases are well, provided they exhibit sufficient contrast ('mismatch') in their properties. Moreover, the grid-indentation technique can be applied for any property obtained from the indentation tests, as long as the scale separability conditions are respected to permit a continuum analysis.

4.1.2 Scale Separability

The grid indentation technique introduces new length scales to the problem. These length scales enter as criteria for statistical independence and statistical sampling, as well as the scale separability condition from continuum mechanics. Considering statistical independence first, we must choose a grid size, l, which is much larger than the imprint of the indentation (a function of the indentation depth, h). To avoid sampling effects, a large number of tests, N, should be carried out over an area much larger than the length scale of the individual material phases, D. On the other hand, if we wish to obtain properties of individual material phases, the indentation depth, h, should be much smaller than the length scale of the phases, D. In addition, finite element simulations have shown that a Berkovich indentation test measures the elastic response of a material volume 3 to 5 times the depth of indentation, h, [115] adding to the requirement that h should be much smaller than D. These conditions may be summarized:

$$3h \ll D \ll l\sqrt{N} \tag{4.1}$$

Moreover, because the analysis and interpretation of the indentation tests depend on continuum mechanics analysis, there is an additional challenge of respecting the separation of scale condition:

$$d \ll \mathcal{L} \ll 3h \tag{4.2}$$

where $\mathcal{L}$ is the characteristic size of the representative elementary volume (*rev*), which must be much greater than the size of the largest heterogeneity of size d contained in the *rev* and much smaller than the indentation depth, h, which defines the volume of material sensed in an indentation test.

4.2 Statistical Analysis - Deconvolution

Introduction of the grid indentation technique has suggested that the histogram (whose continuous analog is a Probability Distribution Function (PDF)) of a particular property measured through a grid of indentations on a composite material displays peaks relating to the property of each material phase (see Fig. 4-1 (c)). As long as the property shows some contrast between phases, the number of peaks resulting from an application of the grid indentation technique should match the number of material phases, and the mean value of each peak should match the property of the individual material phase.

The idea of deconvolution of nanoindentation measurements was first proposed by Constantinides et al. [43] and additional automation of the procedure was developed soon after [45], [46], [53]. This work dealt with the probability distribution functions. It was soon discovered that, analytically, it is more convenient to deconvolute the cumulative distribution functions (CDF) than to deconvolute the PDF, because generation of the experimental PDF requires a choice of bin-sizes [175]. The PDFs are more physically intuitive, however, so for visualization of the procedure and display of the results we will work with PDFs. This latest iteration of the deconvolution technique is reviewed here.

Specifically, the deconvolution technique for indentation measurements allows for the quantitative estimation of mechanical phase properties from a grid indentation data set with the results of many individual indentation tests, given that the scale separability conditions (Eqs. (4.1) and (4.2)) have been satisfied. Each indentation test is considered as a single statistical event, and the extracted indentation modulus, M, and hardness, H, are considered as random variables. The aim of the deconvolution technique is to identify, from the experimental distributions of M and H, the number of mechanically active material phases, and the mechanical phase properties.

4.2.1 Choice of Phase Distribution Functions

The first task is to specify the form of the model distributions associated with the property of a specific material phase and its related peak in the PDF [177]. Recalling from Section 2.3.4, distributions are uniquely defined by their moments, so it is worthwhile to anticipate

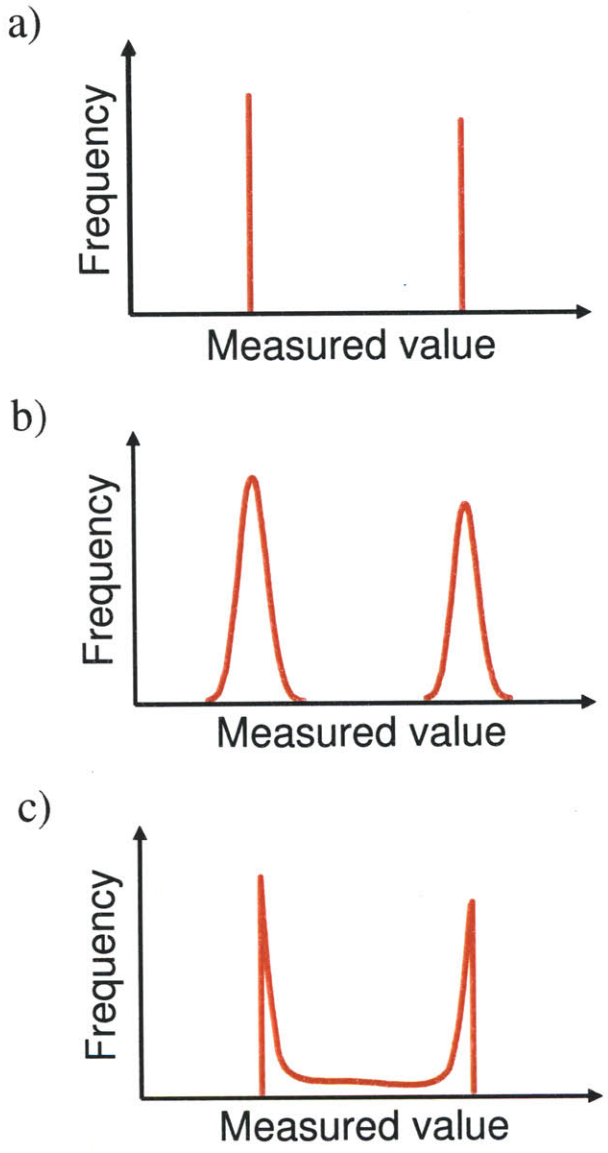

Figure 4-2: Expected frequency plots (PDFs) for a two-phase material. (a) Perfect measurements and materials; (b) imperfect measurements or materials; (c) perfect measurements and material with some composite responses. From [177].

what the moments of each phase distribution should be like. It is assumed that each phase of the heterogeneous material should have its own value of indentation modulus and indentation hardness, associated with the actual properties of this phase. These phase properties are the mean of the model phase distributions. If the measurements and material were perfect, the peaks would be expected to be infinitely sharp (Fig. 4-2 (a)). However, some spread is anticipated in the data, relating to random noise in experimental data as well as inherent variability in the phase properties of a natural material. It is assumed that the inherent variability and random noise is, on average for each phase, distributed evenly around the mean (Fig. 4-2 (b)). Finally, it should be expected that some randomly placed indentations in the grid indentation technique will solicit the composite mechanical response of two or more phases simultaneously. Quantifying this composite response is difficult, but it should be clear that the composite response must be bound by the values of the individual peaks (see Fig. 4-2 (c)). In the case of such a composite response, the peaks may display some asymmetry: the lowest peak is skewed to the right (positive skewness) while the highest peak is skewed to the left (negative skewness). To keep the deconvolution process as automated as possible, a single form of distribution is used to characterize all peaks, so the choice of a distribution with zero skewness is most appropriate.

These observations and assumptions lead to considering the normal, or Gaussian, distribution (Eq. (2.6)) as a good approximation for each phase. It is possible that other model distributions provide a closer fit to the experimental data, especially in the tails of the distribution. The focus of the deconvolution procedure, however, is to estimate the mean and standard deviation of each phase property, as well as the volume fraction of each phase. Choosing more sophisticated distributions would add very little precision to these results.

4.2.2 Implementation

Implementation of the deconvolution technique begins with the generation of the experimental CDF. Let N be the number of indentation tests performed on a specimen, and $\{M_i\}$ and $\{H_i\}$ $(i = 1, N)$ the sorted values of the measured indentation modulus M and indentation hardness H. The N points of the experimental CDF of M and H, denoted by F_M and F_H respectively,

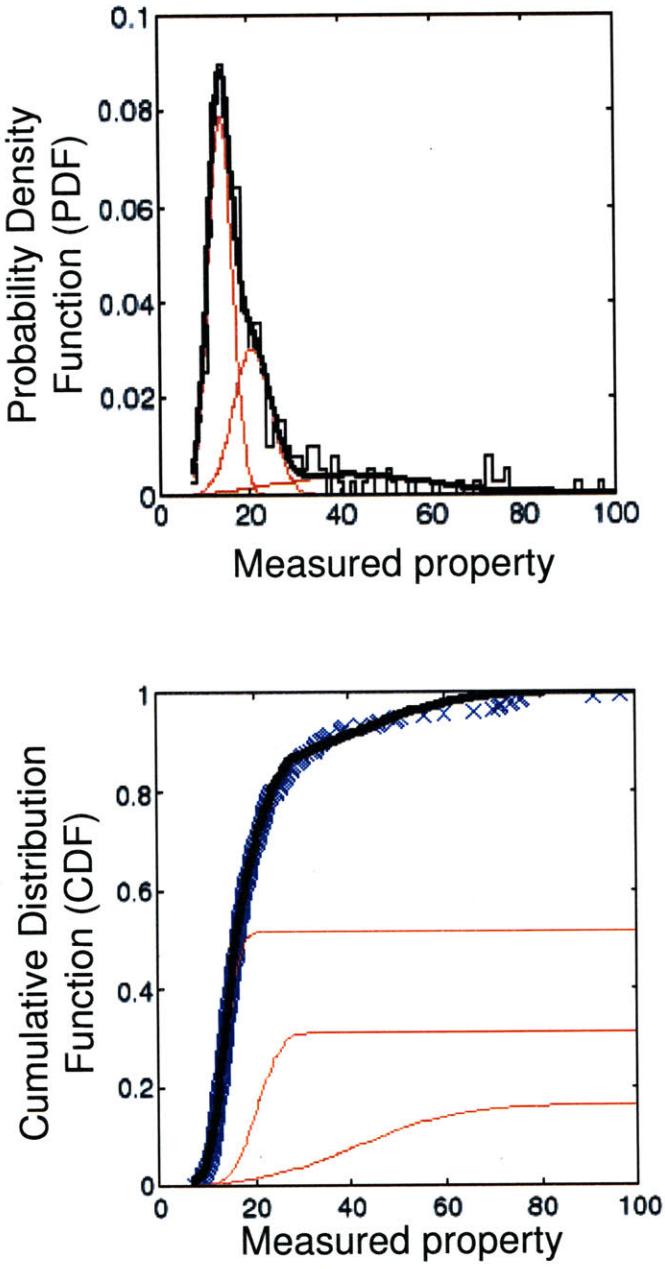

Figure 4-3: Example of a 3-Gaussian deconvolution. Top: Histogram and probability distribution function with experimental data (stepped thin black line) model phase distribution functions (thin red lines) and overall model distribution (thick black line). Bottom: Cumulative distribution function with experimental data (blue x's) model phase distribution functions (thin red lines) and overall model distribution (thick black line).

are obtained from:

$$\left.\begin{aligned} F_M(M_i) &= \frac{i}{N} - \frac{1}{2N} \\ F_H(H_i) &= \frac{i}{N} - \frac{1}{2N} \end{aligned}\right\} \; for\; i \in [1; N] \tag{4.3}$$

Next, the overall model distribution may be constructed by superposing the individual model phase distributions. Consider the heterogeneous material to be composed of $j = 1, n$ material phases with sufficient contrast in mechanical phase properties. Each phase occupies a surface fraction, f_j, of the indented surface. The distribution of the mechanical properties of each phase is assumed to be approximated by Gaussian distributions, identified by the mean values μ_j^M and μ_j^H and the standard deviations s_j^M and s_j^H, of the indentation modulus M and the indentation hardness H, respectively. The CDF for each (Gaussian distributed) phase is given by:

$$j = 1, n;\; F(M_i; \mu_j^M, s_j^M) = \frac{1}{s_j^M \sqrt{2\pi}} \int_{-\infty}^{M_i} \exp\left(\frac{-(u - \mu_j^M)^2}{2(s_j^M)^2}\right) du \tag{4.4}$$

The $n \times 5$ unknowns $\{f_j, \mu_j^M, s_j^M, \mu_j^H, s_j^H\}, j = 1, n$ are determined by minimizing the difference between the experimental CDFs and the weighted model-phase CDFs:

$$\min \left[\sum_{X=M,H} \left(\sum_{i=1}^{N} \left(\sum_{j=1}^{n} f_j F(X_i; \mu_j^X, s_j^X) - F_X(X_i) \right)^2 \right) \right]$$

$$s.t. \tag{4.5}$$

$$\sum_{j=1}^{n} f_j = 1$$

where the constraint of the minimization problem requires that the surface fractions of the different phases sum to one. To ensure that phases have sufficient contrast in properties, and thus to avoid that two neighboring Gaussians do not overlap, the optimization problem is additionally constrained by [53]:

$$\mu_J^X + s_J^X \leq \mu_{J+1}^X - s_{J+1}^X,\; X = (M, H) \tag{4.6}$$

The deconvolution is automated and performed by a non-linear least-squares solver in MATLAB.

The only choice to be made is how many material phases, j, are to be considered in the analysis.

To illustrate the procedure, Figure 4-3 displays the results of a deconvolution by three Gaussians, in terms of the CDF and the PDF. The experimental data in Figure 4-3 (Top) is precisely described as a histogram, but as the continuous analog of a discrete histogram is a PDF, and the histogram for grid indentation data usually summarizes many hundreds of data points, the experimental histograms are also referred to as PDFs throughout this work. It is clear from Figure 4-3 that the PDF is more physically and visually appealing, as it is easier to understand the mean value, spread of data, and volume fractions for each phase than in the CDF.

In summary, the results of the deconvolution technique are estimates of the mean and standard deviation of indentation modulus and hardness for each mechanically distinct phase, and an estimate of the volume fraction of each phase. The grid nanoindentation technique provides reliable estimates of the mechanical behavior of each phase in a complex heterogeneous composite based on direct mechanical measurements.

4.3 Sample Preparation & Surface Roughness

A major challenge for nanoindentation on a heterogeneous material such as shale is to develop an appropriate sample preparation procedure that minimizes surface roughness while also keeping sample disturbance to a minimum. Minimizing surface roughness is important for nanoindentation because analysis of a single nanoindentation tests assumes that the indentation occurs on an infinitely flat surface. The presence of surface roughness adds another length scale to the nanoindentation problem and can break the self-similarity of the problem (Sec. 3.2). In this case, the Galin-Sneddon solution (Eq. (3.15)) for elastic contact may not be valid and, by extension the Oliver and Pharr method for elasto-plastic indentation may also be invalidated. Of course, the idealization of a perfectly flat surface is not possible in practice, but surface roughness criteria for nanoindentation are limited, especially for applications to heterogeneous materials.

This section introduces AFM testing as the experimental means for assessing surface roughness at the appropriate scale. Following this introduction, a surface roughness criteria, as well

as a related surface preparation technique, is developed for nanoindentation on cement paste, another heterogeneous porous composite material. This surface roughness criteria is thought to be applicable for shale, as well, and the surface preparation procedure is also adapted for shale materials. Finally, the shale roughness results are presented.

4.3.1 AFM Testing

Topographic information about sample surfaces was obtained with a Quesant Q-Scope 250 AFM. The data were acquired using a wavemode, or 'tapping' scan. For each scan, the resolution was 512x512 pixels, and the scan rate was 1.0 Hz. Various scan sizes were used during exploration of the surface roughness criteria, from 1 μm x 1 μm to 80 μm x 80 μm was used. Following the AFM imaging procedure, each file was digitally analyzed in order to extract a roughness value. Before calculation of the roughness, a linear slope correction was performed to account for an alignment difference between the reference plane of AFM imaging and the overall slope of the sample surface. For scan sizes larger than 20 μm x 20 μm, a Gaussian filter was applied to remove any waviness with characteristic wavelengths larger than 8 μm, which would be larger than the scale considered for nanoindentation.

The chosen measurement of roughness was a root-mean-squared average (RMS) of the topography of the surface, R_q, defined by:

$$R_q = \sqrt{\frac{1}{N^2}\sum_{i=1}^{N}\sum_{j=1}^{N} z_{ij}^2} \tag{4.7}$$

where N is the number of pixels in each scan edge and z_{ij} is the height at position (i, j) from the mean plane.

4.3.2 Assessing Surface Roughness Criteria

Experimental evidence from the literature suggests that the presence of significant surface roughness tends to increase the scatter in measured indentation modulus and indentation hardness, along with an overall reduction in these properties [18], [65], [111]. An ISO Standard dealing with nanoindentation warns that "surface finish has a significant influence on the test results" [101]. An infinitely flat surface is impossible to obtain in practice, so criteria for what

surface roughness is "small enough," compared with the indentation depth, must be obtained.

Several researchers have proposed criteria for acceptable surface roughnesses for nanoindentation. The ISO Standard references a study investigating the effect of roughness on hardness measurements of metals [84] which gives a criteria of $h_{\max} > 20R_a$, where R_a is the average roughness. For Berkovich indentation on cancellous bone, a preliminary criterion of $h_{\max} > 3R_q$ has been given by Donnely, et al. [65].

Study on Cement Paste

None of these studies, however, seemed suited to the particular application of grid nanoindentation on a highly heterogeneous composite material. As a result, a more detailed study was made [137] regarding the link between surface roughness and nanoindentation for a highly heterogenous material, where the choice of indentation depth is controlled by the desire for a separation of material length scales (see Sec. 4.1.2). Cement paste was chosen as the studied material because it is easier to work with than shale, and a specific cement paste was chosen because of its expected high contrast in material phase properties. The sample was trimmed to an appropriate size (about 10 mm in diameter and 5 mm in height, see Fig. 4-4 (bottom)) with a diamond saw. Care was taken to keep the sides as parallel as possible. Then the sample was fixed to a stainless steel mounting disk by a very thin layer of cyanoacrylate. The sample polishing process proceeded in two main steps:

1. The first step is a coarse grinding step, designed to make the surface of the sample parallel with respect to the mounting disk. The mounted sample is placed in a jig consisting of a stainless steel sleeve with an opening drilled through at the same diameter of the mounting disk. An interior cylinder fits closely inside, and rests on the back of the specimen disk to apply a lightweight to the sample (see Fig. 4-4 (top)). Inside the jig, the sample is ground on 120 grit ZirMet (Buehler) abrasive paper. The amount of material removed is not measured, but grinding proceeds until the entire surface has been ground. Keeping the sample relatively short and wide compared to the specimen disk helps to prevent the sample from tilting and creating a convex surface. The sample and the jig are then cleaned separately, with the sample in n-decane and the jig in water, in an ultrasonic bath for 5 minutes.

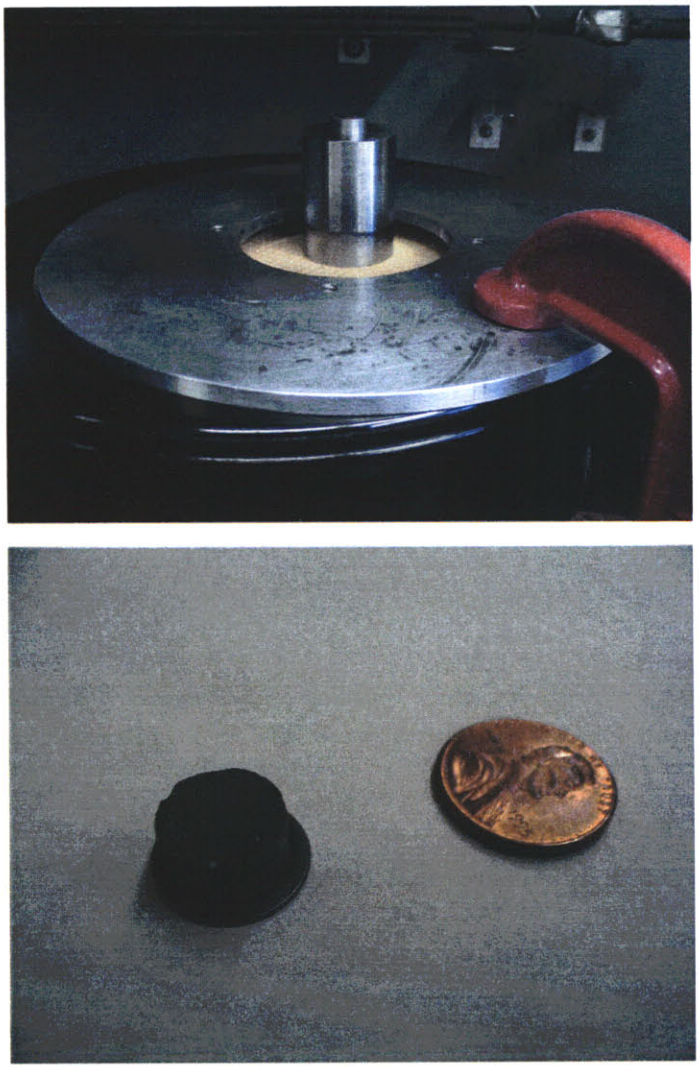

Figure 4-4: Top: Equipment used to polish specimen. The sample rests face down on the TexMet P pad, inside the stainless steel jig. The inner cylinder, which is free to move up and down, rests on the back of the stainless steel mounting plate. The metal collar holds the jig in place on the lapping wheel and pad while allowing the jig and sample to rotate freely. Bottom: Sample on a mounting plate.

2. The second and final step is the polishing step. After much trial and error on cement pastes, with a variety of polishing compounds and polishing mats, the combination presented here gave repeated success. A hard, perforated, non-woven pad (TexMet P, by Buehler) is mounted to a lapping wheel. The hardness of the pad assures that the highest surfaces of the sample are removed first, and the perforation gives a place for the polishing residue to collect without interfering with the polishing itself. This is particularly important because the described polishing process does not include any ongoing cleaning of the pad. The TexMet P pad is charged with approximately 0.5 mL of 1 μm oil-based diamond suspension (Metadi, Buehler). A polishing fluid helps to dissipate any heat build-up, and the oil-base specifically helps to prevent any further hydration and change in water-to-cement ratio. Using only one size of diamond suspension aids in the repeatability of the procedure, as there is no need for the extensive cleaning required if the sample were polished by a series of smaller and smaller diamond suspensions. While this may result in a longer polishing time, it requires much less operator intervention, and therefore increases the repeatability of the procedure. The sample and jig are held on the pad, approximately 3 to 4 cm from the center of the lapping wheel, and the jig is allowed to freely rotate. The wheel is then spun at 1 cycle per second, so a typical velocity underneath the sample is 18 to 25 cm/s. The relatively slow lapping speed is essential in minimizing the sample disturbance and creating a smooth surface. This polishing lasts for 8 hours. As before, the sample and the jig are then cleaned separately, with the sample in n-decane and the jig in water, in an ultrasonic bath for 5 minutes.

To study the effect of scanning size on the variability of the roughness measurements, five topographic images were obtained at different locations for scan sizes of 2 μm x 2 μm, 10 μm x 10 μm, 50 μm x 50 μm, and 80 μm x 80 μm. This variability study suggested that the scan size should be larger than the scale of largest heterogeneity in a composite sample, in order to achieve good spatial averaging. For the case of cement paste, the 50 μm x 50 μm scan is appropriate.

To study the effects of surface roughness of indentation results, the polishing procedure was interrupted at various intervals, including just after grinding, and after 1, 2, 4 and 8 hours of polishing. (See Fig 4-5). The surface roughness at each polishing stage was measured, using

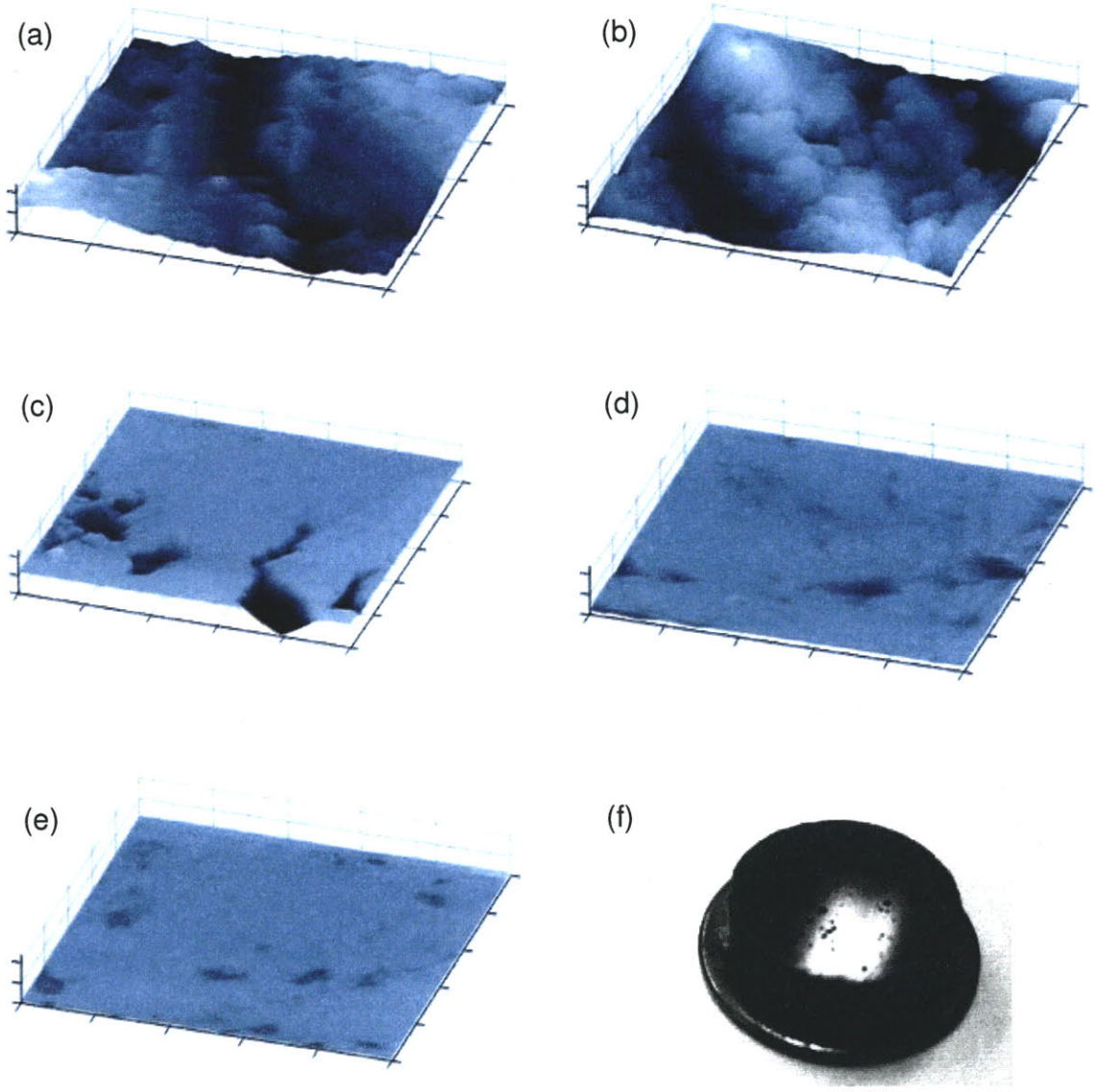

Figure 4-5: AFM images of different stages of the polishing process and a photograph of the sample showing the final polished surface. Each AFM image is of a 50 micron by 50 micron area, and the maximum value of the height axis for each image is 5000 nanometers. Image (a) is of the rough ground sample surface. Image (b) is taken after 1 hour of polishing and minor flattening of the surface is visible. Image (c) is taken after 2 hours. At this stage, the highest surfaces are flat and polished, but lower surfaces are still rough. Image (d) is taken after 4 hours. As polishing continues, the surface is nearly flat across the entire area. Image (e) is taken after the full 8 hours of polishing. Image (f) is a photograph showing the reflective sample surface after the full 8 hours of polishing. From [137].

Polishing Time	R_q	Peak 1			Peak 2			Peak 3		
		mean	st. dev.	f	mean	st. dev.	f	mean	st. dev.	f
0 hours	159	23.41	16.33	0.23	68.08	23.54	0.61	116.56	24.95	0.16
1 hour	136	17.52	6.43	0.40	36.58	8.30	0.36	72.93	25.62	0.25
2 hours	104	43.83	6.77	0.60	67.88	6.46	0.10	114.27	32.070	0.30
4 hours	29	44.28	7.42	0.59	60.53	8.84	0.12	120.97	23.29	0.29
8 hours	20	43.00	7.07	0.59	63.70	12.80	0.17	126.30	20.16	0.24

Table 4.1: Results of deconvolution of Indentation Modulus (in GPa) and phase volume fractions as a function of RMS roughness (in nm).

Polishing Time	R_q	Peak 1			Peak 2			Peak 3		
		mean	st. dev.	f	mean	st. dev.	f	mean	st. dev.	f
0 hours	159	0.51	0.36	0.23	2.99	1.42	0.61	6.81	1.80	0.16
1 hour	136	0.46	0.22	0.40	1.15	0.43	0.36	2.90	1.32	0.25
2 hours	104	1.74	0.47	0.60	3.33	0.49	0.10	8.04	2.48	0.30
4 hours	29	1.88	0.42	0.59	3.34	0.46	0.12	8.64	2.21	0.29
8 hours	20	1.59	0.39	0.59	2.96	0.98	0.17	8.94	1.65	0.24

Table 4.2: Results of deconvolution of Hardness (in GPa) and phase volume fractions as a function of RMS roughness (in nm).

the 50 μm x 50 μm scan size as the benchmark for comparison.

A deconvolution procedure (Sec. 4.2) was employed, identifying three material phases. Figure 4-6 shows the results of the deconvolution technique in terms of both CDFs and the PDFs for indentation modulus and indentation hardness for the cement paste polished for eight hours. The PDFs, which are more physically intuitive, show the presence of three phases present in the hardened material system, which are referred from left (soft) to right (hard) as the first phase, second phase, and third phase. In this particular sample, the first phase corresponds to a high-density C-S-H phase, the second phase is an ultra-high-density C-S-H phase, and the third phase is the clinker phase.

The mean values and volume fractions associated with each peak were compared for different surface roughnesses. Tables 4.1 and 4.2 give the indentation modulus and hardness values for each phase, along with the roughnesses, associated with each polishing interval. Figure 4-7 illustrates the relationship between decreasing roughness (using a 50 x 50 μm scan size) and the convergence of the mean, standard deviation, and volume fraction results to unique, repeatable values. Below a roughness of about 100 nm (corresponding to the roughness achieved after two

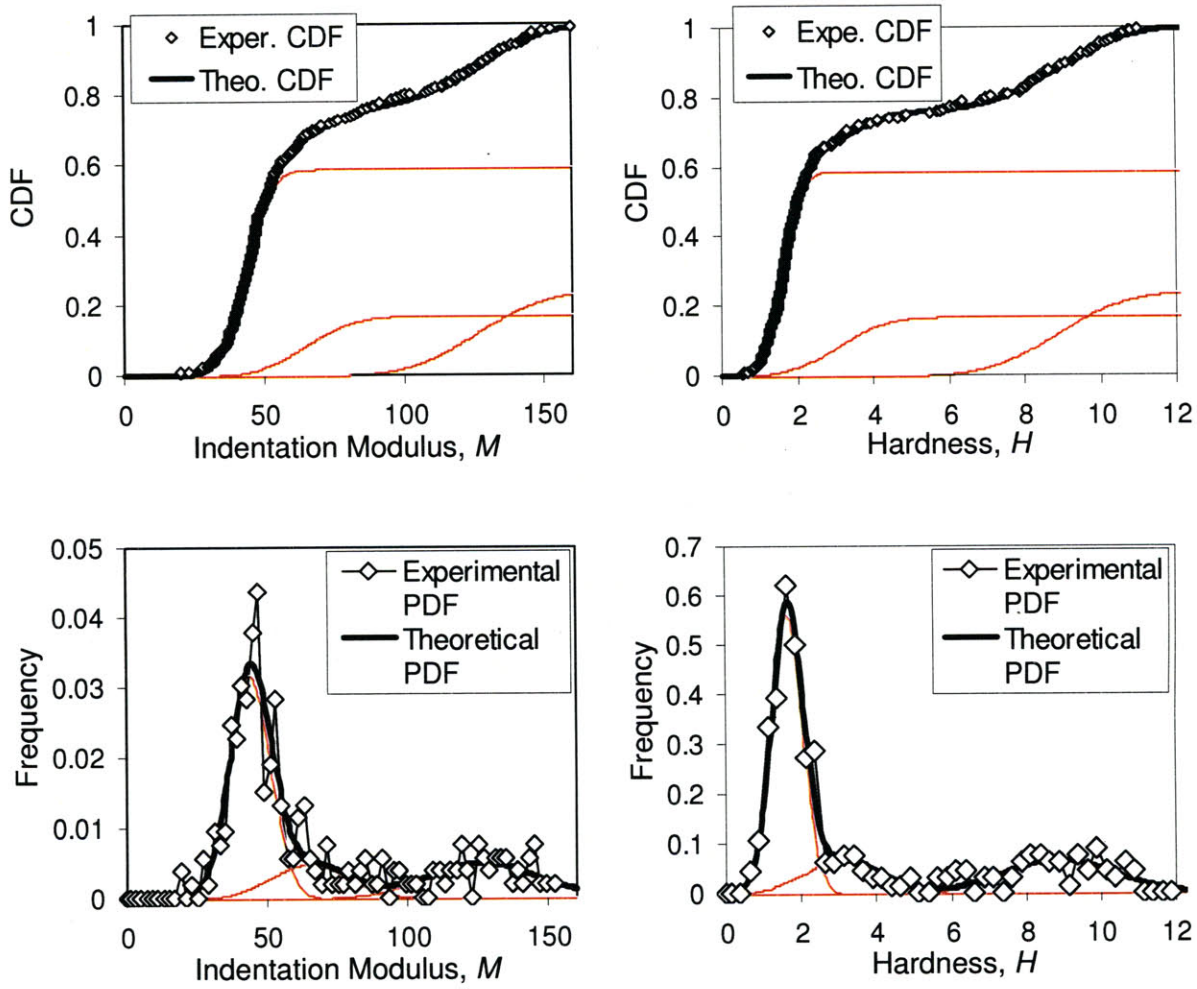

Figure 4-6: Statistical indentation analysis of the cement paste: cumulative distribution functions (CDF - top) and probability density functions (PDF - bottom) of indentation modulus, M, (left) and hardness, H (right). The experimental CDF is constructed from the (M, H) data points from a 20 by 15 grid. It is deconvoluted in a series of three phase-specific CDF's, which are assumed to be Gaussian, and which are also displayed.

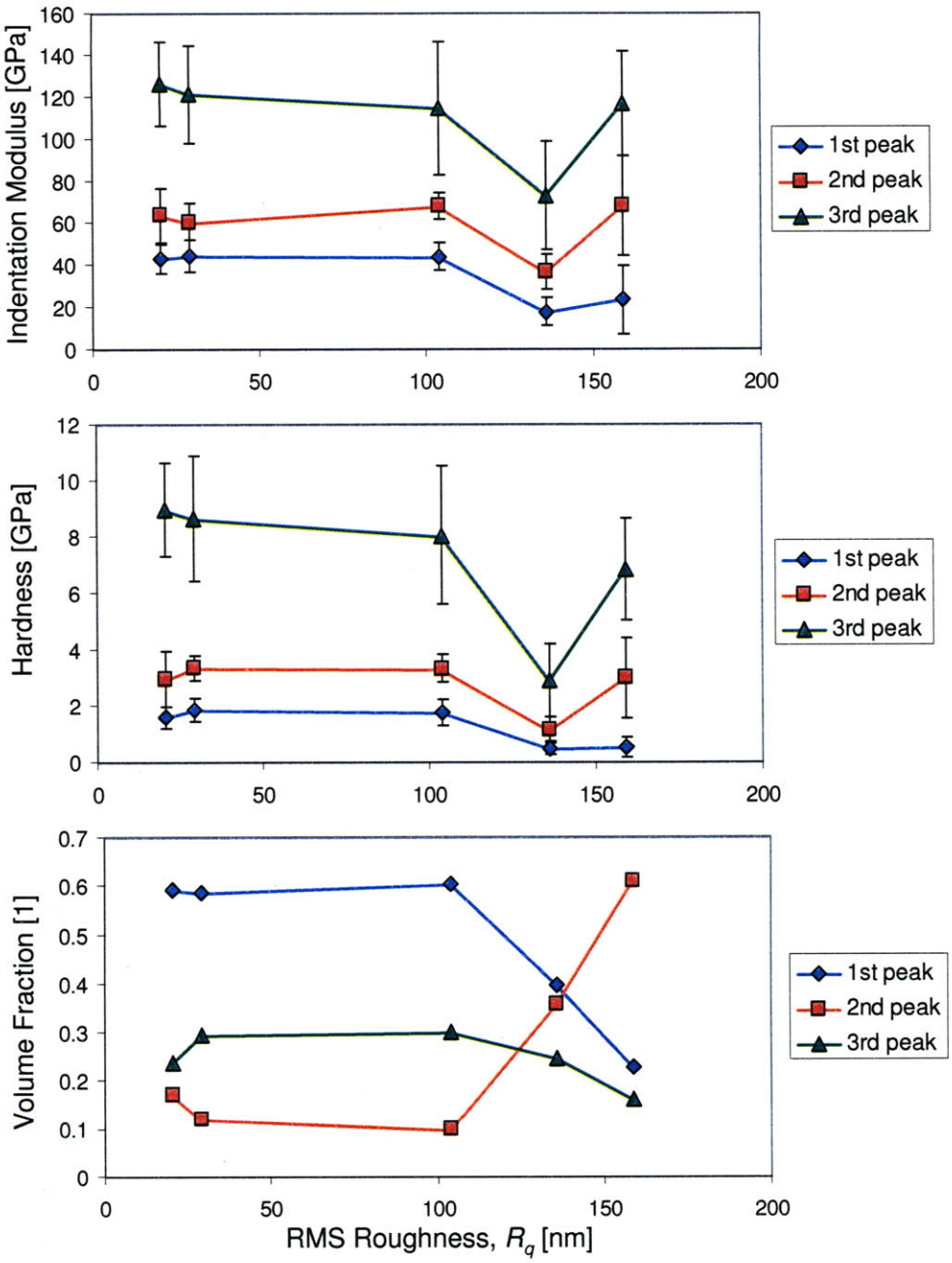

Figure 4-7: Nanoindentation deconvolution results versus RMS Roughness, R_q. Top: Average Indentation Modulus, M, of each phase. Middle: Average Hardness, H, for each phase. Bottom: Volume Fraction of each phase. The error bars in Indentation Modulus and Hardness represent plus and minus one standard deviation. The mean properties and volume fractions converge to within about 5% of the final values when the RMS roughness is less than 100 nm.

hours of polishing), the results for the extracted indentation hardness and moduli for the first two peaks are within 5% of the values for the fully (eight hour) polished sample.

Proposed Criteria

The final results are specifically tailored to indentation on heterogenous materials. The proposed criteria deal with choosing the appropriate scan size for AFM testing and determining the roughness that is "smooth enough" for giving repeatable results from deconvolution. Since the choice of length scale, as introduced by the choice of indentation depth, h, is so critical for the grid indentation technique on heterogeneous materials, both parts of the proposed criteria relate to the indentation depth. For a highly heterogeneous material, the indentation depth varies with material phase for a given indentation load (the typical parameter which is prescribed in indentation testing). As a result, the proposed criteria are based on the indentation depth, h, associated with the first peak, which has the deepest indentation depths:

$$l \approx 200h \tag{4.8a}$$

$$h > 5R_q \tag{4.8b}$$

where l is the edge length of the AFM scan.

4.3.3 Application to Shale

A similar surface preparation program was developed for the shale samples, with only minor modifications from the one developed for cement pastes. This program minimizes both the roughness and sample disturbance of the material to effectively approximate an infinite half-space model. Samples were trimmed from small core sections with a diamond saw to expose surfaces parallel and perpendicular to the isotropy planes of the material (for indentation in the $x3$- and $x1$-directions, respectively). The typical size of each sample was a cylinder with a diameter of approximately 10 mm and a height of 5 mm. These samples were mounted to stainless steel plates with a very thin layer of cyanoacrylate. Polishing of the shale specimens proceeded in the same two-step process, as for cement pastes, with only a few differences:

1. In the first coarse grinding step, a 250 μm diamond paper was used because it was less

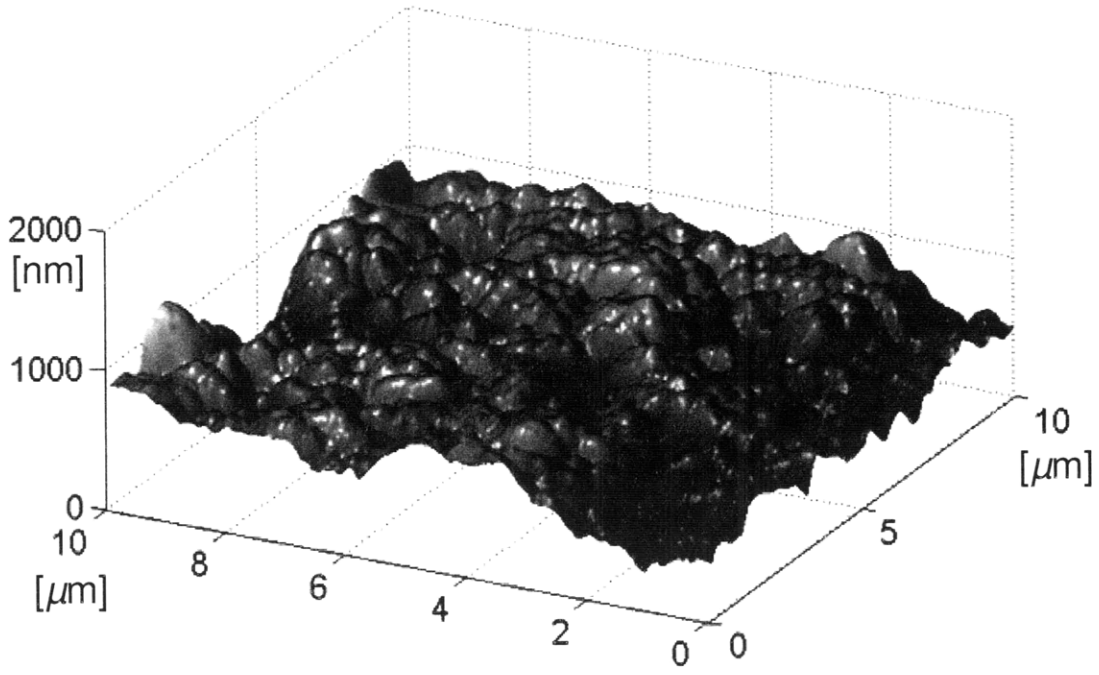

Figure 4-8: Three-dimensional representation of the AFM topography image for Shale 3.

aggressive than the 120 grit ZirMet paper. The shale samples are generally much softer and weaker than the cement pastes.

2. The polishing step was the same as for the cement pastes for all samples except for the Boston Blue Clay samples. The diamond suspension, even though it is oil-based, caused these samples to completely disintegrate when polishing. Additional trial and error led to a solution; for the Boston Blue Clay samples 1 μm diamond paper was used in a hand polish, which proceeded until the entire sample surface was polished.

4.3.4 Shale roughness results

A three-dimensional view of an AFM topography measurement on polished shale is shown in Figure 4-8. RMS roughness values from AFM testing are presented in Table 4.3. Rather than using a very large AFM scan, the reported values represent the mean results from three or four 20 x 20 μm scans. Values were not obtained for Shale 1 or the Boston Blue Clay samples,

Shale	RMS Roughness, R_q [nm]			
	$x1$-direction		$x3$-direction	
	mean	S.D.	mean	S.D.
GeoGenome Shales				
2	256	25	204	21
3	128	32	152	7
4	170	44	120	47
7	223	59	227	51
Light	252	111	166	124
Dark	163	81	205	50
Pierre	246	147	329	106
Woodford Shales				
110	85	9	112	2
131	81	14	113	37
154	166	34	170	20
166	201	18	240	56
175	198	52	176	7
185	236	41	243	44

Table 4.3: RMS Roughness of the polished shale samples, calculated over 20 micron by 20 micron areas (512 by 512 pixel resolution) measured with a non-contact tip. Topography with a wavelength greater than 10 microns was filtered out.

as the AFM would not give satisfactory results. High water content of these samples is the likely culprit, as the surface tension of the water interacts with the AFM tip. The typical RMS roughness obtained with the polishing procedure was found to be on the order of 150 to 300 nm. These roughness results will be compared with the surface roughness criteria after the typical indentation depth is chosen.

4.4 Chapter Summary

This chapter has introduced tools that allow the extraction of meaningful mechanical measurements from nanoindentation on shale, the complex natural porous composite material under investigation. The grid indentation technique and the statistical deconvolution technique were reviewed as a means to identify material phase properties and volume fractions in a composite material, given that scale separability conditions are met. In this case, the grid nanoindentation technique, along with the deconvolution procedure, provides reliable estimates of the mechanical behavior of each phase in a complex composite based on direct mechanical measurements.

The chapter closed by reviewing the importance of minimizing surface roughness for nanoindentation tests, and presenting recently developed criteria for acceptable surface roughnesses based on systematic tests on cement paste. These tests also provided a good example of application of the grid indentation and deconvolution technique. Based on the exercise for cement materials, a surface preparation procedure for shale was developed, and surface roughness measurements were made for each shale. This procedure is essential for making repeatable measurements.

The grid indentation technique uses a large number of indentations to obtain a few reliable parameters for each phase. For shale, the phase of primary interest at Level '1' is the porous clay phase, and the grid indentation technique provides unique, direct access to the mechanical behavior of this porous composite, in average terms for each shale sample. The idea that indentation senses a composite material even at this scale, however, leads to the possibility for further analysis and interpretation of indentation tests. This further analysis, based on an inverse approach to micromechanics results, is explored in the next chapter.

Chapter 5

Micromechanics Scaling Analysis for Nanoindentation on a Heterogeneous Composite - Application to Shale

This chapter continues the review and discussion of nanoindentation analysis techniques, and introduces and applies an inverse micromechanics approach to nanoindentation results associated with a porous composite material. Although the deconvolution analysis technique discussed in the previous chapter is very powerful, it takes the results of many tests and gives a single estimate of a behavior for each phase. While the deconvolution technique can give good estimates of mean indentation modulus and mean hardness, it offers no help in relating these measurements of mechanical properties to microstructure, a primary goal of this thesis. Another approach is required to use nanoindentation results to link elastic and cohesive-frictional strength properties to microstructure.

The idea behind the indentation modulus, hardness, and packing density scaling analysis ($M - H - \eta$ analysis) is to use the results of each indentation test on a porous composite to generate estimates of the mechanical behavior of the solid phase in the porous composite, as well as packing density distributions. For shale materials, the porous composite to be considered is the porous clay at Level '1' of the multiscale thought model for shale (Sec. 2.2), with solid properties at the scale of Level '0.' The approach is called a scaling approach

because micromechanics is used to develop scaling relationships for indentation measurements that depend on the properties of the solid and vary with the packing density. Used in an inverse approach with a large number of indentation experiments, these scaling relationships translate measurements from nanoindentation into mechanical properties of the solid phase and local packing densities associated with each indentation test.

The presentation in this chapter begins with development of the scaling problem formulation. Then the scaling relationships for indentation moduli are derived, and concepts of linear micromechanics are reviewed and employed to generate the scaling relationship. Next, development of the scaling relationship for indentation hardness is reviewed, based on recent implementation of a strength homogenization approach. Finally, these scaling relationships are combined and implemented in the inverse analysis approach.

5.1 Scaling Problem Formulation

To begin development of the scaling relationships, the problem is formally developed. This includes a description of the porous composite material to be indented, a form for the sought scaling relationships, and relevant assumptions for application to the porous clay in shale materials.

5.1.1 Indentation in a Porous Composite

Consider the situation displayed in Figure 5-1, where an indentation is made on an *rev* consisting of a solid phase and pore space. The solid phase has stiffness properties defined by C^s_{ijkl}, and strength properties defined by cohesive frictional strength parameters, c_s and μ_s. The volume fraction of the solid phase is characterized by the packing density, η. This situation models the typical nanoindentation test on the porous clay in shale materials, at the scale of Level '1' in the multiscale thought model for shale (Sec. 2.2 and Fig. 2-1).

The aim of the property-packing density scaling relationships is to better understand the link between the properties of the solid phase, the packing density, and results of nanoindentation

measurements. For indentation modulus, relationships of the form:

$$M_{(\beta)} = m_{(\beta),s} \times \Pi_{M_{(\beta)}} \left(\eta, \frac{C^s_{ijkl}}{m_{(\beta),s}} \right) \tag{5.1}$$

where the subscript $\beta = 1, 3$ stands for indentation modulus in $x1$- or $x3$-directions, are sought. This form suggests that indentation modulus measured in a given direction scales directly with the packing density and some form of anisotropy ratios captured by $C^s_{ijkl}/m_{(\beta),s}$. For hardness, relationships of the form:

$$H = h_s \left(c_s, \mu_s \right) \times \Pi_H \left(\mu_s, \eta \right) \tag{5.2}$$

are sought where $h_s \left(c_s, \mu_s \right)$ is the solid hardness as a function of the solid strength parameters c_s and μ_s (see Sec. 3.4.2). This form suggests that hardness does not depend on direction of indentation, and that the scaling relationship varies not only with the packing density, but also with the friction coefficient μ_s.

Micromechanics provides the theoretical framework for developing the sought scaling relationships. This framework permits the development of homogenized estimates of composite material behavior. Two categories of input information are required in a micromechanics framework: information about the microstructure and morphology in the composite material, and information about the mechanical properties of each phase in the composite material.

5.1.2 Shale Model Assumptions

For application to shales, several model assumptions are required to define the input quantities for development of the scaling relationships. These assumptions are based on preliminary work investigating shale materials within the framework of the multiscale thought model for shale [172], [174] and will be tested through an analysis of experimental results presented in upcoming chapters. Consider first, assumptions about the microstructure of the material:

- The porous clay composite at the scale of Level '1' in the multiscale thought model for shale has a granular microstructure, rather than a matrix of clay solid with embedded pores.
- The mechanical morphology of the solid particle in the porous clay composite may be

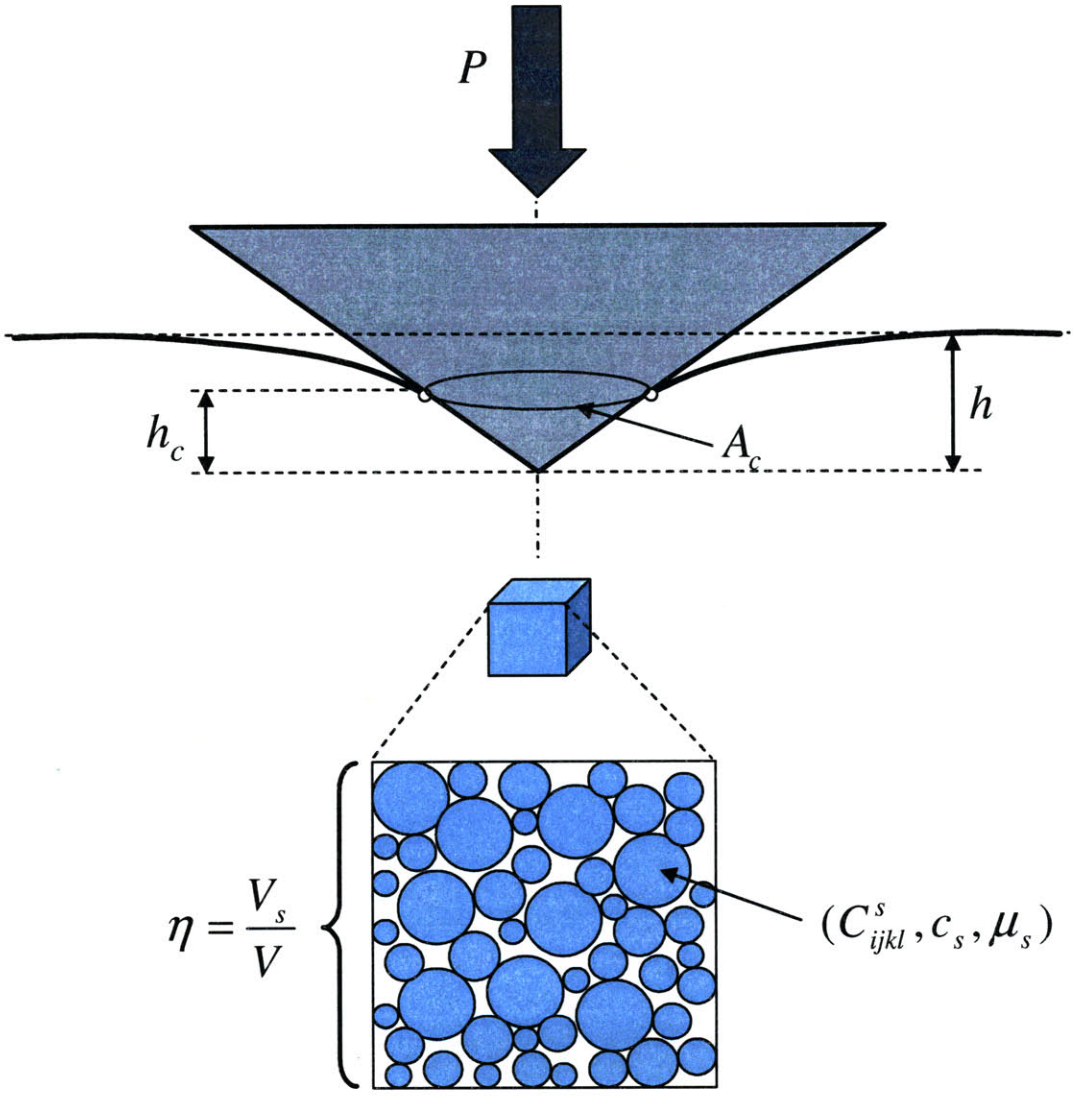

Figure 5-1: Conical indentation in a porous material composed of a solid phase and pore space (adapted from [33]).

represented by a sphere, as suggested by an apparent percolation threshold at a packing density of $\eta_0 = 0.5$, below which a continuous stress path cannot be formed through the material. This percolation threshold is associated with the random packing of spheres.

Assumptions about the mechanical properties of the solid and the composite are also required:

- The solid particle possesses intrinsic transverse isotropy in elasticity, as suggested by back-analysis of macroscopic measurements and preliminary nanoindentation experiments [145], [174].
- The solid particle has cohesive-frictional strength behavior, as discussed in more detail in the next section on indentation hardness.
- The solid particles have isotropic strength properties, as expressed by isotropic hardness measurements.
- Nanoindentation on the porous clay in shale is a drained test based on the length scales and loading rates involved in a typical nanoindentation test [51], meaning that nanoindentation does not measure any additional stiffening effect from any pore fluid.

5.2 Indentation Modulus - Packing Density Scaling

This section introduces the packing density scaling relationships for the indentation modulus obtained from indentation on a porous composite. The next section will introduce similar relationships for indentation hardness on a porous composite. This section begins with a brief review of the tools of linear micromechanics, which are used to develop the dimensionless elasticity functions $\Pi_{M_{(\beta)}}$ as in Eq. (5.1).

5.2.1 Elements of Linear Homogenization Theory

Continuum micromechanics, based on the scale separability conditions, involves two scales: The microscale, where the composite is heterogeneous, and the macroscale, where the composite behaves mechanically in a homogeneous manner. Microscopic and macroscopic quantities are

	Microscopic quantities	Macroscopic quantities
Position	$\underline{x}$	$\underline{X}$
Strain	$\boldsymbol{\varepsilon}(\underline{x})$	$\mathbf{E}(\underline{X})$
Stress	$\boldsymbol{\sigma}(\underline{x})$	$\boldsymbol{\Sigma}(\underline{X})$
Energy	$\omega(\underline{x})$	$\mathcal{W}(\underline{X})$

Table 5.1: Microscopic and macroscopic quantities.

defined in Table 5.1. The macroscopic quantities $A(\underline{X})$ are defined as the local average of the microscopic ones $a(\underline{x})$. If $\Omega(\underline{X})$ is the *rev* centered at point $\underline{X}$, then for any quantities $A(\underline{X})$ and $a(\underline{x})$ we have:

$$A(\underline{X}) = \langle a(\underline{x}) \rangle_{\Omega(\underline{X})} = \frac{1}{|\Omega|} \int_{\Omega(\underline{X})} a(\underline{x}) \, d\underline{x} \tag{5.3}$$

where the angled brackets define a volume average over the material domain Ω.

The aim of linear homogenization theory is to find from the local distribution of microscopic stiffness tensors $\mathbb{C}(\underline{x})$, which link the local stress $\boldsymbol{\sigma}(\underline{x})$ to the local strain $\boldsymbol{\varepsilon}(\underline{x})$ by $\boldsymbol{\sigma}(\underline{x}) = \mathbb{C}(\underline{x}) : \boldsymbol{\varepsilon}(\underline{x})$, the homogenized stiffness tensor $\mathbb{C}^{\text{hom}}$, which links the macroscopic stress $\boldsymbol{\Sigma}(\underline{X})$ to the macroscopic strain $\mathbf{E}(\underline{X})$:

$$\boldsymbol{\Sigma}(\underline{X}) = \mathbb{C}^{\text{hom}} : \mathbf{E}(\underline{X}) \tag{5.4}$$

It is common in homogenization theory to work with regular strain or stress boundary conditions [66]:

- For fixed $\mathbf{E}$, the displacement is prescribed at the boundary $\partial\Omega$ of the *rev*:

$$\underline{\xi} = \mathbf{E} \cdot \underline{x} \qquad \text{on } \partial\Omega \tag{5.5}$$

- For fixed $\boldsymbol{\Sigma}$, the stress vector is prescribed at the boundary $\partial\Omega$ of the *rev*:

$$\boldsymbol{\sigma} \cdot \underline{n} = \boldsymbol{\Sigma} \cdot \underline{n} \qquad \text{on } \partial\Omega \tag{5.6}$$

For regular boundary conditions, and by neglecting the effect of an externally applied load density so that $\operatorname{div} \boldsymbol{\sigma} = \underline{0}$, the Hill lemma [92] applies:

$$\langle \boldsymbol{\sigma} : \boldsymbol{\varepsilon} \rangle = \langle \boldsymbol{\sigma} \rangle : \langle \boldsymbol{\varepsilon} \rangle \tag{5.7}$$

which stipulates that the macroscopic energy $\mathcal{W}(\underline{X}) = \boldsymbol{\Sigma}(\underline{X}) : \mathbf{E}(\underline{X})$ is indeed the volume average of the microscopic strain energy $\omega(\underline{x})$.

Localization Tensor

From now on we restrict ourselves to regular displacement boundary conditions of the form in Eq. (5.5). In this case, due to the linearity of all microscopic material behaviors, the microscopic strain $\boldsymbol{\varepsilon}(\underline{x})$ is proportional to the applied macroscopic strain $\mathbf{E}(\underline{X})$:

$$\boldsymbol{\varepsilon}(\underline{x}) = \mathbb{A}(\underline{x}) : \mathbf{E} \tag{5.8}$$

where $\mathbb{A}(\underline{x})$ is called the strain concentration or strain localization tensor. Then the stress field reads:

$$\boldsymbol{\sigma}(\underline{x}) = \mathbb{C}(\underline{x}) : \mathbb{A}(\underline{x}) : \mathbf{E} \tag{5.9}$$

So that:

$$\boldsymbol{\Sigma} = \langle \boldsymbol{\sigma}(\underline{x}) \rangle_\Omega = \langle \mathbb{C}(\underline{x}) : \mathbb{A}(\underline{x}) \rangle_\Omega : \mathbf{E} \tag{5.10}$$

A comparison of Eqs. (5.10) and (5.4) yields the expression for the homogenized stiffness tensor:

$$\mathbb{C}^{\text{hom}} = \langle \mathbb{C}(\underline{x}) : \mathbb{A}(\underline{x}) \rangle_\Omega \tag{5.11}$$

Determining the homogenized stiffness tensor is hence reduced to the determination of the strain localization tensor $\mathbb{A}(\underline{x})$. Estimates of the strain localization tensor are obtained by considering the Eshelby inclusion problem, presented next.

Eshelby Inclusion Problem

In 1957, Eshelby [70] considered the case of an isolated ellipsoidal inclusion ($\mathcal{I}$) with constant elasticity tensor $\mathbb{C}_1$ embedded in an infinite medium with a different elasticity tensor $\mathbb{C}_0$ and subjected to a uniform strain $\mathbf{E}^\infty$ at infinity (Figure 5-2).

The domain occupied by the inclusion is defined by:

$$\mathcal{I} = \left\{ \underline{x} \in \mathbb{R}^3 \,|\, \underline{x} \cdot \left({}^t\mathbf{A} \cdot \mathbf{A} \right)^{-1} \cdot \underline{x} \leq 1 \right\} \tag{5.12}$$

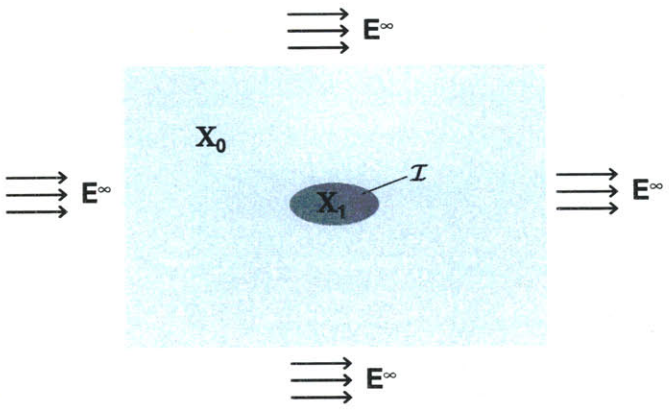

Figure 5-2: Eshelby problem: Ellipsoidal inclusion ($\mathcal{I}$) embedded in an infinite elastic medium (from [77]).

where $\mathbf{A}$ is a second order tensor. If $\underline{e}_1$, $\underline{e}_2$, $\underline{e}_3$ are the directions of the main axis and a_1, a_2, a_3 are the half lengths of the axis, then:

$$\mathbf{A} = a_1\,\underline{e}_1 \otimes \underline{e}_1 + a_2\,\underline{e}_2 \otimes \underline{e}_2 + a_3\,\underline{e}_3 \otimes \underline{e}_3 \tag{5.13}$$

and the equation of the ellipsoid is:

$$\left(\frac{x_1}{a_1}\right)^2 + \left(\frac{x_2}{a_2}\right)^2 + \left(\frac{x_3}{a_3}\right)^2 \leq 1 \tag{5.14}$$

Eshelby showed that the strain field inside the inclusion is constant and that the value of the strain inside the inclusion is:

$$\forall \underline{x} \in \mathcal{I}, \quad \boldsymbol{\varepsilon}\,(\underline{x}) = \left(I + \mathbb{P}_0 : (\mathbb{C}_1 - \mathbb{C}_0)\right)^{-1} : \mathbf{E}^{\infty} \tag{5.15}$$

where:

$$\mathbb{P}_0 = \frac{\det \mathbf{A}}{4\pi} \int_{||\underline{v}||=1} \frac{\underline{v} \overset{s}{\otimes} \left(\underline{v} \cdot \mathbb{C}_0 \cdot \underline{v}\right)^{-1} \overset{s}{\otimes} \underline{v}}{\left(\underline{v} \cdot \left({}^t\mathbf{A} \cdot \mathbf{A}\right)^{-1} \cdot \underline{v}\right)^{\frac{3}{2}}} dS \tag{5.16}$$

is the Hill tensor. The Hill tensor depends only on the shape of the inclusion and not on its size.

If the reference medium is isotropic,

$$\mathbb{C}_0 = 3K_0\,\mathbb{J} + 2G_0\,\mathbb{K} \tag{5.17}$$

and if the inclusion is a sphere (i.e. $\mathbf{A} = \mathbf{1}$), then

$$\mathbb{P}_0 = \frac{1}{3K_0 + 4G_0}\,\mathbb{J} + \frac{3}{5G_0}\frac{K_0 + 2G_0}{3G_0 + 4G_0}\,\mathbb{K} \tag{5.18}$$

where $\mathbb{J}$ and $\mathbb{K}$ are the fourth-order tensors defined by:

$$\mathbb{J} = \mathbf{I} \otimes \mathbf{I};\ \mathbb{K} = \mathbb{I} - \mathbb{J} \tag{5.19}$$

where $\mathbf{I}$ is the second order unit tensor.

From Eq. (5.16), expressions for the Hill tensor can also be derived for more complicated material behaviors (e.g., for an anisotropic reference medium [117]) and other shapes of inclusions (e.g., ellipsoidal inclusions in an isotropic reference medium [70] [13]).

The Eshelby inclusion problem can be used to obtain estimates of the homogenized stiffness tensor $\mathbb{C}^{\text{hom}}$. Here the composite material is assumed to be made of N phases, and the inclusions are assumed to be spherical. The i-th phase ($i \in \{1, .., N\}$) is characterized by the stiffness tensor $\mathbb{C}_i$ and occupies the volume Ω_i and a volume fraction ϕ_i of the composite. Using Eshelby's result (5.15), the mean strain tensor in each inclusion of phase i is estimated by:

$$\langle \boldsymbol{\varepsilon}(\underline{x}) \rangle_{\Omega_i} = \left(I + \mathbb{P}_0 : (\mathbb{C}_i - \mathbb{C}_0)\right)^{-1} : \mathbf{E}^{\infty} \tag{5.20}$$

In the above expression, the strain $\mathbf{E}^{\infty}$ 'felt' by the inclusion and the stiffness tensor $\mathbb{C}_0$ of the embedding medium must be determined. $\mathbf{E}^{\infty}$ is determined by enforcing the regular strain boundary condition:

$$\mathbf{E} = \langle \boldsymbol{\varepsilon}(\underline{x}) \rangle_{\Omega} \tag{5.21}$$

Making use of Eq. (5.20) yields:

$$\mathbf{E} = \sum_{i=1}^{N} \phi_i \left(I + \mathbb{P}_0 : (\mathbb{C}_i - \mathbb{C}_0)\right)^{-1} : \mathbf{E}^{\infty} \tag{5.22}$$

It follows:

$$\mathbf{E}^{\infty} = \left[\sum_{i=1}^{N} \phi_i \left(I + \mathbb{P}_0 : (\mathbb{C}_i - \mathbb{C}_0)\right)^{-1}\right]^{-1} : \mathbf{E} \tag{5.23}$$

Therefore, from Eq. (5.15), the mean strain in each inclusion of phase i is:

$$\langle \varepsilon(\underline{x}) \rangle_{\Omega_i} = \left(I + \mathbb{P}_0 : (\mathbb{C}_i - \mathbb{C}_0)\right)^{-1} : \left[\sum_{i=1}^{N} \phi_i \left(I + \mathbb{P}_0 : (\mathbb{C}_i - \mathbb{C}_0)\right)^{-1}\right]^{-1} : \mathbf{E} \tag{5.24}$$

A comparison of Eqs. (5.24) and (5.8) yields the expression of the mean strain localization tensor:

$$\langle \mathbb{A}(\underline{x}) \rangle_{\Omega_i} = \left(I + \mathbb{P}_0 : (\mathbb{C}_i - \mathbb{C}_0)\right)^{-1} : \left[\sum_{i=1}^{N} \phi_i \left(I + \mathbb{P}_0 : (\mathbb{C}_i - \mathbb{C}_0)\right)^{-1}\right]^{-1} \tag{5.25}$$

and, finally, the expression of the homogenized stiffness tensor $\mathbb{C}^{\text{hom}}$:

$$\mathbb{C}^{\text{hom}} = \sum_{i=1}^{N} \phi_i \mathbb{C}_i : \langle \mathbb{A}(\underline{x}) \rangle_{\Omega_i} \tag{5.26}$$

$$= \left[\sum_{i=1}^{N} \phi_i \mathbb{C}_i : \left(I + \mathbb{P}_0 : (\mathbb{C}_i - \mathbb{C}_0)\right)^{-1}\right] : \left[\sum_{i=1}^{N} \phi_i \left(I + \mathbb{P}_0 : (\mathbb{C}_i - \mathbb{C}_0)\right)^{-1}\right]^{-1} \tag{5.27}$$

In Eq. (5.27) the stiffness tensor $\mathbb{C}_0$ (and consequently $\mathbb{P}_0$) of the embedding medium remains to be determined and depends on the morphology of the composite. Choosing this morphology will allow development of the form of the indentation modulus-packing density scaling relation.

5.2.2 Self-Consistent Scheme and Percolation Threshold

The assumptions about the microstructure and morphology of the porous clay composite enter in the choice of the strain localization tensor $\mathbb{A}(\underline{x})$. If no phase in the composite plays the role of a matrix, one can consider that the embedding medium is the homogenized medium itself. Such an estimate of the homogenized stiffness tensor $\mathbb{C}^{\text{hom}}$ is called the self-consistent (or polycrystal) estimate $\mathbb{C}^{SC}$, which originated independently from Hershey [90] and Kröner [112]. Granular materials are well captured by a self-consistent model, and a spherical solid and pore morphology with the self-consistent scheme results in a modeled percolation threshold

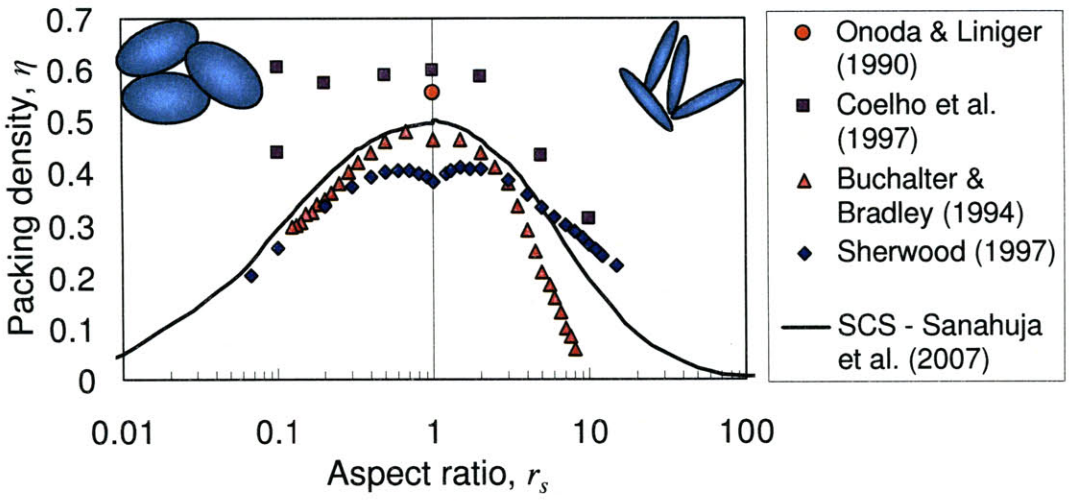

Figure 5-3: Effect of the solid particle aspect ratio r_s on the percolation threshold from oblates ($r_s < 1$) to prolates ($r_s > 1$). Results from experiments (Onoda & Liniger, 1990) [144], granular computational approaches (Coehlo et al., 1997, Buchalter & Bradley, 1994, and Sherwood, 1997) [41], [29], [163] and modeling with the self consistent scheme (Sanahuja et al., 2007) [154] are included.

of $\eta_0 = 0.5$.

The self-consistent scheme for non-spherical morphologies gives different results. In fact, recent results from Sanahuja et al. [154] have explored the percolation threshold captured by a self-consistent scheme for spheroids. These shapes are defined by their aspect ratio, r_s, which is expressed as the ratio of the length of the symmetry axis over the diameter in the symmetry plane. Particles with $r_s < 1$ are oblate spheroids (reminiscent of M & M candies) and particles with $r_s > 1$ are prolate spheroids (cigar shapes). Sanahuja et al. [154] confirmed that the percolation threshold for a composite of randomly oriented spheres is $\eta_0 = 0.5$, and further demonstrated that this value is the maximum percolation threshold captured by the self-consistent scheme when considering spheroidal particles. As shown in Figure 5-3, any aspect ratio not equal to one, that is for non-spherical particles, gives lower percolation thresholds.

The random packing of particles is a focus of research in the granular physics community, and granular physics experiments and computational approaches give results which match well to the predictions given by the self-consistent scheme. These results are also shown in Figure

5-3. In particular, Onoda and Liniger determined that the random-loose packing fraction of uniform spheres, at the limit of zero graviational force, is 0.555 ± 0.005. Buchalter and Bradley [29] performed Monte Carlo simulations of the porosity of oblate and prolate ellipsoids, and showed that increasing asphericity (oblate and prolate) yields lower percolation thresholds. Similar results were obtained by Coehlo et al. [41] and Sherwood [163], using a sequential deposition algorithm of rigid particles of different shapes. This good agreement confirms that the self-consistent scheme in micromechanics captures the percolation threshold associated with granular materials. In this context, with the model assumptions of granular behavior with a percolation threshold of $\eta_0 = 0.5$ in mind, the self-consistent scheme with spherical particle shapes is employed. Further discussion around these assumptions and choices will be made after the presentation of results.

Letting $\mathbb{C}_0 \rightarrow \mathbb{C}^{\text{hom}} = \mathbb{C}^{SC}$ in Eq. (5.27), the self-consistent estimate is found by solving:

$$\mathbb{C}^{SC} = \left[\sum_{i=1}^{N} \phi_i \mathbb{C}_i : \left(I + \mathbb{P}^{SC} : \left(\mathbb{C}_i - \mathbb{C}^{SC}\right)\right)^{-1}\right] : \left[\sum_{i=1}^{N} \phi_i \left(I + \mathbb{P}^{SC} : \left(\mathbb{C}_i - \mathbb{C}^{SC}\right)\right)^{-1}\right]^{-1} \tag{5.28}$$

Analytical solutions for this estimate are available for isotropic materials [46].

5.2.3 Results: Indentation Modulus-Packing Density Scaling Relationships

The remaining input required for development of the indentation modulus-packing density scaling relationships is knowledge of the stiffness of the solid phase, i.e. $\mathbb{C}_i = \mathbb{C}^s$ in Eq. (5.28) (the stiffness of the pore space is zero in drained conditions). Recall the assumption that the solid phase has transverse isotropy of elasticity. The quantitative properties of this solid are to be determined through the nanoindentation experiments, although estimates from preliminary work and back-analysis approaches have been made [145], [174]. Implementation of Eq. (5.28) for transversely isotropic materials is complex. Recent work by Ortega et al. [145], based on the work of Hellmich et al. [86] has employed a definition of $\mathbb{P}^{SC}$ that can be evaluated numerically. All the theoretical tools are in place to assess the link between indentation modulus M and microstructure for the solid-pore composite presented in Figure 5-1.

Ortega et al.'s work [145] has provided estimates of the solid stiffness for the porous clay in

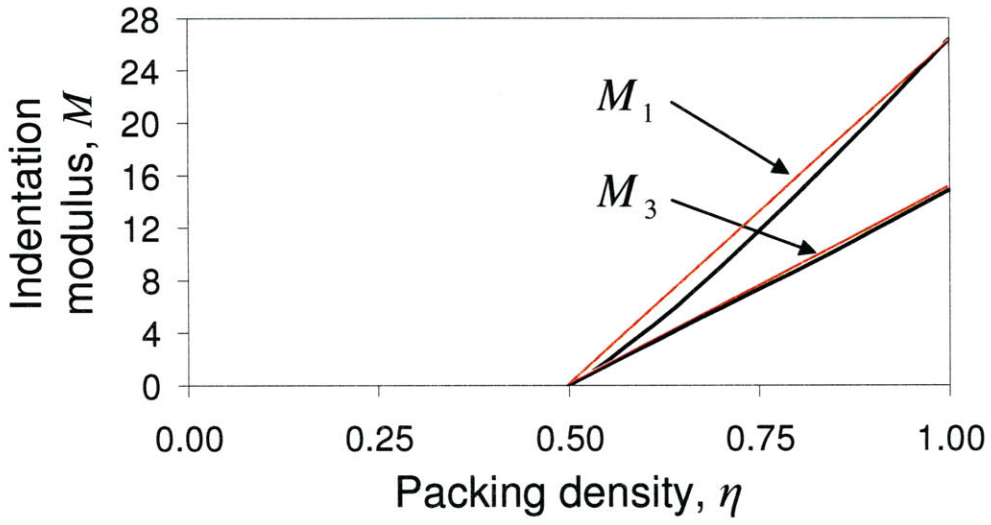

Figure 5-4: Scaling of equivalent indentation moduli, M_1, M_3 for a transversly isotropic material with clay packing density, η. The thick black are generated numerically using the self-consistent scheme, while the thin red lines are linear approximations.

shale, using a back analysis approach. The estimated stiffness coefficients are:

$$\begin{aligned} C^s_{11} &= 44.9 \text{ GPa} \\ C^s_{12} &= 21.7 \text{ GPa} \\ C^s_{13} &= 18.1 \text{ GPa} \\ C^s_{33} &= 24.2 \text{ GPa} \\ C^s_{44} &= 3.7 \text{ GPa} \end{aligned} \tag{5.29}$$

Ortega et al. have also performed the numerical evaluation of the micromechanics problem to develop the expressions for $\mathbb{C}^{SC}$ as a function of packing density. Equivalent indentation moduli based on the homogenized stiffness tensor, $\mathbb{C}^{SC}$ can be developed with Eq. (3.46):,

$$m_{1,s} = 26.3 \text{ GPa} \tag{5.30a}$$

$$m_{3,s} = 14.9 \text{ GPa} \tag{5.30b}$$

giving expressions in the sought form (Eq. (5.1)):

$$M_1 = m_{1,s} \times \Pi_{M_1} \left(\eta, \frac{C^s_{11}}{C^s_{33}} = 1.9, \frac{C^s_{11} - C^s_{12}}{C^s_{44}} = 3.1, \frac{C^s_{33} - C^s_{13}}{C^s_{44}} = 0.8, \frac{C^s_{12}}{C^s_{13}} = 1.2 \right) \quad (5.31a)$$

$$M_3 = m_{3,s} \times \Pi_{M_3} \left(\eta, \frac{C^s_{11}}{C^s_{33}} = 1.9, \frac{C^s_{11} - C^s_{12}}{C^s_{44}} = 3.1, \frac{C^s_{33} - C^s_{13}}{C^s_{44}} = 0.8, \frac{C^s_{12}}{C^s_{13}} = 1.2 \right) \quad (5.31b)$$

The results of this work are shown in Figure 5-4. These numerical results are nonlinear but the dimensionless expressions $\Pi_{M_{(\beta)}}$ may be approximated by power functions of the packing density:

$$\Pi_{M_1} = 1.28\,(\eta - 0.5) + 3.09\,(\eta - 0.5)^2 - 5.05\,(\eta - 0.5)^3 + 3.54\,(\eta - 0.5)^4 \quad (5.32a)$$

$$\Pi_{M_3} = 2.10\,(\eta - 0.5) - 1.15\,(\eta - 0.5)^2 + 3.14\,(\eta - 0.5)^3 - 2.43\,(\eta - 0.5)^4 \quad (5.32b)$$

which are valid for $0.5 \leq \eta \leq 1$ and give a value of zero at the percolation threshold $\eta_0 = 0.5$. The scaling relationships are non-linear and slightly different for M_1 and M_3, but they may both be well approximated by straight lines, with a horizontal intercept at packing density of $\eta = 0.5$. The approximated linear scaling relationships are summarized:

$$\frac{M_{(\beta)}}{m_{(\beta),s}} = \Pi_M(\eta) = 2\eta - 1 \quad (5.33)$$

where $m_{(\beta),s}$ is the equivalent indentation modulus of the solid in the direction $\beta = 1, 3$ for the $x1$- or $x3$- directions.

5.3 Indentation Hardness - Packing Density Scaling Analysis

This section introduces the packing density scaling relationships for the hardness obtained from indentation on a porous composite, analogous to the scaling relationships for the indentation modulus presented in the previous section. Recall that the situation under consideration is displayed in Figure 5-1, where an indentation is made on an *rev* consisting of a solid phase and pore space. The solid phase has stiffness properties defined by C^s_{ijkl} and Drucker-Prager strength properties c_s and α_s, where α_s is the Drucker-Prager friction coefficient, as explained in more detail in Section 5.3.1. The volume fraction of the solid phase is characterized by

the packing density, η. We assume that the hardness, as well as the strength properties, are isotropic. Once again, the aim of the property-packing density scaling relationships is to better understand the link between the properties of the solid phase, the packing density, and results of nanoindentation measurements.

As before, micromechanics provides the theoretical framework for developing the sought scaling relationships by developing homogenized estimates of composite material behavior, recalling Eq (5.2):

$$H = h_s\left(c_s, \alpha_s\right) \times \Pi_H\left(\alpha_s, \eta\right) \tag{5.34}$$

where the strength criteria are updated to reflect the use of the Drucker-Prager strength parameters. While homogenization techniques for elastic behavior are relatively well established, homogenization of strength criteria is still an area of active research. This section reviews the latest developments, as implemented for the porous clay in shale materials by Gathier [77]. The section begins with a discussion of cohesive-frictional strength criteria commonly used for shale materials, and reviews a recent micromechanics work that highlights the Drucker-Prager strength criterion. Next, a dimensional analysis frames the problem and provides a context for the form of the hardness-packing density scaling relation while reviewing earlier attempts. The strength homogenization approach, based on the Linear Comparison Composite technique, is then reviewed, which paves the way for making the application to the solid-pore composite. A computational technique, the Limit Analysis solver, permits evaluation of the solutions and finally results in a hardness-packing density scaling relationship for a porous composite with a cohesive-frictional solid phase.

5.3.1 Cohesive-Frictional Plastic Material Properties

A variety of strength criteria have been proposed to capture the failure of cohesive frictional materials (see Tab. 3.1) in stress space. The most important and widely used criteria are the Mohr-Coulomb, Drucker-Prager, and Modified Lade criteria. This section describes the different criteria, how they differ from each other, and how they may be related. Colmenares and Zoback [42] have recently reviewed these criteria and others in terms of the macroscopic, intact strength behavior of some rocks. To date, no study has investigated the validity of the criteria for microscopic strength at the scale of the elementary building block.

Mohr-Coulomb

The Mohr-Coulomb criterion is a surface traction criterion reading:

$$f\left(\underline{T} = \boldsymbol{\sigma} \cdot \underline{n}\right) = |T_t| + \mu\, T_n - C \leq 0 \tag{5.35}$$

where $T_t = \underline{t} \cdot (\boldsymbol{\sigma} \cdot \underline{n})$ is the tangential shear stress on the material surface oriented by unit outward normal $\underline{n}$, and $T_n = \underline{n} \cdot (\boldsymbol{\sigma} \cdot \underline{n})$ is the normal stress acting on this surface. The two parameters of the criterion are C, the Mohr-Coulomb cohesion, and $\mu = \tan\varphi$, the Mohr-Coulomb friction coefficient, where φ is defined as the Mohr-Coulomb friction angle. The Mohr-Coulomb criterion may also be expressed as a function of the principal stresses, $\sigma_I \geq \sigma_{II} \geq \sigma_{III}$:

$$f\left(\boldsymbol{\sigma}\right) = \sigma_I - \sigma_{III} + (\sigma_I + \sigma_{III}) \sin\varphi - 2C\cos\varphi \leq 0 \tag{5.36}$$

Drucker-Prager

The Drucker-Prager criterion can be viewed as a Mohr-Coulomb criterion on the deviatoric stress plane defined by the orientation of the hydrostatic axis, i.e. $\underline{n} = \frac{1}{\sqrt{3}}\left(\underline{u}_I + \underline{u}_{II} + \underline{u}_{III}\right)$, with $\underline{u}_J$ the eigenvectors of the stress tensor corresponding to principal stress directions. In contrast to the Mohr-Coulomb criterion, which depends only on the minimum and maximum principal stresses, the Drucker-Prager criterion involves all three principal stresses. The confining stress on the deviator stress plane is the mean stress, $\sigma_m = \frac{1}{3} I_1 = \frac{1}{3}\,\mathrm{tr}\left(\boldsymbol{\sigma}\right) = \frac{1}{3}\left(\sigma_I + \sigma_{II} + \sigma_{III}\right)$. The shear stress magnitude on the deviator plane is expressed by the second invariant of the stress deviator, $\mathbf{s} = \boldsymbol{\sigma} - \sigma_m \mathbf{1}$, defined as

$$J_2 = \frac{\sigma_d^2}{2} = \frac{\mathbf{s} : \mathbf{s}}{2} = \frac{\mathrm{tr}\left(\mathbf{s} \cdot \mathbf{s}\right)}{2} \tag{5.37}$$

The Drucker-Prager criterion then reads as a function of these two stress invariants:

$$f\left(\boldsymbol{\sigma}\right) = \sqrt{J_2} + \alpha\, \sigma_m - c \leq 0 \tag{5.38}$$

where α is the Drucker-Prager friction coefficient, and c is the Drucker-Prager cohesion. It is important to note that there is a limitation on the choice of the Drucker-Prager friction

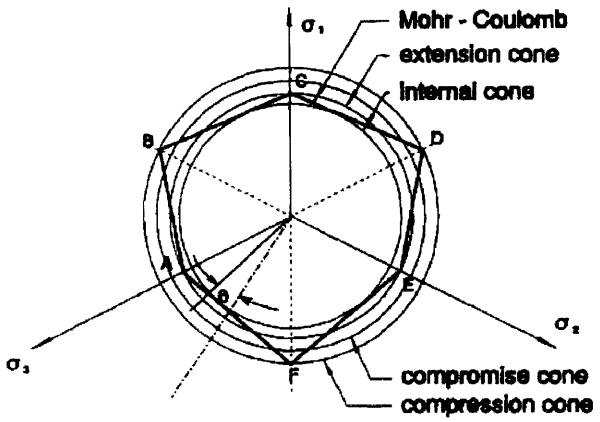

Figure 5-5: Correspondance between the Mohr-Coulomb and the Drucker-Prager criterion in the deviatoric stress plane (from [159]).

coefficient,

$$\alpha < \sqrt{\frac{3}{4}} \tag{5.39}$$

Indeed, it has been shown that this value corresponds to a friction angle of $\varphi = 90°$ for the corresponding Mohr-Coulomb criterion [60].

It is possible to link the Drucker-Prager friction coefficient α to the Mohr-Coulomb friction coefficient $\mu = \tan\varphi$, by considering the deviator plane representation of both criteria (Eqs. (5.36) and (5.38)), as shown in Figure 5-5. Considering respectively the internal cone and the compression cone of the Drucker-Prager criterion [159], yields the following links between the material properties of the Drucker-Prager material (c, α) and of the Mohr- Coulomb criterion $(C, \sin\varphi)$:

$$\begin{aligned} &\text{Compression Cone} \quad C = \frac{3-\sin\varphi}{2\sqrt{3}\cos\varphi}c \quad \sin\varphi = \frac{3\alpha}{\alpha+2\sqrt{3}} \\ &\text{Internal Cone} \quad C = \sqrt{\frac{3+(\sin\varphi)^2}{3(\cos\varphi)^2}} \quad \sin\varphi = \sqrt{\frac{3\alpha^2}{3-\alpha^2}} \end{aligned} \tag{5.40}$$

Finally, from a practical point of view, the Drucker-Prager model involves only regular functions of the principal stresses, and from a computational point of view, it is usually easier to handle than the Mohr-Coulomb criterion.

Modified Lade Criteria

The modified Lade criterion was developed by Ewy [71] to bridge between the Mohr-Coulomb criterion, which does not take the intermediate principal stress into account at all, and the Drucker-Prager criterion, which gives equal weight to all three principal stresses. The modified Lade criterion reads:

$$\frac{(I_1')^3}{I_3'} = 27 + \eta_{ML} \tag{5.41}$$

where

$$I_1' = (\sigma_1 + S) + (\sigma_2 + S) + (\sigma_3 + S) \tag{5.42a}$$

$$I_3' = (\sigma_1 + S)(\sigma_2 + S)(\sigma_3 + S) \tag{5.42b}$$

where S and η_{ML} are material constants. Ewy suggests that S is related to the cohesion of the rock and η_{ML} is related to the internal friction of the material. These parameters may be directly related to the Mohr-Coulomb parameters by

$$S = \frac{C}{\tan\varphi} \tag{5.43a}$$

$$\eta_{ML} = \frac{4(\tan\varphi)^2(9 - 7\sin\varphi)}{1 - \sin\varphi} \tag{5.43b}$$

Micromechanics link between Mohr-Coulomb and Drucker-Prager

Recent work by Fritsch et al. [72] provides an interesting micromechanical approach to the frictional strength behavior of a solid polycrystal. Fritsch, et al. studied the brittle failure of a polycrystal with weak interfaces (Fig. 5-6 (top). In their formulation, both the crystals and their interfaces are assumed to have linear elastic behavior. The interface is assumed to fail in a brittle manner once the shear stress at the interface reaches a threshold defined by a Mohr-Coulomb type criterion (Eq. (5.35)):

$$|T_t| \leq C - \mu T_n \tag{5.44}$$

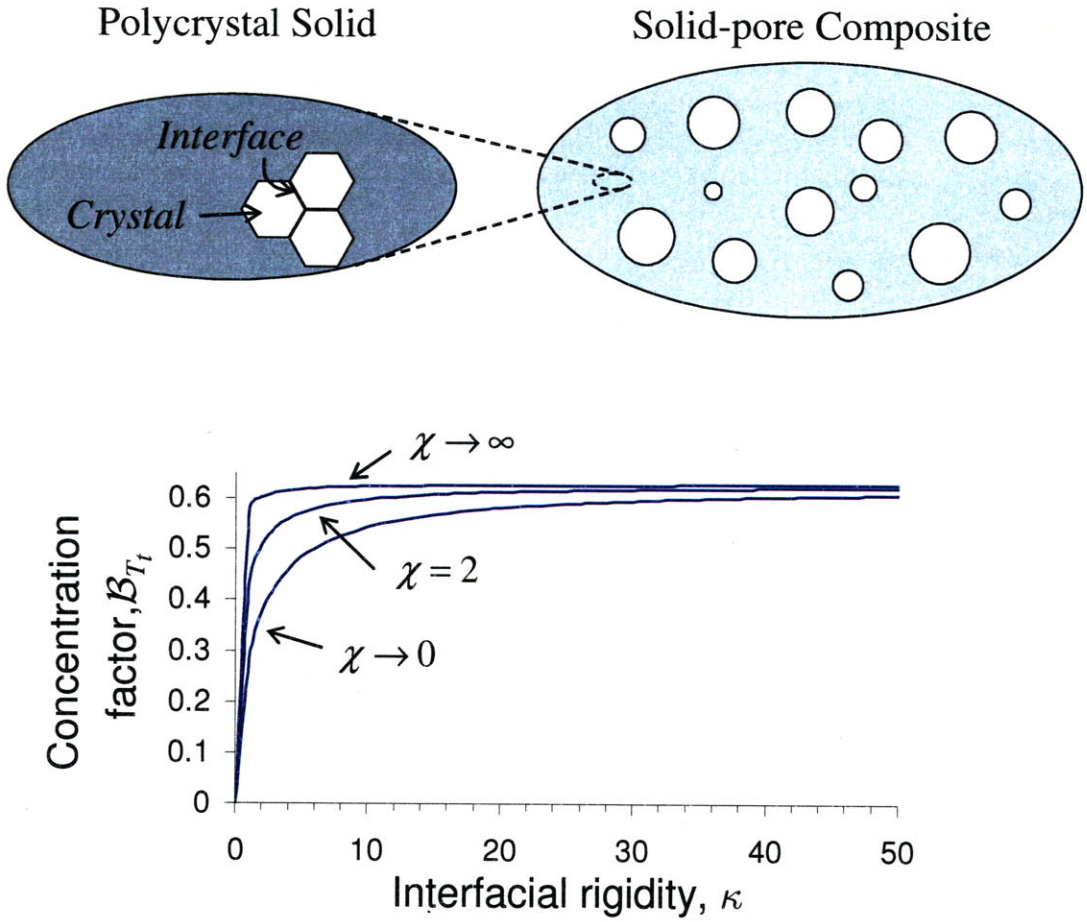

Figure 5-6: Top: Polycrystal solid model with weak interfaces is homogenized with porosity at a larger scale to form a solid-pore composite. Bottom: The concentration factor $\mathcal{B}_{T_t}$ relates the macroscopic deviatoric stress on the polycrystal to an effective tangential stress in the intercrystalline interfaces, as a function of dimensionless expressions for the interfacial rigidity, κ, and the crystal compressibility, χ. Adapted from [72].

Application of the polycrystal model with weak interfaces to the problem yields a Drucker-Prager type criterion for the onset of brittle failure of the polycrystal-interface composite:

$$\mathcal{B}_{T_t}\sqrt{J_2} \leq C - \mu\sigma_m \tag{5.45}$$

where $\mathcal{B}_{T_t}$ is a concentration factor which varies between 0 and $\sqrt{2/5}$ and depends on dimensionless expressions of the interfacial rigidity, κ, and the crystal compressibility, χ, as seen in Figure 5-6 (bottom).

These recent results of advanced micromechanics show that a Drucker-Prager criterion can be seen as a representation of a distinct weakness of the intercrystalline interfaces at smaller scales. It is in this sense that the Drucker-Prager strength model is employed to describe the strength domain of the polycrystal clay particles at level '0'. The dual definition of the strength domain is given by:

$$\boldsymbol{\sigma} \in G_s(\underline{x}) \Leftrightarrow \begin{cases} f(\boldsymbol{\sigma}) = \sqrt{J_2} + \alpha_s\,\sigma_m - c_s \leq 0 \\ \\ \pi(\mathbf{d}) = \sup(\boldsymbol{\sigma} : \mathbf{d}) = \begin{cases} \dfrac{c_s}{\alpha_s} d_v & \text{if } d_v \geq \sqrt{2}\alpha\; d_d \\ \infty & \text{else} \end{cases} \end{cases} \tag{5.46}$$

where subscript s stands for 'solid', $\alpha_s < \sqrt{3}/2$ is the solid's friction coefficient, c_s is the solid's cohesion, $J_2 = \frac{1}{2}\operatorname{tr}(\mathbf{s}\cdot\mathbf{s})$ and $\sigma_m = \dfrac{1}{3}I_1 = \frac{1}{3}\operatorname{tr}(\boldsymbol{\sigma})$ are stress invariants of the micro-stress tensor $\boldsymbol{\sigma} = \mathbf{s} + \sigma_m\,\mathbf{1}$, while $d_d = \sqrt{\boldsymbol{\delta} : \boldsymbol{\delta}} = \sqrt{2J_2'}$ and $d_v = \operatorname{tr}(\mathbf{d})$ are the strain rate invariants of the micro-strain rate tensor $\mathbf{d} = \boldsymbol{\delta} + \frac{1}{3}d_v\mathbf{1}$.

5.3.2 Dimensional Analysis

In this section, the dimensional analysis originally presented for indentation in a homogeneous solid (Sec. 3.4) is revisited for indentation on a porous composite material. To simplify the presentation, isotropic elastic behavior is considered for the purposes of dimensional analysis, but the same results would hold for an elastic anisotropic behavior, with minor modifications. A schematic of the considered situation is displayed in Figure 5-1. It is assumed that the indentation test feels the homogeneous behavior of the porous composite; this homogeneous

behavior is a result of the packing density of the porous composite and the mechanical behavior of the solid.

For this dimensional analysis, again consider the two dependent variables in the contact problem [38] that define the hardness, namely the indentation load, P, and the projected contact area, A_c, analogous to Eq. (3.52):

$$P = f(h, \theta, M_0, \nu, c_s, \alpha_s, \eta) \tag{5.47a}$$

$$A_c = f(h, \theta, M_0, \nu, c_s, \alpha_s, \eta) \tag{5.47b}$$

which, as before, depend on the indentation depth, h, and the indenter cone angle, θ. The variables now also depend on the packing density, η and on elasto-plastic properties of the solid, i.e. stiffness, represented by M_0 and ν (again assuming elastic isotropy for the dimensional analysis) and strength properties associated with the Drucker-Prager strength criterion, cohesion, c_s, and friction coefficient, a_s.

Application of the Buckingham-Π theorem yields invariants similar to Eq. (3.53):

$$\frac{P}{c_s h^2} = \Pi_P\left(\frac{M_0}{c_s}, \nu, \alpha_s, \eta\right) \tag{5.48a}$$

$$\frac{A_c}{h^2} = \Pi_{A_c}\left(\frac{M_0}{c_s}, \nu, \alpha_s, \eta\right) \tag{5.48b}$$

where the dependence on θ has been dropped because this study considers only Berkovich indentation. Applying Eqs. (5.48a) and (5.48b) to the definition of hardness, Eq. (3.51), readily yields a new invariant, the hardness–to–solid cohesion ratio:

$$\frac{H}{c_s} = \frac{\Pi_P}{\Pi_{A_c}} = \Pi_H\left(\frac{M_0}{c_s}, \nu, \alpha_s, \eta\right) \tag{5.49}$$

Very recently, Cariou et al. [33], [34] used yield design assumptions and an elliptical strength criterion for a porous composite derived from Barthelemy and Dormieux's effective strain rate approach [12]. With yield design assumptions, the dimensionless scaling reads:

$$\frac{M_0}{c_s} \to \infty; \; \frac{H}{c_s} = \Pi_H(\alpha_s, \eta) \tag{5.50}$$

Cariou's relation is promising and points the way for a micromechanics based approach to interpreting strength behavior from nanoindentation testing on a porous composite. The limitation to an elliptical strength criterion, however, limits the range of applicability of Cariou et al.'s relations to certain packing densities and solid friction coefficients. Gathier has recently considered a new strength homogenization approach that leads to scaling relationships of similar form to Eq. (5.50), but with significantly fewer restrictions on packing density and friction coefficient than Cariou et al.'s relations [77]. This section proceeds by introducing and employing micromechanics homogenization techniques to develop the invariant scaling relation for hardness.

5.3.3 Strength Homogenization Approach

Gathier has recently considered the prediction of strength domains of porous composites with cohesive-frictional solid phases, based on the Linear Comparison Composite (LCC) strength homogenization approach proposed by Ponte Castañeda [148], [150]. This approach, used for homogenization between Level '0' and Level '1' in the multiscale model for shale (Sec. 2.2), is able to generate both elliptical and hyperbolic strength criteria for the porous composite. The principles of the approach are reviewed here.

Yield Design

Yield design theory provides a useful framework for strength homogenization. In this context, yield design aims to find the macroscopic load, $\boldsymbol{\Sigma}$, corresponding to the plastic collapse of the composite material. The strength domain of phase i is denoted by G_i. The behavior of each phase at plastic collapse is assumed to follow the principle of maximum dissipation, linking the stress, $\boldsymbol{\sigma}$, on the boundary of G_i to the strain rate, $\mathbf{d}$, by:

$$\boldsymbol{\sigma} = \frac{\partial \pi_i}{\partial \mathbf{d}} (\mathbf{d}) \tag{5.51}$$

where $\pi_i (\mathbf{d})$ is the maximum dissipation capacity of phase i:

$$\pi_i (\mathbf{d}) = \sup_{\boldsymbol{\sigma}^* \in G_i} \boldsymbol{\sigma}^* : \mathbf{d} \tag{5.52}$$

The continuum mechanics problem consists of subjecting a *rev* to a homogeneous strain rate boundary condition and enforcing the static admissibility of the stress field solution to the problem formulated in strain rates. The relevant equations are summarized:

$$\underline{\mathrm{div}}(\boldsymbol{\sigma}) = 0 \qquad \text{in } V \tag{5.53a}$$

$$\boldsymbol{\sigma} = \frac{\partial \pi_i}{\partial \mathbf{d}}(\mathbf{d}) \qquad \text{in } V_i \tag{5.53b}$$

$$\mathbf{d} = \frac{1}{2}\left(\mathbf{grad}\,\underline{v} + {}^t\mathbf{grad}\,\underline{v}\right) \qquad \text{in } V \tag{5.53c}$$

$$\underline{v} = \mathbf{D}\cdot\underline{x} \qquad \text{on } \partial V \tag{5.53d}$$

where $\mathbf{D}$ is the macroscopic strain rate. Then, from convex analysis [49], [127], [153], the maximum dissipation capacity of the system:

$$\begin{aligned} \Pi^{\mathrm{hom}}(\mathbf{D}) &= \sup_{\boldsymbol{\Sigma}\in G^{\mathrm{hom}}} \boldsymbol{\Sigma} : \mathbf{D} \\ \text{with} \qquad \boldsymbol{\Sigma} &= \langle \boldsymbol{\sigma} \rangle_V = \overline{\boldsymbol{\sigma}} \end{aligned} \tag{5.54}$$

is the solution to the variational problem:

$$\Pi^{\mathrm{hom}}(\mathbf{D}) = \inf_{\underline{v}^* \in \mathcal{K}(\mathbf{D})} \langle \pi(\mathbf{d}(\underline{v}^*), \underline{x}) \rangle \tag{5.55}$$

where $\mathcal{K}(\mathbf{D})$ is the set of kinematically admissible strain rates:

$$\mathcal{K}(\mathbf{D}) = \{\underline{v}^*(\underline{x}) \,|\, \underline{v}^*(\underline{x}) = \mathbf{D}\cdot\underline{x} \quad \text{on } \partial V\} \tag{5.56}$$

Analogously to the microscopic quantities, we obtain the following relation between the macroscopic stress at plastic collapse, $\boldsymbol{\Sigma}$, and the macroscopic strain rate, $\mathbf{D}$:

$$\boldsymbol{\Sigma} = \frac{\partial \Pi^{\mathrm{hom}}}{\partial \mathbf{D}} \tag{5.57}$$

Linear Comparison Composite Approach

The principle of the LCC approach is to approximate the non-linear behavior by a linear one with suitably chosen stiffness parameters. The first iteration of the LCC approach, proposed by Ponte

Castañeda in 1992 [148], considered the introduction of an elastic composite with continuously varying stiffness properties. In other words, the stiffness tensor $\mathbb{C}(\underline{x})$ constantly varies with $\underline{x}$, or alternatively, the elastic composite has an infinite number of phases. Implementation of this approach in practice, however, proved difficult, leading to further research in which the LCC is approximated by an $N-$phase composite with a piecewise constant definition of $\mathbb{C}(\underline{x})$ [149], [150].

A strict application of the LCC variational approach gives an upper bound for Π^{hom}:

$$\Pi^{\text{hom}}(\mathbf{D}) \leq \mathcal{W}_0(\mathbf{D}) + \sum_i \phi_i \mathcal{V}_i \tag{5.58}$$

where $\mathcal{W}_0(\mathbf{D})$ is the macroscopic strain rate energy of the LCC, and $\mathcal{V}_i$ is a measure of the non-linearity in each phase of volume fraction ϕ_i:

$$\mathcal{V}_i = \sup_{\mathbf{d}} \langle \pi_i(\mathbf{d}) - \omega_i(\mathbf{d}) \rangle \tag{5.59}$$

where $\mathbf{d}$ is the microscopic strain rate in each material phase i with maximum plastic dissipation function $\pi_i(\mathbf{d})$ and strain rate energy function $\omega_i(\mathbf{d})$. The goal, therefore, is to find the stiffness parameters of the comparison composite that lead to the lowest possible upper bound, thus yielding the best possible estimate of Π^{hom}.

Preserving a true upper bound status, however, may sometimes prove difficult, and the infima or maxima can be replaced by just stationary points [150]. The resulting estimates are then stationary variational estimates and not bounds in general. This new estimate, $\widetilde{\Pi}^{\text{hom}}$, reads:

$$\widetilde{\Pi}^{\text{hom}}(\mathbf{D}) = \underset{\mathbb{C}_i, \boldsymbol{\tau}_i}{\text{stat}} \left[\mathcal{W}_0(\mathbf{D}) + \sum_i \phi_i \mathcal{V}_i \right] \tag{5.60}$$

where each phase in the composite has stiffness tensor $\mathbb{C}_i$, and internal prestress $\boldsymbol{\tau}_i$, and with the functions measuring non-linearity calculated as:

$$\mathcal{V}_i = \underset{\mathbf{d}}{\text{stat}} \{ \pi_i(\mathbf{d}) - \omega_i(\mathbf{d}) \} \tag{5.61}$$

There are usually different points of stationarity, which is why each particular case must be

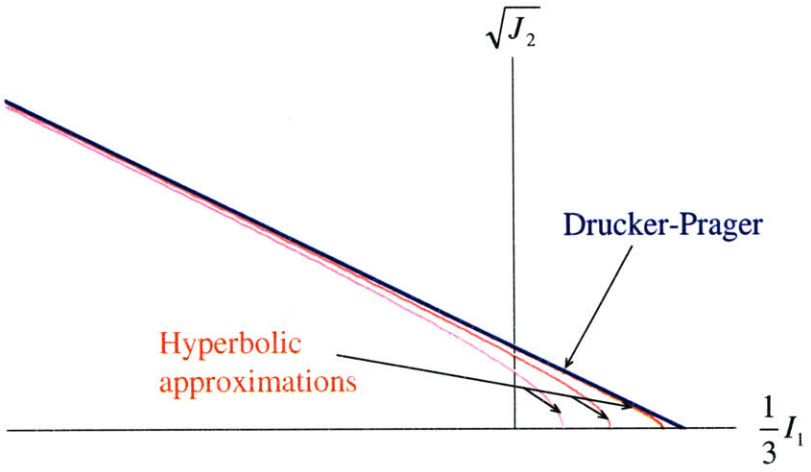

Figure 5-7: Approximation of a Drucker-Prager strength domain by a family of hyperbolic strength domains.

analyzed separately [150].

Drucker-Prager Regularization

A necessary condition for the application of the variational approach to strength homogenization is that the strength domain is *strictly* convex. This is not the case for the Drucker-Prager strength criterion (Eq. (5.38)), and the function has a point of singularity at ($J_2 = 0; I_1 = 3\frac{c_s}{\alpha_s}$). Gathier circumvented this issue by introducing a family of regular strength criteria that asymptotically tend to the Drucker-Prager criterion [77]. This is achieved by considering a family of hyperbolas, as shown in Figure 5-7, of the form:

$$f(\boldsymbol{\sigma}) = 1 - \left(\frac{\sigma_m - S_0}{A}\right)^2 + \left(\frac{\sigma_d}{\sqrt{2}B}\right)^2 \leq 0 \tag{5.62}$$

where $\sigma_d = \sqrt{2J_2}$. The Drucker-Prager criterion is obtained by letting:

$$\begin{cases} B = \alpha_s A \\ S_0 = \dfrac{c_s}{\alpha_s} \\ A \to 0 \end{cases} \tag{5.63}$$

The following set of equations defining the mechanical situation at plastic failure can be solved to obtain the function $\pi(\mathbf{d})$:

$$\mathbf{d} = \overset{\circ}{\lambda} \frac{\partial f}{\partial \boldsymbol{\sigma}}(\boldsymbol{\sigma}) \tag{5.64a}$$

$$f(\boldsymbol{\sigma}) = 0 \tag{5.64b}$$

$$\boldsymbol{\sigma} : \mathbf{d} = \pi(\mathbf{d}) \tag{5.64c}$$

where $\overset{\circ}{\lambda}$ is the plastic multiplier. The $6+1+1=8$ equations allow solving for the 8 unknowns: $\pi(\mathbf{d})$, $\overset{\circ}{\lambda}$ and $6 \times \sigma_{ij}$ at the boundary of the strength domain. It follows:

$$\pi_s(\mathbf{d}) = \pi(d_v, d_d) = S_0 d_v - \sqrt{(A d_v)^2 - \left(\sqrt{2} B d_d\right)^2} \tag{5.65}$$

with $d_v = \operatorname{tr} \mathbf{d} = I_1'$ and $d_d = \sqrt{\boldsymbol{\delta} : \boldsymbol{\delta}} = \sqrt{2 J_2'}$. Eq. (5.65) reduces to $\pi(\mathbf{d}) = (c_s/\alpha_s)\ d_v$ for the Drucker-Prager conditions (Eq. 5.63); this is identically the $\pi-$ function expression given in Eq. (5.46).

5.3.4 Solid-Pore Composite Strength Homogenization

The case of a composite with one solid phase (volume fraction η) and one pore phase, such as in the porous clay composite, offers simplification of the LCC approach. The two-phase description of the microscopic stiffness $\mathbb{C}(\underline{x})$ and prestress $\boldsymbol{\tau}(\underline{x})$, with spatial distribution within the *rev* is given by:

$$\mathbb{C}(\underline{x}) = \begin{cases} \mathbb{C}_s = 3\kappa \mathbb{J} + 2\mu \mathbb{K} & (V_s) \\ 0 & (V_p) \end{cases} \; ; \; \boldsymbol{\tau}(\underline{x}) = \begin{cases} \tau \mathbf{1} & (V_s) \\ 0 & (V_p) \end{cases} \tag{5.66}$$

where V_s stands for the domain occupied by the solid phase and V_p stands for the domain occupied by the voids. Gathier has shown that the strength homogenization problem can be solved through a series of steps to define a stationary estimate of the homogenized dissipation function, $\widetilde{\Pi}^{\text{hom}}(\mathbf{D})$, thus leading to a homogenized strength domain.

Step 1: Determine the Strain Rate Energy Function, $\mathcal{W}_0(\mathbf{D})$

The first step in solving the strength homogenization problem is to determine the strain rate energy function $\mathcal{W}_0(\mathbf{D})$ of the LCC. Using classical results of linear micromechanics, the corresponding macroscopic stress equation of state reads:

$$\boldsymbol{\Sigma} = \mathbb{C}^{\text{hom},I} : \mathbf{D} + \mathbf{T}^I \tag{5.67}$$

where $\mathbb{C}^{\text{hom},I}$ and $\mathbf{T}^I$ are respectively the macroscopic stiffness tensor and the macroscopic prestress given by:

$$\mathbb{C}^{\text{hom},I} = \langle \mathbb{C}(\underline{x}) : \mathbb{A}(\underline{x}) \rangle = \mathbb{C}_s : \eta \langle \mathbb{A}^s \rangle = 3\kappa^I \mathbb{J} + 2\mu^I \mathbb{K} \tag{5.68a}$$

$$\mathbf{T}^I = \langle \boldsymbol{\tau}(\underline{x}) : \mathbb{A}(\underline{x}) \rangle = \tau \mathbf{1} : \eta \langle \mathbb{A}^s \rangle = \tau \mathbf{1} : \mathbb{C}_s^{-1} : \mathbb{C}^{\text{hom},I} = \tau \frac{\kappa^I}{\kappa} \mathbf{1} \tag{5.68b}$$

with:

$$\kappa^I = \eta\, \kappa\, \mathbb{J} : \langle \mathbb{A}^s \rangle = \mu\, \mathcal{K}_I \left(\frac{\kappa}{\mu}, \eta \right) \tag{5.69a}$$

$$\mu^I = \eta\, \mu\, \mathbb{K} : \langle \mathbb{A}^s \rangle = \mu\, \mathcal{M}_I \left(\frac{\kappa}{\mu}, \eta \right) \tag{5.69b}$$

where $\mathbb{A}(\underline{x})$ is the fourth-order strain (rate) localization tensor and $\langle \mathbb{A}^s \rangle$ the volume average of $\mathbb{A}(\underline{x})$ over the solid phase. The second part of the equalities are readily obtained from dimensional analysis, where κ/μ is the bulk–to–shear modulus ratio of the solid phase, while the dimensionless functions $\mathcal{K}_I$ and $\mathcal{M}_I$ are Level 'I' pore morphology factors that depend on the bulk–to–shear modulus ratio, the pore morphology, and the solid concentration η.

The strain rate energy function $\mathcal{W}_0(\mathbf{D})$ is obtained by an application of linear homogenization theory. The resulting strain rate energy function for the solid–void composite is:

$$\begin{aligned} \mathcal{W}_0(D_v, D_d) &= \frac{1}{2}\kappa^I D_v^2 + \mu^I D_d^2 + \frac{\kappa^I}{\kappa}\tau D_v + \frac{1}{2\kappa}\left(\frac{\kappa^I}{\kappa} - \eta\right)\tau^2 \\ &= \frac{1}{2}\mu\, \mathcal{K}_I D_v^2 + \mu\, \mathcal{M}_I D_d^2 + \frac{\mu}{\kappa}\mathcal{K}_I \tau D_v + \frac{1}{2\kappa}\left(\frac{\mu}{\kappa}\mathcal{K}_I - \eta\right)\tau^2 \end{aligned} \tag{5.70}$$

where $D_v = \text{tr}(\mathbf{D})$ and $D_d = \sqrt{\boldsymbol{\Delta} : \boldsymbol{\Delta}}$ with $\boldsymbol{\Delta} = \mathbf{D} - \frac{1}{3} D_v \mathbf{1}$.

Step 2: Determine the $\mathcal{V}$ Function for the Solid

The second step consists of determining the $\mathcal{V}$ function (Eq. (5.61)) for the solid phase ($\mathcal{V}$ for the pore space is zero). This requires the expression of the π-function (Eq. (5.65)) along with an expression for the strain rate energy of the solid:

$$\omega_s(\mathbf{d}) = \frac{1}{2}\kappa d_v^2 + \mu d_d^2 + \tau d_v \tag{5.71}$$

Then, applying the stationary condition of the $\mathcal{V}$ function implies that:

$$\kappa d_v + \tau = S_0 - \frac{A^2 d_v}{\sqrt{(Ad_v)^2 - \left(\sqrt{2}Bd_d\right)^2}} \tag{5.72a}$$

$$2\mu d_d = \frac{2B^2 d_d}{\sqrt{(Ad_v)^2 - \left(\sqrt{2}Bd_d\right)^2}} \tag{5.72b}$$

The microscopic LCC stiffness components κ and μ must be positive. Introduction of the prestress provides a means to ensure that κ and μ are positive, by requiring that:

$$\tau = S_0 - \frac{2A^2 d_v}{\sqrt{(Ad_v)^2 - \left(\sqrt{2}Bd_d\right)^2}} \tag{5.73a}$$

$$\kappa = \frac{A^2}{\sqrt{(Ad_v)^2 - \left(\sqrt{2}Bd_d\right)^2}} > 0 \tag{5.73b}$$

$$\mu = \frac{B^2}{\sqrt{(Ad_v)^2 - \left(\sqrt{2}Bd_d\right)^2}} > 0 \tag{5.73c}$$

Then we have just two independent parameters for the behavior of the comparison composite, τ and μ, since:

$$\frac{\kappa}{\mu} = \frac{A^2}{B^2} \tag{5.74}$$

is a constant, which reads for the Drucker-Prager case (Eq. (5.63)):

$$\frac{\kappa}{\mu} = \frac{A^2}{B^2} = \frac{1}{\alpha_s^2} \tag{5.75}$$

These expressions yield the sought expression of $\mathcal{V}$ for the hyperbolic criterion as a function

of the independent parameters τ and μ:

$$\mathcal{V}_s = \left(\frac{B\left(S_0 - \tau\right)}{2A}\right)^2 \frac{1}{\mu} - \frac{1}{2}\frac{B^2}{\mu} \tag{5.76}$$

In the Drucker-Prager case (Eq. (5.63)), $\mathcal{V}_s$ becomes:

$$\mathcal{V}_s = \left(c_s - \alpha\tau\right)^2 \frac{1}{4\mu} \tag{5.77}$$

Step 3: Use Stationarity of $\widetilde{\Pi}^{\text{hom}}$

The third step consists in exploring the stationarity of $\widetilde{\Pi}^{\text{hom}}$, that is Eq. (5.60). Note, however, that Eq. (5.74) reduces the degrees of freedom from three (κ, μ, τ) to two (μ, τ), such that:

$$\widetilde{\Pi}^{\text{hom}} = \underset{\mu,\boldsymbol{\tau}}{\text{stat}} \left[\mathcal{W}_0\left(D_v, D_d\right) + \eta\mathcal{V}_s\right] \tag{5.78}$$

The condition is explicitly expressed as:

$$\frac{\partial\widetilde{\Pi}^{\text{hom}}}{\partial\mu} = \frac{\partial\kappa}{\partial\mu}\frac{\partial\mathcal{W}_0}{\partial\kappa} + \frac{\partial\mathcal{W}_0}{\partial\mu} + \eta\frac{\partial\mathcal{V}_s}{\partial\mu} = 0 \tag{5.79a}$$

$$\frac{\partial\widetilde{\Pi}^{\text{hom}}}{\partial\tau} = \frac{\partial\mathcal{W}_0}{\partial\tau} + \eta\frac{\partial\mathcal{V}_s}{\partial\tau} = 0 \tag{5.79b}$$

Using Eq. (5.70) and Eq. (5.76) in Eq. (5.79b) while making use of Eq. (5.74) yields:

$$\tau = \frac{A^2\left(2\mathcal{K}_I\mu D_v - \eta S_0\right)}{\eta A^2 - 2\mathcal{K}_I B^2} \tag{5.80}$$

Then, substituting Eq. (5.80) into Eq. (5.79a) gives:

$$\mu^2 = \frac{B^2}{A^2}\frac{\eta\left(\eta A^2\left(S_0^2 - A^2\right) + \mathcal{K}_I B^2\left(2A^2 - S_0^2\right)\right)}{\left(\eta\mathcal{K}_I A^2 D_v^2 + \left(2\eta\mathcal{M}_I A^2 - 4\mathcal{K}_I\mathcal{M}_I B^2\right) D_d^2\right)} \tag{5.81}$$

Finally, using the values of (μ, τ) corresponding to the stationarity of $\widetilde{\Pi}^{\text{hom}}$ in Eq. (5.78) provides the following estimate for $\widetilde{\Pi}^{\text{hom}}$:

$$\widetilde{\Pi}^{\text{hom}} = \Sigma_0^{\text{hom}} D_v - \text{sign}\left(2\mathcal{K}_I B^2 - \eta A^2\right)\sqrt{\left(A^{\text{hom}}\right)^2 D_v^2 + 2\left(B^{\text{hom}}\right)^2 D_d^2} \tag{5.82}$$

where:

$$\left(A^{\text{hom}}\right)^2 = \frac{\eta^2 B^2 \mathcal{K}_I \left(\eta A^2 \left(S_0^2 - A^2\right) + B^2 \left(2A^2 - S_0^2\right) \mathcal{K}_I\right)}{\left(\eta A^2 - 2\mathcal{K}_I B^2\right)^2} \tag{5.83a}$$

$$\left(B^{\text{hom}}\right)^2 = \frac{\eta B^2 \mathcal{M}_I \left(\eta A^2 \left(S_0^2 - A^2\right) + B^2 \left(2A^2 - S_0^2\right) \mathcal{K}_I\right)}{A^2 \left(\eta A^2 - 2B^2 \mathcal{K}_I\right)} \tag{5.83b}$$

$$\Sigma_0^{\text{hom}} = \frac{\eta B^2 \mathcal{K}_I}{2\mathcal{K}_I B^2 - \eta A^2} S_0 \tag{5.83c}$$

A comparison of Eq. (5.82) with Eq. (5.65) readily reveals that Eq. (5.82) is the Π function of a hyperbolic criterion, provided that $2\mathcal{K}_I B^2 - \eta A^2 > 0$. In return, for $2\mathcal{K}_I B^2 - \eta A^2 < 0$, the function $\widetilde{\Pi}^{\text{hom}}$ corresponds to an elliptical strength criterion:

$$\frac{\left(\Sigma_m - \Sigma_0^{\text{hom}}\right)^2}{\left(A^{\text{hom}}\right)^2} + \frac{\left(\Sigma_d/\sqrt{2}\right)^2}{\left(B^{\text{hom}}\right)^2} = 1 \tag{5.84}$$

where $\Sigma_m = \text{tr}\left(\boldsymbol{\Sigma}\right)$ is the mean stress and $\Sigma_d = \sqrt{\mathbf{s} : \mathbf{s}}$ with $\mathbf{s} = \boldsymbol{\Sigma} - \frac{1}{3}\Sigma_m \mathbf{1}$ is the mean deviatoric stress.

In the Drucker-Prager case (Eq. (5.63)), the strength homogenization factors (Eq. (5.83)) simplify:

$$\left(\frac{A^{\text{hom},I}}{c_s}\right)^2 = \frac{\eta^2 \mathcal{K}_I \left(\eta - \alpha_s^2 \mathcal{K}_I\right)}{\left(\eta - 2\alpha_s^2 \mathcal{K}_I\right)^2} \tag{5.85a}$$

$$\left(\frac{B^{\text{hom},I}}{c_s}\right)^2 = \frac{\eta \mathcal{M}_I \left(\eta - \alpha_s^2 \mathcal{K}_I\right)}{\eta - 2\alpha_s^2 \mathcal{K}_I} \tag{5.85b}$$

$$\frac{\Sigma_0^{\text{hom},I}}{c_s} = \frac{\eta \alpha_s \mathcal{K}_I}{2\mathcal{K}_I \alpha_s^2 - \eta} \tag{5.85c}$$

and the class of criterion is now determined by the sign of $X = 2\alpha_s^2 \mathcal{K}_I - \eta$: $X > 0$ for an hyperbole, $X < 0$ for an ellipse.

Step 4: Specify Morphology Factors

The final required theoretical development is a specification of the morphology factors, $\mathcal{K}_I$ and $\mathcal{M}_I$, of the solid–void composite. Based on the definition of these factors (Eq. (5.69)), we refer to linear micromechanics and again consider the self-consistent scheme, with a spherical particle

shape for solids and pores. The same assumptions and logic as for elasticity homogenization apply, although in the case of hardness and strength, isotropy is assumed. With these assumptions, the linear self-consistent scheme provides the following expressions for $\mathcal{K}_I$ and $\mathcal{M}_I$ [46]:

$$\mathcal{K}_{sc} = \mathcal{K}_I\left(\frac{\kappa}{\mu} = \frac{1}{\alpha_s^2}, \eta\right) = \frac{4\eta\,\mathcal{M}_{sc}}{4\alpha_s^2\,\mathcal{M}_{sc} + 3\,(1-\eta)} \tag{5.86}$$

$$\begin{aligned}\mathcal{M}_{sc} &= \mathcal{M}\left(\frac{\kappa}{\mu} = \frac{1}{\alpha_s^2}, \eta\right) = \frac{1}{2} - \frac{5}{4}\,(1-\eta) - \frac{3}{16\alpha_s^2}\,(2+\eta) \\ &+ \frac{1}{16\alpha_s^2}\sqrt{144\,(\alpha_s^4 - \alpha_s^2) - 480\alpha_s^4\eta + 400\alpha_s^4\eta^2 + 408\alpha_s^2\eta - 120\alpha_s^2\eta^2 + 9\,(2+\eta)^2}\end{aligned} \tag{5.87}$$

Note that $\mathcal{K}_{sc} = \mathcal{M}_{sc} = 0$ at the percolation threshold $\eta_0 = 1/2$.

5.3.5 Parametric Development with the Limit Analysis Solver

The goal of strength homogenization is to develop a scaling relationship in the form of Eq. (5.50):

$$\frac{H}{c_s} = \Pi_H\,(\alpha_s, \eta) \tag{5.88}$$

A two-dimensional mapping of the possible hardness/cohesion ratios for Berkovich indentation on shale is then possible by varying α_s from 0 to $\sqrt{3/4}$ (according to the limits defined by Eq. (5.39)) and by varying η from 0.5, the percolation threshold for perfect disordered (spherical representation) morphology, to 1, the highest possible packing.

To make this mapping of hardness/cohesion ratios, Gathier employed a computational approach, the Limit Analysis Solver [19]. To use the solver, a model material domain was discritized by an axisymmetric finite element mesh and loaded by a conical indenter with equivalent cone angle to a Berkovich tip (i.e. $\theta^{eq} = 70.32°$, see Sec. 3.2.1). Limit Analysis employs both stresses and velocities as degrees of freedom, and requires that the stress fields satisfy equilibrium and the chosen strength criterion, and that the velocity fields are kinematically admissible and obey an associated flow rule. The principle of limit analysis is to directly find a numerical estimate of the stress and velocity fields which obey these conditions of plasticity.

In order to map the values of the hardness/cohesion ratio for any parameter of the system,

vary the parameters $\alpha_s \in [0, \sqrt{3/4}[$ and $\eta \in [0.5, 1]$. This mapping covers the entire range of both the elliptical strength domain, $\eta \in [0.5, \eta^{cr}[$, and the hyperbolic strength domain, $\eta \in]\eta^{cr}, 1]$, according to:

$$\eta - \eta^{cr}(\alpha_s) \begin{cases} > 0 & \text{Hyperbolic Criterion} \\ = 0 & \text{Limit Parabola} \\ < 0 & \text{Elliptical Criterion} \end{cases} \tag{5.89}$$

where $\eta^{cr}(\alpha_s)$ is the critical packing density for self-consistent morphology, given by:

$$\eta_{sc}^{cr} = 1 - \frac{1}{2} \frac{\sqrt{81 + 432\alpha_s^2 + 1216\alpha_s^4} - (9 + 16\alpha_s^2)}{3 + 20\alpha_s^2}$$

The Limit Analysis Solver would not converge, however, for high values of $\alpha_s > 1/\sqrt{3} = 0.577\,35$. The reason for this computational limitation is unknown. Hence, all results below are strictly valid for $\alpha_s \in [0, \sqrt{1/3}[$.

Figure 5-8 presents a sampling of results in terms of relationships between packing density and hardness to cohesion ratios for various friction coefficients, α_s. Similar results were first obtained by Cariou et al. [34] by employing an upper bound yield design approach for an elliptical strength criterion based on the work of Barthelemy and Dormieux [12]. Comparison of Gathier's results with Cariou's results, also presented in Figure 5-8, shows excellent agreement (where there are any discrepancies, Cariou's solutions prove to be an upper bound, as expected), despite the fact that the two approaches employ differently derived homogenized strength criteria and different methods of solving for the stress and displacement fields. The comparison also highlights the limitation of the elliptical strength criterion; for cases where $\eta > \eta^{cr}(\alpha_s)$, the transition to a hyperbolic criterion permits solutions which were previously unknown.

5.3.6 Indentation Hardness-Packing Density Scaling

It is possible to derive fitting functions that summarize the discrete simulation results in a closed form expression as in Eq. (5.2). Based on the dimensional analysis, the format of the

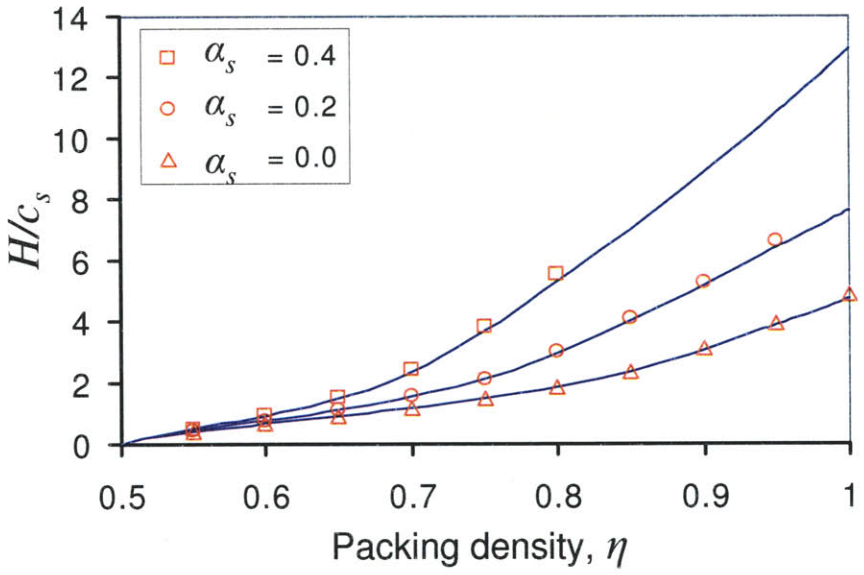

Figure 5-8: Relationships between hardness to cohesion ratios and packing density for solid friction angles of 0, 0.2, and 0.4. Solid lines are the scaling results developed through use of the limit analysis solver by Gathier [77]. Points are data from [34], which employed an upper bound in conjunction with the effective strain rate approach.

scaling relations is chosen in the following form:

$$H = h_s\left(c_s, \alpha_s\right) \times \Pi_H^I\left(\alpha_s, \eta\right) \tag{5.90}$$

where $\Pi_H^I\left(\alpha_s, \eta\right)$ is a dimensionless function to be developed, and $h_s = h_s\left(c_s, \alpha_s\right) = \lim_{\eta \to 1} H$ is the asymptotic hardness of a cohesive–frictional solid phase that obeys the Drucker-Prager criterion. This asymptotic value does not depend on the employed linear homogenization scheme, but relates only to the solid's cohesion, c_s, and friction coefficient, α_s, by the fitted function:

$$h_s = c_s \times A\left(1 + B\alpha_s + \left(C\alpha_s\right)^3 + \left(D\alpha_s\right)^{10}\right) \tag{5.91}$$

with:

$$\begin{cases} A = 4.76438 \\ B = 2.5934 \\ C = 2.1860 \\ D = 1.6777 \end{cases}$$

The dimensionless function $\Pi_H^I \in [0, 1]$ depends on the packing density η and the solid's friction coefficient α_s in the form

$$\Pi_H^I\left(\alpha_s, \eta\right) = \Pi_1\left(\eta\right) + \alpha_s\left(1 - \eta\right)\ \Pi_2\left(\alpha_s, \eta\right) \tag{5.92}$$

where the first part of the function is independent of the friction coefficient. The following fitted expressions for $\Pi_1\left(\eta\right)$ and $\Pi_2\left(\alpha, \eta\right)$ were obtained:

$$\begin{aligned} \Pi_1\left(\eta\right) &= \frac{\sqrt{2\left(2\eta - 1\right)} - \left(2\eta - 1\right)}{\sqrt{2} - 1}\left(1 + a\left(1 - \eta\right) + b\left(1 - \eta\right)^2 + c\left(1 - \eta\right)^3\right) \\ \Pi_2\left(\alpha_s, \eta\right) &= \frac{2\eta - 1}{2}\left(d + e\left(1 - \eta\right) + f\left(1 - \eta\right)\alpha_s + g\alpha_s^3\right) \end{aligned} \tag{5.93}$$

with

$$\begin{cases} a = -5.3678 & d = 6.7374 \\ b = 12.1933 & e = -39.5893 \\ c = -10.3071 & f = 34.3216 \\ & g = -21.2053 \end{cases}$$

The scaling problems, as formulated in Section 5.1, are now resolved. Scaling relationships between packing density, cohesive-frictional strength parameters, and indentation hardness, as well as anisotropic scaling relationships for indentation moduli, are now in place and well approximated by smooth, closed-form fitting functions.

5.4 Inverse Analysis - Packing Density Distributions and Solid Properties

This section combines the scaling relationships reviewed in the previous two sections and implements them in an inverse approach. The idea of this technique, labeled the $M - H - \eta$ scaling approach, is to use a back analysis of indentation measurements on a porous composite to estimate the local packing density associated with each indent, and the average properties of the solid phase for a given sample.

5.4.1 Proof of Concept

The inverse approach with $M - H - \eta$ scaling is first understood by checking the feasibility of implementation. Consider a typical array of indentations consisting of N individual tests, with N^{porous} tests associated with the response of a porous composite (these tests may be isolated, for example, based on the deconvolution analysis). The properties of the solid phase ($m_{1,s}$, $m_{3,s}$, c_s, and α_s) are assumed to be constant for a given solid material, but the locally observed packing density, η_i, where $i = 1...N^{porous}$, may vary from indented location to indented location. The indentation modulus M_i and indentation hardness H_i are the extracted values of each indentation test, and are composite properties that represent the homogenized (Level '1') response of the porous materials (pores and Level '0'). The scaling relationships for indentation

modulus and hardness have been derived in the previous sections, i.e. Eqs. (5.33) and (5.90):

$$M_{(\beta),\iota} = m_{(\beta),s} \times \Pi_M(\eta) \tag{5.94}$$

$$H_\iota = c_s \times \Pi_H(\alpha_s, \eta_\iota) \tag{5.95}$$

In an inverse application, the unknowns of the problem are the properties of the solid phase, $m_{1,s}$, $m_{3,s}$, c_s, and α_s, and the N^{porous} local packing densities, $\{\eta_\iota\}$, for a total of $n = N^{porous}+4$ unknowns. The results of each indentation test, $M_{(\beta),\iota}$ and H_ι, are known, for a total of $2N^{porous}$ known quantities. Consequently, for any large number of indentation tests on a porous composite, the system of equations is highly over-determined and an estimation of $m_{1,s}$, $m_{3,s}$, c_s, and α_s, and the N^{porous} local packing densities, $\{\eta_\iota\}$, should be feasible.

5.4.2 Implementation and Statistical Considerations

Although the inverse problem is feasible, the implementation of such a problem is a challenge, first because of the complexity of the problem, and second because of the sensitivity of many of the parameters on the overall procedure. To help overcome these challenges, a simplifying assumption is made; for implementation of the inverse $M-H-\eta$ scaling approach on the porous clay in shale, the solid indentation moduli, $m_{1,s}$ and $m_{3,s}$ are assumed to be known. Ample evidence for this assumption should be provided by the statistical analysis of the indentation data, as well as the results from back-calculation of macroscopic measurements and a first approach to nanoindentation on shale [145], [174]. With this assumption in mind, the rest of the procedure can be reviewed, as developed in collaboration with Gathier [77].

Minimization Implementation of the Inverse Analysis

The first step is to consider the error definition used in the minimization routine. For a given set of parameters $\{\eta_\iota, m_{1,s}, m_{3,s}, c_s, \alpha_s\}$, the error created by a point of the data set is due to the difference between the value of the predicted indentation modulus $M_\iota(\eta_\iota, m_{(\beta),s})$ and hardness $H_\iota(\eta_i, c_s, \alpha_s)$ and the experimental values $M_{\iota,\text{exp}}$ and $H_{\iota,\text{exp}}$. The values of M and H are not generally of the same order of magnitude, so choosing an absolute error would lead to a fitting that favored one measured property over another. Instead, a "normalized absolute error" was

chosen so that the error on each point is calculated as:

$$S_i = \left(\frac{M_{i,\text{exp}} - M_i\left(\eta_i, m_{(\beta),s}\right)}{M_{(\beta),0}} \right)^2 + \left(\frac{H_{i,\text{exp}} - H_i\left(\eta_i, c_s, \alpha_s\right)}{H_0} \right)^2 \tag{5.96}$$

where $M_{1,0}$, $M_{3,0}$ and H_0 are normalization factors, constant for the entire data set, that are typically chosen close to $m_{1,s}$, $m_{3,s}$ and h_s.

The next step in implementing the inverse approach is to choose the appropriate (M, H) data set that represents the porous composite phase to be analyzed. This amounts to finding the indentation tests that gave results which fall under the first peak in the deconvolution analysis (see Sec. 4.2). To make a first cut, a common threshold was identified for all the shale materials, based on estimates for the solid indentation moduli, $m_{1,s}$, and $m_{3,s}$. The cut value is expressed as a percentage of the solid modulus:

$$\frac{M_{(\beta),i}}{m_{(\beta),s}} \leq X_{cut} \tag{5.97}$$

A refinement to this cut is made based on a first iteration of fitting the packing densities and solid properties. Some points clearly fall far from the trends described in the scaling relations (Eqs. (5.33) and (5.90)), and can be discarded. These points are usually the result of a composite response with an inclusion. The $x\%$ worst points that fall farthest from the scaling relationships, as defined by the normalized absolute error, Eq. (5.96) are discarded from the analysis (typically, $x = 5$), and a total of N^{porous} tests associated with the porous composite remain for consideration in the inverse analysis.

The parameters that lead to the best fit in the inverse analysis are the solution of the minimization problem:

$$\min_{\{\eta\}, c_s, \alpha_s} \sum_i S_i\left(\eta_i, m_{1,s}, m_{3,s}, c_s, \alpha_s\right) \tag{5.98}$$

where $\{\eta\}$ is the vector of packing densities associated with each considered indentation test i, such that $\{\eta_i\} = \{\eta_1 ... \eta_{N^{porous}}\}$. Recall that in the grid indentation technique, each indentation is considered as an individual statistical event. As a result, the packing density associated with

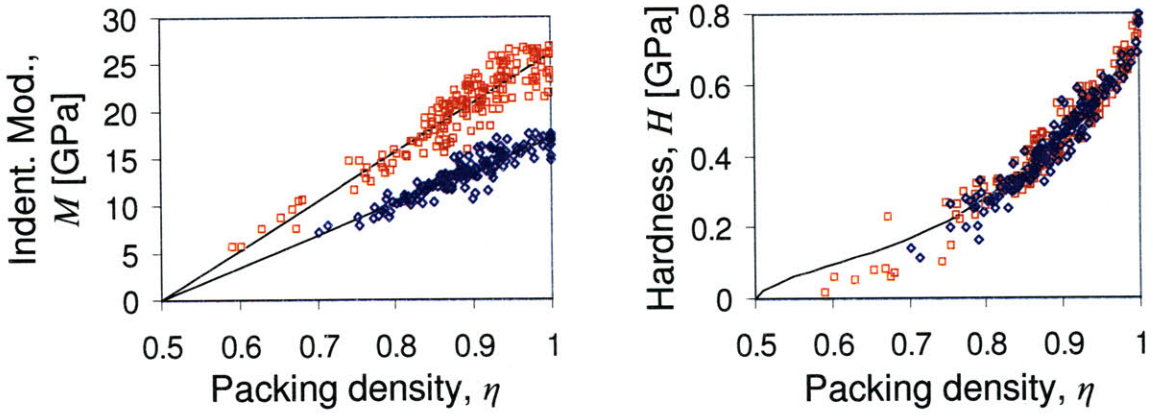

Figure 5-9: Sample scaling results from the $M - H - \eta$ scaling approach (Results from GeoGenome Shale 3).

each test should be independent and the minimization problem can be rewritten as:

$$\min_{c_s,\alpha_s} \sum_i \left[\min_{\eta_i} S_i \left(\eta_i, m_{1,s}, m_{3,s}, c_s, \alpha_s \right) \right] \tag{5.99}$$

In a routine implemented in MATLAB, the optimal packing density for each considered indentation test is found based on a given set of parameters $\{m_{1,s}, m_{3,s}, c_s, \alpha_s\}$ by minimizing the total error $\sum_i \left[\min_{\eta_i} S_i \left(\eta_i, m_{1,s}, m_{3,s}, c_s, \alpha_s \right)\right]$. Then the best set of parameters $\{c_s, \alpha_s\}$ are sought. The minimization functions are not always convex, so a testing procedure is used rather than a gradient algorithm. Figure 5-9 displays a sample result of the fitting procedure.

Statistical Determination of Solid Properties

For implementation on shale materials, the search for optimal parameters $\{c_s, \alpha_s\}$ is still a challenge and may not give reproducible, accurate estimates. Additional developments are required to overcome this problem. Some flexibility in the choice of the solid indentation moduli $m_{1,s}$ and $m_{3,s}$ is introduced by also considering values $\pm 10\%$ the fixed values. In addition, flexibility in the cut value X_{cut} is introduced, and values of 95%, 100%, and 105% are used. As a result, $3 \times 3 \times 3 = 27$ possible combinations for the values of the cut and moduli are used.

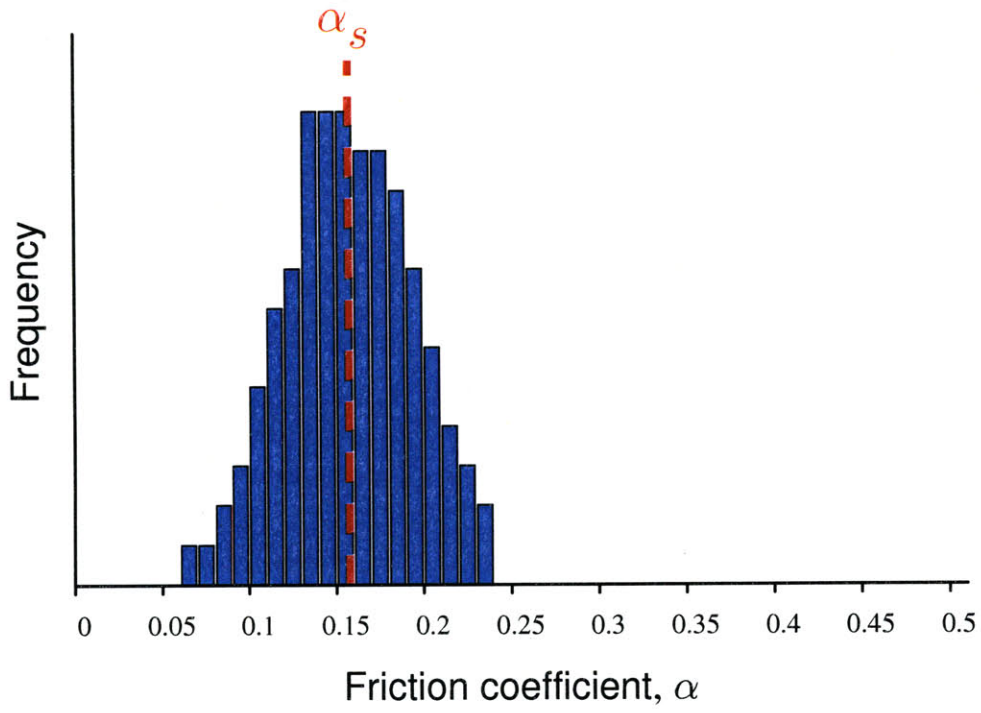

Figure 5-10: Histogram of the selected values of the solid friction coefficient (for Shale 4).

Introducing this flexibility aims at determining if the estimate for α_s, based on the different combinations, converges to a central estimate for the strength parameters. For even more flexibility, individual estimates of α_s which give results almost as good as the optimal ones are also considered. This set of values does tend to converge around a central peak, as seen in an example shown in Figure 5-10. As a result, the technique yields a stable estimate of α_s, based on the mean value of the set of optimal and near optimal values, and an estimate of the sensitivity of α_s, as described by the standard deviation of the optimal and near optimal values.

Finally, c_s and the vector of packing densities, $\{\eta_i\}$, are yet to be determined. These properties turn out to be more sensitive to the choice of $m_{1,s}$, $m_{3,s}$ and X_{cut}, so these parameters are fixed to their central values. With $m_{1,s}$, $m_{3,s}$ and X_{cut}, and now α_s fixed, the minimization is run once more to estimate c_s and the vector of packing densities, $\{\eta_i\}$. The entire procedure is implemented and automated in a MATLAB routine.

5.5 Chapter Summary

In this chapter, the $M-H-\eta$ scaling approach was reviewed and adapted for analyzing the results of indentation on a porous composite whose solid phase is transversely isotropic in elasticity. Linear micromechanics was reviewed as a means to develop the scaling relationships for indentation moduli, varying with packing density. A strength homogenization approach was reviewed in order to develop the scaling relationship for indentation hardness, varying with packing density and the Drucker-Prager strength parameters. Finally, these scaling relationships were implemented in an inverse approach. This approach provides a way to assess the cohesive-frictional strength behavior of the solid phase of a porous composite, as well as a means to identify an array of local packing densities associated with the area where each indentation test took place.

Together with the grid indentation technique and statistical deconvolution analysis, the advanced experimental microporomechanics analysis methods discussed here can provide unprecedented access to mechanical behavior of the porous clay in shale materials. These tools enable the search for material invariant shale properties and the link between microstructure

and mechanical performance that is the primary goal of this thesis.

With the tools now well developed, the next part of this thesis presents the results of a massive nanoindentation campaign on the shale materials presented in Chapter 2. The nanoindentation analysis tools dicussed in Chapter 3 are used to interpret the raw data. Chapter 6 is devoted to results using the deconvolution approach presented in the previous chapter, while Chapter 7 employs the $M - H - \eta$ scaling approach discussed in this chapter.

Part III

RESULTS - MECHANICAL BEHAVIOR OF POROUS CLAY IN SHALE

Chapter 6

Assessing the Mechanical Behavior of Porous Clay by Statistical Analysis of Nanoindentation

This chapter is the first of two devoted to the presentation of nanoindentation results on porous clay in shale. Both chapters aim to use nanoindentation, the primary tool of experimental microporomechanics, to characterize the mechanical behavior of the porous clay in shale. A compilation of results from a wide variety of shale materials will lead to an understanding of mechanical behavior that is common to all shale materials.

The specific focus of this chapter is the presentation of results from statistical analysis of nanoindentation (Chap. 4). These results are obtained by employing the grid indentation technique (Sec. 4.1), with careful attention paid to the scale separability criteria (Eqs. (4.1) and (4.2)), along with statistical deconvolution analysis (Sec. 4.2) to isolate material phase properties. The first section of this chapter provides an in-depth investigation regarding the choice of length scale and the scale separability criteria. Two possible scales relating to the porous clay are identified; a scale where the porous clay behaves (in each sample) as a homogeneous composite, and the scale where locally densely packed areas of clay particles may be tested. This investigation lays out the experimental grid nanoindentation program.

This chapter continues by presenting the results of the statistical deconvolution analysis.

Beginning with the tests designed to assess the behavior of the porous clay composite, an examination of individual indentation responses demonstrates the value of the deconvolution procedure. As predicted from consideration of the multiscale thought model for shale, as well as dimensional analysis, the measured indentation modulus and hardness properties of the porous clay phase are seen to scale with the clay packing density, with some differences between kerogen-free shales and the kerogen-rich Woodford shales. This scaling will give important clues to the morphology and material invariant properties of porous clay.

The last section of this chapter presents the results of shallower indentations that are designed to test the mechanical properties of a locally densely packed area of clay particles. Here there is little scaling with the clay packing density, but the average behavior for the clay in each shale matches well the asymptotic behavior observed from the scaling relationships. Again, the presence of kerogen in the Woodford shales appears to modify this behavior.

6.1 Choosing a Length Scale: Scale Separability and Nanoindentation on Shale

The proper choice of indentation depth is essential to satisfy the grid indentation scale separability conditions (Eqs. (4.1) and (4.2)) which we recall:

$$3h \ll D \ll l\sqrt{N} \tag{6.1a}$$

$$d \ll \mathcal{L} \ll 3h \tag{6.1b}$$

and the surface roughness criteria (Eq. (4.8)) which we recall:

$$l \approx 200h \tag{6.2a}$$

$$h > 5R_q \tag{6.2b}$$

for the porous clay. The goal is to test both the porous clay as an overall composite and as a locally packed state; two sets of length scales are required to obtain two appropriate target indentation depths.

6.1.1 Porous Clay Composite

First, consider the porous clay as a composite material. First the largest heterogeneity, d, contained in an *rev* of porous clay is sought. From porosimetry (Sec. 2.3.4), a candidate for the largest heterogeneity, d, is the typical pore throat radius on the order of 10 nm. TEM and AFM images (Figs. 2-5 and 4-8, see also Secs. 2.2.3 and 4.3.4), along with information about typical clay mineral sizes (Sec. 2.3.1) give the typical maximum dimension of solid clay, on the order of one micron as a larger candidate for d. The RMS roughness measurements determined from the AFM tests (Sec. 4.3.4) are on the order of 150 to 300 nm (Tab. 4.3). We wish to resolve the properties of the porous clay composite as distinct from the properties of the inclusion phases, with characteristic length scale, D. From the imaging experiments, characteristic sizes of the inclusion (non-clay) material phases are observed to be as small as $20\,\mu$m. Combining the lower limits, d and R_q, and the upper limit, D, we ideally wish to test with indentations that sense depths greater than 750 nm to less than $3\,\mu$m. Note that this range is significantly narrower than the ranges explored by other researchers in previous applications of the grid indentation technique for cement paste and its primary binding material, C-S-H [46], [53]. Consequently, special care must be taken to isolate the appropriate target indentation depth for sensing properties of the porous clay composite in shale materials. Finally, we need enough tests over a wide area to achieve statistical independence and good sampling representation. With about $N = 300$ tests, a grid size of $l = 30\,\mu$m is more than sufficient.

Figure 6-1 uses the results of an AFM scan to show a 3-d representation of the surface of the sample after an indent. This test achieved the target indentation depth, and it is clear that the indentation depth is greater than the scale of the roughness and that the indentation response will depend on the composite behavior of a large number of particles.

6.1.2 Locally Densely Packed Areas

Second, consider testing locally densely packed areas of the porous clay. Here we expect the largest heterogeneity, d, to correspond to the pore throat radii in the vicinity of a locally densely packed region of solid clay, so it is reasonable to assume that the pore throat radius values of just a few nanometers are applicable here. The roughness of the sample may be a limitation, but, as the least stringent of the length scale criteria, we relax this restriction for now. We

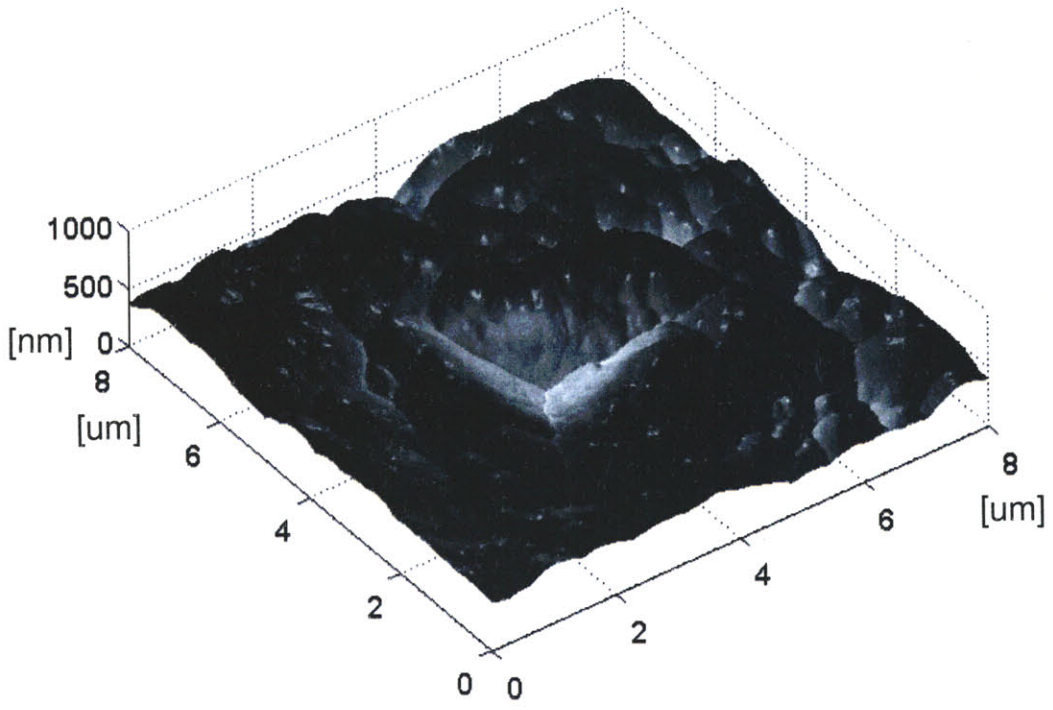

Figure 6-1: 3-d representation of AFM data, after an indent. The indent is clearly deeper than scale of the roughness, and is large enough to feel the response of a porous composite of clay particles.

will return to the roughness issue in the discussion of these results. In the case of the locally densely packed region, we wish to resolve properties distinct from the porous clay composite, whose length scale, D, is identified above at around $1\,\mu$m. Consequently, we wish to test with indentation depths smaller than 300 nm (although depths larger than 100 nm will keep within the effective resolution of the indentation instruments). Again, about $N = 300$ tests and a grid size of $l = 5\,\mu$m satisfy the scale separability criteria (Eqs. (4.1) and (4.2)).

6.1.3 Testing Program

The shale samples were tested at both target indentation depths, indenting in the (macroscopically identified) direction of symmetry, the $x3$-direction, and normal to the direction of symmetry, the $x1$-direction (Fig. 3-7). A few iterations over a range of loads on the shale materials demonstrated that a maximum indentation load of $P = 0.3\,$mN on shale materials yielded an average maximum indentation depth of $h \approx 250\,$nm, while a maximum indentation load of $P = 4.8\,$mN gave maximum indentation depths in the range of $h \approx 1\,\mu$m. Reminding ourselves of the scaling relation Eq. (3.10), that is,

$$\frac{P}{P_0} = \left(\frac{h}{h_0}\right)^{\frac{2+\kappa(d-1)}{d}} \tag{6.3}$$

the indentation forces and depths scale on-average with $P \propto h^2$ as one would expect for a Berkovich indenter, for which $d = 1$ (see Section 3.2.3). Furthermore, for the pore throat radius giving $d = 10\,$nm, and the larger indentation depths, Eq. (4.2) gives a reference length of the *rev*, $\mathcal{L}$, on the order of 100 nm. For the smaller depths, the reference length is smaller, on the order of tens of nanometers.

For the Boston Blue Clay samples, the maximum indentation load of $P = 4.8\,$mN gave maximum indentation depths which were too large, owing to the relatively low stiffness of these materials. As a result, the maximum indentation load for these tests was reduced by a factor of four to $P = 1.2\,$mN. This gave typical maximum indentation depths on the order of 2 to 4 μm. This range is comparable to the range of depths for the GeoGenome shales, and permits evaluation of the mechanical properties of the porous clay composite in the Boston Blue Clay samples. Limitations on the load resolution of the nanoindentation equipment prevented

	$x1$-direction			$x3$-direction		
Sample	$\overline{P}^{\max}$ [mN]	$\overline{h}_{\max}$ [nm]	N	$\overline{P}^{\max}$ [mN]	$\overline{h}_{\max}$ [nm]	N
GeoGenome Shales						
S1	0.324	854	401	0.222	483	292
S2	0.329	249	208	0.308	183	292
S3	0.282	112	400	0.304	124	299
S4	0.325	252	275	0.318	200	374
S7	0.227	142	400	0.295	145	296
Light	0.351	597	335	0.327	517	259
Dark	0.310	327	273	0.287	81	299
Pierre	0.268	181	300	0.311	294	293
L-C	0.316	580	242	0.323	650	242
Woodford Shales						
110	0.327	170	293	0.322	156	288
131	0.307	286	289	0.317	210	298
154	0.315	263	292	0.312	183	354
166	0.297	316	269	0.300	361	258
175	0.305	197	284	0.301	179	285
185	0.295	343	271	0.297	219	284

Table 6.1: Indentation test parameters for the 0.3 mN indentation tests on shale.

testing of locally densely packed areas on the Boston Blue Clay samples.

A summary of the average achieved maximum indentation loads, $\overline{P}^{\max}$, maximum indentation depths $\overline{h}_{\max}$, and number of tests, N, for each sample in each direction, are presented in Tables 6.1 and 6.2 for the shale samples and Table 6.3 for the Boston Blue Clay samples. The overbar denotes mean values of experimental data.

6.1.4 Preliminary Results - Mechanical Homogenization

To demonstrate the importance of choosing the length scale of indentation on a heterogeneous composite, consider a first look at the results of the statistical deconvolution analysis (Sec.4.2). Figure 6-2 displays a typical set of frequency plots for indentation modulus and indentation hardness derived from the indentation experiments and analysis on Shale 3 in the $x3$-direction. Two load cases are shown here; the top two plots in Figure 6-2 are from the 0.3 mN tests, which have an average indentation depth of 124 nm, the bottom two plots are from the 4.8 mN tests, which have an average indentation depth of 613 nm. Similar plots are obtained for the other

	$x1$-direction			$x3$-direction		
Sample	$\overline{P}^{\max}$ [mN]	$\overline{h}_{\max}$ [nm]	N	$\overline{P}^{\max}$ [mN]	$\overline{h}_{\max}$ [nm]	N
GeoGenome Shales						
S1	4.806	1810	388	4.741	1713	289
S2	4.830	1189	336	4.956	692	428
S3	4.852	584	382	4.850	613	300
S4	4.908	920	337	4.907	941	273
S7	4.776	678	400	4.865	689	291
Light	4.801	1926	299	4.850	2182	295
Dark	4.884	455	297	4.898	344	299
Pierre	4.778	624	299	4.854	824	294
L-C	4.830	2204	224	4.844	2551	253
Woodford Shales						
110	4.913	639	271	4.909	856	287
131	4.833	701	281	4.844	697	277
154	4.861	775	270	4.863	600	276
166	4.853	1053	261	4.891	871	219
175	4.852	704	284	4.847	693	282
185	4.859	1052	255	4.861	701	272

Table 6.2: Indentation test parameters for the 4.8 mN indentation tests on shale.

	$x1$-direction			$x3$-direction		
Sample	$\overline{P}^{\max}$ [mN]	$\overline{h}_{\max}$ [nm]	N	$\overline{P}^{\max}$ [mN]	$\overline{h}_{\max}$ [nm]	N
Boston Blue Clay						
4 MPa	0.910	2028	262	1.644	4679	316
6.5 MPa	1.593	2317	228	1.501	3634	247
10 MPa	1.003	1294	281	1.662	5824	278

Table 6.3: Indentation test parameters for the 1.2 mN indentation tests on Boston Blue Clay.

shales, in both indentation directions, $x1$ and $x3$.

For the 0.3 mN tests, four material phases are required to model the peaks in the experimental frequency distributions. From the phase with the smallest properties to the phase with the highest, they are identified as two peaks associated with the porous clay phase, one peak associated with an inclusion-clay composite response, and one peak associated with the inclusions. For the 4.8 mN tests, the progression is similar, but only one peak is needed for the porous clay phase, leading to a requirement of three material phases in the deconvolution model (the identification of these material phases is discussed further in the next section). For each shale, the two peaks associated with the porous clay phase at low indentation loads converge, via mechanical homogenization [45], to one single peak associated with the porous clay at the higher load case (with the quartz remaining as before).

6.2 Porous Clay Composite Results

Consider first the results of indentation testing designed to sense the porous clay composite. These are the 4.8 mN tests, which measure average indentation depths between 500 and 2500 nm. Indentations of these depths sense a roughly half-spherical volume with a radius of 3 - 18 μm.

6.2.1 Indentation Responses

Figure 6-3 displays three representative indentation curves to a maximum load of 4.8 mN, with the corresponding AFM images of the residual imprint of the indents. Two distinct types of indentation responses are evident. The response associated with indentation on quartz inclusions (curve and AFM image (a) in Fig. 6-3) gives a lower indentation depth, a higher unloading slope (and higher indentation modulus) and exhibits only a small amount of irrecoverable deformation. The response associated with indentation in clay (curves and AFM images (b) and (c) in Fig. 6-3) is different. These responses have deeper indentation depths, lower unloading slopes (and lower indentation moduli) and exhibit a great deal of irrecoverable deformation. The indentation on porous clay in the $x1$-direction (curves and AFM images (b) in Fig. 6-3) gives a smaller indentation depth and steeper unloading slope than the indentation on porous clay

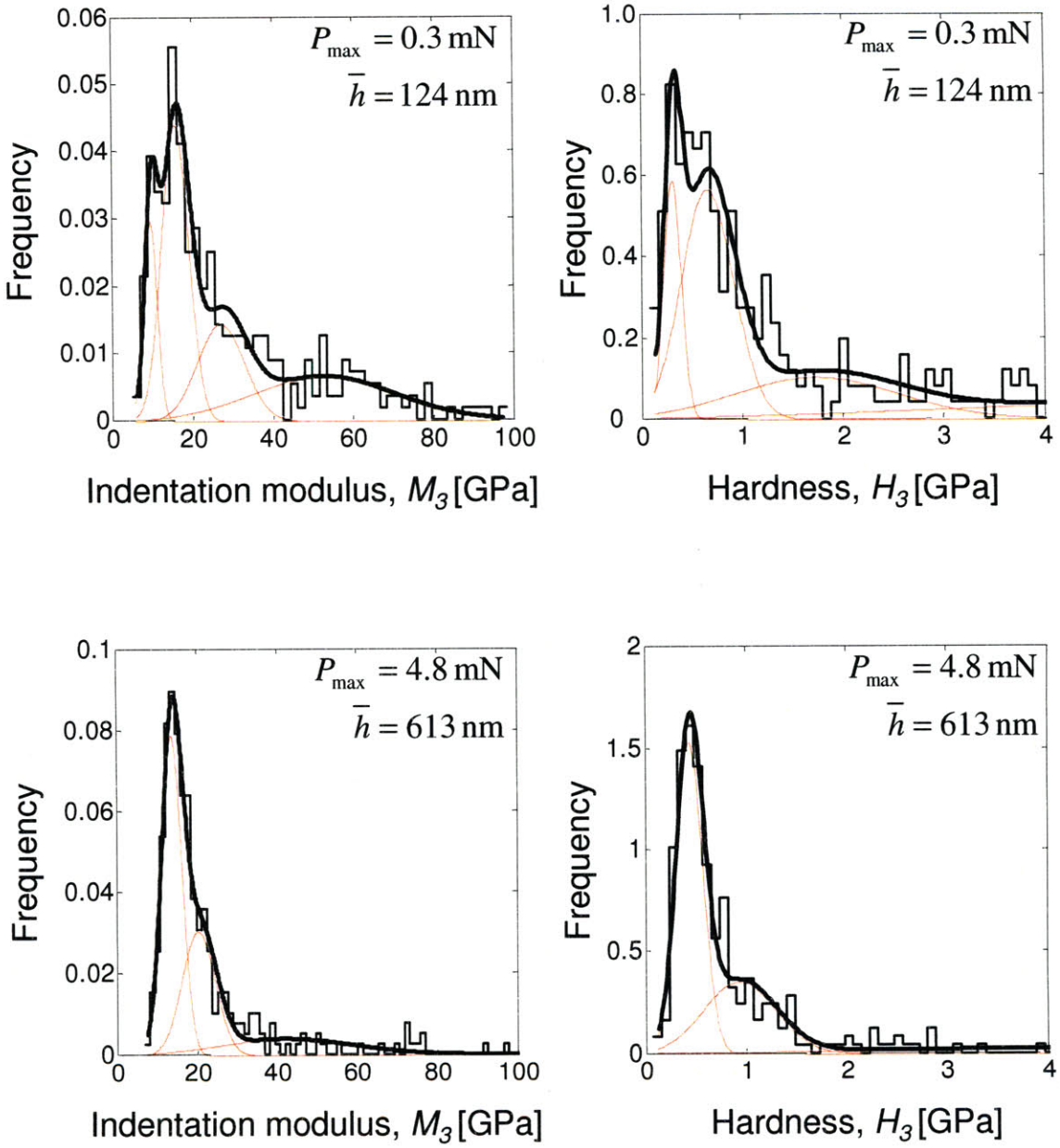

Figure 6-2: PDFs of indentation modulus (left) and hardness (right) for Shale 3 in the $x3$-direction to a maximum indentation load of 0.3 mN (top) and 4.8 mN (bottom). Shown are experimental data in the form of histograms (stepped thin black line), model phase distribution functions (thin red lines), and the overall model distribution (thick black line). Note the convergence of the two left-most peaks in the low-load tests (top) to one peak in the high-load tests (bottom).

in the $x3$-direction (curves and AFM images (c) in Fig. 6-3), which testifies to the anisotropic behavior of the porous clay phase in shales. There are possibilities for responses ranging between the characteristic clay and inclusion responses, and sometimes the distinction between responses is a bit unclear. The statistical deconvolution procedure gives results which are easier to obtain and interpret, with guidance from the individual responses providing a useful insight into the relationships between materials and indentation responses.

6.2.2 Deconvolution Results

As introduced in the preliminary presentation of deconvolution results, in the context of scale separability, three material phases are required to model the experimental distributions of indentation modulus and hardness of the porous clay composite for a given shale material. Tables 6.14 through 6.25, presented at the end of this chapter, summarize the results of the deconvolution procedure for all tested samples, in both directions, for the 4.8 mN load case designed to assess the mechanical behavior of the porous clay composite.

The indentation responses associated with the first phase (with smallest mean indentation modulus and hardness) are like those in curves (b) and (c) in Figure 6-3. This identifies the first phase as representative of the porous clay phase. The indentation responses associated with the third phase (with largest mean indentation modulus and hardness) are like the one shown in curve (a) in Figure 6-3, identifying the third phase as representative of the silt inclusion phase, composed predominantly of quartz and feldspar. To check this assertion, it is possible to compare the deconvolution results to the expected properties. Although single quartz crystals are anisotropic, it is unlikely that these crystals are ordered or aligned in the shale composite. As a result, quasi-isotropic elastic constants for quartz can be used, as found in handbooks [133]:

$$K_{quartz} = 37.9 \text{ GPa}$$
$$G_{quartz} = 44.3 \text{ GPa}$$

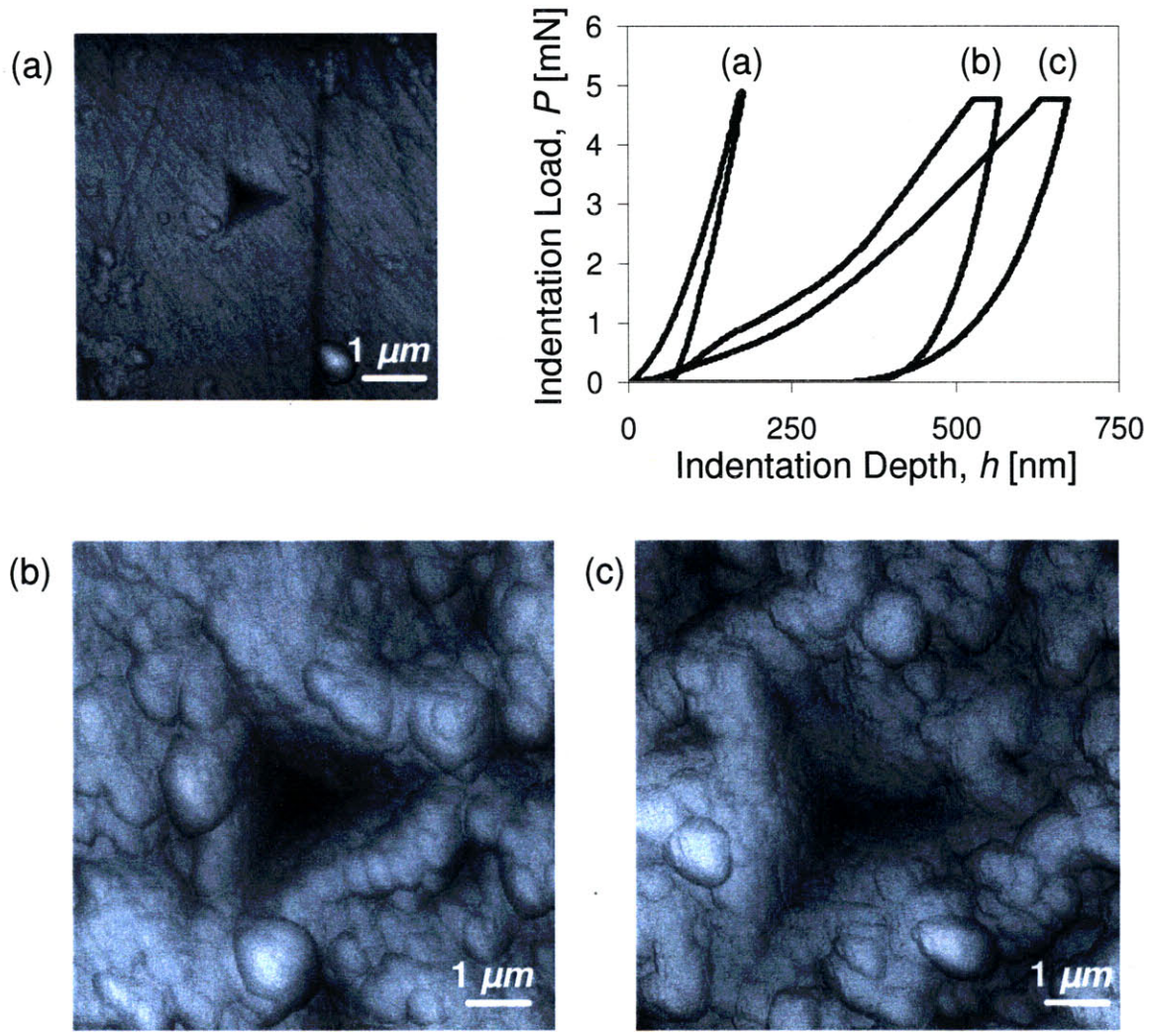

Figure 6-3: Indentation responses on shales indented to a maximum load of 4.8 mN: Curve (a) is typical of indentation on a quartz inclusion, while the curves (b) and (c) are typical of indentation on the porous clay composite. Curve (b) is from indentation in the $x1$-direction and curve (c) is from indentation in the $x3$-direction. The other three images are AFM photo simulations after a 4.8 mN indent on (a) a quartz inclusion in the $x3$-direction, (b) the porous clay composite in Shale 3 in the $x1$-direction, and (c) the porous clay composite in Shale 3 in the $x3$-direction.

which, using Eq. (3.16) give an indentation modulus of:

$$M_{quartz} = 96.2 \text{ GPa} \tag{6.5}$$

Although this large a value was not seen for the mean value of the third peak in every shale, it does identify the correct order of magnitude. Given that the focus of this study is the porous clay phase, indentation depths were tuned to assess the porous clay composite, so some deviation from the expected stiffness is not surprising. In fact, the third phase typically has the largest standard deviation of the three phases, suggesting larger experimental variabilities for this phase.

Identification of the first and thrid phases leaves an apparent middle material phase yet to be identified. However, the multiscale thought model for the structure of shale does not suggest the presence of a third phase. This phase must not be an actual material phase, but instead represents composite behavior of the porous clay and the silt inclusions. As the grid indentation technique leads to random placements of indentations with respect to the material phases, indents can occur on or very near the boundary of porous clay and silt inclusions. Composite behavior may also be measured when an inclusion lies just below the surface. With the silt inclusions existing at a much larger length scale than the porous clay, this apparent composite behavior is expected.

6.2.3 Repeatability Study

To check the repeatability of values obtained from the grid indentation technique, two grids of 300 indents, to a maximum load of 0.3 mN, were performed on GeoGenome Shale 7, in the $x3$-direction. One grid was performed in the Hysitron, while another was performed in the CSM (see Sec. 3.1.1). Then, a four-phase deconvolution analysis was applied to both datasets. The results are shown in Figure 6-4 and in Table 6.4. For the porous clay, measured by the first two phases in the deconvolution, the values coincide very well. The agreement is not as good for Phases 3 and 4, associated with the composite response and the silt inclusions. Such a result is not too surprising, as the indentation depth is tuned to assess the mechanical behavior of the porous clay phase. As the focus of this study is on the porous clay, the repeatability

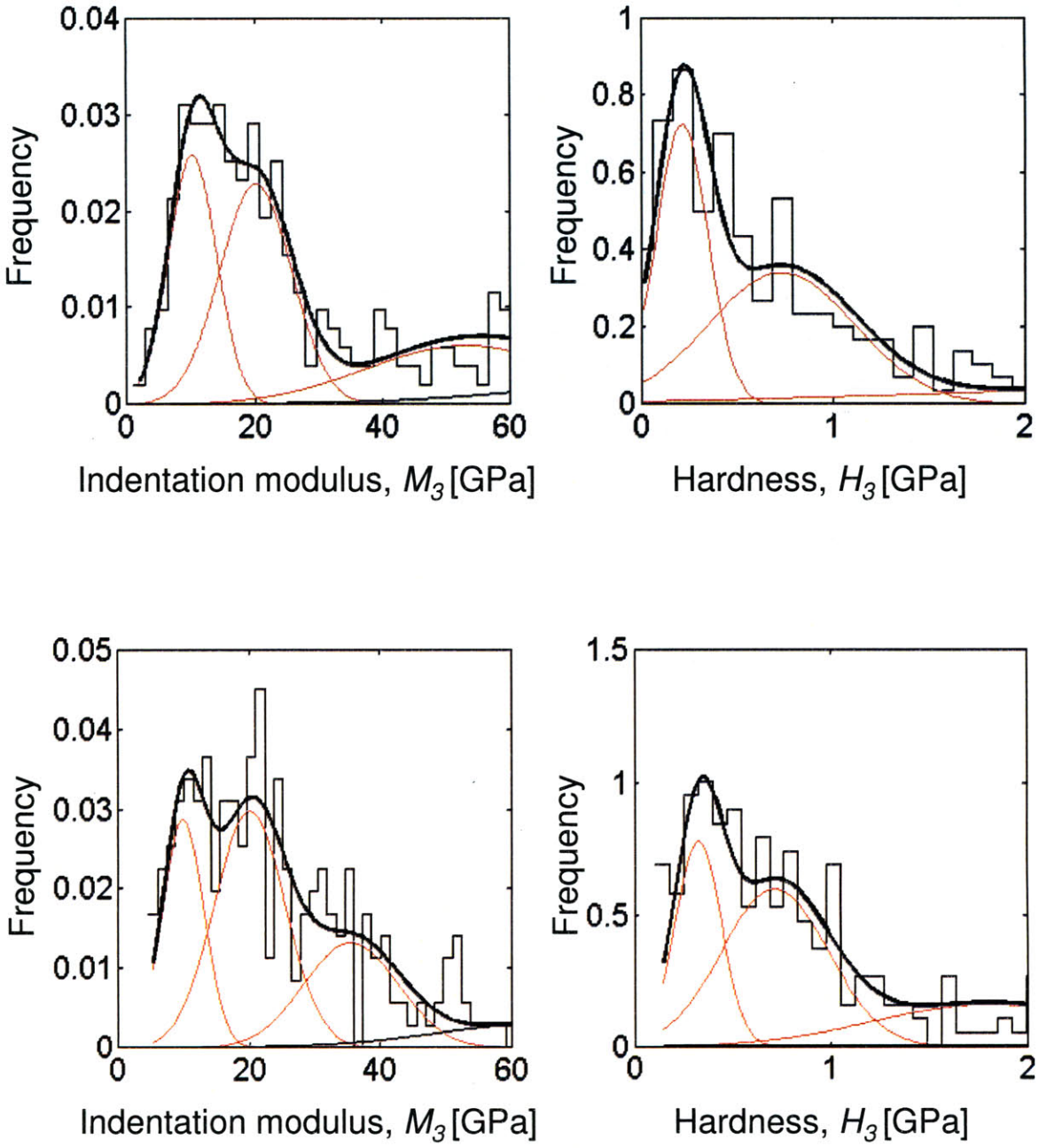

Figure 6-4: Repeatability study for the deconvolution technique. Indentation results in terms of indentation modulus, M (left), and hardness, H (right) for Shale 7, in the $x3$-direction obtained in the Hysitron (top) and the CSM (bottom) on different sample surfaces. Shown are experimental data in the form of histograms (stepped thin black line), model phase distribution functions (thin red lines), and the overall model distribution (thick black line). The values and the model distributions are similar for both cases.

	Indentation Modulus, M_3							
Equipment	Phase 1		Phase 2		Phase 3		Phase 4	
	mean	S.D.	mean	S.D.	mean	S.D.	mean	S.D.
CSM	10.38	3.79	20.32	5.70	54.59	16.09	102.73	32.05
Hysitron	9.94	3.19	20.15	5.47	35.67	7.24	64.42	15.91

	Hardness, H_3							
	Phase 1		Phase 2		Phase 3		Phase 4	
	mean	S.D.	mean	S.D.	mean	S.D.	mean	S.D.
CSM	0.22	0.13	0.74	0.38	3.75	2.02	10.33	2.52
Hysitron	0.32	0.12	0.72	0.27	1.81	0.60	7.58	4.04

	Volume Fraction, f			
	Phase 1	Phase 2	Phase 3	Phase 4
CSM	0.24	0.32	0.24	0.20
Hysitron	0.23	0.41	0.24	0.12

Table 6.4: Results of the repeatability study for grid indentation and deconvolution analysis on GeoGenome Shale 7 in the $x3$-direction, using the CSM and the Hysitron nanoindentation equipment.

study gives satisfactory results.

6.3 Porous Clay Composite Scaling

Recall the clay packing density (Eq. (2.21)) as a volume fraction parameter associated with the porous clay composite at Level '1' in the multiscale thought model for the structure of shale:

$$\eta = 1 - \varphi = 1 - \frac{\phi}{1 - f_{inc}} \tag{6.6}$$

Dimensional analysis revealed this parameter as a key scaling variable for mechanical behavior of the porous clay composite, and scaling relationships were developed in Sections 5.2 and 5.3, which are recalled here (Eqs. (5.31) and (5.90)):

$$M_1 = m_{1,s} \times \Pi_{M_1}(\eta) \tag{6.7a}$$

$$M_3 = m_{3,s} \times \Pi_{M_3}(\eta) \tag{6.7b}$$

t-test of Statistical Significance
The statistical significance of a set of apparent differences between quantities measured on the same sample is assessed by considering a dependent samples, or matched-pairs, t-test. The test consists of comparing the t statistic calculated for the sample populations with a reference t value obtained from Student's t-distribution for a given confidence level for the degrees of freedom of the t statistic. The t statistic in for the dependent case is calculated by: $$t = \frac{\overline{X}_D}{s_D/\sqrt{N}}$$ where $\overline{X}_D$ is the mean of the differences between the measurements for each sample, s_D is the standard deviation of these differences, and N is the number of samples. The reference t value is obtained from Student's t-distribution based on the confidence level p and the number of degrees of freedom, $N-1$. The confidence level sets the probability that observed differences occurred as a result of random chance. Choosing a confidence level of $p = 0.05$, for example, means that observed differences had less than a 5% chance of occurring randomly. If the calculated t statistic is larger than the reference value obtained from Student's t-distribution, the difference is statistically significant at the given confidence level.

Table 6.5: Background: T-test for statistical significance testing [136]

$$H = h_s\left(c_s, \alpha_s\right) \times \Pi_H^I\left(\alpha_s, \eta\right) \tag{6.8}$$

where Ortega et al. [145] have used back analysis of macroscopic measurements to estimate $m_{1,s} = 26.3$ GPa and $m_{3,s} = 14.9$ GPa as in Eq. (5.30), and employed a numerical implementation of the self-consistent scheme to generate fitted functions for the dimensionless expressions $\Pi_{M_1}(\eta)$ and $\Pi_{M_3}(\eta)$ as in Eq. (5.32). A similar approach does not yet exist for the hardness measurements, so for the purposes of this analysis, it is assumed that $\alpha_s = 0$ and a best fit for h_s will be made.

Recall from the discussion in Section 2.4 that there is some uncertainty in the calculation of the clay packing density arising from assessment of porosity. As a result, the packing density data are reported and displayed as mean values with plus-minus uncertainty associated with different methods for assessing porosity, as in Eq. (2.22).

6.3.1 Kerogen-Free shales: GeoGenome Shales and Boston Blue Clay

First, we examine the results of the kerogen-free GeoGenome Shales and the Boston Blue Clay samples. The scaling of the indentation moduli (in both the $x1$- and $x3$-directions) and

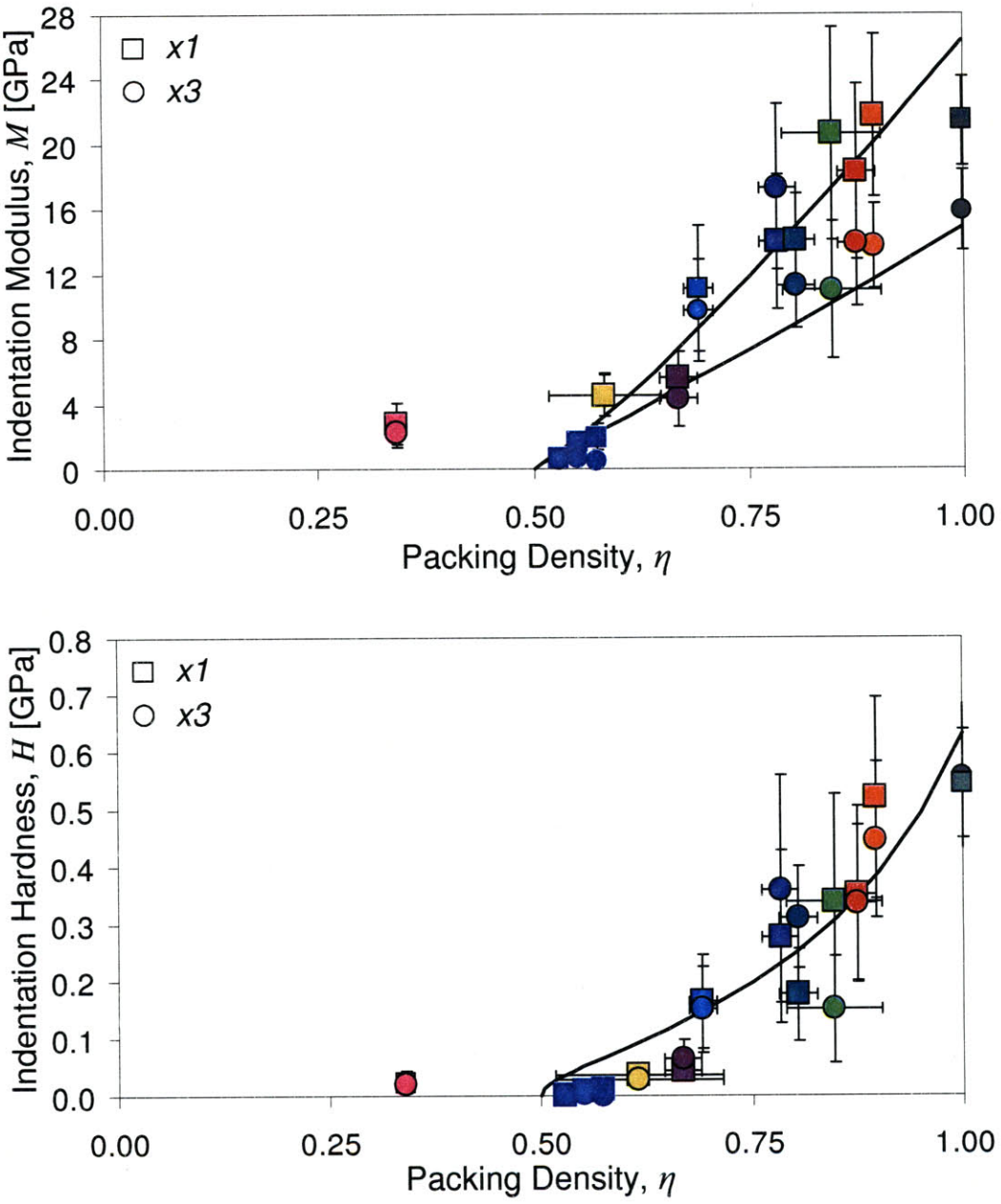

Figure 6-5: GeoGenome Shale and Boston Blue Clay indentation modulus, M, (top) and hardness, H, (bottom) measured in both directions, versus mean clay packing density, η. The horizontal error bars in η represent the variation of minimum and maximum packing densities determined by porosimetry or bulk density (see Eq. 2.22 and Tab. 2.6). The vertical error bars in M and H represent the standard deviation of the fitted peaks from the deconvolution analysis. The solid black lines are the scaling results, i.e. Eqs. (5.31) with Eq. (5.30) for indentation moduli and Eq. (5.90) with $\alpha_s = 0$ and a best fit for $h_s = \lim_{\eta \to 1} H = 0.62$ GPa for hardness.

hardness with the clay packing density, shown graphically in Figure 6-5, is quite interesting. There is some variation of the experimental data around the trend, but on first order, scaling relationships with clay packing density fit the trend quite well. The coefficient of determination between experimental values and model predictions for indentation moduli (in both directions) is $r^2 = 0.88$, while the coefficient of determination between experimental values and model predictions for hardness is $r^2 = 0.86$.

The indentation modulus appears to demonstrate intrinsic anisotropy, as the indentation moduli measured the $x1$-direction scale to higher asymptotic values at $\eta = 1$ than the indentation moduli measured in the $x3-$direction. The statistical significance of the observation of apparent differences between indentation modulus measurements in the two testing directions is assessed by considering a dependent samples, or matched-pairs, t-test (Tab. 6.5) [136]. Based on an understanding from macroscopic observations of shale, the values for M_1 are expected to be higher than the values for M_3, so a comparison with the one-sided Student's t-distribution can be used, and a confidence level of $p = 0.05$ is used. For the nine GeoGenome shales, the t-statistic is calculated as $t = 2.02$, while the value of the one-sided Student's t-distribution for $p = 0.05$ and 8 degrees of freedom is 1.895. Because the calculated t-statistic is larger than the value of the one-sided Student's t-distribution, the observed anisotropy for the GeoGenome shales is statistically significant at the 5% confidence level. Adding in the three Boston Blue Clay samples results in a t-statistic calculated as $t = 2.20$, while the value of the one-sided Student's t-distribution for $p = 0.05$ and 11 degrees of freedom is 1.796. Again, the observed anisotropy of indentation modulus for the GeoGenome shales and the Boston Blue Clay samples is statistically significant at the 5% confidence level.

The relationship between the indentation hardness (in both the $x1$- and $x3$-directions) and the clay packing density is similar to the indentation modulus relationship, although there is one key difference. While the indentation modulus measurements are clearly anisotropic, the hardness measurements are apparently isotropic. Although there is some scatter in the data, the vertical "error bars" (that represent the standard deviation of the peaks) in the hardness plot (Figure 6-5, bottom) are consistently overlapping. There is no trend of one direction giving a larger hardness than another. From a statistical perspective, the t-test gives further confirmation that any difference between measurements is not significant. For the nine

GeoGenome shales, the t-statistic is calculated as $t = 0.28$, while the value of the one-sided Student's t-distribution for $p = 0.05$ and 8 degrees of freedom is 1.895. Adding in the three Boston Blue Clay samples results in a t-statistic calculated as $t = 0.33$, while the value of the one-sided Student's t-distribution for $p = 0.05$ and 11 degrees of freedom is 1.796. In both cases, the reference value from the Student's t-distribution is much larger than the experimental statistic, demonstrating that any difference is not statistically significant.

6.3.2 Kerogen-Rich Shale: Woodford Shales

In Section 2.3.2, the Woodford Shale samples were identified as being kerogen-rich. Section 2.3.1 provided evidence that kerogen should be considered at Level '0' of the multiscale model for shale. Such a consideration could lead to a slightly different observations of scaling between measured properties and the clay-kerogen packing density. Figure 6-6 displays the scaling results for indentation modulus and hardness for the Woodford Shales. The Woodford Shale results are less dramatic than the results for the GeoGenome Shales and the Boston Blue Clay samples. The values for the Woodford Shale samples are relatively close to each other because the samples were less than 100 feet apart in the earth. This makes interpretation of the scaling rather difficult. With the few points clustered in a relatively small packing density, the coefficients of determination between experimental values and scaling model predictions for the Woodford Shale samples alone are very low, giving $r^2 = 0.09$ for indentation moduli in both directions and $r^2 = 0.03$ for hardness. In general, however, the Woodford Shale samples fit in with the trends observed for the GeoGenome and Boston Blue Clay samples, except that elastic isotropy is not as apparent in the Woodford Shale. For all samples together, the coefficients of determination comparing experimental values and scaling model predictions are nearly as good as those without considering the Woodford Shale samples. The values are $r^2 = 0.82$ for indentation moduli in both directions, and $r^2 = 0.65$ for hardness in both directions.

Statistically speaking, only four of the six Woodford Shale samples have indentation modulus values for the $x1$-direction higher than the $x3$-direction. Using the same one-sided t-test as for the GeoGenome shales results in a t-statistic of $t = 1.21$. The value of the one-sided Student's t-distribution for $p = 0.05$ and 5 degrees of freedom is 2.015. In this case, because the calculated t-statistic is less than the value of the one-sided Student's t-distribution, any

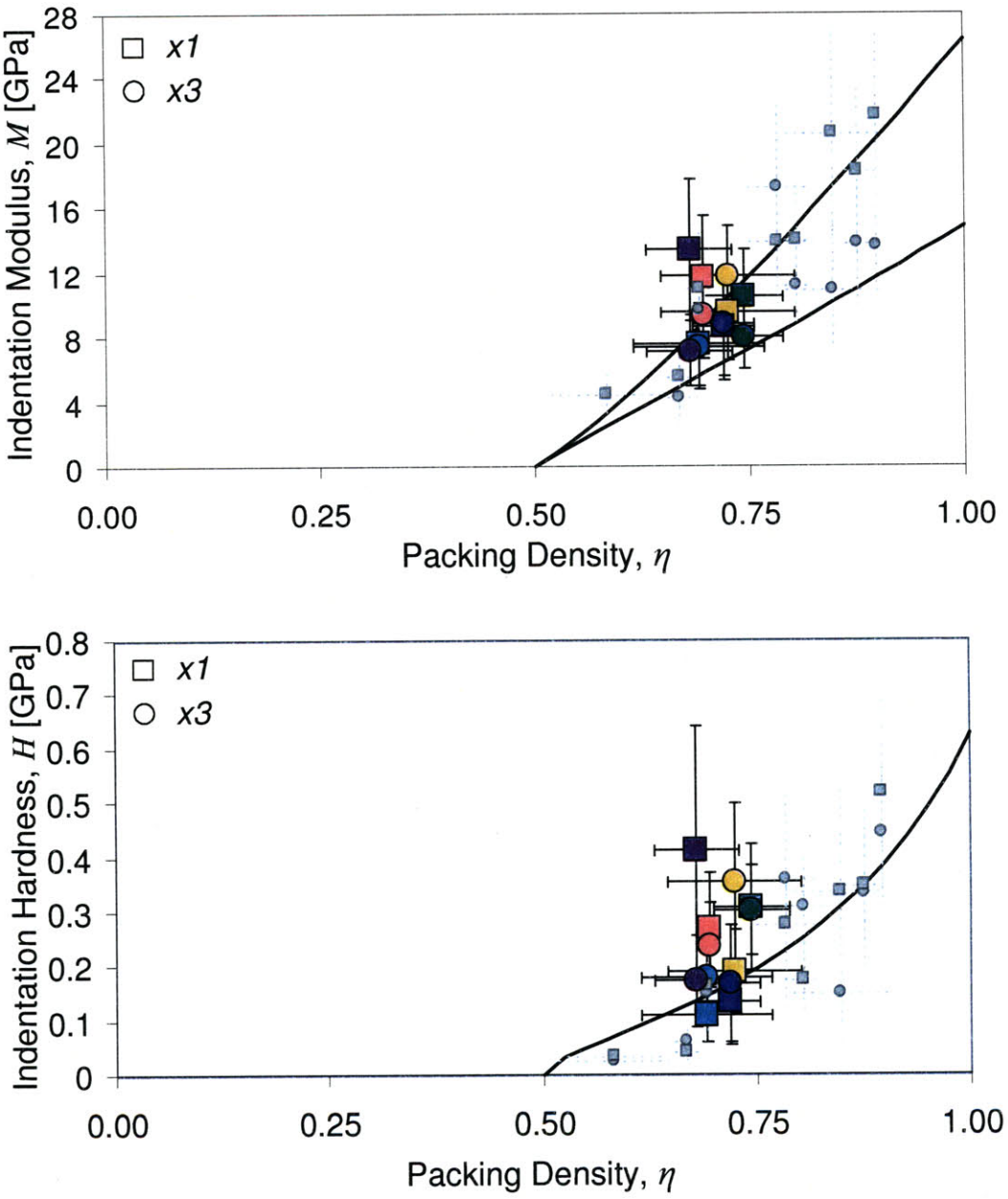

Figure 6-6: Woodford shale indentation modulus, M, (top) and hardness, H, (bottom) measured in both directions, versus clay-kerogen packing density, η. The horizontal error bars in η represent the variation of minimum and maximum packing densities determined by porosimetry or bulk density (see Eq. 2.22 and Tab. 2.6). The vertical error bars in M and H represent the standard deviation of the fitted peaks from the deconvolution analysis. The grey points are the GeoGenome shale results from Fig. 6-5 for comparison.

difference between indentation moduli in both tested directions for the Woodford Shales is not statistically significant at the 5% confidence level. The presence of kerogen, which is expected to behave as an isotropic solid at the testing temperatures, reduces the anisotropy of the porous clay composite. When combined with the GeoGenome and Boston Blue Clay samples, however, the story changes. For all tested samples, the calculated t-statistic is $t = 2.559$, while the value of the one-sided Student's t-distribution for $p = 0.05$ and 17 degrees of freedom is 1.74. The observed anisotropy is statistically significant at the 5% confidence level. In fact, the value of the one-sided Student's t-distribution for $p = 0.025$ and 17 degrees of freedom is 2.110, meaning that the differences in the combined data set are actually statistically significant at the 2.5% confidence level.

Finally, it appears that hardness of the porous clay in the Woodford Shale samples is isotropic. To check this statistically, the t-statistic is $t = 0.045$, while the value of the one-sided Student's t-distribution for $p = 0.05$ and 5 degrees of freedom is 2.015, so any difference is clearly not statistically signficant. Considering all the shale samples together, we have $t = 0.241$ which is lower than the reference value of 2.110. Hardness of the porous clay in shale is seen to be isotropic in a statistical sense.

6.3.3 Percolation Threshold and Material Invariant Properties

The two limits of the scaling relationships warrant further discussion. The observed phenomena are highlighted here, while further discussion of their physical interpretation follows in subsequent discussion chapters.

Lower Limit: Percolation Threshold

The lower limit of the scaling trends define an asymptotic state where a shale material loses its stiffness and strength properties, defining the percolation threshold of the porous clay phase. Below this percolation threshold, the volume fraction of particles is not enough to form a continuous stress path through the system. Recall from Sec. 5.2.2 that an assumption was made for the percolation threshold of porous clay in shale of $\eta_0 = 0.5$, which led to the consideration of a granular, spherical mechanical morphology when developing the scaling relationships. The percolation threshold observed from the deconvolution analysis appears to occur at a pack-

ing density of $\eta_0 = 0.5$, giving a first verification of the assumptions about the mechanical microstructure of the porous clay in shale.

The data points associated with the Low-Clay shale, whose clay packing density is less than 0.5 are discounted in this analysis for several reasons. First, this sample gave the most difficulty in the sample preparation process, thanks to the high inclusion content and low clay content. Second, while the clay packing density lies below the percolation threshold, it is impossible to mechanically indent a material with zero stiffness. We suggest that the porous clay in this sample, agglomerated in local packings, has an extremely small stiffness when compared with the stiffness measured in the other samples. This suggestion is further supported by reported macroscopic dynamic measurements of the elasticity of this shale material, showing (1) an almost isotropic macroscopic elasticity (namely, in Voigt notation, $C_{11}/C_{33} = 1.1; C_{66}/C_{44} = 1.2; C_{12}/C_{13} = 1.0$), that (2) is close to the isotropic self-consistent estimate of the stiffness of a porous composite in which the silt inclusion (56%, see Tab. 2.6) solely contributes to the stiffness. In other words, this low-clay shale behaves more like a sandstone, with sand particles forming the dominating load bearing phase, than a shale with the porous clay composite phase as the dominating load bearing phase. Finally, this observation and careful inspection of the nanoindentation results implies that the indentation process may have compacted the clay particles in the low-clay shale. This compaction could result in measurement of a local state residing just above the percolation threshold upon unloading (the point at which each individual indentation experiment is analyzed using the Oliver and Pharr method, see Sec. 3.5). This consolidation experienced in the low-clay shale indentation should be much less significant in the other samples, which are more densely packed to begin with.

Macroscopic tests on a series of resedimented Boston Blue Clay samples also provide evidence in favor of a percolation threshold for shale-like behavior at a clay packing density of $\eta_0 = 0.5$. Abdulhadi measured a uniaxial Young's modulus in the $x3$-direction, at the beginning of a shearing test in the triaxial load cell [2]. Assuming a Poisson's ratio of $\nu = 0.3$, the Young's modulus may be translated into an indentation modulus by Eq. (3.16). Then, a Reuss-bound downscaling approach, similar to that employed by Ulm and Abousleiman [174], is used to subtract the mechanical effect of the silt inclusion, resulting in an estimated indentation

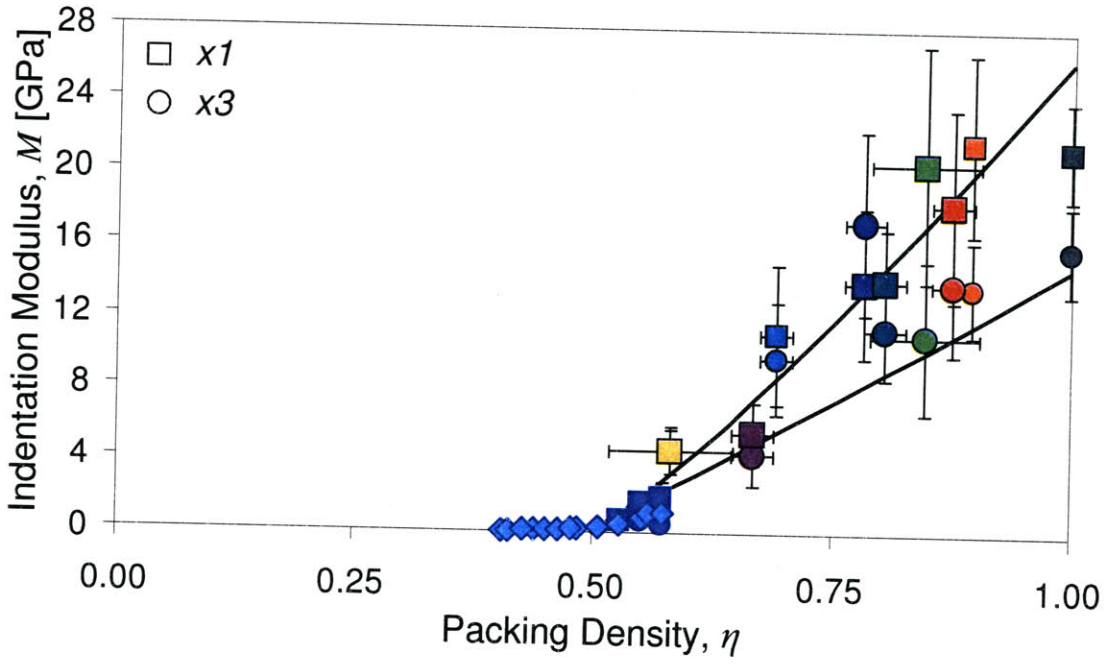

Figure 6-7: Same figure as Fig. 6-5 (top) with porous clay indentation modulus in the $x3$-direction estimated from macroscopic data on Resedimented Boston Blue Clay (light blue diamonds). Estimated indentation moduli correspond well to the experimental indentation moduli above the percolation threshold $\eta_0 = 0.5$. Below the percolation threshold, the developed stiffness is an order of magnitude less than that seen in the porous clay in shale.

modulus of the porous clay:

$$\frac{1}{M^{\text{triaxial}}} = \frac{1-f^{inc}}{M^{\text{porous}}} - \frac{f^{inc}}{M^{\text{inc}}} \tag{6.9a}$$

$$\Downarrow$$

$$M^{\text{porous}} = \frac{1-f^{inc}}{\left(\frac{1}{M^{\text{triaxial}}} - \frac{f^{inc}}{M^{\text{inc}}}\right)} \tag{6.9b}$$

where M^{triaxial} is the equivalent indentation modulus from the triaxial experiment, $M^{\text{inc}} = 69$ GPa is the equivalent indentation modulus of quartz, and M^{porous} is the (sought) estimate of the equivalent indentation modulus of the porous clay composite. These results are plotted with indentation data in Figure 6-7. Although some stiffness is measured in these clay materials when the packing density is below the percolation threshold of $\eta_0 = 0.5$, the stiffness is an order of magnitude below the stiffnesses that are seen for materials with average packing densities larger than the percolation threshold for the porous clay in shale. This dataset provides further evidence for a percolation threshold for shale materials at a clay packing density of $\eta_0 = 0.5$.

Upper Limit: Material Invariant Properties

The upper limit is the material invariant asymptotic state which would be achieved if the porous clay in shale could pack to a packing density of $\eta = 1$. These values correspond to $m_{1,s}$, $m_{3,s}$, and h_s in the scaling relationships, Eqs. (5.31) and (5.90). By 'material invariant' we mean properties that do not depend neither on the mineralogy nor the porosity of the specific shale material. These material invariant properties are not necessarily the pure clay mineral properties, as they still encompass the contact interaction between particles, in combination with the pure mineral properties. Following the trend of the indentation moduli data with packing density upwards, towards an asymptotic packing density of $\eta = 1$, allows an estimation of the asymptotic stiffness of the porous clay in shale. This extrapolation gives values of:

$$m_{1,s} = \lim_{\eta=1} M_1 = 25 \text{ GPa} \tag{6.10a}$$

$$m_{3,s} = \lim_{\eta=1} M_3 = 16 \text{ GPa} \tag{6.10b}$$

as shown in Figure 6-5 (top). These values match well to the values obtained by Ortega et al.

[145] from back calculation of macroscopic measurements, i.e. $m_{1,s} = 26.3$ GPa and $m_{3,s} = 14.9$ GPa as in Eq. (5.30). Together, they clearly demonstrate that the elasticity of the porous clay is anisotropic.

Similarly, we follow the trend of the hardness data with packing density towards an asymptotic packing density of $\eta = 1$ to estimate the asymptotic hardness of the porous clay in shale. This extrapolation gives values of:

$$h_s = \lim_{\eta=1} H_1 \approx \lim_{\eta=1} H_3 = 0.62 \text{ GPa} \tag{6.11}$$

as shown in Figure 6-5 (bottom). Unlike the stiffness, the material invariant hardness is isotropic.

6.4 Measurement of Material Invariant Properties on Locally Densely Packed Areas

Thus far, in seeking information regarding the porous clay phase of the shale materials, we have considered only the "deep" indentations that sense the porous clay composite. We now turn to "shallow" indentations that should sense locally densely packed areas of porous clay, as introduced in Section 6.1.2. Inspection of the progression of frequency plots in Figure 6-2, as previously discussed, reveals that mechanical homogenization takes place with increasing load and indentation depth. That is, for the shallow indentation depths, the frequency plots in the top of Figure 6-2 show two lower-value peaks which converge to a single peak in the series of deeper indentations. But a question arises: if the smallest-valued peaks at higher depths correspond to the homogenized porous clay composite phase, what is the meaning of the two smallest peaks measured from lower load tests?

Returning again to the surface roughness criteria (Eq. (4.8)) and considering the indentation depths for the smallest load (less than 400 nm), one possible explanation is that roughness effects intervene and create additional scatter in the data, because R_q is on the order of 150 to 300 nm (see Tab. 4.3). This explanation would be more plausible, however, if there was a simpler trend – that is, a consistent shift up or down in measured properties, or a broadening of the peak, indicating greater uncertainty in the measurements. The roughness explanation does

	M_1		H_1			M_3		H_3		
Sample	mean	S.D.	mean	S.D.	f_2	mean	S.D.	mean	S.D.	f_2
GeoGenome Shales										
S2	15.14	5.00	0.17	0.08	0.38	17.20	3.02	0.45	0.15	0.24
S3	21.72	4.62	0.62	0.26	0.32	15.84	3.35	0.67	0.26	0.37
S4	10.51	3.87	0.16	0.08	0.25	16.81	3.75	0.43	0.19	0.27
S7	18.31	2.92	0.43	0.14	0.27	20.32	5.70	0.74	0.38	0.32
Light	23.84	7.14	0.72	0.29	0.13	21.05	9.48	0.93	0.53	0.14
Dark	18.63	6.93	0.56	0.31	0.30	7.21	3.78	0.29	0.19	0.29
Average	21.4		0.54			15.9		0.56		
Standard Error	2.4		0.10			2.2		0.12		

Table 6.6: Middle Peak results for the GeoGenome shales with average indentation depths less than 400 nm. M and H values in GPa.

not address the consistent observation of two distinct peaks in both the modulus and hardness measurements.

Recalling the scale separability criterion (Eq. (4.2)) in the context of the small indentation depths is helpful. We have achieved our target depth, which is not large enough to sense the overall porous clay composite, nor is it small enough to sense the mechanical response of a single clay particle in isolation (with typical dimensions of $0.5 - 2\,\mu$m in the long direction). Tables 6.8 through 6.13 (presented at the end of this chapter) summarize the results of the 4-phase deconvolution analysis for the 0.3 mN load case.[1] An inspection of the values from the "first peak" and "second peak" of the low depth responses (the first and second phases presented in Tabs. 6.8 through 6.13), however, reveals interesting results for the GeoGenome shales and the Woodford shales. It appears that the "first peak" values are still associated with the clay packing density, but the "second peak" values are common to all the shale materials, as long as the average indentation depths fall in the desired range, i.e. less than 400 nm.

6.4.1 GeoGenome Shales - Level '0'

Table 6.6 highlights the pertinent experimental data for each GeoGenome shale which was tested at average indentation depths below 400 nm. Figure 6-8 (top) displays the indentation

[1] We were unable to achieve low enough indentation depths for the highly compressed resedimented Boston Blue Clays.

moduli of the "middle peak" for each of these shales. It is noteworthy that these values do not scale with the clay packing density, η, but instead have generally similar "middle peak" values in each direction. This similarity suggests that the tests measure the same property in each sample, despite differences in mineralogy and porosity. The average indentation moduli values are:

$$m_{1,s} = 21.4 \pm 2.4GPa \tag{6.12a}$$

$$m_{3,s} = 15.9 \pm 2.2GPa \tag{6.12b}$$

with the uncertainty calculated as the standard error of the measured quantities. Figure 6-8 (middle) displays the hardness of the "middle peak" for these shales. Again, there is no scaling with the clay packing density, but each shale has generally similar "middle peak" values, suggesting we measure the same property in each sample. The average hardness values are:

$$h_{1,s} = 0.54 \pm 0.10 \text{ GPa} \tag{6.13a}$$

$$h_{3,s} = 0.56 \pm 0.12 \text{ GPa} \tag{6.13b}$$

with the uncertainty calculated as the standard error of the measured quantities.

The surface fraction of "middle peak," which represents the probability of finding this response on a given sample surface, shows a very strong correlation with the overall clay packing density, as shown in Figure 6-8 (bottom). This observation, in conjunction with mechanical measurement that are relatively constant, suggests that the "middle peak" data obtained from the 0.3 mN indentation measurements tested an asymptotic, locally densely packed state. Indeed, samples with a higher clay packing density have more solid phase; consequently, the likelihood of indenting on a locally densely packed state during a grid indentation campaign is greater in samples with higher clay packing density.

Figure 6-5 also shows the mean and standard error "middle peak" values, plotted at the asymptotic packing density of $\eta = 1$, along with the high-depth results discussed previously. The agreement of these four points, at this asymptotic value, to the overall trends is remarkably good. This "middle peak" analysis presents another independent measurement of the material invariant properties of shale materials, the asymptotic stiffness and hardness, $m_{(\beta),s} = \lim_{\eta=1} M_i$

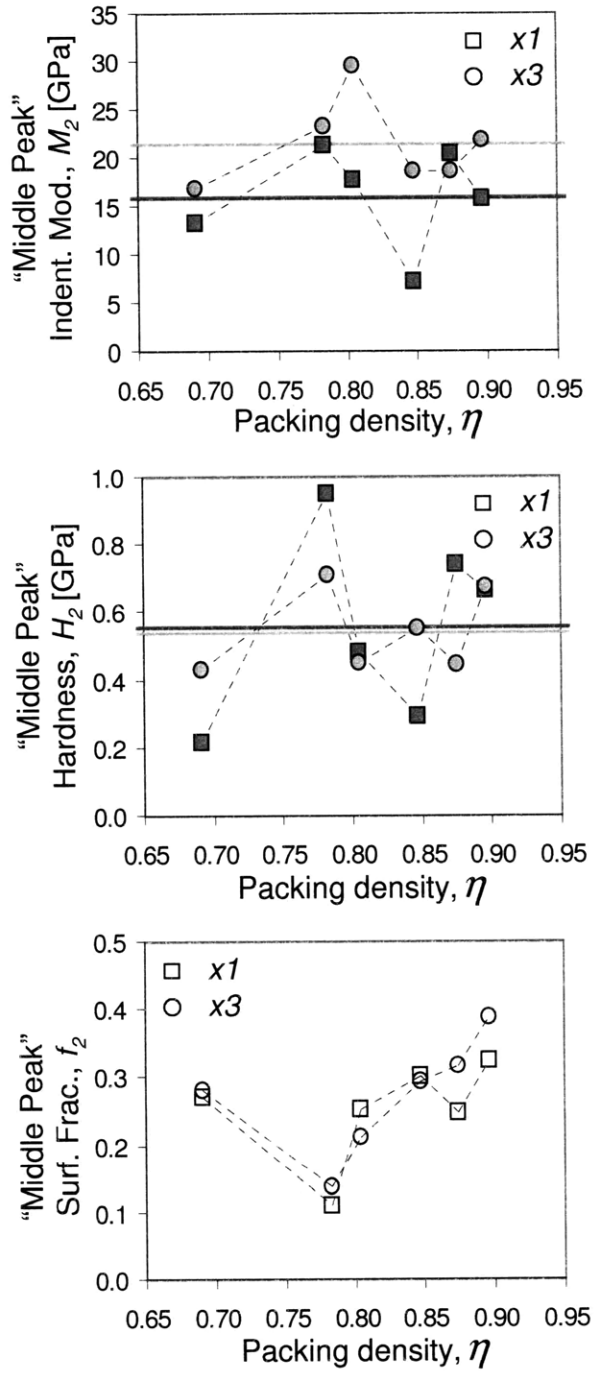

Figure 6-8: "Middle peak" results versus clay packing density, η. Indentation moduli, M_2 in the $x1$- and $x3$-directions (top) and hardness, H_2, in the $x1$- and $x3$-directions (middle) show no consistent trend with clay packing density. The surface fraction of indents corresponding to the "middle peak," f_2, (bottom) increase with packing density.

	M_1		H_1			M_3		H_3		
Sample	mean	S.D.	mean	S.D.	f_2	mean	S.D.	mean	S.D.	f_2
Woodford Shales										
110	25.26	4.43	0.60	0.24	0.28	17.30	5.35	0.83	0.47	0.27
131	6.92	1.73	0.25	0.10	0.26	9.84	2.77	0.37	0.16	0.25
154	13.24	3.34	0.27	0.14	0.22	11.79	4.40	0.38	0.23	0.28
166	14.84	3.25	0.42	0.21	0.24	13.89	3.12	0.49	0.27	0.16
175	11.40	4.11	0.27	0.13	0.31	17.65	6.84	0.72	0.42	0.25
185	8.98	3.27	0.18	0.09	0.29	11.42	4.40	0.36	0.21	0.23
Average	13.4		0.33			13.6		0.53		
Standard Error	1.4		0.07			1.9		0.13		

Table 6.7: Middle Peak results for the Woodford shales with average indentation depths less than 400 nm. M and H values in GPa.

and $h_s = \lim_{\eta=1} H_i$ $(i = 1, 3)$, of the homogenized porous clay phase.

6.4.2 Woodford Shales - Level '0'

A similar analysis as with the GeoGenome shales applies to the Woodford shale samples, but with some important differences which arise from the unique characteristics of this set of samples. Most importantly, the presence of kerogen in the Woodford shales is considered at the scale of Level '0', as discussed in Section 6.1.2. This implies that the mechanical properties sensed by 'shallow' indents on Woodford shale do not represent an asymptotic, locally densely pack of clay particles, but a composite of clay particles and kerogen. These tests must be treated separately from the GeoGenome tests.

Table 6.7 highlights the pertinent experimental data for the Woodford shales. Figure 6-9 (top) displays the indentation moduli of the "middle peak" for each of the Woodford shales. Again, these values apparently do not scale with the clay packing density, η, but instead have generally similar "middle peak" values. As before, this similarity suggests that the tests measure the same property in each sample. For the Woodford shales, there is no apparent difference between the middle peak values for the $x1$-direction or the $x3$-direction. The average values

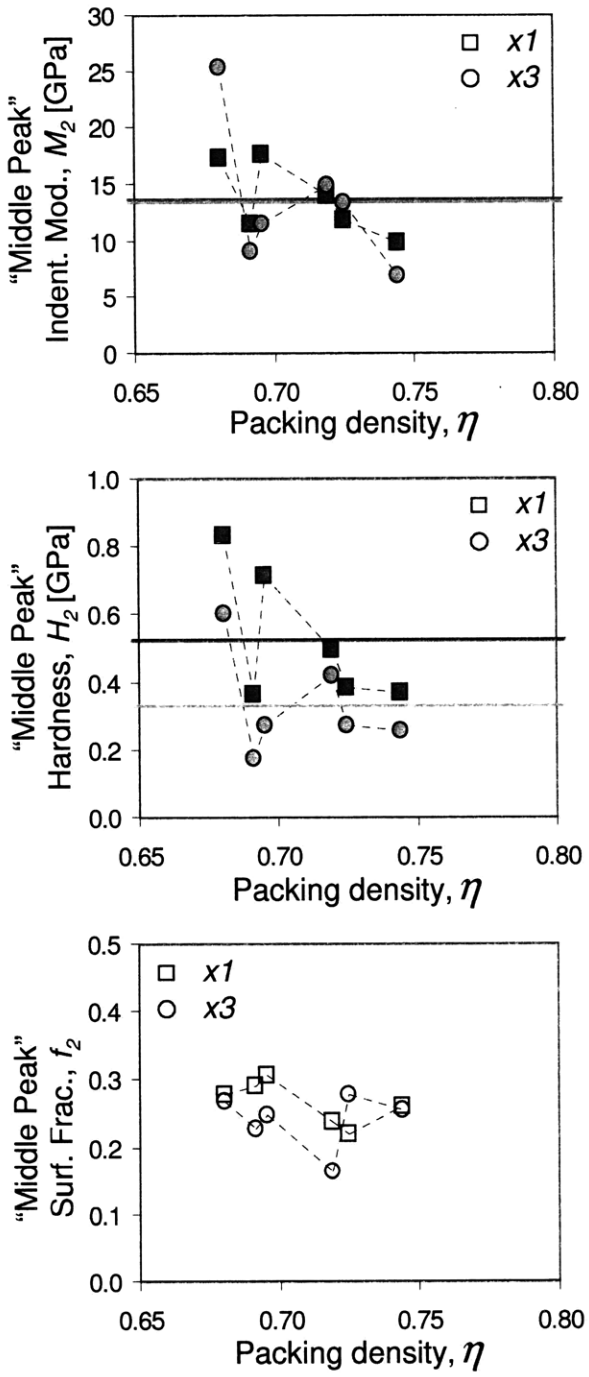

Figure 6-9: Woodford shale "middle peak" results versus clay-kerogen packing density, η. Indentation moduli, M_2 in the $x1$- and $x3$-directions (top), hardness, H_2, in the $x1$- and $x3$-directions (middle), and surface fraction of indents corresponding to the "middle peak," f_2, show no consistent trend with clay-kerogen packing density.

are:

$$m_{1,s}^{k} = 13.4 \pm 1.4 \text{ GPa} \tag{6.14a}$$

$$m_{3,s}^{k} = 13.6 \pm 1.9 \text{ GPa} \tag{6.14b}$$

with the superscript k indicating the presence of kerogen and with the uncertainty calculated as the standard error of the measured quantities. Figure 6-9 (middle) displays the hardness of the "middle peak" for the Woodford shales. Once more, there is no apparent scaling with the clay packing density. The average values are:

$$h_{1,s}^{k} = 0.33 \pm 0.07 \text{ GPa} \tag{6.15a}$$

$$h_{3,s}^{k} = 0.53 \pm 0.13 \text{ GPa} \tag{6.15b}$$

Figure 6-9 (bottom) displays the surface fractions of "middle peak" values. Unlike the GeoGenome shales, there is no apparent correlation with the overall clay packing density. It is unclear why this relationship is not apparent, but the presence of kerogen or the similarity of the Woodford shale materials may play a role. Similarly, the identification of different mean hardness values for each direction in the Woodford shale remains unexplained.

Note that the average indentation moduli for the Woodford shales are significantly lower than the values for the GeoGenome shales. This difference can be directly attributed to the presence of kerogen present in Woodford shale. The isotropic stiffness of the solid kerogen phase is documented in the literature in terms of bulk modulus, $k^k = 6.8$ GPa, and shear modulus $g^k = 3.6$ GPa [181] which gives an equivalent indentation modulus of $M^k = 9.9$ GPa. A rough estimate that averages the elastic response of kerogen with the response of the asymptotic, locally densely packed clay from the GeoGenome shales, weighted by the volume fractions of kerogen, f^k, for the Woodford shales can be calculated:

$$m_{1,s}^{k} \approx f^k M^k + \left(1 - f^k\right) M_1^{\text{no kerogen}} \tag{6.16a}$$

$$m_{3,s}^{k} \approx f^k M^k + \left(1 - f^k\right) M_3^{\text{no kerogen}} \tag{6.16b}$$

which, with $f^k \approx 0.45$ gives estimates of $m^k_{1,s} \approx 17$ GPa and $m^k_{3,s} \approx 13.8$ GPa. These estimates, particularly the one for $m^k_{3,s}$, compare very well to the experimental data. In other words, the experimental results suggest that the presence of kerogen tends to reduce the anisotropy and magnitude of elasticity at Level '0' in the Woodford shale.

6.5 First Clues About the Mechanical Microstructure and Properties of Porous Clay in Shale

The results from the statistical deconvolution analysis of grid nanoindentation results provide some first clues about the microstructure and properties of the porous clay in shale. In particular, the assumptions about porous clay behavior, presented in Sec. 5.1.2, can be addressed. These assumptions are recalled and addressed here.

6.5.1 Microstructure

It was assumed from earlier work that the porous clay in shale exhibited a percolation threshold of $\eta_0 = 0.5$. Following this assumption, recall from the discussion in Sec.5.2.1 that a combination of observations from granular physics experiments and recent results from micromechanics led to a consideration of a granular microstructure for the porous clay composite, with a perfectly disordered mechanical morphology. This morphology was represented by spheres, and modeled with the self consistent scheme to arrive at the scaling relationships for indentation moduli with packing density.

The statistical analysis of nanoindentation results, for indentation moduli and for hardness, provides clear evidence in support of a percolation threshold at $\eta_0 = 0.5$ for the porous clay in shale, as discussed in Section 6.3.3, and seen in Figure 6-5. With the percolation threshold solidified, its implications for microstructure and particle shape are also solidified. In addition, the good agreement between the scaling relationships for indentation moduli and hardness, Eqs. (5.31) and (5.90), and the experimental nanoindentation data, as seen in Figure 6-5, verifies the model assumptions of a granular microstructure with a mechanical morphology represented by spheres.

6.5.2 Mechanical Properties

It was assumed that the elastic behavior of solid clay in the porous clay composite possesses intrinsic transverse isotropy in elasticity. The statistical analysis of nanoindentation results, both from the analysis for indentations designed to assess the porous clay composite (Sec. 6.3), and from the analysis of indentations designed to assess the locally densely packed areas of porous clay (Sec. 6.4), confirm this assumption. Statistical significance testing demonstrated that differences between indentation moduli of the porous clay composite in the $x1$-direction and the $x3$-direction were statistically significant, when considering the kerogen-free shales or all of the tested shales together. The asymptotic values of indentation moduli, determined from the experimental scaling analysis of kerogen-free shales, are (Eq. (6.10)) $m_{1,s} = \lim_{\eta \to 1} M_1 = 25$ GPa and $m_{3,s} = \lim_{\eta \to 1} M_3 = 16$ GPa at a limit packing density of one. These values match well with the values (Eq. 5.30) determined by Ortega et al. [145] from back-analysis of macroscopic measurements, $m_{1,s} = 26.3$ GPa and $m_{3,s} = 14.9$ GPa. Further agreement is seen when considering the average results from nanoindentation on locally densely packed areas, with values (Eq. (6.12)) of $m_{1,s} = 21.4 \pm 2.4$ GPa and $m_{3,s} = 15.9 \pm 2.2$ GPa.

The presence of kerogen, known to be isotropic and less stiff than the clay solid in the porous clay composite, was seen to reduce both the magnitude and degree of anisotropy of the asymptotic indentation moduli, when investigating the locally densely packed areas (Eq. (6.14)). The results for indentation on the porous clay-kerogen composite for the Woodford shales, however, were still fit well by the kerogen-free scaling relations for indentation moduli, as seen in Figure 6-6 (top). The packing densities for this material are not high enough for differences resulting from the presence of kerogen to be distinguished.

Finally, it was assumed that the strength behavior is isotropic. The results from statistical deconvolution analysis of hardness measurements justify this assumption. For the nanoindentation tests designed to assess the porous clay composite, statistical signficance testing demonstrated that, on average, there was no significant difference between hardnesses measured in the $x1$-direction and hardnesses measured in the $x3$-direction. The scaling trend of mean hardness with mean packing density (Eq. (5.90)) was shown in Figure 6-5 (bottom) to fit well the hardnesses from both directions of testing on kerogen-free shales. Similar results were seen in Figure 6-6 (bottom) for the Woodford shales. The asymptotic value of hardness determined

from the experimental scaling analysis of the mean values, is (Eq. (6.11)) $h_s = \lim_{\eta \to 1} H = 0.62$ GPa. Average analysis of the hardness measured on locally densely packed areas of kerogen-free shales (Sec. 6.4) provided further confirmation of the isotropy of hardness, giving values of (Eq. (6.13)) $h_{s,1} = 0.54 \pm 0.10$ GPa and $h_{s,3} = 0.56 \pm 0.12$ GPa. The presence of kerogen slightly reduced these values for the Woodford shales (Eq. (6.15)), but as with indentation modulus, results for indentation on the porous clay-kerogen composite were still fit well by the kerogen-free scaling relation, as seen in Figure 6-6 (bottom). Dimensional analysis has shown hardness to be intimately related to strength properties (see Sec. 5.3.2), and as a result, isotropy of hardness implies isotropy of strength properties.

6.6 Chapter Summary

A massive nanoindentation campaign was performed on a wide variety of shale materials, with different mineralogies and porosities. Appropriate indentation depths for accessing the properties of the porous clay composite in shale materials were carefully chosen based on consideration of scale separability criteria. The results of these indentation tests were analyzed with the statistical deconvolution procedure to assess the mechanical properties of individual material phases. The experimental observations that these data gave in terms of scaling with mean clay packing density for each shale sample led to important insights, giving first clues to the microstructure and material invariant properties of the porous clay in shale materials. An average analysis of the nanoindention results designed to assess locally densely packed areas helped to confirm some of these clues.

A primary goal of this thesis is to assess the microstructure and material invariant properties of shale. This information can provide the link between material composition and engineering performance of shale materials. The results presented in this chapter have taken an important step towards this goal. Evidence from the mean scaling relationships, and the observed percolation threshold in particular, gives evidence in support of a granular microstructure for the porous clay in shale, with a mechanical morphology represented by a sphere. These scaling relationships, along with other evidence from nanoindentation experiments, also point towards material invariant properties, with intrinsic anisotropy of elastic properties and intrinsic isotropy

of hardness. These properties are apparently common to the solid in the porous clay phase of all shale materials, irrespective of mineral composition.

These remarkable results, however, are not enough to give a complete characterization of the porous clay composite in shale. To gain further information about the microstructure and the cohesive-frictional strength properties of the porous clay composite, the $M - H - \eta$ scaling approach is employed. The validity of this approach is bolstered by the results presented here, which confirmed the assumptions used to develop the scaling relationships for indentation modulus and hardness. The next chapter presents more remarkable results about the microstructure and material invariant properties of the porous clay in shale, based on the $M - H - \eta$ scaling approach.

	Phase 1		Phase 2		Phase 3		Phase 4	
Sample	mean	S.D.	mean	S.D.	mean	S.D.	mean	S.D.
GeoGenome Shales								
S1	2.41	1.00	4.50	1.09	13.17	5.45	40.70	21.45
S2	6.63	3.50	15.14	5.00	29.54	8.01	69.00	31.11
S3	12.78	2.90	21.72	4.62	33.60	7.26	64.62	23.18
S4	5.14	1.49	10.51	3.87	20.63	6.25	51.87	18.44
S7	11.46	3.48	18.31	2.92	28.87	5.01	66.91	22.42
Light	13.10	3.60	23.84	7.14	38.95	7.67	72.97	26.04
Dark	6.56	3.52	18.63	6.93	68.53	26.26	-	-
Pierre	1.59	0.59	3.38	1.20	9.30	4.53	46.30	7.34
L-C	1.35	0.57	3.12	1.19	9.41	3.40	29.91	13.84
Woodford Shales								
110	13.28	3.70	25.26	4.43	37.49	7.80	55.83	10.54
131	3.45	1.47	6.92	1.73	15.96	4.21	55.03	23.89
154	5.19	2.21	13.24	3.34	27.32	9.68	73.50	30.80
166	8.06	2.96	14.84	3.25	27.39	7.10	58.46	23.97
175	5.87	1.42	11.40	4.11	24.54	9.01	57.75	21.90
185	3.37	1.65	8.98	3.27	28.38	8.55	71.56	24.69

Table 6.8: Deconvolution results for Indentation Modulus for the 0.3 mN indentation tests on shale in the x1-direction. Values in GPa.

	Phase 1		Phase 2		Phase 3		Phase 4	
Sample	mean	S.D.	mean	S.D.	mean	S.D.	mean	S.D.
GeoGenome Shales								
S1	0.03	0.02	0.07	0.02	0.24	0.12	4.08	2.35
S2	0.05	0.03	0.17	0.08	0.47	0.17	3.44	1.57
S3	0.29	0.10	0.67	0.26	2.66	1.36	8.22	4.20
S4	0.05	0.02	0.16	0.08	0.55	0.31	3.40	2.27
S7	0.21	0.08	0.43	0.14	1.35	0.77	7.43	4.52
Light	0.20	0.11	0.72	0.29	2.09	0.78	8.10	3.96
Dark	0.15	0.08	0.56	0.31	9.53	5.72	-	-
Pierre	0.02	0.01	0.05	0.02	0.14	0.08	10.19	0.14
L-C	0.02	0.01	0.05	0.02	0.17	0.10	1.61	1.10
Woodford Shales								
110	0.23	0.13	0.60	0.24	1.47	0.55	3.74	1.29
131	0.10	0.06	0.25	0.10	0.78	0.43	4.76	2.70
154	0.09	0.04	0.27	0.14	1.67	0.86	4.82	1.58
166	0.13	0.07	0.42	0.21	1.26	0.61	5.38	2.57
175	0.11	0.03	0.27	0.13	1.20	0.13	5.19	2.56
185	0.05	0.03	0.18	0.09	1.46	0.80	4.60	2.08

Table 6.9: Deconvolution results for Hardness for the 0.3 mN indentation tests on shale in the x1-direction. Values in GPa.

Sample	Phase 1	Phase 2	Phase 3	Phase 4
GeoGenome Shales				
S1	0.49	0.20	0.17	0.16
S2	0.21	0.38	0.23	0.18
S3	0.20	0.32	0.22	0.26
S4	0.12	0.25	0.23	0.40
S7	0.27	0.27	0.15	0.31
Light	0.15	0.13	0.11	0.61
Dark	0.38	0.30	0.32	-
Pierre	0.27	0.39	0.29	0.05
L-C	0.34	0.25	0.20	0.21
Woodford Shales				
110	0.37	0.28	0.22	0.13
131	0.37	0.26	0.20	0.17
154	0.40	0.22	0.23	0.15
166	0.47	0.24	0.14	0.15
175	0.21	0.31	0.21	0.27
185	0.40	0.29	0.16	0.15

Table 6.10: Deconvolution results for surface fraction for the 0.3 mN indentation tests on shale in the x1-direction.

	Phase 1		Phase 2		Phase 3		Phase 4	
Sample	mean	S.D.	mean	S.D.	mean	S.D.	mean	S.D.
GeoGenome Shales								
S1	1.08	0.55	3.00	1.37	7.93	3.56	45.12	31.95
S2	10.53	3.05	17.20	3.02	28.53	8.30	66.17	26.52
S3	9.59	1.75	15.84	3.35	27.16	5.85	52.68	17.64
S4	8.00	3.13	16.81	3.75	31.89	5.03	59.66	19.42
S7	10.38	3.79	20.32	5.70	54.59	16.09	102.73	32.05
Light	6.43	3.67	21.05	9.48	49.27	18.75	95.09	19.29
Dark	2.16	1.27	7.21	3.78	34.43	7.08	77.16	14.18
Pierre	3.07	1.13	5.45	0.88	9.32	2.92	29.66	14.67
L-C	1.25	0.48	3.51	1.54	10.13	4.82	81.78	45.05
Woodford Shales								
110	8.55	3.37	17.30	5.35	34.38	4.32	66.28	15.85
131	4.68	11.73	9.84	2.77	21.51	6.93	58.25	23.27
154	5.14	2.25	11.79	4.40	23.28	7.09	69.24	32.13
166	6.00	2.31	13.89	3.12	40.85	19.43	0.63	1.05
175	7.31	3.50	17.65	6.84	40.61	16.13	81.40	24.66
185	4.05	1.57	11.42	4.40	31.32	11.48	67.95	25.15

Table 6.11: Deconvolution results for Indentation Modulus for the 0.3 mN indentation tests on shale in the x3-direction. Values in GPa.

	Phase 1		Phase 2		Phase 3		Phase 4	
Sample	mean	S.D.	mean	S.D.	mean	S.D.	mean	S.D.
GeoGenome Shales								
S1	0.01	0.01	0.05	0.02	0.23	0.12	3.47	1.93
S2	0.21	0.09	0.45	0.15	1.04	0.43	4.02	2.55
S3	0.32	0.09	0.67	0.26	1.75	0.82	5.91	2.69
S4	0.15	0.08	0.43	0.19	1.68	1.06	4.97	1.37
S7	0.22	0.13	0.74	0.38	3.75	2.02	10.33	2.52
Light	0.16	0.13	0.93	0.53	5.50	1.92	15.78	5.05
Dark	0.04	0.03	0.29	0.19	3.44	1.67	7.32	2.21
Pierre	0.03	0.01	0.06	0.02	0.18	0.10	1.24	0.79
L-C	0.01	0.01	0.05	0.03	0.28	0.14	7.96	4.59
Woodford Shales								
110	0.20	0.13	0.83	0.47	2.60	0.99	6.24	2.65
131	0.14	0.07	0.37	0.16	1.47	0.84	6.94	3.11
154	0.10	0.04	0.38	0.23	1.44	0.65	4.72	1.97
166	0.11	0.04	0.49	0.27	3.33	2.08	0.04	0.02
175	0.17	0.10	0.72	0.42	2.62	1.02	6.31	1.48
185	0.10	0.05	0.36	0.21	1.63	0.86	5.03	1.63

Table 6.12: Deconvolution results for Hardness for the 0.3 mN indentation tests on shale in the x3-direction. Values in GPa.

Sample	Phase 1	Phase 2	Phase 3	Phase 4
GeoGenome Shales				
S1	0.23	0.34	0.25	0.18
S2	0.35	0.24	0.19	0.22
S3	0.13	0.37	0.21	0.29
S4	0.34	0.27	0.13	0.26
S7	0.24	0.32	0.24	0.20
Light	0.10	0.14	0.12	0.65
Dark	0.22	0.29	0.40	0.08
Pierre	0.40	0.28	0.19	0.13
L-C	0.34	0.23	0.14	0.29
Woodford Shales				
110	0.28	0.27	0.17	0.28
131	0.44	0.25	0.19	0.11
154	0.17	0.28	0.21	0.34
166	0.34	0.16	0.19	0.31
175	0.36	0.25	0.24	0.15
185	0.32	0.23	0.24	0.21

Table 6.13: Deconvolution results for surface fraction for the 0.3 mN indentation tests on shale in the x3-direction.

	Phase 1		Phase 2		Phase 3	
Sample	mean	S.D.	mean	S.D.	mean	S.D.
GeoGenome Shales						
S1	5.54	1.69	10.57	3.33	22.97	9.07
S2	12.25	4.81	22.15	5.10	53.40	26.15
S3	21.67	5.01	32.39	5.70	63.35	20.45
S4	11.04	3.88	20.44	5.52	50.16	24.20
S7	18.28	5.36	28.81	5.17	59.45	21.49
Light	13.95	4.16	31.92	9.84	71.72	27.18
Dark	20.57	6.57	35.58	8.43	69.53	20.06
Pierre	4.50	1.24	7.91	2.18	15.55	5.46
L-C	2.82	1.24	9.71	5.23	36.99	17.58
Woodford Shales						
110	13.39	4.38	23.46	5.69	46.72	14.92
131	10.56	2.89	17.10	3.64	43.31	11.57
154	9.53	2.92	17.29	4.94	48.35	23.24
166	8.64	3.31	17.67	5.72	48.92	23.35
175	11.68	3.82	20.63	5.14	42.64	16.87
185	7.54	2.57	16.06	5.95	41.91	19.90

Table 6.14: Deconvolution results for Indentation Modulus for the 4.8 mN indentation tests on shale in the x1-direction. Values in GPa.

	Phase 1		Phase 2		Phase 3	
Sample	mean	S.D.	mean	S.D.	mean	S.D.
GeoGenome Shales						
S1	0.04	0.02	0.11	0.04	0.63	0.33
S2	0.13	0.09	0.54	0.23	4.58	2.30
S3	0.52	0.18	1.23	0.50	7.34	3.78
S4	0.16	0.08	0.64	0.35	4.86	2.87
S7	0.35	0.15	1.04	0.49	5.55	3.16
Light	0.28	0.15	1.28	0.77	7.91	4.12
Dark	0.34	0.19	1.61	0.75	7.82	4.11
Pierre	0.04	0.01	0.10	0.04	0.49	0.26
L-C	0.03	0.01	0.16	0.08	3.25	1.71
Woodford Shales						
110	0.41	0.23	1.39	0.60	4.59	2.04
131	0.31	0.12	0.67	0.24	4.02	1.58
154	0.19	0.08	0.77	0.39	4.71	2.82
166	0.13	0.08	0.58	0.25	4.04	2.35
175	0.27	0.10	0.77	0.34	3.95	2.32
185	0.11	0.05	0.48	0.31	3.00	1.46

Table 6.15: Deconvolution results for Hardness for the 4.8 mN indentation tests on shale in the x1-direction. Values in GPa.

Sample	Phase 1	Phase 2	Phase 3
GeoGenome Shales			
S1	0.52	0.34	0.14
S2	0.61	0.26	0.14
S3	0.59	0.27	0.14
S4	0.48	0.26	0.26
S7	0.62	0.21	0.18
Light	0.17	0.19	0.64
Dark	0.52	0.24	0.23
Pierre	0.47	0.35	0.17
L-C	0.63	0.22	0.15
Woodford Shales			
110	0.54	0.28	0.18
131	0.49	0.26	0.24
154	0.39	0.34	0.26
166	0.50	0.28	0.22
175	0.40	0.35	0.25
185	0.44	0.33	0.23

Table 6.16: Deconvolution results for surface fraction for the 4.8 mN indentation tests on shale in the x1-direction.

	Phase 1		Phase 2		Phase 3	
Sample	mean	S.D.	mean	S.D.	mean	S.D.
GeoGenome Shales						
S1	4.65	1.93	9.68	2.53	45.79	33.23
S2	11.77	3.17	23.36	6.75	60.75	23.16
S3	13.67	2.62	20.43	4.14	41.95	16.80
S4	9.73	3.12	18.52	5.68	56.68	32.49
S7	13.87	3.87	25.52	6.79	66.04	33.73
Light	17.42	6.81	48.39	12.71	97.80	18.89
Dark	10.95	4.23	24.50	9.20	78.12	24.32
Pierre	4.74	1.45	8.41	2.23	23.02	5.67
L-C	2.21	0.84	4.72	1.55	11.98	5.71
Woodford Shales						
110	7.15	2.19	12.63	3.29	42.30	20.85
131	8.02	1.95	13.95	2.79	35.51	16.33
154	11.82	3.05	21.76	6.40	52.41	22.04
166	8.82	3.25	22.86	10.78	55.74	22.11
175	9.37	2.71	17.04	4.96	39.98	17.98
185	7.42	2.67	16.08	5.70	46.45	24.05

Table 6.17: Deconvolution results for Indentation Modulus for the 4.8 mN indentation tests on shale in the x3-direction. Values in GPa.

	Phase 1		Phase 2		Phase 3	
Sample	mean	S.D.	mean	S.D.	mean	S.D.
GeoGenome Shales						
S1	0.07	0.04	0.25	0.11	0.51	0.11
S2	0.34	0.11	0.84	0.44	5.56	3.02
S3	0.45	0.14	0.94	0.36	5.04	2.72
S4	0.15	0.08	0.48	0.23	5.95	3.91
S7	0.33	0.14	0.84	0.37	7.02	4.10
Light	0.56	0.40	4.49	2.72	12.81	2.63
Dark	0.15	0.09	0.75	0.45	10.25	4.38
Pierre	0.03	0.01	0.07	0.03	3.71	1.01
L-C	0.02	0.01	0.06	0.03	0.33	0.18
Woodford Shales						
110	0.17	0.08	0.54	0.24	3.92	2.34
131	0.30	0.08	0.72	0.34	3.97	2.67
154	0.35	0.14	1.17	0.55	5.43	3.06
166	0.16	0.11	1.27	0.75	5.95	2.95
175	0.24	0.08	0.72	0.36	3.50	1.80
185	0.18	0.07	0.65	0.33	4.19	2.70

Table 6.18: Deconvolution results for Hardness for the 4.8 mN indentation tests on shale in the x3-direction. Values in GPa.

Sample	Phase 1	Phase 2	Phase 3
GeoGenome Shales			
S1	0.72	0.26	0.02
S2	0.54	0.29	0.17
S3	0.52	0.32	0.16
S4	0.43	0.34	0.23
S7	0.53	0.24	0.22
Light	0.22	0.20	0.57
Dark	0.39	0.32	0.29
Pierre	0.49	0.42	0.09
L-C	0.45	0.33	0.21
Woodford Shales			
110	0.45	0.34	0.21
131	0.42	0.30	0.28
154	0.39	0.33	0.28
166	0.45	0.26	0.29
175	0.34	0.38	0.28
185	0.30	0.23	0.48

Table 6.19: Deconvolution results for surface fraction for the 4.8 mN indentation tests on shale in the x3-direction.

	Phase 1		Phase 2		Phase 3	
Sample	mean	S.D.	mean	S.D.	mean	S.D.
Boston Blue Clay						
4 MPa	0.76	0.38	2.07	0.91	30.15	16.79
6.5 MPa	1.69	0.43	2.88	0.76	5.52	1.18
10 MPa	2.02	0.81	4.28	1.44	15.31	6.73

Table 6.20: Deconvolution results for Indentation Modulus for the 1.2 mN indentation tests on Boston Blue Clay in the x1-direction. Values in GPa.

	Phase 1		Phase 2		Phase 3	
Sample	mean	S.D.	mean	S.D.	mean	S.D.
Boston Blue Clay						
4 MPa	0.002	0.002	0.012	0.007	1.18	0.64
6.5 MPa	0.01	0.004	0.03	0.01	0.09	0.04
10 MPa	0.01	0.006	0.04	0.02	0.26	0.14

Table 6.21: Deconvolution results for Hardness for the 1.2 mN indentation tests on Boston Blue Clay in the x1-direction. Values in GPa.

Sample	Phase 1	Phase 2	Phase 3
Boston Blue Clay			
4 MPa	0.48	0.37	0.15
6.5 MPa	0.49	0.38	0.13
10 MPa	0.62	0.27	0.11

Table 6.22: Deconvolution results for surface fraction for the 1.2 mN indentation tests on Boston Blue Clay in the x1-direction.

	Phase 1		Phase 2		Phase 3	
Sample	mean	S.D.	mean	S.D.	mean	S.D.
Boston Blue Clay						
4 MPa	0.59	0.13	1.01	0.12	n.a.	n.a.
6.5 MPa	0.70	0.24	1.36	0.11	2.15	0.34
10 MPa	0.58	0.16	1.01	0.10	n.a.	n.a.

Table 6.23: Deconvolution results for Indentation Modulus for the 1.2 mN indentation tests on Boston Blue Clay in the x3-direction. Values in GPa.

	Phase 1		Phase 2		Phase 3	
Sample	mean	S.D.	mean	S.D.	mean	S.D.
Boston Blue Clay						
4 MPa	0.004	0.001	0.45	0.01	n.a.	n.a.
6.5 MPa	0.006	0.003	5.19	0.97	7.15	0.50
10 MPa	0.003	0.001	0.63	0.12	n.a.	n.a.

Table 6.24: Deconvolution results for Hardness for the 1.2 mN indentation tests on Boston Blue Clay in the x3-direction. Values in GPa.

Sample	Phase 1	Phase 2	Phase 3
Boston Blue Clay			
4 MPa	0.90	0.10	n.a.
6.5 MPa	0.89	0.07	0.04
10 MPa	0.91	0.09	n.a.

Table 6.25: Deconvolution results for surface fraction for the 1.2 mN indentation tests on Boston Blue Clay in the x3-direction.

Chapter 7

Assessing Microstructure and Strength Properties of Porous Clay: Nanoindentation Scaling Analysis

The experimental results in a statistical analysis, presented in the previous chapter, confirm that the measured properties scale with the clay packing density as a first order parameter. These results provided first clues to the microstructure of the porous clay in shale and to material invariant mechanical properties, including elasticity and indentation hardness. These clues helped to confirm the assumptions used to develop the scaling relationships for indentation moduli and indentation hardess, presented in Chapter 5. With these assumptions verified, this chapter employs the $M-H-\eta$ scaling approach for each tested shale sample to gain further information from each of the nanoindentation experiments that tested the porous clay.

While the results from the statistical analysis presented in the previous chapter were extremely useful, they take the results of a large number of indentation tests as input, and give the mechanical phase properties as output. The $M-H-\eta$ scaling approach is designed to go beyond the statistical analysis approach and make use of the results of each nanoindentation test on a porous composite, i.e. the porous clay composite in the case of shale materials. The results of the $M-H-\eta$ scaling approach are two-fold. Presented and discussed first is the microstructural information given in the form of local estimates of packing density. Subsequent

sections are devoted to the investigation of cohesive-frictional strength properties of the solid in the porous clay composite, at Level '0' in the multiscale model for the structure of shale. These properties have never been assessed until now, and the results are remarkable.

7.1 Scaling Results and Packing Density Distributions

The implementation of the $M-H-\eta$ scaling approach, developed in conjunction with Gathier [77], was reviewed in Section 5.4.2. The basic idea of the approach, which works with the indentation moduli $M_{(\beta),i}$ and indentation hardness H_i that represent the homogenized (Level '1') response of the porous materials (pores and Level '0'), is summarized. Micromechanics yields the scaling relations, Eqs. (5.33) and (5.90):

$$M_{(\beta),i} = m_{(\beta),s} \times \Pi_M(\eta_i) \tag{7.1a}$$

$$H_i = c_s \times \Pi_H(\alpha_s, \eta_i) \tag{7.1b}$$

In an inverse application where indentation testing in both directions is considered at the same time, the unknowns of the problem are the properties of the solid phase, $m_{s,1}$, $m_{s,3}$, c_s, and α_s, as well as the local packing densities, η_i. Recall from Section 5.4.2 that the procedure implemented in MATLAB uses a testing approach to develop the best fit for α_s for each shale sample, followed by the best fit for c_s and then the local packing densities, η_i.

7.1.1 Nanoindentation Scaling Analysis Assumptions

Recall the list of assumptions used to generate the scaling relationships, as first presented in Section 5.1.2:

- The porous clay composite has a granular microstructure with a spherical representation of the mechanical morphology, as evidenced by a percolation threshold of $\eta_0 = 0.5$.
- The solid particle in the porous clay composite has intrinsic anisotropy of elastic properties, with $m_{1,s} = 26$ GPa and $m_{3,s} = 17$ GPa fixed for the purposes of implementing the $M-H-\eta$ scaling approach, as discussed in Sec. 5.4.2.

- The solid particle in the porous clay composite is isotropic in strength, with cohesive-frictional strength parameters.

The results presented in Chapter 6 and summarized for this hypothesis testing in Section 6.5 have provided additional evidence in support of each of these assumptions. A successful implementation of the $M-H-\eta$ scaling approach will provide additional evidence in support of these assumptions.

7.1.2 Scaling Results

The inverse approach was applied to each tested shale sample, and a first set of outputs, the scaling results for all the shale samples, are provided in Figures 7-1 through 7-6. Shown are plots of indentation modulus, M, and indentation hardness, H, versus the local clay packing density associated with each individual indentation test in each shale. In general, the experimental points are randomly distributed on both sides of the model curves, and fit well, justifying the scaling models. In particular, the models feature anisotropic behavior in elasticity (indentation modulus), but isotropic behavior in strength (hardness).

Table 7.1 presents an analysis of the mean and standard deviation of the normalized error, calculated similar to the definition of error used in the fitting procedure, Eq. (5.96):

$$s_i = \frac{X_{i,\text{exp}} - X_i\left(\eta_i, \text{solid properties}\right)}{x_0} \tag{7.2}$$

where $X = M_1, M_3$ and H, $X_i\left(\eta_i, \text{solid properties}\right)$ are the predictions from the scaling relationships (Eqs. (5.33) and (5.90)), and x_0 is the normalization factor, i.e. $m_{1,s}$, $m_{3,s}$ or h_s. The notation $\overline{s}$ stands for the mean normalized error, quantifying how well the data correspond to the scaling relationships, while the notation s_d stands for the standard deviation of the normalized errors, and quantifies the dispersion of the experimental data around the scaling relationships. The low overall errors testify to the excellent correspondence between the experimental data, the fitted packing densities, and the scaling relationships.

Some of the shale samples deserve specific comment. Note that only a few tests for the Light and Dark shales (Fig. 7-3) are taken to be associated with the porous clay phase. Recall from Table 2.6 that these samples have high inclusion volume fractions. The $M-H-\eta$ scaling

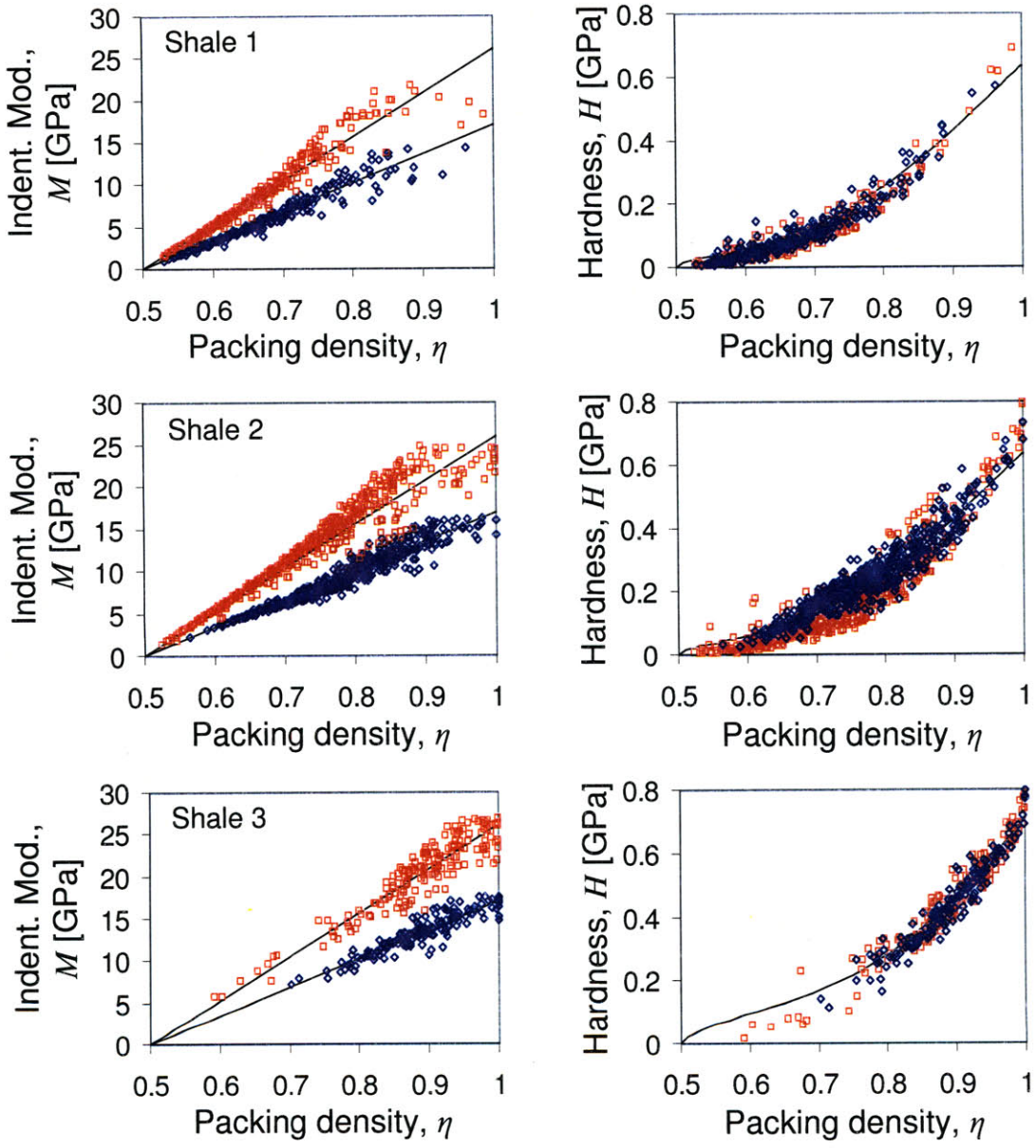

Figure 7-1: Scaling of individual nanoindentation test results for Shale 1, Shale 2, and Shale 3. Results for indentation modulus (left) and hardness (right) are from testing in the $x1$-direction (red squares) and the $x3$-direction (blue diamonds).

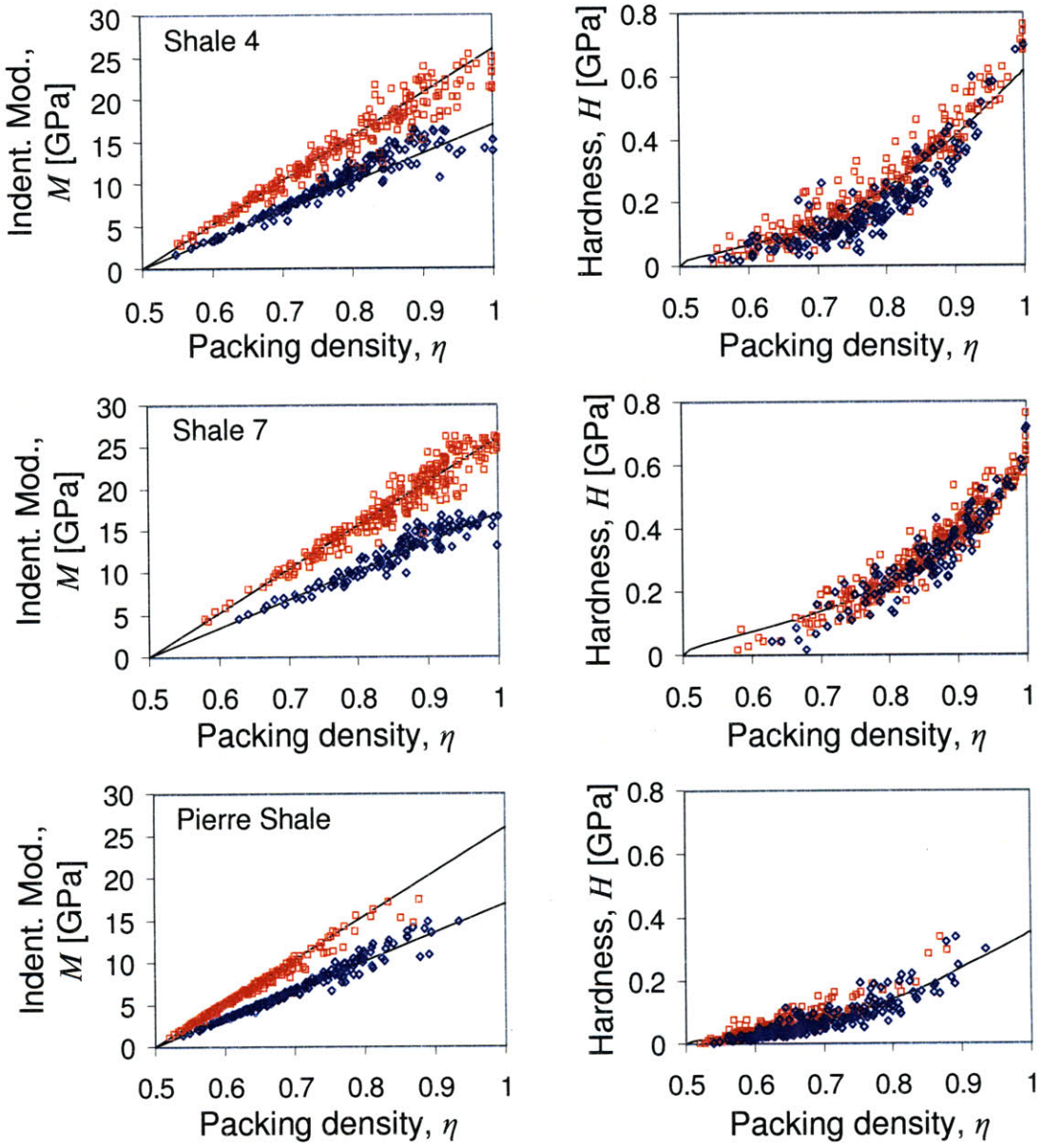

Figure 7-2: Scaling of individual nanoindentation test results for Shale 4, Shale 7, and Pierre Shale.

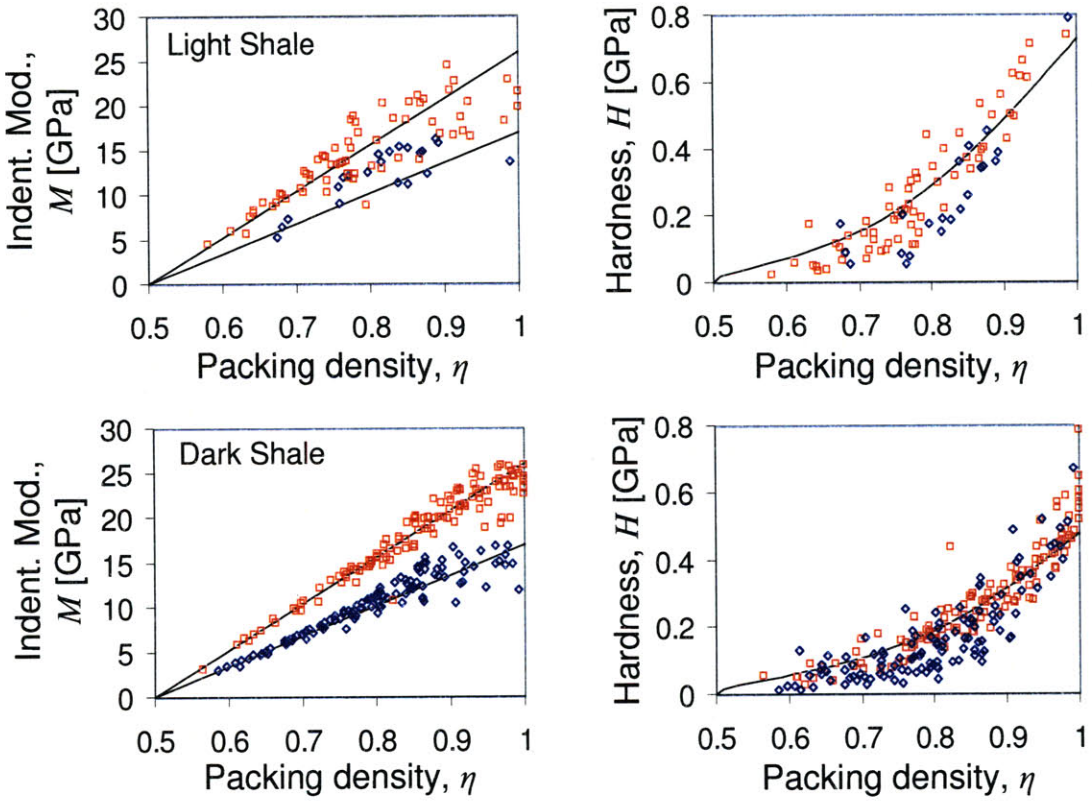

Figure 7-3: Scaling of individual nanoindentation test results for Light Shale and Dark Shale.

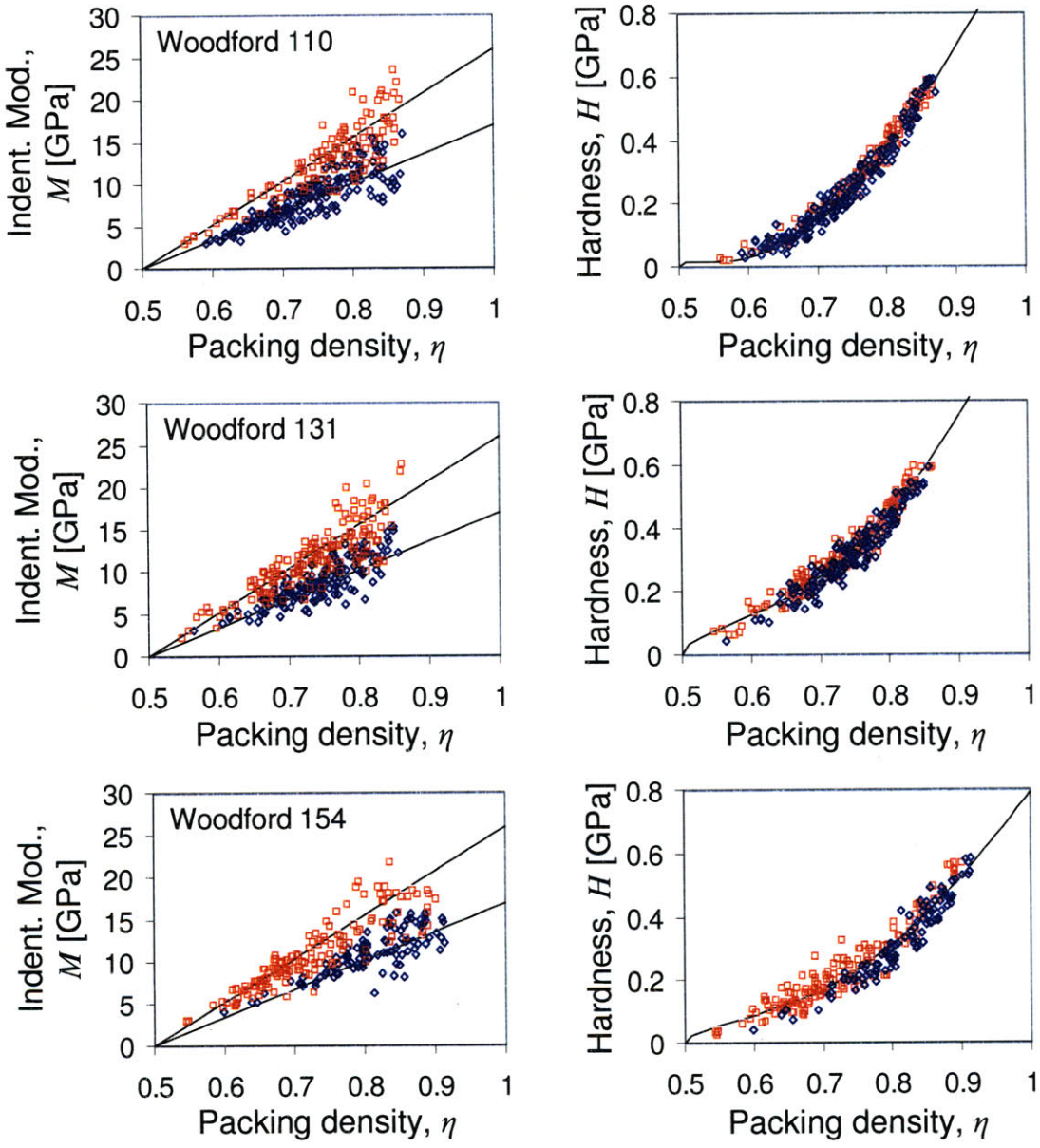

Figure 7-4: Scaling of individual nanoindentation test results for Woodford 110, Woodford 131, and Woodford 154.

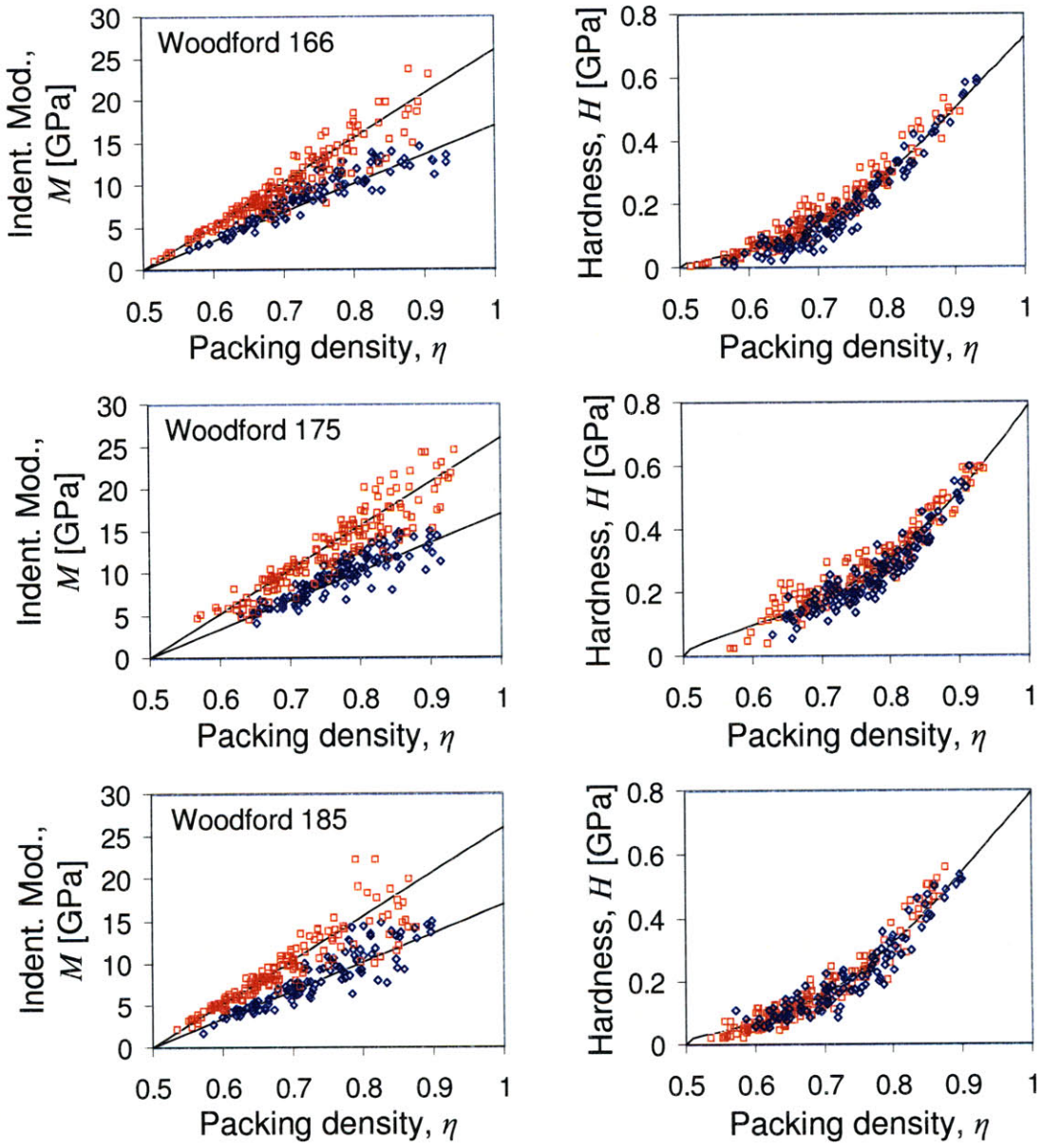

Figure 7-5: Scaling of individual nanoindentation test results for Woodford 166, Woodford 175, and Woodford 185.

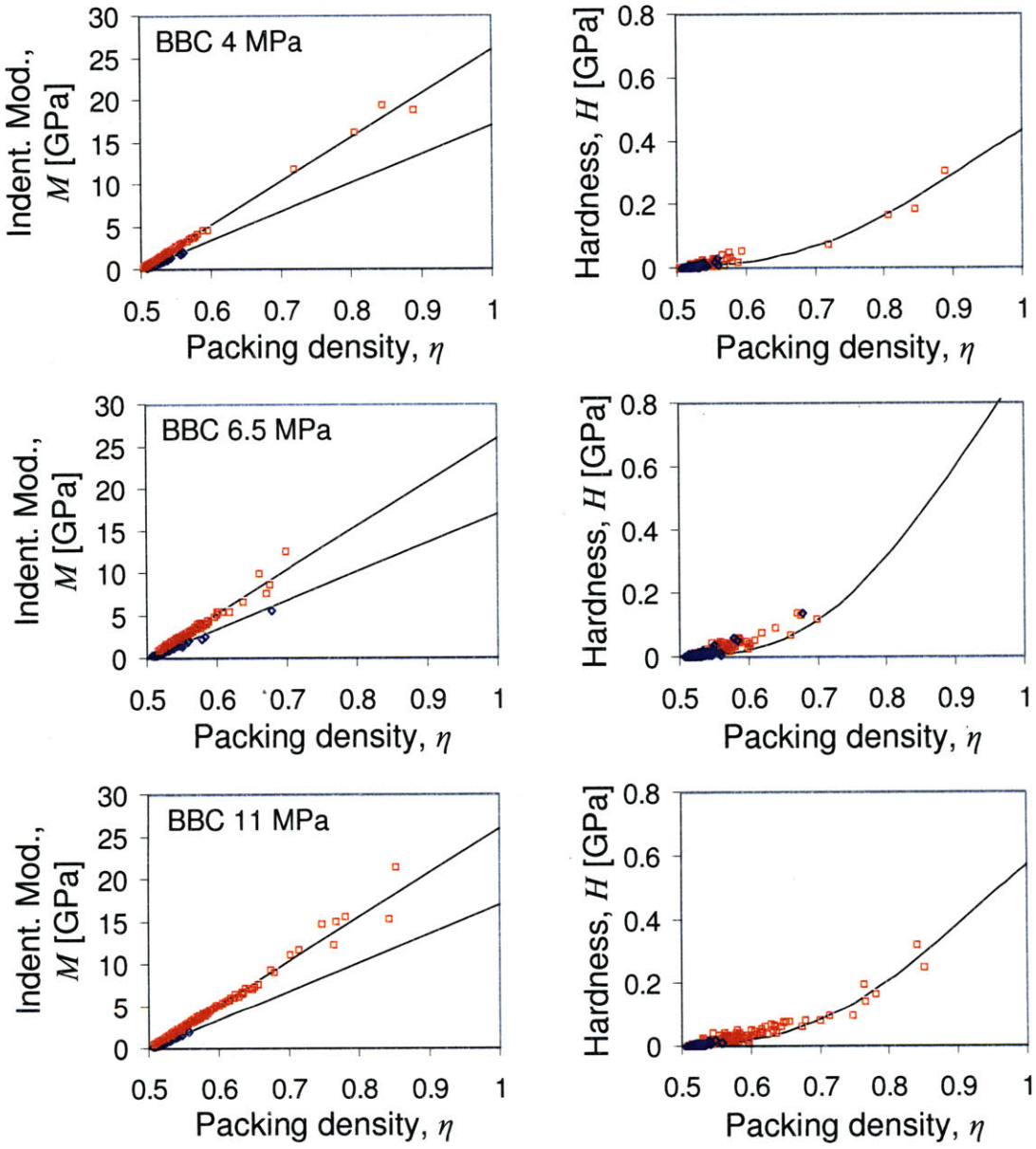

Figure 7-6: Scaling of individual nanoindentation test results for Boston Blue Clay 4 MPa, Boston Blue Clay 6.5MPa, and Boston Blue Clay 11 MPa.

Shale	M_1 and M_3		H	
	$\overline{s}$	s_d	$\overline{s}$	s_d
GeoGenome Shales				
S1	-0.05	4.0	-0.6	3.7
S2	-0.2	5.5	0.5	7.8
S3	-0.9	5.7	0.8	6.7
S4	-0.7	6.3	1.5	9.8
S7	-0.5	6.0	0.9	8.4
Light	-1.4	11.6	2.7	13.4
Dark	-0.8	6.4	2.0	11.0
Woodford Shales				
110	-0.1	8.8	-2.3	4.4
131	0.0	8.6	0.8	5.2
154	-0.1	9.0	0.1	6.4
166	-0.1	5.5	0.4	5.5
175	-0.1	7.9	0.6	6.4
185	-0.1	7.7	0.2	5.7
Boston Blue Clay				
4 MPa	0.0	0.4	0.6	3.2
6.5 MPa	-0.1	0.7	-0.2	2.2
10 MPa	0.0	0.9	0.2	1.7

Table 7.1: Study of the mean and standard deviation of the relative normalized error, calculated by Eq. (7.2), for each of the analyzed shales. Values are in %.

approach is expected to be less robust for these samples, with fewer data points. The Boston Blue Clay samples (Fig. 7-6) also have interesting scaling behavior. In these samples, nearly all of the indentation tests measured very low indentation moduli and hardness. Interestingly, the indentation tests in the $x1$-direction seem to have much greater variability than the indentation tests in the $x3$-direction.

7.1.3 Packing Density Distributions

The local packing densities associated with each individual indentation test can be summarized as statistical distributions of packing density. The results for all the tested shale samples are presented in Figures 7-7 through 7-12, which display frequency plots (both PDFs and CDFs) of packing densities in both the $x1$-direction and the $x3$-direction. Because the indentation tests have already been selected to correspond to indentation on the porous clay phase (Sec. 5.4.2), there is no need for deconvolution. Instead, mean values and standard deviations may be calculated directly from the vector of fitted η_i values. The model lines in Figures 7-7 through 7-12 are Gaussian distributions characterized by these means and standard deviations of the experimental packing densities. The good fit of the Gaussian distributions suggests that the different packing densities are randomly distributed around the mean packing density. The large range of possible packing densities, even after the considered tests were selected to be representative of the porous clay phase only, demonstrates the highly heterogeneous nature of the porous clay phase in shales.

The packing density distributions obtained from the $M - H - \eta$ scaling relationships are roughly Gaussian, and the distributions from each direction of indentation testing tend to overlap. Again, some samples are deserving of individual comments. The small number of porous clay indentation tests for the Light Shale and Dark shale become more apparent in the packing density distributions (Fig. 7-9). For two of the Woodford shales, the packing density distributions do not overlap (Woodford 110 and 154 in Fig. 7-10). However, the difference is not consistent. In one case, the packing densities in the $x1$-direction are higher than the packing densities in the $x3$-direction, while in the other case, packing densities in the $x3$-direction are higher. Finally, the overlap for the Boston Blue Clay samples is not as robust as for the other samples (Fig. 7-12), although the difference apparently lies more in the overall variation of

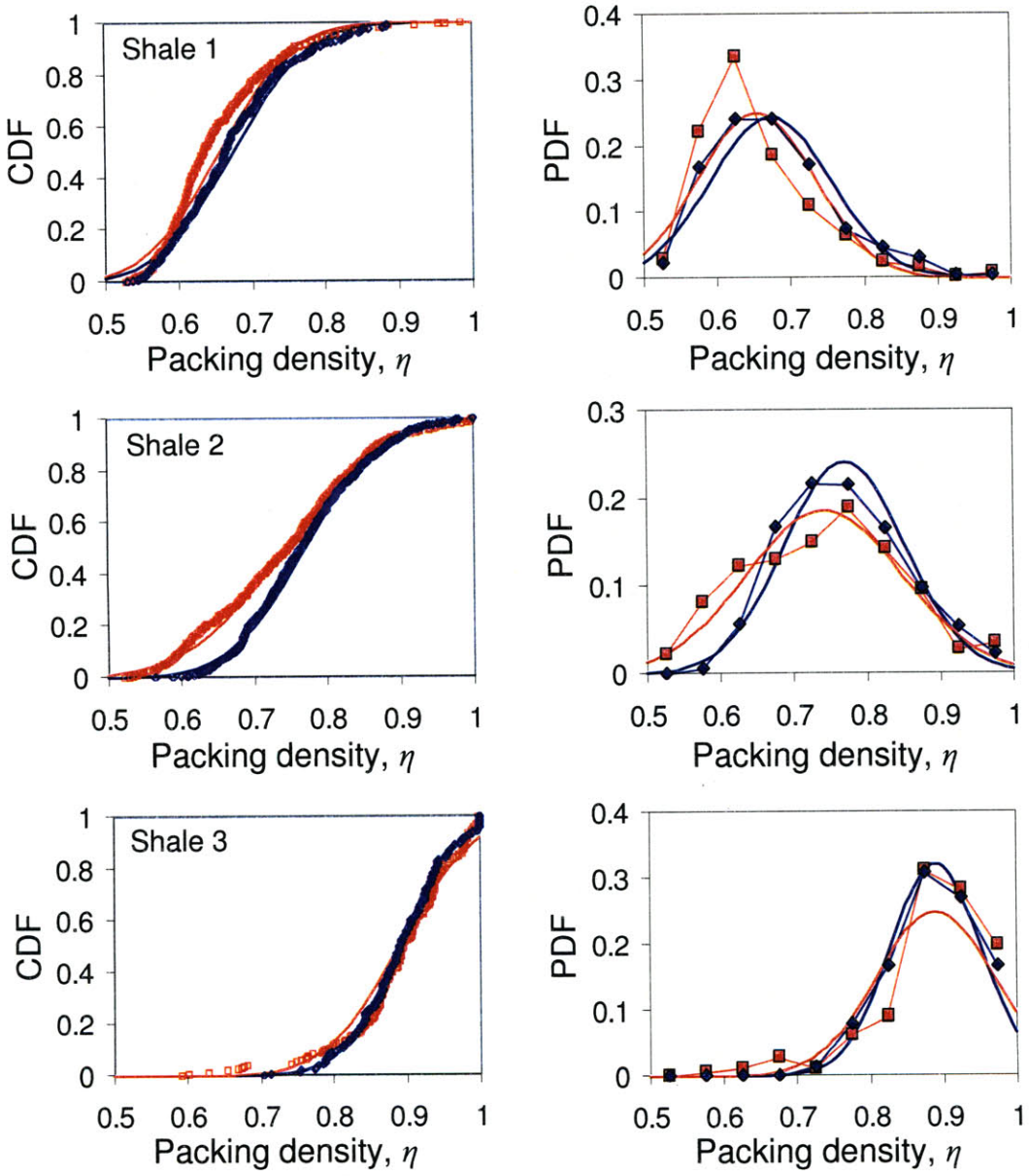

Figure 7-7: Packing density distributions for Shale 1, Shale 2, and Shale 3, derived from indentation in the x1-direction (red squares) and the x3-direction (blue diamonds). The CDF is plotted on the left, and the PDF on the right.

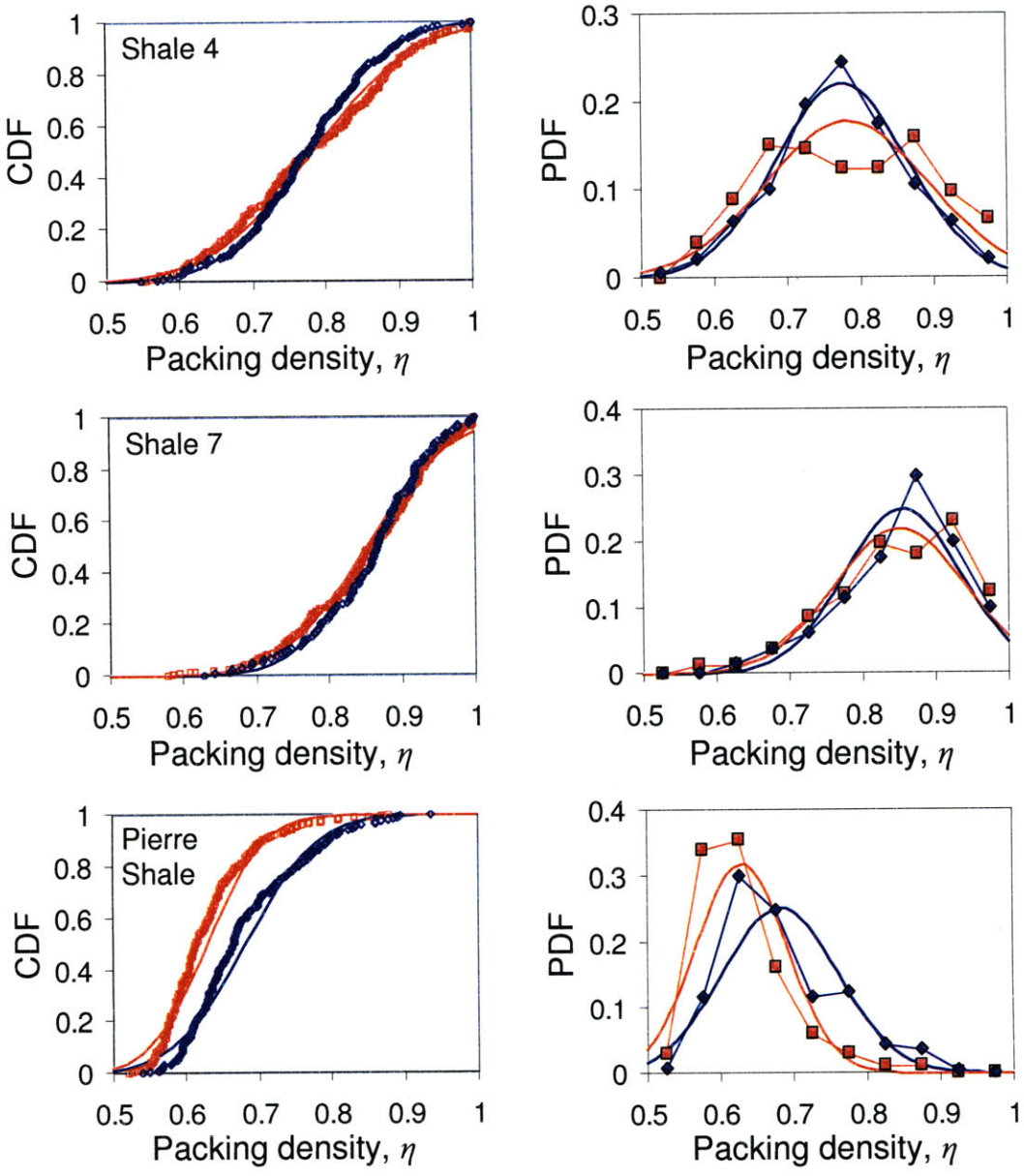

Figure 7-8: Packing density distributions for Shale 4, Shale 7, and Pierre Shale.

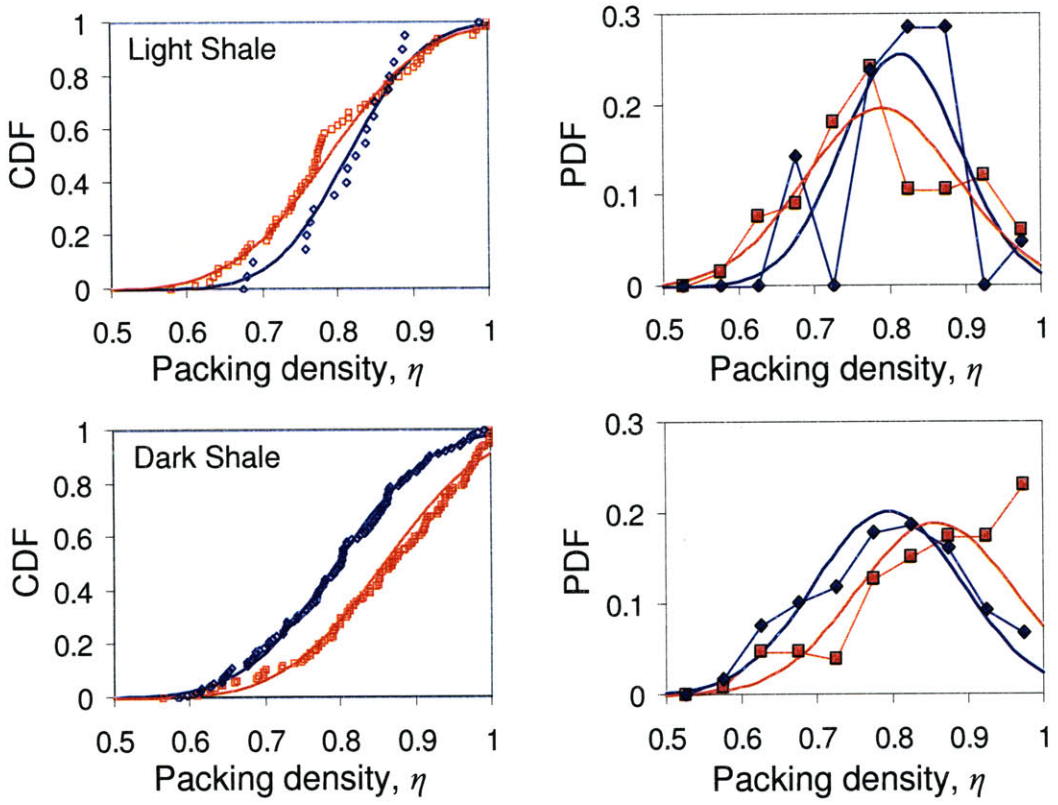

Figure 7-9: Packing density distributions for Light Shale and Dark Shale.

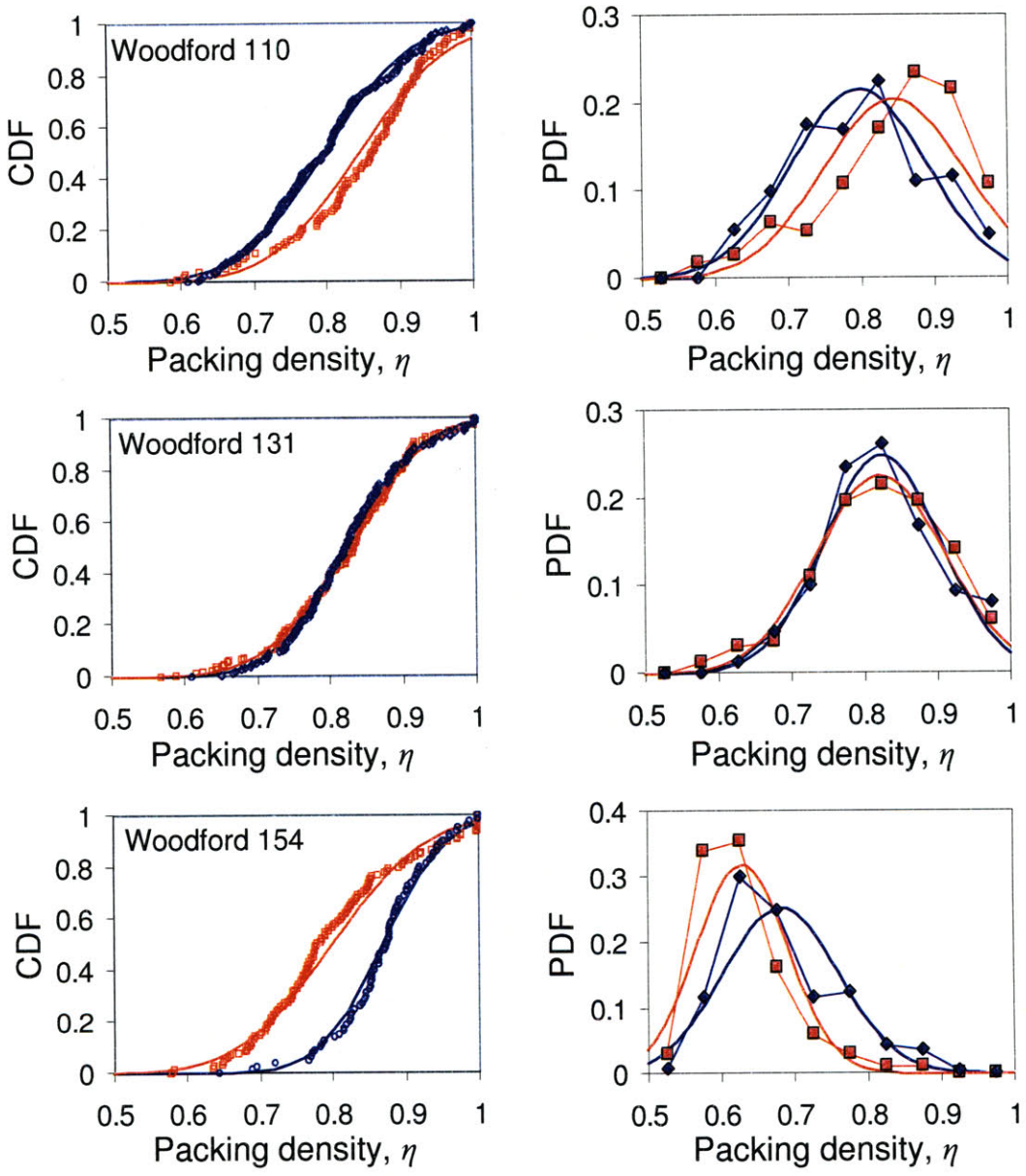

Figure 7-10: Packing density distributions for Woodford 110, Woodford 131, and Woodford 154.

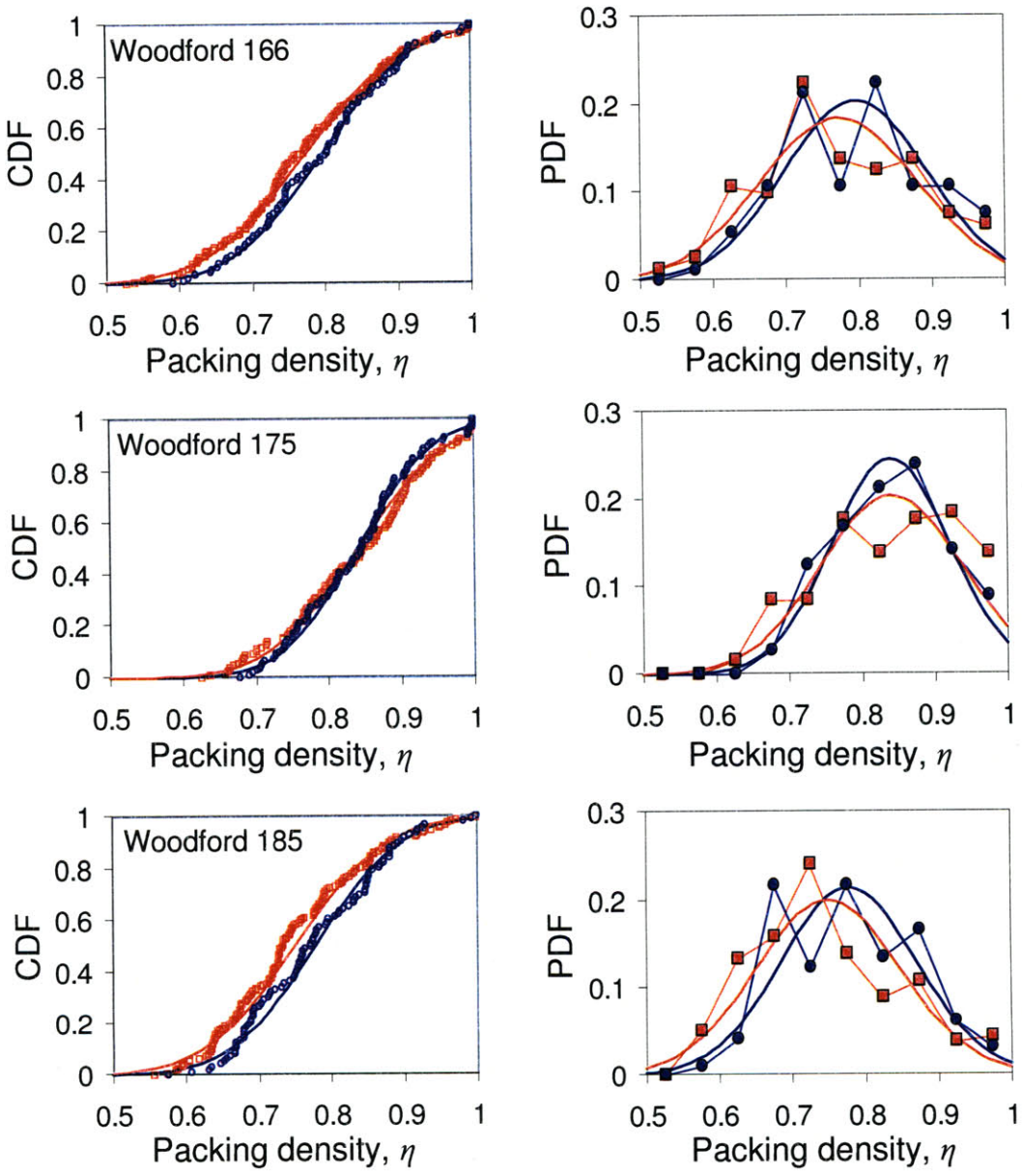

Figure 7-11: Packing density distributions for Woodford 166, Woodford 175, and Woodford 185.

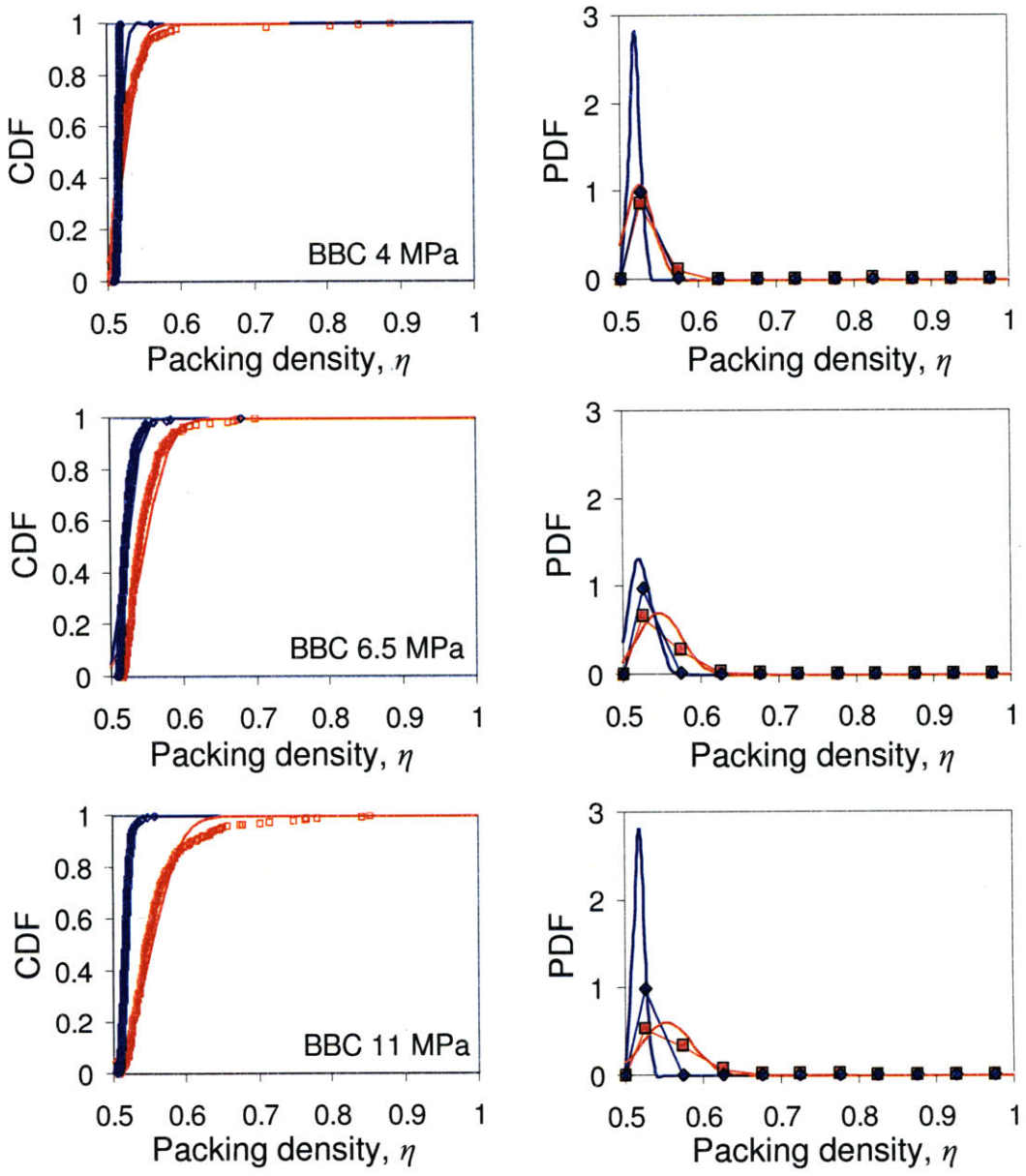

Figure 7-12: Packing density distributions for Boston Blue Clay 4 MPa, Boston Blue Clay 6.5MPa, and Boston Blue Clay 11 MPa.

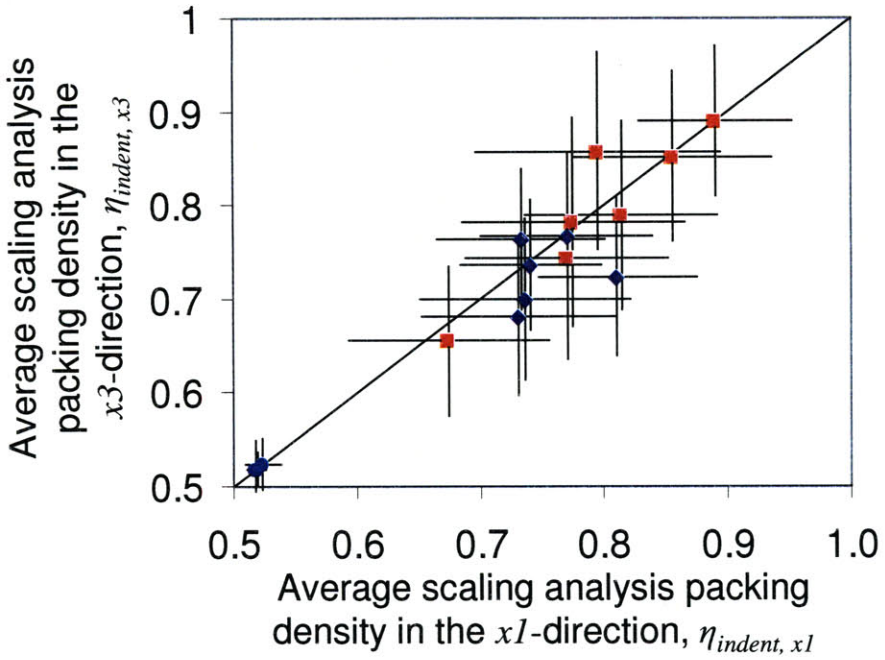

Figure 7-13: Comparison of average packing densities obtained from the $M-H-\eta$ analysis for indentation results in the $x1$-direction and the $x3$-direction. The error bars represent plus and minus one standard deviation. The values tend to agree in each direction ($r^2 = 0.90$), verifying the assumption of spherical mechanical morphology in the scaling models.

measured properties rather than the mean values. Packing densities have a slightly larger spread in the $x1$-direction than the $x3$-direction, although it is unclear why this is the case.

Table 7.2 summarizes the mean and standard deviation of packing densities estimated from each direction of testing for each tested shale, as well as an overall mean and standard deviation for each shale (with data from both directions of testing). The notation $\eta_{\text{indent, x1}}$ refers to a packing density obtained from the $M-H-\eta$ scaling approach for an indentation in the $x1$-direction, while the notation $\eta_{\text{indent, x3}}$ is similar except that it refers to a packing density associated with an indentation in the $x3$-direction. The notation $\overline{\eta}_{\text{indent}}$ without reference to an indentation direction refers to the average packing density when tests in both directions are considered together. For comparison, the table also recalls the packing density calculated from mineralogy (Tab. 2.6).

The packing density distributions derived from each indentation direction overlap, suggest-

Shale	$\eta_{\text{indent, x1}}$		$\eta_{\text{indent, x3}}$		$\overline{\eta}_{\text{indent}}$		$\overline{\eta}_{\text{mineral}}$	
	mean	s.d.	mean	s.d.	mean	s.d.	mean	+/-
GeoGenome Shales								
S1	0.674	0.081	0.655	0.079	0.666	0.010	0.668	0.021
S2	0.770	0.082	0.743	0.107	0.760	0.012	0.804	0.022
S3	0.890	0.062	0.890	0.080	0.871	0.010	0.896	0.001
S4	0.775	0.090	0.782	0.111	0.771	0.012	0.691	0.016
S7	0.856	0.080	0.852	0.091	0.854	0.013	0.875	0.022
Light	0.814	0.078	0.789	0.101	0.805	0.014	0.783	0.036
Dark	0.795	0.099	0.858	0.105	0.824	0.011	0.847	0.057
Woodford Shales								
110	0.733	0.068	0.763	0.075	0.745	0.014	0.680	0.050
131	0.741	0.057	0.736	0.069	0.742	0.014	0.744	0.044
154	0.811	0.064	0.724	0.084	0.761	0.015	0.721	0.080
166	0.736	0.085	0.699	0.086	0.716	0.014	0.719	0.035
175	0.770	0.069	0.767	0.089	0.771	0.015	0.695	0.001
185	0.731	0.079	0.681	0.084	0.707	0.009	0.691	0.076
Boston Blue Clay								
4 MPa	0.519	0.007	0.525	0.018	0.524	0.013	0.536	0.010
6.5 MPa	0.524	0.015	0.548	0.028	0.535	0.025	0.561	0.010
10 MPa	0.518	0.007	0.554	0.032	0.538	0.029	0.582	0.010

Table 7.2: Packing density and volume fraction information from indentation and from mineralogy for each tested shale. Included is the packing density from analysis of indentation tests in the x1-direction, the packing density from analysis of indentation tests in the x3-direction, and the packing density from analysis of indentation tests in both directions. Also included is the average packing density calculated from mineralogy and porosity, the average inclusion volume fraction calculated from mineralogy and porosity, and the average porosity calculated from mercury intrusion porosimetry and bulk density information. For packing densities from indentation, the standard deviation (s.d.) is that of the distribution of packing densities. For mineralogy data, the variation (+/-) is a result of various methods of assessing porosity, as presented in Tab. 2.6 and calculated by Eq. 2.22.

ing that the microstructure is similar for indentation results in both directions. Figure 7-13 displays this graphically, comparing the mean values $\overline{\eta}_{\text{indent, x1}}$ with $\overline{\eta}_{\text{indent, x3}}$. The observation that packing density distributions do not show a difference in directions (the coefficient of determination, $r^2 = 0.90$) supports the assumption of an isotropic, spherical representation of mechanical morphology, coinciding with random orientations of contact surfaces. Moreover, the mean packing density values obtained from the $M-H-\eta$ scaling approach compare well to the mean packing density values obtained from nanoindentation. This observation is explored in more detail in the next subsection.

7.1.4 Validation with Mean Packing Density

Comparison of the overall mean of estimated packing densities with the average packing densities derived from mineralogy provides a means to validate the $M-H-\eta$ scaling approach and check the consistency of its results. Figure 7-14 compares the results of estimating packing density by two vastly different techniques, nanoindentation and mineralogy. The results are well correlated, with a coefficient of determination, $r^2 = 0.81$. This internal consistency provides another validation for the model assumptions employed in the $M-H-\eta$ scaling analysis.

Note also that there is no apparent trend in the difference between techniques of measuring average packing density. If, for example, indentation analysis predicted a higher packing density than mineralogy for relatively low packing densities, a compaction or consolidation effect (recall that indentation modulus and indentation hardness are calculated at the peak load and peak depth of the indentation test) might be to blame. The experimental observations, however, do not support this argument.

7.1.5 Link with Porosimetry

Researchers working with porous materials have long been interested in understanding the structure of the pore space in porous materials. As discussed in Section 2.3.4, porosimetry, the measurement of pore sizes, is a specific focus of research. Despite the many limitations of the technique, mercury intrusion porosimetry is still widely used, in large part because of the lack of convenient, robust alternatives. For similarly structured geomaterials, comparisons between pore-size distributions can still be reliable [151].

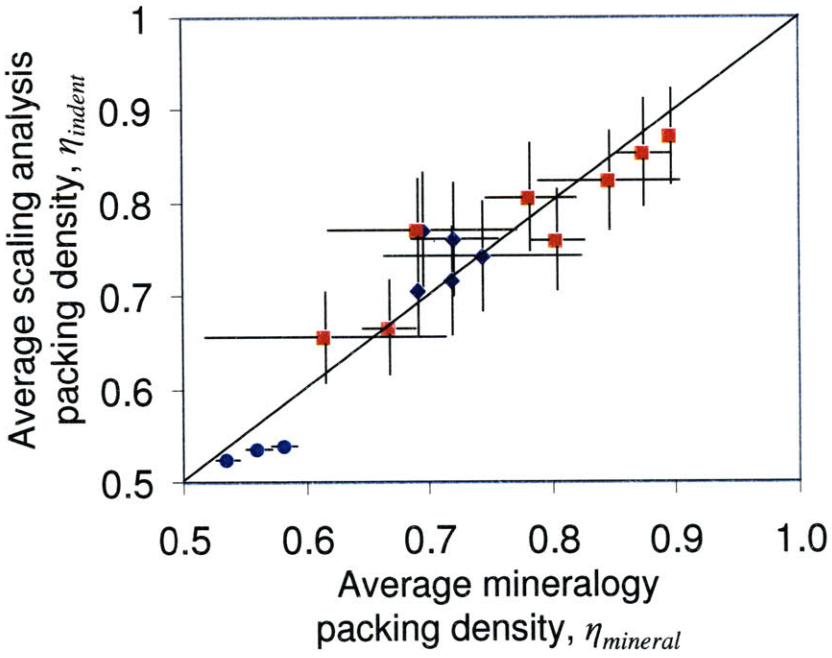

Figure 7-14: Comparison of packing densities derived from mineralogy estimates and from nanoindentation analysis. Included are data from the GeoGenome shales (red squares), Woodford shales (navy diamonds), and Boston Blue Clay samples (light blue circles). Displayed uncertainties in mineralogy estimates come from different porosity measurement techniques, as presented in Tab. 2.6 and calculated by Eq. 2.22. Displayed uncertainties in indentation scaling analysis estimates are representative of plus and minus one standard deviation, while the displayed uncertainties in mineralogy packing density are related to determination of porosity, as defined in Eq. 2.22.

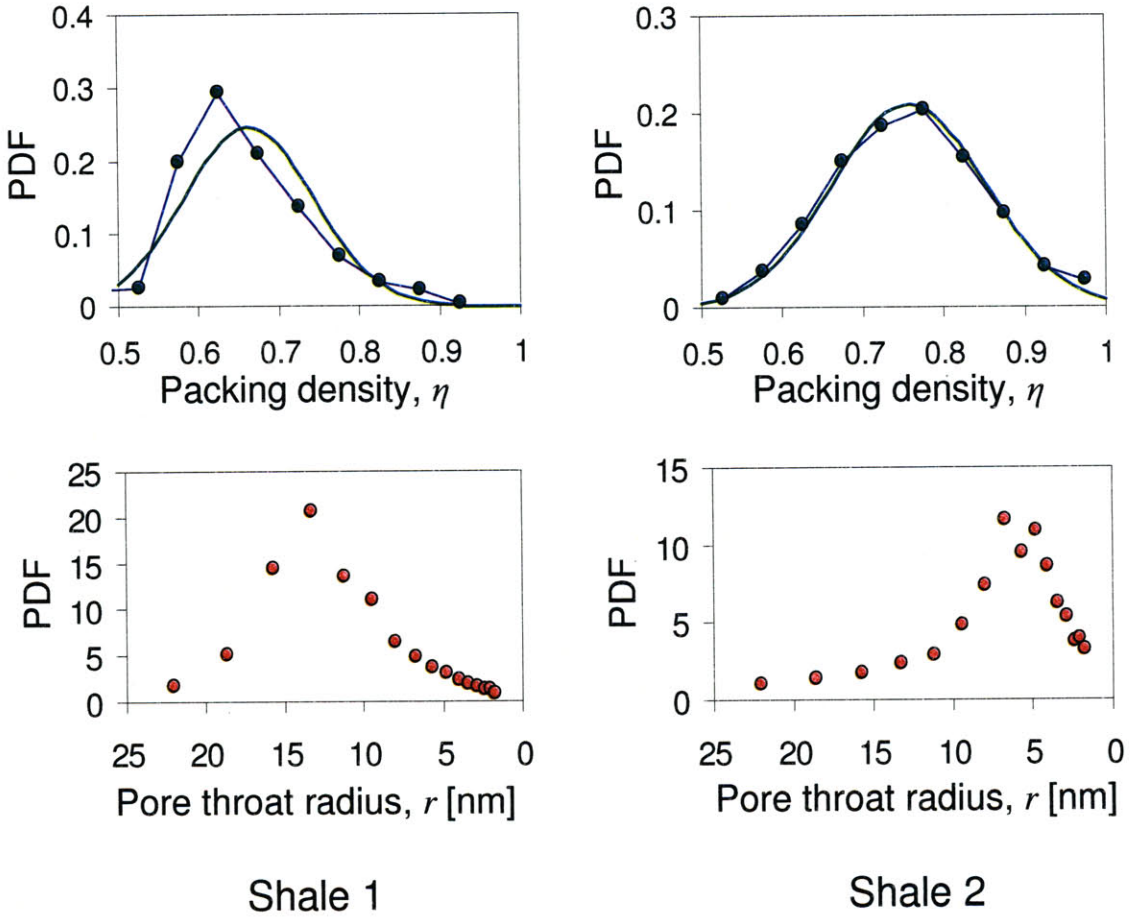

Figure 7-15: Link between packing density distributions with data from both testing directions combined (top) and pore size distributions (bottom). Data from Shale 1 (left) and Shale 2 (right). For this presentation, pore size distributions are presented in a reversed linear scale for comparison to the packing density distributions, because higher packing densities are associated with smaller pore throat radii.

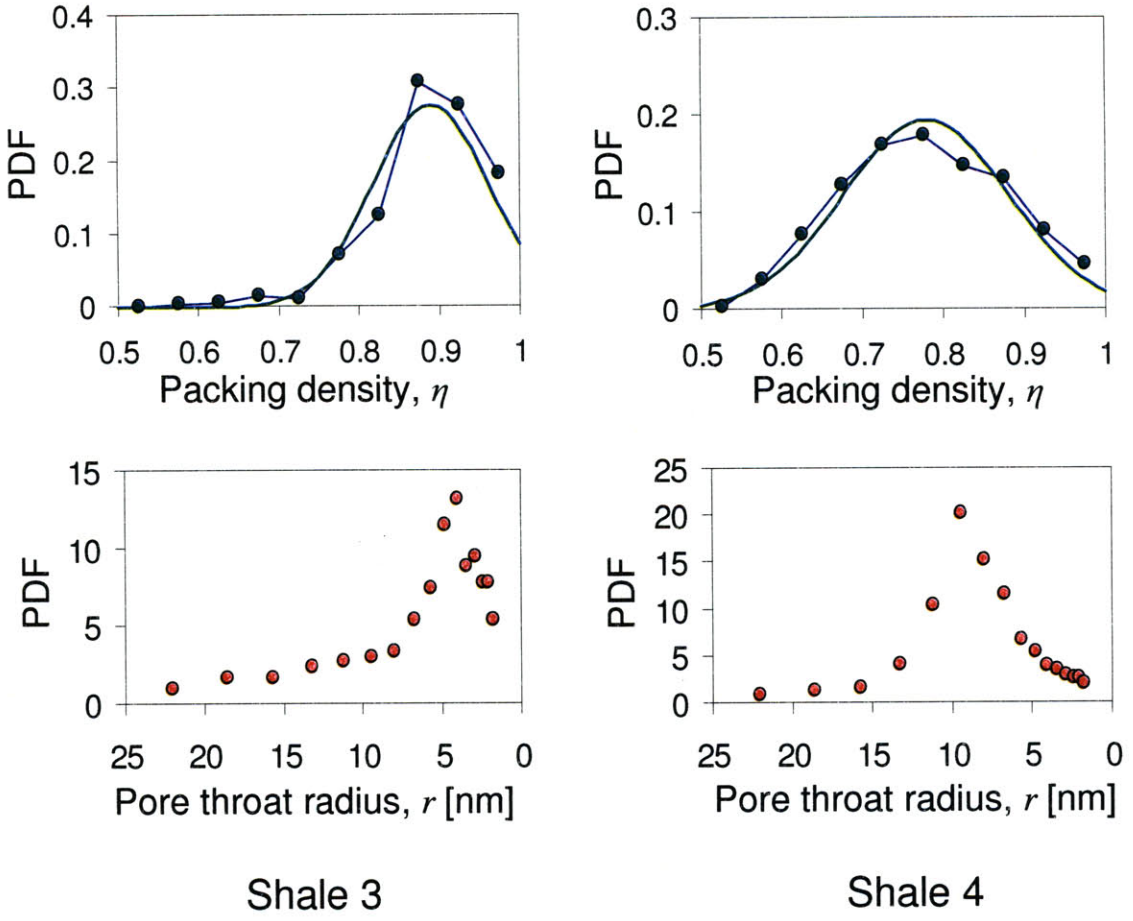

Figure 7-16: Link between packing density distributions with data from both testing directions combined (top) and pore size distributions (bottom). Data from Shale 3 (left) and Shale 4 (right). For this presentation, pore size distributions are presented in a reversed linear scale for comparison to the packing density distributions, because higher packing densities are associated with smaller pore throat radii.

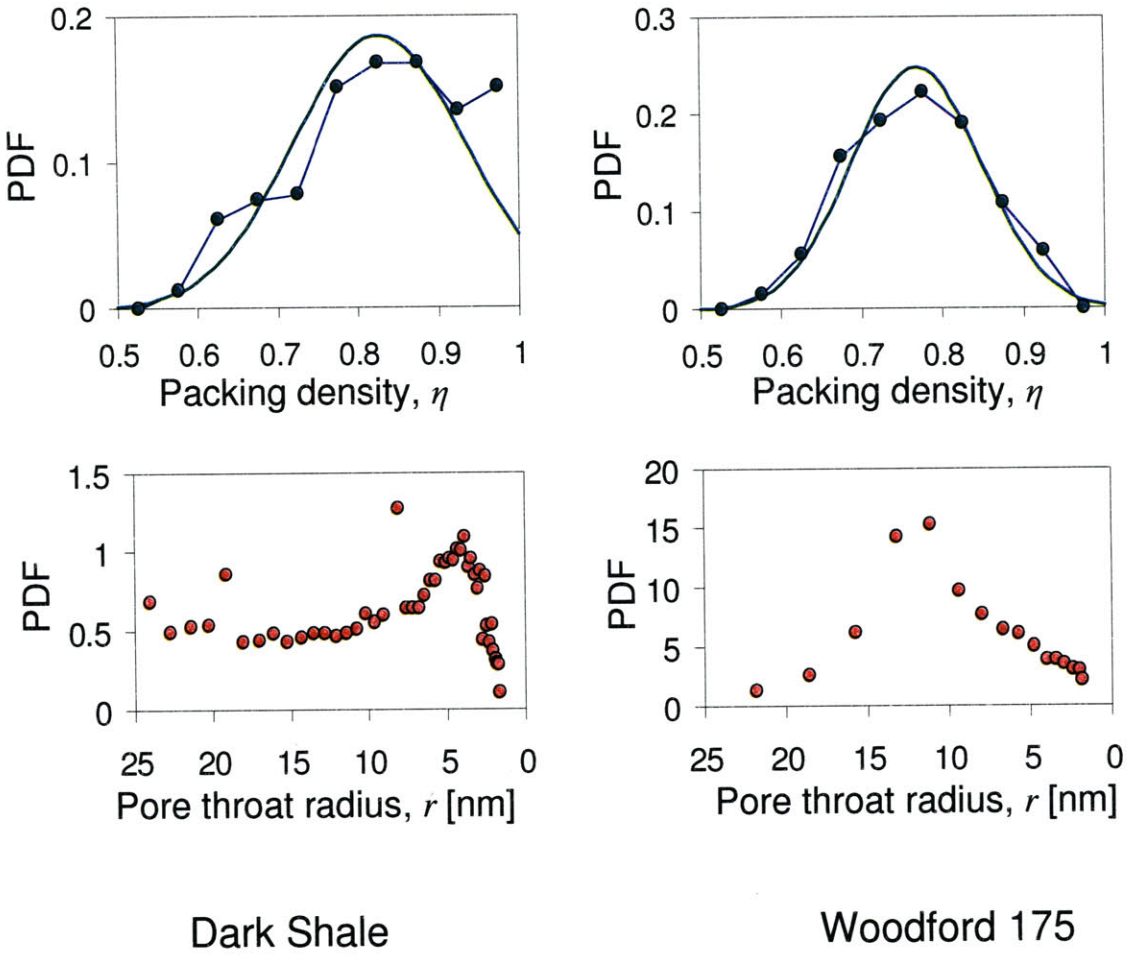

Figure 7-17: Link between packing density distributions with data from both testing directions combined (top) and pore size distributions (bottom). Data from Dark Shale (left) and Woodford 175 (right). For this presentation, pore size distributions are presented in a reversed linear scale for comparison to the packing density distributions, because higher packing densities are associated with smaller pore throat radii.

Shale	r [nm]		$\bar{\eta}_{\text{indent}}$	
	mean	s.d.	mean	s.d.
GeoGenome Shales				
S1	12.46	4.99	0.666	0.010
S2	4.56	3.56	0.760	0.012
S3	3.37	2.35	0.871	0.010
S4	8.32	3.78	0.771	0.012
Dark	4.22	1.08	0.824	0.011
Woodford Shales				
110	10.6	13.0	0.745	0.014
131	11.21	15.3	0.742	0.014
154	10.65	9.48	0.761	0.015
166	11.1	9.91	0.716	0.014
175	9.33	5.83	0.771	0.015
185	11.27	7.69	0.707	0.009

Table 7.3: Mean pore throat radius, calculated from pore throat size distributions, with mean and standard deviation (s.d.) of packing density from indentation analysis duplicated from Table 2.5. Porosimetry information does not exist for all of the Boston Blue Clay samples, or for some of the GeoGenome samples. Mercury porosimetry tests performed by Chevron.

Determination of packing density distributions by nanoindentation provides a compelling complement to porosimetry. Figures 7-15 through 7-17 show comparisons of packing density distributions from nanoindentation analysis (with data from both directions combined) and pore throat radius distributions from mercury intrusion porosimetry.[1] The distributions of pore throat radius provide a means of associating a length scale with average packing density. Table 7.3 makes this association, recalling the mean pore throat radii obtained from mercury intrusion porosimetry for the tested shales from Table 2.5. Recall from Section 2.3.4 that mean pore throat radii come from a deconvolution with the lognormal distribution, while the mean packing density is obtained directly from the experimental data, with the variation appearing to be fit well by a Gaussian distribution. Figure 7-18 compares the mean pore throat radius with the average packing density from nanoindentation analysis. A power law fit highlights the observation that the average packing density tends to decrease as the average pore throat radius increases.

[1] As the Woodford shales have very similar pore throat radius distributions, only one sample is shown here for comparison purposes.

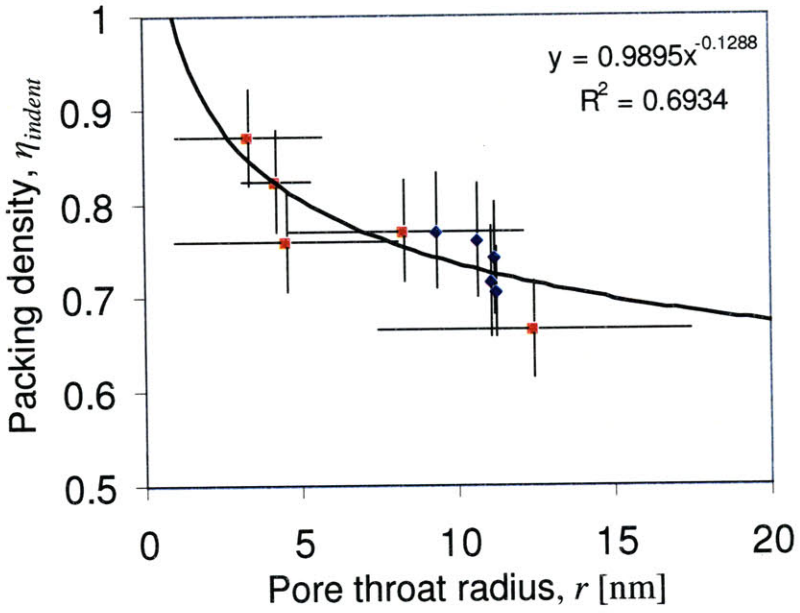

Figure 7-18: Comparison of average pore throat radius obtained from mercury intrusion porosimetry, r, and average packing density obtained from nanoindentation, η_{indent}. Included are data for the GeoGenome shales (red squares) and the Woodford shales (navy circles). Error bars represent uncertainties as plus and minus one standard deviation (although the distributions of pore throat radii fit with lognormal distributions are not distributed symmetrically around the mean, as is the case depicted by the error bars). The black line is a power law fit, highlighting the decrease in packing density with increase in pore throat radius.

Shale	h_s [GPa]		α_s		c_s [GPa]	
	mean	s.d.	mean	s.d.	mean	s.d.
GeoGenome Shales						
1	0.588	0.103	0.408	0.116	0.044	0.012
2	0.620	0.067	0.218	0.058	0.078	0.014
3	0.781	0.069	0.057	0.036	0.143	0.018
4	0.564	0.053	0.152	0.036	0.083	0.006
7	0.567	0.059	0.073	0.038	0.100	0.038
Light	0.699	0.065	0.205	0.114	0.090	0.007
Dark	0.428	0.039	0.108	0.027	0.070	0.005
Woodford Shales						
110	1.032	0.095	0.394	0.006	0.081	0.008
131	1.104	0.085	0.141	0.035	0.166	0.020
154	0.802	0.079	0.160	0.050	0.115	0.013
166	0.720	0.088	0.380	0.060	0.059	0.006
175	0.772	0.082	0.093	0.084	0.129	0.039
185	0.755	0.055	0.292	0.029	0.078	0.006
Boston Blue Clay						
4 MPa	0.433	0.058	0.545	0.042	0.019	0.002
6.5 MPa	1.189	0.185	0.652	0.034	0.031	0.002
10 MPa	0.619	0.087	0.568	0.045	0.025	0.003

Table 7.4: Particle hardness, friction coefficient, and cohesion, for a Drucker-Prager solid, for each of the tested shales.

7.2 Scaling of Strength Properties

While the prior section focused on exploring the packing density results of the inverse homogenization approach, this section focuses on exploring the strength parameter results obtained from the $M-H-\eta$ scaling analysis, as shown in Table 7.4. Recall that the estimated strength parameters correspond to the homogenized Level '0' strength properties; they are the Drucker-Prager parameters associated with a solid polycrystal with weak interfaces (see Sec. 5.3.1). In addition, the model left open the possibility that although Level '0' represents a solid phase, the interfacial behavior (and as a result, the Drucker-Prager parameters) might be somehow affected by the packing density. This is indeed the case.

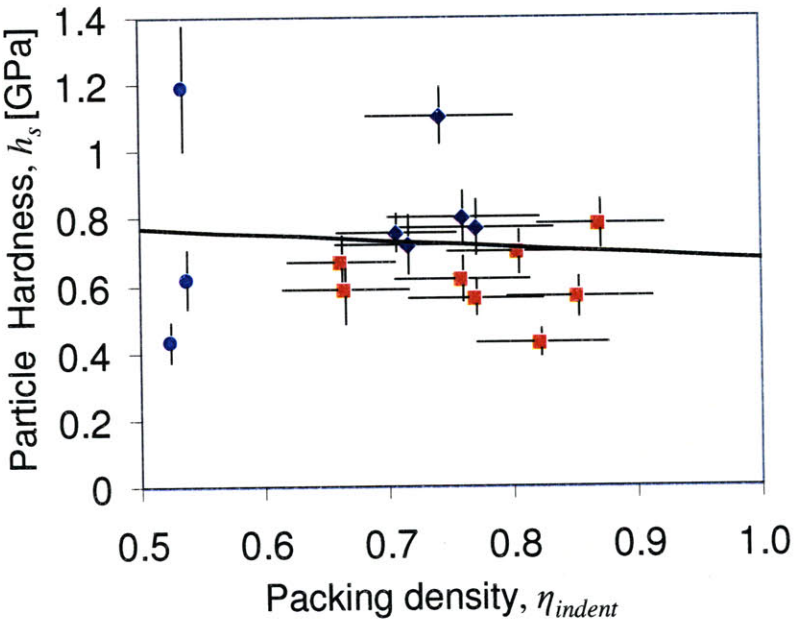

Figure 7-19: Particle hardness versus average clay packing density from indentation analysis. Included are data from the GeoGenome shales (red squares), Woodford shales (navy diamonds), and Boston Blue Clay samples (light blue circles). Particle hardness shows no apparent trend with packing density, instead it is a roughly constant quantity. The trend line (black line) has almost zero slope, and the associated $r^2 = 0.009$. Uncertainties represent two standard deviations.

7.2.1 Invariant Solid Contact Hardness

The Level '0' contact hardness, h_s, is recovered when a clay packing density of $\eta = 1$ is input into the Level 'I' scaling relationship for hardness (Eq. (5.90)). As shown in Figure 7-19, the contact hardness and the average clay packing density are not correlated, and the coefficient of determination, $r^2 = 0.009$ is extremely low. In fact, the porous clay phase in the shale samples, despite possessing wide variations in clay mineralogy, has a relatively constant contact hardness:

$$h_s = 0.69 \pm 0.09 \text{ GPa} \tag{7.3}$$

This value also corresponds well to the ones obtained from the deconvolution results. In Sec. 6.3.3, scaling analysis of the average results from deconvolution for indentation on the porous clay composite gave $\lim_{\eta=1} H_1 \approx \lim_{\eta=1} H_3 = h_s = 0.62$ GPa, as in Eq. (6.11). In Sec. 6.4, the average analysis of locally densely packed areas gave $\overline{H} = h_s = 0.55 \pm 0.10$ GPa, as in Eq. (6.13). Based on three different experimental and analytical approaches, the contact hardness is identified as an intrinsic parameter that characterizes the strength behavior of the solid material in the porous clay in shale.

7.2.2 Scaling of Solid Friction with Packing Density

In contrast to the contact hardness, the Drucker-Prager friction coefficient, α_s, varies strongly from shale to shale. As displayed in Figure 7-20 (top) there is a strong relationship between values of the friction coefficient and the average clay packing density. The friction coefficient, a measure of the pressure sensitivity of the Level '0' building block, decreases as the average clay packing density increases, and appears to tend towards zero as the clay packing density increases to one. A detailed discussion of this important result appears in the next part of this thesis.

For modeling purposes, we initially propose an empirical scaling relationship for the solid Drucker-Prager friction coefficient:

$$\alpha_s = \frac{13}{12}(2 - 2\overline{\eta})^2 + \frac{13}{30}(2 - 2\overline{\eta})^5 \tag{7.4}$$

which captures a horizontal asymptote of $\alpha_s = 0.65$ at $\overline{\eta} = 0.5$, and a horizontal asymptote of

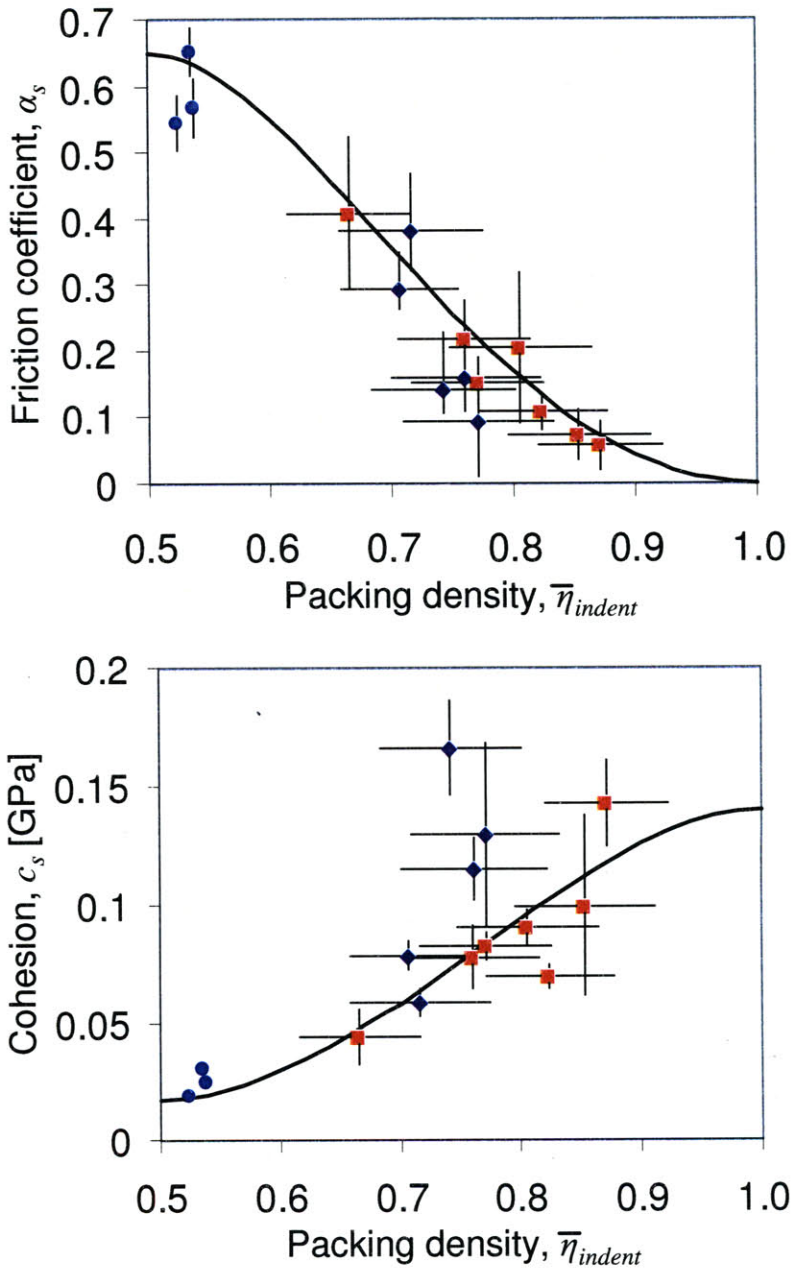

Figure 7-20: Scaling of clay strength properties with packing density. Included are data from the GeoGenome shales (red squares), Woodford shales (navy diamonds), and Boston Blue Clay samples (light blue circles). Top: friction coefficient, Bottom: cohesion. Uncertainties represent two standard deviations.

$\alpha_s = 0$ at $\overline{\eta} = 1$. This relationship is also plotted in Figure 7-20 (top).

7.2.3 Scaling of Solid Cohesion with Packing Density

With the previous results in mind, we should expect that cohesion also has a relationship with the average clay packing density. Recall from Sec. 5.3.6 that the scaling relationship is in the form (Eq. 5.90):

$$H = h_s\left(c_s, \alpha_s\right) \times \Pi_H^I\left(\alpha_s, \eta\right) \tag{7.5}$$

where it is realized that the solid contact hardness h_s is a function of the solid cohesion and the solid friction coefficient. Recall also that that the implementation of the $M - H - \eta$ approach (Sec. 5.4.2) delivers first an estimate for the solid friction coefficient and then an estimate of the solid cohesion. These quantities are combined in Eq. (5.91) to deliver the solid contact hardness. Since the solid contact hardness is apparently constant (Eq. (7.3)), then as the solid friction coefficient varies with packing density (Eq. (8.2)), the solid cohesion must also vary with packing density.

Figure 7-20 (bottom) shows that this is indeed the case. As the average packing density increases, the cohesion increases as well. The cohesion appears to tend towards a minimum as the clay packing density goes to the percolation threshold of 0.5. A scaling relationship for solid cohesion, c_s can be derived based on the fitting function, Eq. (5.91) for indentation hardness of a Drucker-Prager material, the scaling relationship for the friction coefficient, Eq. (7.4), and the mean contact hardness value, Eq. (7.3):

$$c_s = \frac{h_s}{A} \times \left(\frac{1}{1 + B\alpha_s + \left(C\alpha_s\right)^3 + \left(D\alpha_s\right)^{10}}\right) \tag{7.6}$$

with $A = 4.76438$, $B = 2.5934$, $C = 2.1860$, and $D = 1.6777$. The asymptotic cohesion of the elementary building block of shale is obtained for $\alpha_s \to 0$, which corresponds to $\overline{\eta} = 1$, that is:

$$\lim_{\overline{\eta} \to 1} c_s = \frac{h_s}{A} = 0.14 \text{ GPa} \tag{7.7}$$

while for $\overline{\eta} = 0.5$, the cohesion is:

$$\lim_{\overline{\eta} \to 0.5} c_s = 0.017 \text{ GPa} \tag{7.8}$$

There is somewhat more scatter in the cohesion/packing density relationship than there is in the friction/packing density relationship. In fact, the biggest 'outlier' is the same one that appeared in the contact hardness analysis. The source of this behavior is unclear, but does not affect the overall trends.

7.3 Chapter Summary

The $M - H - \eta$ scaling approach has been applied to the massive indentation test database for the porous clay composite in different shale materials. The approach gives scaling results which confirm the elastic anisotropy and hardness isotropy of the solid phase in the porous clay composite. Estimates of local packing densities for each shale sample can be collected as packing density distributions. For each shale, the average packing density obtained from the $M - H - \eta$ scaling approach compares well to the average packing density obtained from mineralogy and porosity data. For each shale, the packing density distributions corresponding to the two directions of indentation testing, the $x1$-direction and the $x3$-direction, tend to overlap. This overlap validates the isotropic, spherical morphology of the clay solid in the porous clay composite.

The other main advantage of the $M - H - \eta$ scaling approach is that it gives an estimate of the cohesive-frictional strength parameters of the solid phase in the porous clay composite. These results are quite remarkable. It was observed that the asymptotic, particle hardness for each shale was roughly the same, and no trend was observed with mean packing density. The Drucker-Prager friction coefficient and cohesion, however, do scale with the average clay packing density. In particular, the friction coefficient is at its maximum when the average clay packing density is close to the percolation threshold, $\eta_0 = 0.5$, and tends towards zero as the packing density increases to one. The cohesion demonstrates the opposite trend; it scales upwards with clay packing density, from a mimimum at the percolation threshold, to its maximum value at a packing density of one.

The new results presented in the previous chapter, devoted to a statistical analysis of the indentation results, and the results from the $M - H - \eta$ scaling approach presented in this chapter give some intriguing new observations about the porous clay composite phase in shale. In the next part of this thesis, these observations are brought together to define a model of the elementary building block of porous clay in shale. This model, which includes information about mechanical microstructure of the porous clay composite and intrinsic elastic and strength properties of the solid clay, characterizes the fundamental unit of material invariant behavior, satisfying a primary goal of this thesis.

Part IV

DISCUSSION - THE ELEMENTARY BUILDING BLOCK OF SHALE

Chapter 8

Defining the Elementary Building Block of Shale

The multiscale thought model for shale (Chapter 2), the detailed review and extension of experimental nanoindentation techniques and analysis approaches for testing shale materials (Chapters 3, 4, and 5), and the presentation of remarkable results from these nanoindentation experiments and analyses (Chapters 6 and 7) have combined to shed new light on the mechanical behavior of shale materials. In short, experimental microporomechanics has provided the opportunity to assess and understand material properties that are common to all shale materials at small scales, despite the macroscopic diversity of shale. Moreover, scaling relationships with clay packing density, solidified by new evidence about the microstructure and morphology of shale materials, suggest an origin for the diversity of macroscopic mechanical properties. The primary goal of this thesis, to understand the mechanical behavior of shale by assessing microstructure and material invariant mechanical properties as the link between composition and engineering performance, is nearly satisfied.

This chapter condenses the information obtained so far from experimental results into a model of the elementary building block of the porous clay in shale. The next two chapters provide more insight into the origin and importance of the elementary building block model, by looking to both smaller and larger scales. In particular, the next chapter explores the physical origin of the elementary building block model, including concerns relating to shape, elastic

behavior, and strength behavior. The final chapter of this part reviews and extends some recent results of micromechanical modeling based on the elementary building block model, helping to validate the elementary building block and demonstrating its significance to engineering applications.

8.1 Introduction

The aim of this chapter is to introduce a model of the elementary building block of the porous clay in shale materials, based primarily on the new results from nanoindentation, but also in combination with other observational methods. This model should summarize all the experimental observations, and should provide all the necessary ingredients for use in micromechanical modeling efforts. As presented in Sec. 5.2.1, micromechanics models require information about the mechanical properties of material phases, and morphology and microstructure of the composite. The model of the elementary building block of the porous clay in shale materials is designed to capture the behavior of Level '1' in the multiscale thought model for shale (Fig. 2-1, Sec. 2.2). As a result, this model should capture the morphology salient to the porous clay composite, and the elastic and strength behavior of the clay solid in the porous clay composite. These features are discussed in this chapter.

8.2 Mechanical Morphology of the Elementary Building Block

A primary ingredient for successful micromechanical modeling is an understanding of the morphology of the composite material. This section presents a variety of tools and results used to assess and choose an appropriate model for microstructure and morphology of the elementary building block of shale. The traditional approach for assessing microstructure and morphology is to make visual observations using various microscopy techniques. These techniques may give conflicting results, however, and do not necessarily isolate the microstructures which are important for developing micromechanical models. Consequently, mechanical evidence from nanoindentation results, in the framework of experimental microporomechanics, is also presented. This mechanical method resolves the important aspects of the microstructure and morphology of the elementary building block of porous clay in shale.

8.2.1 Visual Observations

Researchers have long understood that the microstructure, or "fabric" of clay minerals plays an important role in the behavior of macroscopic materials [138]. In micromechanical modeling, the morphology of the material is a critical input parameter. Various methods exist to make visual observations of the structure of clay in shale materials -- attention is focused here on three visualizations of microstructure.

The most commonly employed visual observation technique is Scanning Electron Microscopy (SEM) in secondary electron mode [93], [157]. These images give a visual understanding of the surface topography of a sample. Recall from Chapter 2 that these kinds of images (Figs. 2-3 and 2-4) were used to develop and motivate the multiscale thought model for shale (Fig. 2-1). Figure 8-1 (top) displays a typical SEM image of a shale surface, exposed to observe the bedding planes associated with the depositional history of the material. The SEM image in Figure 8-1 (top) shows a typically flaky structure, with platelet particles about a micron in their maximum dimensions. These platelets are well-aligned in the bedding planes.

A related technique is Transmission Electron Microscopy (TEM), which gives information about the relative atomic density of a very thin section of material. TEM sample preparation can be difficult, especially for clay materials, and the range of accessible length scales is much smaller. TEM can, however, achieve higher resolution than SEM. Figure 8-1 (middle and inset) displays a typical TEM image from Bryant et al. [28] who produced a series of TEM images of a consolidated clay. Darker regions in TEM images correspond to higher atomic densities, and TEM imaging permits an estimation of the thickness of individual clay minerals: about 10-50 nm. The TEM images in Figure 8-1 suggest a granular microstructure, with equidimensional, submicron-sized groupings of aligned clay minerals.

Finally, Atomic Force Microscopy (AFM) can be used to probe the surface topography of a shale sample. In AFM imaging, a sharp tip is rastered across the sample surface, and the heights at which the tip makes contact with the surface are recorded. This was the same technique used to quantify the roughness of shale surfaces polished for nanoindentation (Sec. 4.3.4). Figure 8-1 (bottom) shows typical AFM images of polished shale surfaces, exposing the $x3$-direction and the $x1$-direction. AFM imaging also suggests a granular microstructure consisting of submicron-sized structures, with no apparent differences between the different

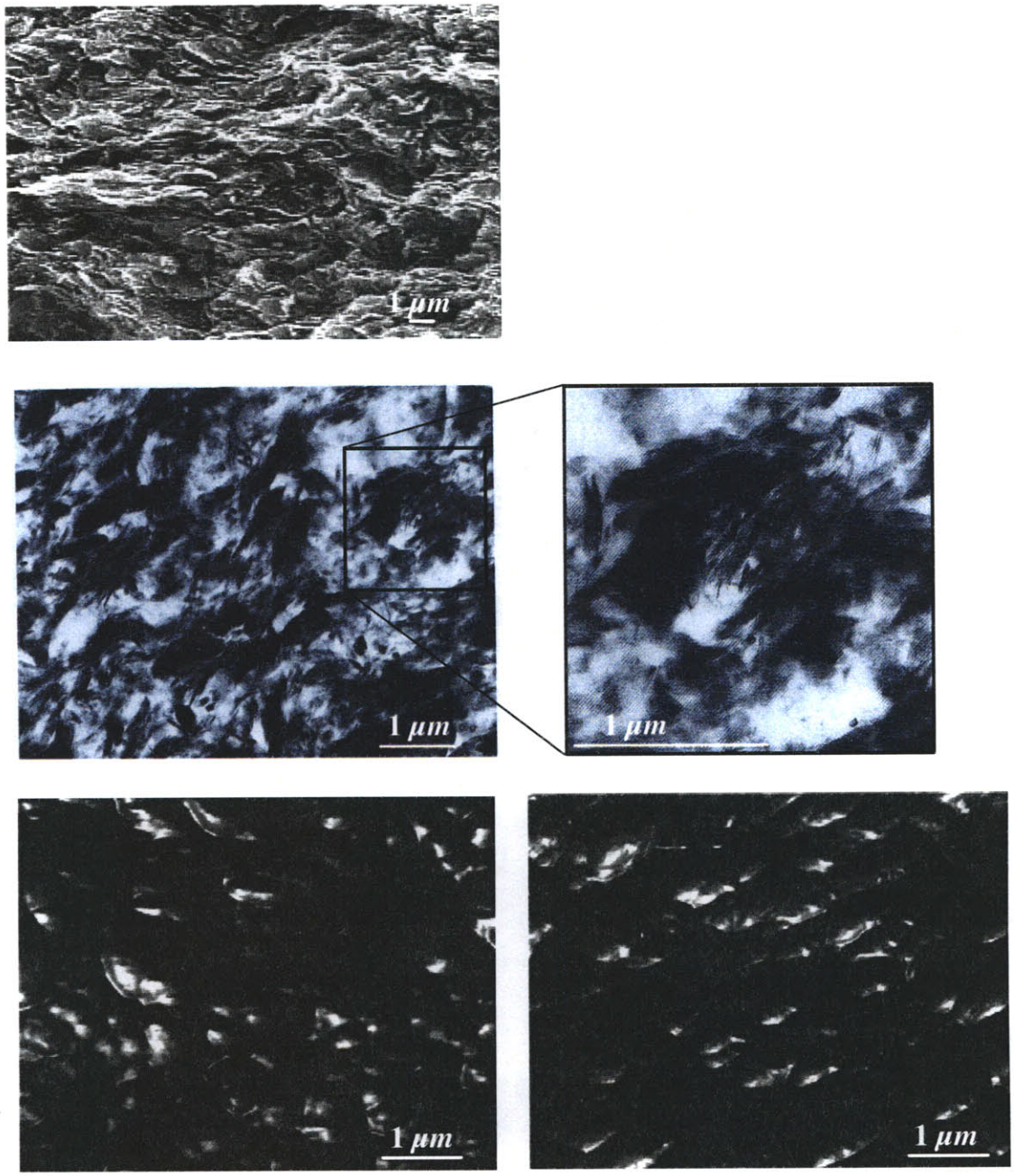

Figure 8-1: Visual observations of structure in shale. The scale bar for each image is 1 μm. Top: SEM image of Shale 3 modified from [172] showing well-aligned flaky structure. Middle: TEM image of consolidated clay from [28], showing an equidimensional submicron-sized granular structure consisting of aligned clay minerals (inset). Bottom: AFM images of Shale 3, showing an equidimensional submicron-sized granular structure, regardless of which surface is exposed (left: $x3$-direction, right: $x1$-direction).

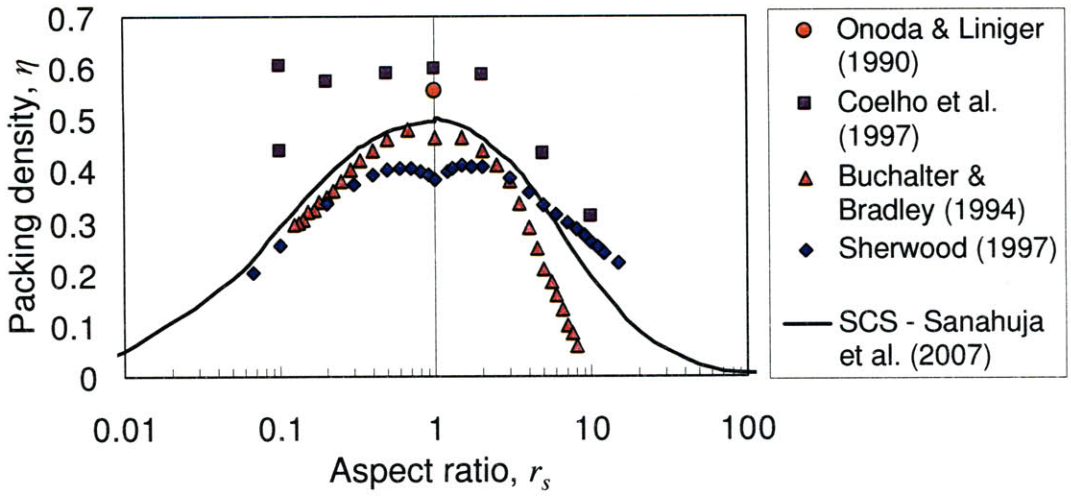

Figure 8-2: Effect of the solid particle aspect ratio r_s on the percolation threshold, recalled from Fig. 5-3. Results from experiments (Onoda & Liniger, 1990) [144], granular computational approaches (Coehlo et al., 1997, Buchalter & Bradley, 1994, and Sherwood, 1997) [41], [29], [163] and modeling with the self consistent scheme (Sanahuja et al., 2007) [154] are included.

directions.

8.2.2 Granular Mechanics - Percolation Threshold & Micromechanics

Recall from Section 5.2.2 that the developed scaling relationships were obtained by considering the self-consistent scheme, with a spherical morphology for both the solid and the pore space. This model choice gives a percolation threshold, the packing density below which macroscopic stiffness and strength cannot be developed, of $\eta_0 = 0.5$. Recall as well from Section 5.2.2 that results from granular physics [29], [41], [163] and from micromechanical modeling with the self-consistent scheme [154] have shown that the percolation threshold of $\eta_0 = 0.5$ is associated with random packings of spheres. Considering other particle shapes in random orientations, such as prolate or oblate spheroids, reduces the percolation threshold as shown in Fig. 8-2 (recalled from Fig. 5-3).

Sec. 6.3.3 provided a presentation of nanoindentation results in the context of the percolation threshold in shale materials. A percolation threshold at a packing density of $\eta_0 = 0.5$ is observed from the deconvolution analysis of nanoindentation results designed to assess the porous clay

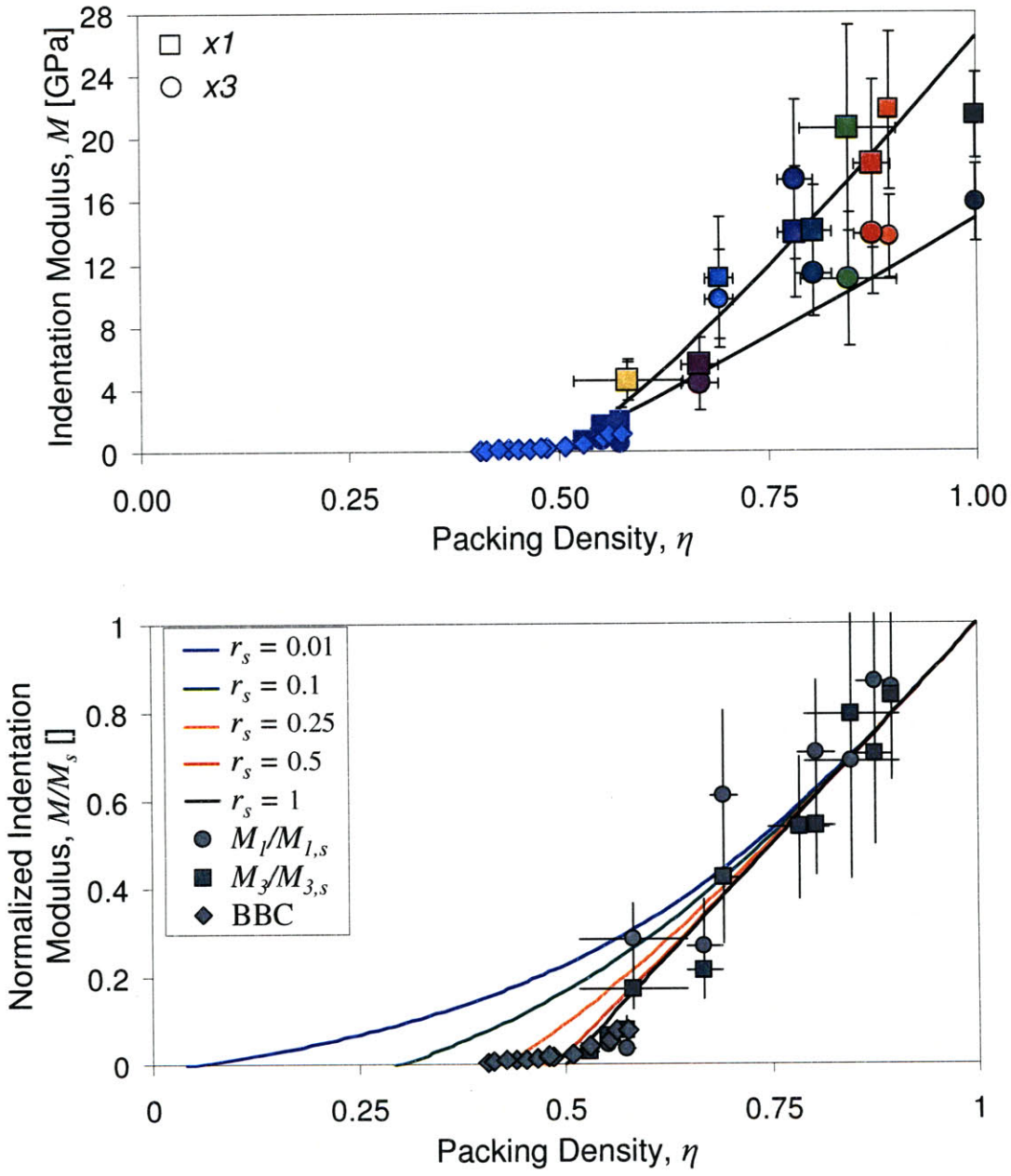

Figure 8-3: Top: Recalling the graph presented in Fig. 6-7, the observed percolation threshold at $\eta_0 = 0.5$ is clear. Bottom: Normalized indentation moduli data compared to isotropic scaling relationships for different particle aspect ratios r_s. The percolation threshold and scaling relationship associated with $r_s = 1$, that is, a spherical morphology, provides the best model for the experimental data.

composite behavior. Additional evidence from macroscopic data on Boston Blue Clay (as seen in Fig. 8-3 (top), recalled from Fig. 6-7) is also in favor of the $\eta_0 = 0.5$ percolation threshold for shale-like stiffnesses. Fig. 8-3 (top) also provides a reminder of the good fit between the experimental nanoindentation data and the scaling relationships, Eqs. (5.31) and (5.90), derived from micromechanics under the assumption of a spherical morphology.

It is possible to derive scaling relationships for indentation modulus using other spheroidal particle shapes. The micromechanics derivations (starting from Eq. (5.24) and requiring the appropriate specifications of the Hill tensor) quickly become a challenge to implement when considering an anisotropic solid with non-spherical particle shapes. A simpler case has recently been reported on by Sanahuja et al. [154], considering the scaling relationships for randomly oriented isotropic elastic particles with spheroidal particle shapes. Normalizing the experimental (transversely isotropic) indentation moduli results by the solid quantities (Eq. (6.10)) allows for a first comparison of trends with the isotropic scalings.[1] This comparison is seen in Figure 8-3 (bottom), with normalized scaling relationships for random packings of spheroids defined by their aspect ratio r_s. Recall that r_s is expressed as the ratio of the length of the symmetry axis over the diameter in the symmetry plane, and particles with $r_s < 1$ are oblate spheroids while particles with $r_s > 1$ are prolate spheroids. For clarity, Figure 8-3 (bottom) only displays scaling relationships associated with oblate spheroids, but similar trends are observed for prolates, as well. It is clear that the scaling relationship associated with $r_s = 1$ provides the best model for the experimental data.

The percolation thresholds and the scaling results for randomly oriented spheroids give the best match to the data when a sphere is considered. In other words, a spherical representation of the mechanical morphology is most appropriate for the model of the elementary building block.

8.2.3 Packing Density Distributions

A final method to investigate the microstructure and morphology for the model of the elementary building block is to consider the packing density distributions obtained through the

[1] The numerical implementation of these scaling relationships was performed by J. Alberto Ortega during his PhD at MIT.

$M - H - \eta$ scaling approach, as presented in Section 7.1.3. Recall that the overlap between distributions for each direction is remarkable, as displayed in Figures 7-7 through 7-12 and summarized in Figure 7-13. The implication of this observation is that the employed scaling models, which feature intrinsic anisotropy in elastic behavior but intrinsic isotropy of strength behavior, are sufficient to capture the mechanical behavior of the porous clay composite. In other words, there is no orientation of pore space which would cause packing densities to have different values in different directions. The observations for shale stand in marked contrast to observations of packing density distributions in the apatite mineral phase of bone [175] which possess an intrinsic isotropic behavior in elasticity and strength, but have anisotropic packing density distributions. In the case of the mineral phase of bone, pores with some ordered orientation (associated with the natural growth and remolding cycles in bone) are felt to a greater extent in one direction than another. This demonstrates that pore morphology should affect both strength and stiffness properties. The contrasting result for shale is another piece of evidence in favor of considering a perfectly disordered (spherical representation) mechanical morphology at Level 'I' in shale.

8.3 Intrinsic Elastic Anisotropy of the Elementary Building Block of Shale

With a spherical representation of the mechanical morphology specified for the model of the elementary building block, intrinsic mechanical properties of the clay solid must now be defined to complete the model. Beginning with the elastic properties, the nanoindentation results have provided the needed information.

It is generally agreed that the macroscopic elastic behavior of shale is anisotropic, but the origin of this anisotropy is still under some debate. With the mechanical morphology of the elementary building block being represented by a sphere, which is an inherently isotropic morphology, the intrinsic elastic behavior of the elementary building block must be anisotropic. This assertion was supported by evidence presented in Section 6.3, where statistical significance testing demonstrated that differences between indentation moduli of the porous clay composite in the $x1$-direction and the $x3$-direction were statistically significant. Recalling the discussion

in Section 6.5 giving first clues about the mechanical behavior of the porous clay in shale, further experimental results and analysis provided support for the intrinsic anisotropy of the solid clay. These clues are now incorporated in the elementary building block model.

In particular, Chapter 6 presented results from nanoindentation at two different scales of observation; one designed to assess the mechanical response of the porous clay composite, and one designed to assess the mechanical response of a locally densely packed area of clay. Experimental scaling analysis of the porous clay composite response of kerogen-free shales gave values of (Eq. (6.10)) $m_{1,s} = \lim_{\eta \to 1} M_1 = 25$ GPa and $m_{3,s} = \lim_{\eta \to 1} M_3 = 16$ GPa at a limit packing density of one. Further agreement was seen when considering the average results from nanoindentation on locally densely packed areas of kerogen-free shales, with values (Eq. (6.12)) of $m_{1,s} = 21.4 \pm 2.4$ GPa and $m_{3,s} = 15.9 \pm 2.2$ GPa.

Recall from Sec. 3.3.3 that the indentation moduli M_1 and M_3 represent a 'snapshot' of the transversely isotropic elastic behavior defined by five independent stiffness coefficients. Also recall that, using back-analysis from macroscopic measurements, Ortega et al. [145] delivered estimates of these stiffness coefficients for the solid clay (Eq. (5.29)):

$$\begin{aligned} C^s_{11} &= 44.9 \text{ GPa} \\ C^s_{12} &= 21.7 \text{ GPa} \\ C^s_{13} &= 18.1 \text{ GPa} \\ C^s_{33} &= 24.2 \text{ GPa} \\ C^s_{44} &= 3.7 \text{ GPa} \end{aligned} \tag{8.1}$$

These stiffness coefficents are translated into equivalent indentation moduli via Eq. (3.46), giving values of (Eq. (5.30)) $m_{1,s} = 26.3$ GPa and $m_{3,s} = 14.9$ GPa. Given the good match between experimental values of indentation moduli, and the indentation moduli calculated from Ortega et al.'s values, it is reasonable to assume that Ortega et al.'s values provide the sought material invariant elastic properties,

When considering a shale with an additional material phase of solid kerogen, as in the Woodford Shales, a homogenization step is required to combine the solid clay with the solid kerogen. In this case, it is proposed that a self-consistent scheme is used to homogenize the

isotropic stiffness of the solid kerogen, with bulk modulus, $k^k = 6.8$ GPa, and shear modulus $g^k = 3.6$ GPa [181], with the transversely isotropic stiffness of the solid clay given in Eq. (8.1). This homogenization step leads to a reduction of the magnitude and degree of anisotropy of the solid in the porous clay-kerogen composite, and matches the observations on the locally densely packed areas for the Woodford Shales, as discussed in Section 6.4.2. The intrinsically transversely isotropic values provided in Eq. (8.1) are in fact material invariant properties.

8.4 Cohesive-Frictional Strength Behavior of the Elementary Building Block

To complete the model, cohesive-frictional strength properties of the elementary building block are sought. The $M - H - \eta$ scaling approach to analysis of nanoindentation measurements led to some remarkable observations. First, recall from Figure 7-19 that the solid particle contact hardness, $h_s = 0.62$ GPa, is apparently a constant (or nearly so) material invariant property (Eq. (7.3)). Also, recall from Eq. (5.91) that h_s is a function of the cohesive-frictional strength parameters (Drucker-Prager criterion) of the solid, i.e. cohesion c_s and friction coefficient α_s. While the solid particle contact hardness was seen to be material invariant, the cohesive-frictional strength parameters are not the same from sample to sample.

Figure 8-4 recalls Figure 7-20 as originally presented in Section 7.2. There is a strong relationship between values of the friction coefficient and the average clay packing density. The solid friction coefficient decreases as the average clay packing density increases, and appears to tend towards zero as the clay packing density increases to one. For modeling purposes, an empirical scaling relationship for the solid Drucker-Prager friction coefficient was proposed (Eq. (7.4)):

$$\alpha_s = \frac{13}{12}(2 - 2\overline{\eta})^2 + \frac{13}{30}(2 - 2\overline{\eta})^5 \tag{8.2}$$

which captures a horizontal asymptote of $\alpha_s = 0.65$ at $\overline{\eta} = 0.5$, and a horizontal asymptote of $\alpha_s = 0$ at $\overline{\eta} = 1$. This relationship is plotted in Figure 7-20 (top).

Given that h_s is both constant and a function of α_s and c_s, cohesion also has a relationship with the average clay packing density of a sample. A scaling relationship for solid cohesion, c_s is derived by combining the fitting function, Eq. (5.91) for indentation hardness of a Drucker-

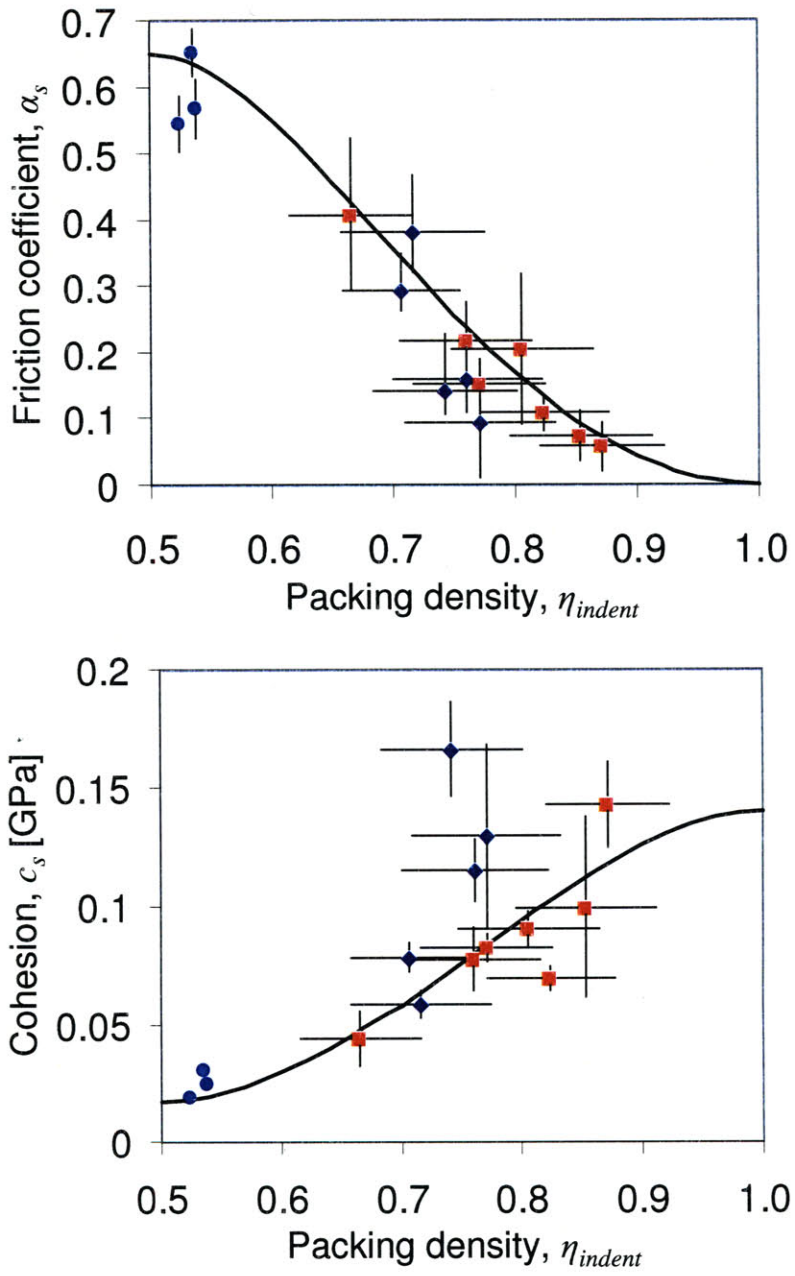

Figure 8-4: Scaling of clay strength properties with packing density, recalled from Fig. 7-20. Included are data from the GeoGenome shales (red squares), Woodford shales (navy diamonds), and Boston Blue Clay samples (light blue circles). Top: friction coefficient, Bottom: cohesion. Uncertainties represent two standard deviations.

Prager material, with the scaling relationship for the friction coefficient, Eq. (8.2), and the mean contact hardness value, Eq. (7.3):

$$c_s = \frac{h_s}{A} \times \left(\frac{1}{1 + B\alpha_s + (C\alpha_s)^3 + (D\alpha_s)^{10}} \right) \tag{8.3}$$

with $A = 4.76438$, $B = 2.5934$, $C = 2.1860$, and $D = 1.6777$. The asymptotic cohesion of the elementary building block of shale is obtained for $\alpha_s \to 0$, which corresponds to $\overline{\eta} = 1$, that is:

$$\lim_{\overline{\eta} \to 1} c_s = \frac{h_s}{A} = 0.14 \text{ GPa} \tag{8.4}$$

Figure 8-4 (bottom) confirms the assertion of this scaling relationship through a comparison to experimental data. The solid cohesion increases as the average packing density increases, while the solid cohesion reaches a minimum (although it remains finite as the solid friction coefficient remains finite) as the clay packing density goes to the percolation threshold of $\eta_0 = 0.5$.

In conclusion, nanoindentation results demonstrated the existence of a material invariant solid particle contact hardness, a combination of solid cohesion and solid friction coefficients that are not material invariant. Instead, it was observed that solid friction and cohesion scale with packing density. Fortunately, on first order, these scaling relationships are the same from sample to sample, and thus define the strength behavior in the model of the elementary building block of porous clay in shale.

8.5 Chapter Summary

This chapter has combined the results presented in the previous two chapters into a unified model of the elementary building block of the porous clay in shale materials. This model is a basis for micromechanics predictions of the behavior of the porous clay composite at Level '1' in the multiscale thought model for the structure of shale. The model of the elementary building block has three primary features, including:

1. Granular microstructure, with a spherical representation of the mechanical morphology.

2. Intrinsic transverse isotropy of elastic properties, with solid stiffness coefficients for kerogen-

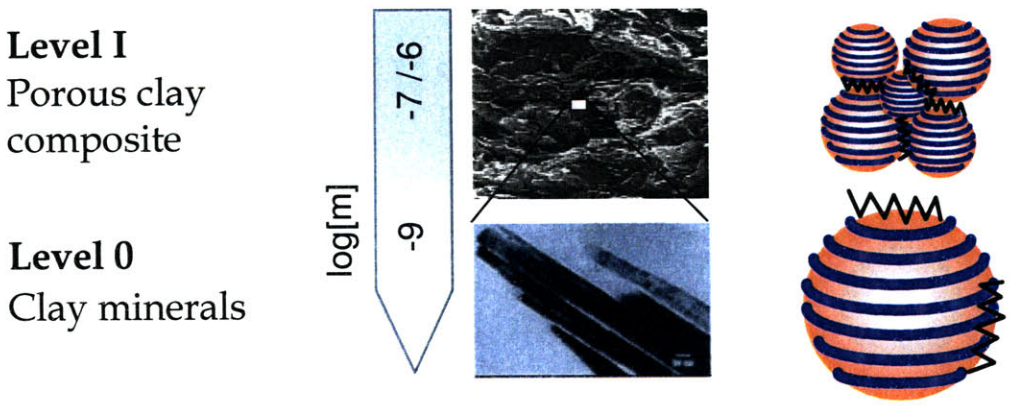

Figure 8-5: The applicable portion of the multiscale thought model for shale, repeated from Fig. 2-1, with a cartoon depiction of the elementary building block model and Level '0', and working together to form the porous clay composite at Level '1.'

free shales defined by Eq. (8.1):

$$\begin{aligned} C^s_{11} &= 44.9 \text{ GPa} \\ C^s_{12} &= 21.7 \text{ GPa} \\ C^s_{13} &= 18.1 \text{ GPa} \\ C^s_{33} &= 24.2 \text{ GPa} \\ C^s_{44} &= 3.7 \text{ GPa} \end{aligned} \tag{8.5}$$

3. Isotropy of cohesive frictional strength properties, with material invariant solid particle contact hardness $h_s = 0.62$ GPa which is the combination of scaling relationships for solid friction coefficient (Eq. (8.2)):

$$\alpha_s = \frac{13}{12}\left(2 - 2\overline{\eta}\right)^2 + \frac{13}{30}\left(2 - 2\overline{\eta}\right)^5 \tag{8.6}$$

and solid cohesion (Eq. (8.3)):

$$c_s = \frac{h_s}{A} \times \left(\frac{1}{1 + B\alpha_s + \left(C\alpha_s\right)^3 + \left(D\alpha_s\right)^{10}}\right) \tag{8.7}$$

with $A = 4.76438$, $B = 2.5934$, $C = 2.1860$, and $D = 1.6777$.

A cartoon representation of the model of the elementary building block is seen in the context of the multiscale thought model for the structure of shale in Figure 8-5. The intrinsic elastic anisotropy is represented by layers within the spherical representation of mechanical morphology, while the presence of friction is suggested by jagged lines at particle contacts. Of course, this cartoon depiction does not resemble the visual observations provided by the SEM images originally employed to motivate the multiscale model for shale, where layered spheres were nowhere to be seen. The next chapter aims to resolve these differences, and enrich the understanding of the elementary building block model, by exploring the physical origins of its properties.

Chapter 9

Origins of the Elementary Building Block

The model of the elementary building block, defined in the previous chapter, does not look like one might expect from a more traditional understanding of clay minerals. The mechanical behavior of the elementary building block is somewhat surprising as well, with intrinsic elastic anisotropy and cohesive frictional strength parameters that vary with the average clay packing density in the materials. This chapter aims to explore possible physical origins of the mechanical morphology and material properties of the elementary building block. Such an exploration will help clarify what the elementary building block actually represents and justify the characteristics of the model.

The chapter begins by considering the spherical representation of mechanical morphology for the elementary building block. The primary question to be resolved is how the model can feature a spherical mechanical morphology when SEM images show platelet microstructures which are far from spherical. The chapter proceeds by considering the origin of intrinsically anisotropic elastic properties of the elementary building block, comparing the model values with previously reported values for single clay platelets and for solid clay in shale materials. This discussion also helps to clarify the origin of the spherical morphology. Finally, the frictional behavior of the elementary building block is discussed in terms of contemporary views on the origin of friction. Links are made between friction, pore sizes, and packing density, justifying

the scaling of strength properties within the elementary building block.

9.1 Physical Origin of the Elementary Building Block's Mechanical Morphology

The mechanical morphology of the elementary building block model is represented by a sphere, based primarily on the mechanical results from nanoindentation experiments and analysis (see Sec. 8.2). However, the most common technique for assessing microstructure in shale materials, SEM imaging, shows a microstructure of semi-aligned platelets that are very far from being spherical. Still, TEM and AFM images provide additional clues in support of the spherical representation. The differences between these observations must be reconciled. Two possibilities emerge, one which considers the critical importance of contacts between clay particles, and another which considers the elementary building block as an "effective" solid composed of many individual clay particles.

9.1.1 Random Orientation of Particle Contact Surfaces

First, understanding the importance of morphology in terms of particle to particle contact drives a new interpretation of SEM images. In this hypothesis, the spherical representation of mechanical morphology is understood as a surrogate for perfectly disordered contact surfaces. These contact surfaces are critical for a granular composite because they are the pathways through which stress is transmitted throughout the composite material. Figure 9-1 displays a cartoon that highlights the possibility of randomly oriented particle-to-particle contact surfaces even for platelet particles. Traces of individual platelets are drawn, and potential contact surfaces between these platelets are identified. These contact surfaces do not show the same aligned structures as the particles themselves. Note that this is a conceptual depiction of the scenario, without the benefit of any automated image analysis procedures. Instead Figure 9-1 suggests that the shapes and structures seen directly in SEM images may not be the ones which control the mechanical behavior of the porous clay composite.

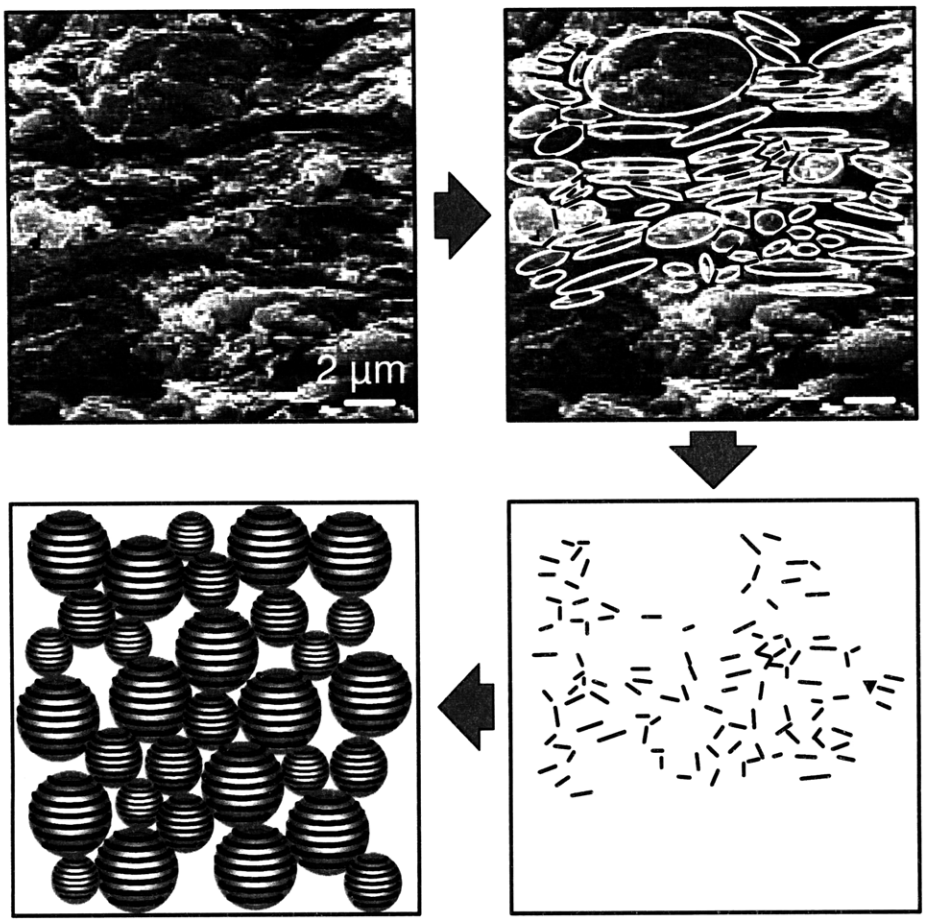

Figure 9-1: A logical origin of the spherical representation of the mechanical morphology for the elementary building block model. The top left image is an ESEM image showing individual clay particles. The top right image has traces of particle shapes. The bottom right drawing shows the contact surfaces remaining between traces of particle shapes. While orientation is clearly visible in the particle shape diagram, an ordered orientation of contact surface is much less apparent. As a result, the mechanical representation of this averaged random contact is a sphere, as seen in the bottom left drawing.

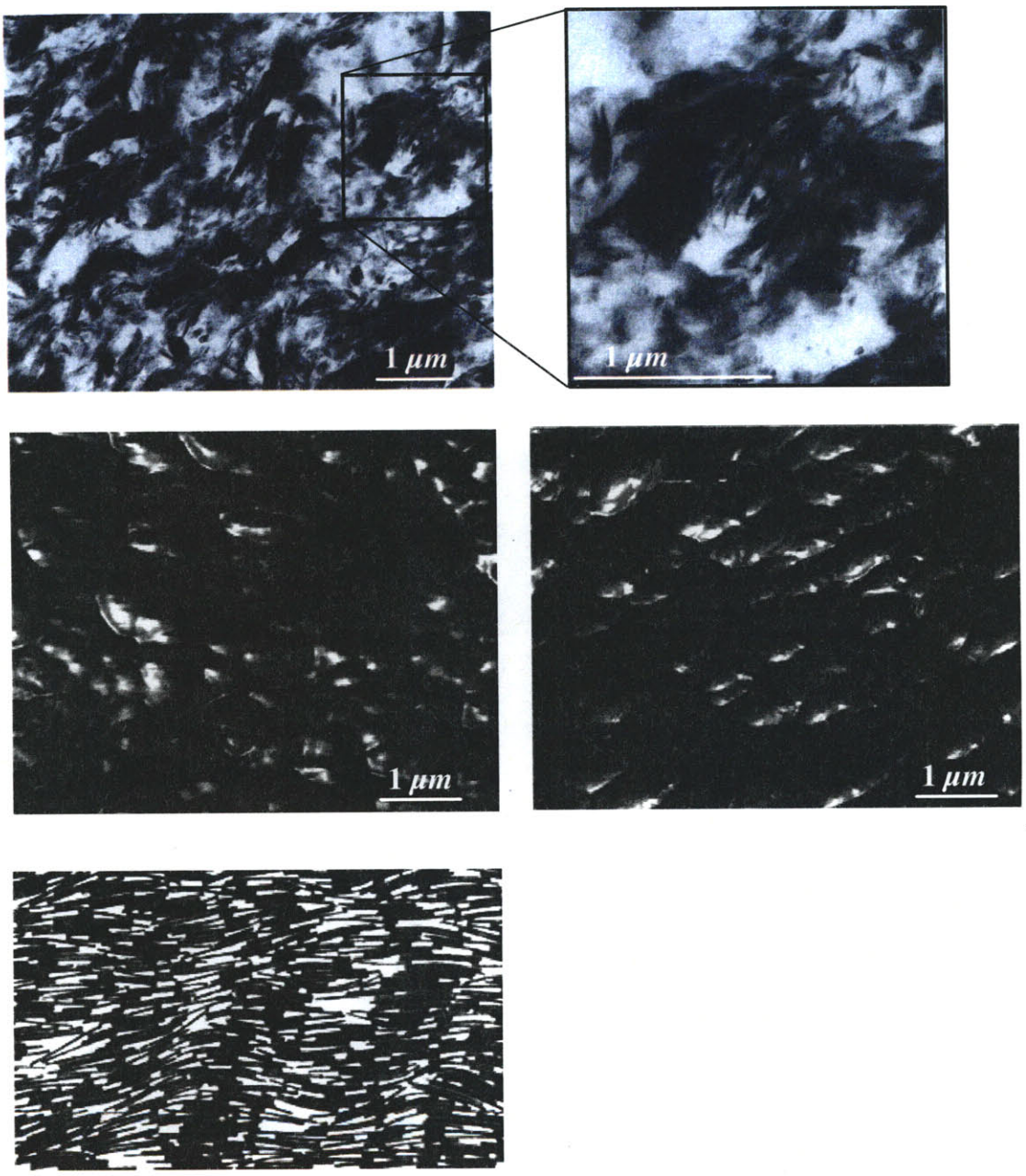

Figure 9-2: Top: TEM image of consolidated clay from [28], showing an equidimensional submicron-sized granular structure consisting of aligned clay minerals (inset). Recalled from Fig. 8-1. Middle: AFM images of Shale 3, showing an equidimensional submicron-sized granular structure, regardless of which surface is exposed (left: $x3$-direction, right: $x1$-direction). Recalled from Fig. 8-1. Bottom: Photograph of a compressed 2-d system of randomly deposited cardboard platelets. Density of platelets is non-uniform, with areas of higher density possessing characteristic length scales on the order of the long dimension of the 2-d platelet model (image scaled so this long dimension corresponds to the 1 μm scale bar in the other images). From [162].

9.1.2 The Elementary Building Block as an Effective Solid Particle

The second hypothesis is that the elementary building block represents an effective solid which is composed of an aggregate of clay particles. In this case, the morphology of the elementary building block corresponds to the aggregated clay particles rather than individual clay platelets. TEM images obtained by Bryant et al. [28] provide good visual evidence for this hypothesis. Figure 9-2 (top), recalled from Figure 8-1, suggests that individual clay platelets have agglomerated to form effective particles, roughly circular in cross section. The idea that individual clay particles come together to form layered clusters, groups, or domains, was proposed as early as 1960 by Aylmore and Quirk [10], and some variation of this concept has been employed in many subsequent models of clay in shale [93], [157], [172]. It is agreed that the depositional history of the clay platelets, and the ensuing stress history of the buried shale, leads to alignment of clay minerals within these groups. In the emerging field of polymer-clay nanocomposites, Brune and Bicerano [27] introduced the concept of a 'pseudoparticle' consisting of an isotropic stack of individual clay platelets, which was also adopted and expanded upon by Sheng et al. [161].

The AFM images seen in Fig. 9-2 (middle), recalled from Figure 8-1, also provide evidence consistent with the hypothesis that the elementary building block represents agglomerations of clay particles. Under this hypothesis, the 'blobby' shapes seen in the AFM images are, in fact, the sought agglomerated packings of individual clay platelets. The radius of curvature of the AFM tip employed in this study is about 10 nm, which means the tip is too large to fit in the small spaces between individual clay platelet particles when they are clumped together. In other words, the AFM scan is unable to image individual clay particles, but provides evidence of a random organization of aggregations of clay particles.

Model experiments from Sherwood and Van Damme [162], who considered the granular physics of platelet particles undergoing slow deposition and compaction, may be sufficient to explain the origins of the microstructure of the elementary building block of shale materials. Sherwood and van Damme [162], [178] performed experiments and simulations of the 2-dimensional deposition and compaction of elastic, platelet-like particles. Inspection of their results, as seen in Figure 9-2 (bottom), suggests that the compacted platelets tend to pack with areas of higher and lower density. The areas with higher density are roughly equidimensional, with a characteristic size that is similar to the long dimension of the platelet. It is likely

that this effect is enhanced by the surface chemistry (i.e. double-layer theory of clays [138]) in natural shale materials, which was not modeled by Sherwood and Van Damme's cardboard platelets. Even without this enhancement, the results are compelling.

In the first hypothesis, the mechanical behavior of the elementary building block should be related to the mechanical behavior of single clay platelet particles, and the contacts between them. For the second hypothesis, the mechanical behavior of the elementary building block should instead be related to the mechanical behavior of a composite group of clay platelet particles.

9.2 Origin of Intrinsic Anisotropy of the Elementary Building Block

This discussion centers on a quantitative description of the various approaches to modeling the elastic anisotropy of shale, and on comparisons with other measurements and estimations of the elastic behavior of the clay minerals in shale. Comparing these approaches and measurements with the model of the elementary building block can provide some additional insight about the origin of intrinsic anisotropy in the model. In addition, comparing previously measured elastic properties of single clay minerals and groups of clay minerals may validate one of the hypotheses regarding the mechanical morphology of the elementary building block.

9.2.1 Comparison with Single Clay Minerals

Direct measurements of clay minerals are scarce because of the difficulty of probing the mechanical behavior of such a small particle. One widely cited attempt assessed the anisotropic stiffness of a large single crystal of muscovite using ultrasonic techniques [5]. Vaughan and Guggenheim [180] used a Brillouin scattering technique to assess the anisotropic stiffness of muscovite and found similar values. Katahara [109] suggested that the structure and composition of illite and muscovite are very similar, so that muscovite results could be used for illite. Katahara also suggested that anisotropic elasticity values for chlorite and kaolinite could be estimated from the muscovite results by scaling with the bulk density of the minerals. The scaling of elastic moduli with bulk density for silicate minerals is confirmed in a review of the

	C_{11}	C_{33}	C_{44}	C_{12}	C_{13}	M_1	M_2	M_3
Muscovite								
Ultrasonic [5]	178	55	12	42	15	118		46
Brillouin Scattering [180]	181	59	17	48	24	127		55
Mol. Dyn. [160]	238	80	30	60	30	178		82
Montmorillonite								
Mol. Dyn.(crystal + space) [130]	348	288	346	170	105	117	127	107
Mol. Dyn.(crystal only) [130]	543	449	540	265	164	183	199	167
Chlorite								
Density Scaling [109]	182	111	12	52	21	120		67
Kaolinite								
Density Scaling [109]	190	58	16	43	30	131		53
Clay Minerals								
Nanoindent. Scaling (Eq. 6.10)						25		16
Nanoindent. Measurement (Eq. 6.12)						21		16
Elementary Building Block (Eq. 8.1)	45	24	4	22	18	26		15

Table 9.1: Reported stiffness properties of single clay crystals.

literature presented by Chen and Evans [37].

Elasticity results from Molecular Dynamics simulations of clay and clay-like minerals also demonstrate intrinsic elastic anisotropy. Orthotropic results for montmorillonite have recently been reported by Manevitch and Rutledge [130], and Seo et al. [160] reported results for muscovite. These studies demonstrate that the atomic structure of the clay minerals are responsible for their intrinsic elastic anisotropy. Table 9.1 summarizes the reported data from measurements, extrapolations based on measurements and density scaling relationships, and molecular dynamics simulations. For comparison to nanoindentation results, Table 9.1 also reports equivalent indentation moduli, translated via Eqs. (3.46) and (3.48).

Despite all the evidence in favor of anisotropic elastic properties for clay minerals, many researchers still model individual clay minerals as isotropic particles. Hornby et al. [93] used an isotropic clay mineral as the starting point for their pioneering modeling work for shale elasticity, and in the polymer-clay nanocomposite community, isotropic clay particles are often seen as sufficient for modeling composite behavior [161], [37].

While the nanoindentation results do demonstrate intrinsic anisotropy of the elementary building block (data recalled from Eqs. (6.10), (6.12), and (8.1) are also presented in Tab. 9.1) they give results which are almost an order of magnitude less than the reported stiffness values of individual clay minerals. Although the clay mineral contact stiffness may differ from the clay mineral particle stiffness, these data do not provide strong support for the hypothesis that the elementary building block represents a single clay particle.

9.2.2 Comparison with Groupings of Clay Minerals

Debates over the origin of anisotropy continue amongst researchers who consider 'effective' particles as a microstructural unit of clay behavior. Most researchers who model shale starting from a basic unit consisting of a group of clay particles consider isotropic properties. These modeling approaches must introduce macroscopic anisotropy through the geometry of particles or pores. Hornby et al. [93] pioneered this approach, employing anisotropic particle shapes in an effective-medium modeling approach. Like the other models that follow a similar approach, Hornby's model requires the use of shale-specific orientation distribution functions to describe the microstructure of the material. Hornby et al. [93] considered digital image processing of SEM images to determine orientation distribution functions, while Lonardelli et al. [124] used an X-ray synchrotron diffraction technique to attempt to quantify orientation distribution functions. Ulm et al. [172] also employed a geometrical approach to introducing anisotropy, but modeled the orientation of pores rather than the orientation of particles, calibrating an orientation distribution function from macroscopic data. All these approaches suggest that the degree of anisotropy increases with porosity. Hornby provided some experimental evidence for this suggestion [94], but porosity differences in these data arose from changes in the sample confining pressure rather than actual porosity differences between samples.

Most other macroscopic observations, however, demonstrate an increase in the degree of anisotropy with an increase in the density of shale [108] or a decrease in the overall porosity [56], [62], [94], [103], [107], [183]. These observations give support to the theory that individual clay particles, whether they are single clay minerals or 'effective' particles, are anisotropic. Modeling approaches that assume intrinsically anisotropic clays suggest that shales with more tightly packed clays have greater anisotropy than shales with more loosely packed clays [157],

[69]. In other words, although the most-cited shale models typically consider isotropic clay properties, anisotropic clay properties are more appropriate.

To compare the transversely isotropic stiffness values for the elementary building block model, provided in Eq. (8.1), with previously reported isotropic stiffness values, quasi-isotropic experimental values need to be calculated. The Voigt-Reuss-Hill average of transversely isotropic crystals (see e.g. [7]) permits this estimation by considering quasi-isotropic bulk and shear moduli:

$$K_{VRH} = \frac{1}{2}(K_V + K_R) \tag{9.1a}$$

$$G_{VRH} = \frac{1}{2}(G_V + G_R) \tag{9.1b}$$

where K_V, and G_V represent the Voigt estimates of bulk and shear moduli:

$$K_V = \frac{1}{9}(2C^s_{11} + C^s_{33}) + \frac{2}{9}(C^s_{12} + 2C^s_{13}) \tag{9.2a}$$

$$G_V = \frac{1}{15}(2C^s_{11} + C^s_{33}) - \frac{1}{15}(C^s_{12} + 2C^s_{13}) + \frac{1}{5}(2C^s_{44} + C^s_{66}) \tag{9.2b}$$

and where K_R, and G_R represent the Reuss estimates of bulk and shear moduli:

$$K_R = \frac{1}{A(C^s_{11} + C^s_{12} + 2C^s_{33} - 4C^s_{13})} \tag{9.3a}$$

$$G_R = \frac{15}{2A(2(C^s_{11} + C^s_{12}) + 4C^s_{13} + C^s_{33}) + 6(1/C^s_{44} + 1/C^s_{66})} \tag{9.3b}$$

where $A = \left[C^s_{33}(C^s_{11} + C^s_{12}) - 2(C^s_{13})^2\right]^{-1}$. The results of this calculation for the stiffness coefficients associated with the elementary building block model (Eq. 8.1) are:

$$K^s_{VRH} = 23.9 \text{ GPa} \tag{9.4a}$$

$$G^s_{VRH} = 6.7 \text{ GPa} \tag{9.4b}$$

The Voigt-Reuss-Hill average enables a direct comparison between various estimates of the elastic behavior of groups of clay available in the literature and the elastic behavior of the elementary building block, represented by $\mathbb{C}_s$. This comparison is shown in Table 9.2. The

	K^s (GPa)	G^s (GPa)
Hornby et al. [93]	22.9	10.6
Berge and Berryman [14]	21.4	6.7
Mavko et al. [133]	25	9
Vanorio et al. [179]	12	6
Voigt-Reuss-Hill average of $\mathbb{C}_s$ (Eq. (8.1))	23.9	6.7

Table 9.2: Reported stiffness properties of groups of clay platelets, extrapolated for solid clays in shale.

bulk modulus reported by Hornby et al. [93] was obtained by extrapolating to zero porosity the results of core data analysis by Marion et al. [131] for a shale specimen with 25% porosity. Berge and Berryman [14] suggested their values to be representative properties of natural clay composites based on a large compilation of laboratory measurements by Castagna et al. [32]. The values cited by Mavko et al. [133] correspond to properties of gulf clays that were extrapolated from empirical relations for mixed lithologies to 100% clay. Finally, the clay properties suggested by Vanorio et al. [179] were obtained from acoustic velocity measurements of clay powders in dry, compacted form and in water suspensions. The quasi-isotropic elastic properties of the elementary building block compare extremely well to the values reported by Hornby et al., Berge and Berryman, and Mavko et al. for extrapolated values of the solid clay in shale. There is a discrepancy with the elastic content reported by Vanorio et al. [179] which may be related to their use of a different experimental methodology. In particular, they compacted clay powders into aggregates or diluted them into water suspensions in order to make measurements, while the data sources for the other studies are directly related to testing of actual clay-bearing rocks.

It is clear that the elastic behavior of the elementary building block compares much better to previously reported values for groups of clay minerals than to previously reported values for single clay particles. The elastic constants of single clay minerals are consistently and significantly larger than those of the elementary building block, while isotropic values for groups of clay minerals are in good agreement with the quasi-isotropic values associated with the elementary building block (Tab. 9.2). The good agreement of the Voigt-Reuss-Hill averaged quasi-isotropic properties with previously reported isotropic values is an indication that the elastic properties of the elementary building block of shale are a good representation of the in

situ elastic behavior of shale. The main difference, however, is that the elementary building block model presented here captures the experimental observations of intrinsic anisotropy, where previous models considered an isotropic solid.

Understanding that the elementary building block represents the mechanical behavior of a group of clay minerals, based on the good agreement between elastic properties for the elementary building block and previously reported elastic properties for groups of clay minerals, has implications about the origin of the elementary building block model. First, this understanding points to the reason why clay mineralogy apparently plays little role in the mechanical behavior of porous clay in shale. The building block already represents averaged properties of the different clay minerals. In addition, the understanding for elastic behavior provides additional support for the hypothesis that the elementary building block model represents a group of clay particles.

9.3 The Nano-Granular Origin of Friction and Cohesion

With the origin of spherical mechanical morphology and intrinsic elastic anisotropy better understood, focus is turned towards the origin of the cohesive-frictional strength behavior of the elementary building block. Recall from Section 5.3.1 that Fritsch et al. [72] provided a micromechanical basis for the Drucker-Prager strength criterion, based on rigid polycrystals with Mohr-Coulomb type interfaces. Understanding of the elementary building block as a group of clay particles fits in well with this idea, and suggests that the strength behavior of the elementary building block may find its origin in the interfaces between individual clay particles. This understanding is explored first for cohesion, and then in terms of some contemporary views on the physical basis for friction. Finally, fractal packing concepts associated with space filling bearings may provide a rational basis for the scaling of friction with average clay packing density.

9.3.1 Cohesion and Coordination Number or Bond Length

Exploring the physical mechanisms at the origin of cohesion between clay particles requires investigating a morphological parameter linked with packing density, the coordination number.

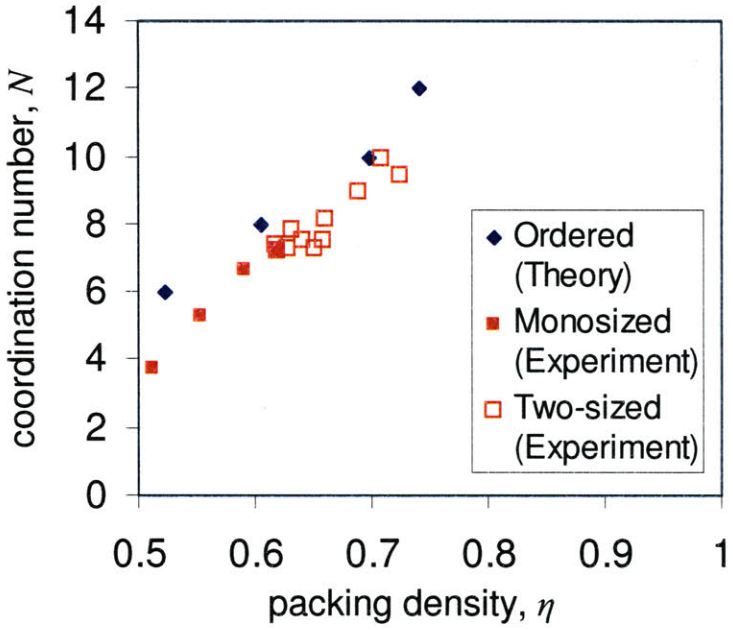

Figure 9-3: Mean coordination numbers determined for theoretical packings of particles and for experiments on random packings of monosized and two-sized glass beads. For experimental values, the mean packing densities are reported. Mean coordination numbers increase roughly linearly with packing density. Data from [141], replotted in terms of packing density.

The coordination number, the number of contacts between particles, increases with the packing of particles. Oda [141] has determined the mean coordination numbers of randomly packed monosize and two-sized spherical assemblies. These results, as well as theoretical packings of spheres, are recalculated in terms of packing density and displayed in Figure 9-3. The relationship between coordination number and packing density is relatively linear, and corresponds well to the trend of cohesion and friction angle displayed in Figure 7-20 (bottom).

The concept of a constant attraction force between two particle surfaces, such as that which comes from cementation, highlights the link with coordination number. Consider first that there exists a constant attraction force between two particles in contact. The presence of a cement, in the form of carbonates, silica, alumina, or organic compounds, can lead to cohesive forces between particles [138]. For a random assembly of cemented spheres, Ingles [100] has derived an estimate of the cohesion of the system that varies linearly with the coordination number, as well as on the relative amount of cement and the average bond strength per contact zone.

On the other hand, a concept of attraction forces which vary with bonding distances suggests that cohesion, like friction, may be linked with the spacing between particles. If the source of cohesion is hydrogen bonding or electrostatic attraction, then the cohesive forces between particle surfaces can vary with the bond distance between the materials. Electrostatic attractions become significant for separation distances less than 2.5 nm [138]. In shales, where the average pore throat radius is on the order of 10-20 nm (Tab. 2.5), separation distances between some particles should be smaller than 2.5 nm, with smaller distances for more densely packed samples. Either explanation agrees with the experimental observations.

9.3.2 The Physical Origin of Friction: Contemporary Views

The origin of friction is still a thriving research topic [76], [78], [88], [140], [176], particularly in granular materials [113], [120], [152]. Researchers have long sought to understand the physical mechanisms responsible for friction between solids. Frictional behavior is described by Amontons' Laws (recall Tab. 3.1); the surface friction force increases linearly with the load pushing two objects together, while remaining independent of the surface area of the contact. The traditional model used to explain these observations is purely geometric - that frictional forces are generated by the interlocking of surface asperities [25]. For one surface to slide past another, it must be lifted up and over a surface asperity of some slope. An energy argument against this model was presented as early as 1804 by Leslie [76]. Surfaces with asperities that are both periodic and aligned fit the geometrical model well. But for randomly rough surfaces, upwards sloping asperities are balanced by downwards sloping asperities. In this case, frictional force vanishes, and Amontons' Laws remain unexplained.

A theory which recognizes that material surfaces are covered by adsorbed molecules (i.e. hydrocarbons, water molecules, etc.) has been proposed as a solution to this problem by Müser et al. [140]. Introducing enough of these small, mobile molecules into the interface yields a frictional coefficient that obeys Amontons' Laws. Another new modeling approach to the origin of friction has been presented Gerde and Marder [78]. This approach suggests that a propagation of self-healing cracks, similar to sliding a rug across the floor by moving a bump, is a micro-scale mechanism which leads to the results described by Amontons' Laws.

With the models of Müser et al. and Gerde and Marder in mind, the relationship between

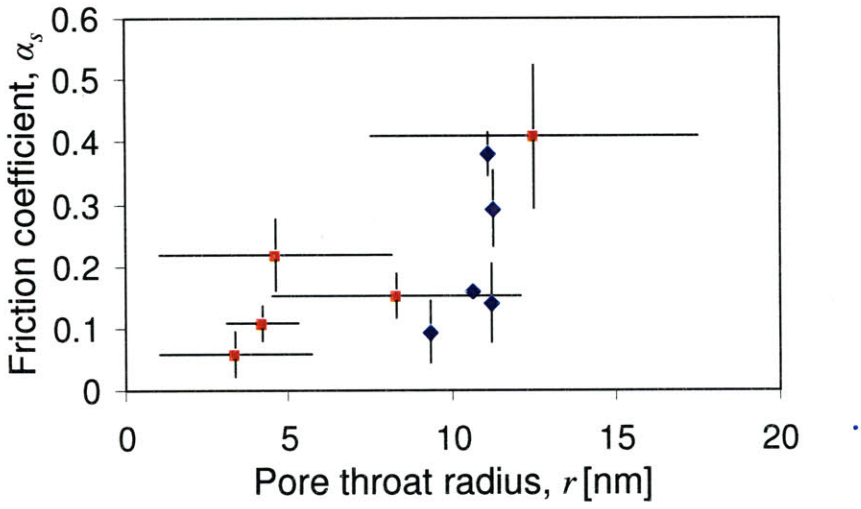

Figure 9-4: Friction coefficient determined from indentation analysis versus mean pore throat radius determined from mercury porosimetry (Tab. 7.3) for the GeoGenome Shales (red squares) and Woodford Shales (navy diamonds). Uncertainties for experimental data represent plus and minus one standard deviation.

friction and packing density (Fig. 7-20 (top)) might be better explained by considering the interactions of particles and pores. For adsorbed molecules to be present and mobile between surfaces, some space must exist between particles. Similarly, some space between particles must be present to permit a self-healing microcrack to form. In Section 2.3.4, a link was established between the average clay packing density and pore throat radius determined by mercury porosimetry. Figure 9-4 redisplays the friction results as a function of the mean pore throat radius where this data is available. The friction coefficient increases as the mean pore throat radius increases. Loose packings of particles apparently permit larger pore spaces, which in turn permit the possibility of larger asperities under a conventional frictional model, more space for mobile molecules in the Müser et al. model, or greater ability for microcracks to form in the Gerde and Marder model. The result in any case is that the friction coefficient is increased when the spaces between particles are larger. Conversely, in the limit of zero porosity, or infinitely small pore throat radius, the problem is reduced to particles without asperities, bare incommensurate surfaces, or inhibition of microcracks; the friction coefficient goes to zero.

9.3.3 Space-Filling Bearings and Fractal Packing

The reviewed mechanisms at the origin of friction seem to agree with the experimental shale data, but they do not yet provide an explanation for the form of the scaling relationship between friction and packing density. To explore this link, concepts of space-filling bearings and fractal packings are reviewed. The highly compacted states of many of the shale materials cannot be achieved with monosized spherical packings, with maximum packing densities of $\eta = 0.74$ corresponding to the face-centered cubic packing [64]. Instead, the effective particle sizes in the densely packed shales must be highly disperse. The limit case of a dense packing of disperse grain sizes is the space-filling bearing [89] which almost perfectly fills a 3-D space. The property defining a bearing is that slipless rotations around an arbitrary axis are allowed [89], [129] [128].

Background

The idea of the space filling packing is motivated by considering the Apollonian sphere packing, a perfect space filling packing which starts with mutually touching spheres on the vertices of a tetrahedron. A solid sphere is then placed inside an existing pore so that the new sphere occupies the maximum volume. This procedure creates smaller pores, which are again filled with smaller solid spheres that occupy the maximum volume, and this recursive filling is naturally associated with fractals.

In any fractal packing, the number of spheres with radii larger than ϵ follows an asymptotic relation [20]:

$$N(\epsilon) \sim \epsilon^{-D} \tag{9.5}$$

in which D is the fractal dimension of the packing. Other means of determining the fractal dimension are by the sum of perimeters (sphere circumferences) $s(\epsilon)$, the sum of surface area $p(\epsilon)$, or the sum of volume $v(\epsilon)$ of spheres [20]:

$$s(\epsilon) \sim \epsilon^{1-D} \tag{9.6a}$$

$$p(\epsilon) \sim \epsilon^{2-D} \tag{9.6b}$$

$$v(\epsilon) \sim \epsilon^{3-D} \tag{9.6c}$$

The Apollonian sphere packing is well-studied, and is known to be self-similar; the fractal dimension of the Apollonian packing has been computed numerically to a high degree of precision [20]:

$$D = 2.474 \tag{9.7}$$

Fractal Dimension of Clay Particles

Relating the concept of a space-filling bearing to the packing of clay particles requires identification of their fractal dimension. The available experimental data provide two possibilities, one relating to the characteristic pore sizes of each shale material, and the other relating to the apparent frictional behavior of each material.

The first approach uses a relation between the clay porosity and the pore throat radius for each shale sample. Recall from Eq. (2.21) that clay porosity $n = 1-\eta$. A relationship between clay packing density and pore throat radius was first suggested in Sec. 7.1.5 (Fig. 7-18). Figure 9-5 redisplays this data in terms of clay porosity versus the pore throat radius for each shale where the data are available. A power function representative of a volume fractal is fit to this data, giving:

$$n = \left(\frac{\epsilon}{\epsilon_0}\right)^{3-D} \; ; \; D = 2.523; \epsilon_0 = 168 \text{ nm} \tag{9.8}$$

where D is the fractal dimension, and ϵ_0 is a characteristic size (correlation length).

The second approach to identifying the fractal dimension of the clay packings is to investigate the scaling of friction with packing density. Recall from Table 3.1 that Amontons' Laws of friction state that the frictional force is proportional to the normal force or load holding the two surfaces together, and that this force is independent of the area of the surfaces. This means that either forces or stresses (force per area) can be used to express this observation; i.e. in force:

$$|F_t| + \mu F_n = 0 \tag{9.9}$$

or in stress:

$$|T_t| + \mu \, T_n = 0 \tag{9.10}$$

where $T_t = F_t/A_s = \underline{t} \cdot (\boldsymbol{\sigma} \cdot \underline{n})$ is the tangential shear stress on the material surface oriented by

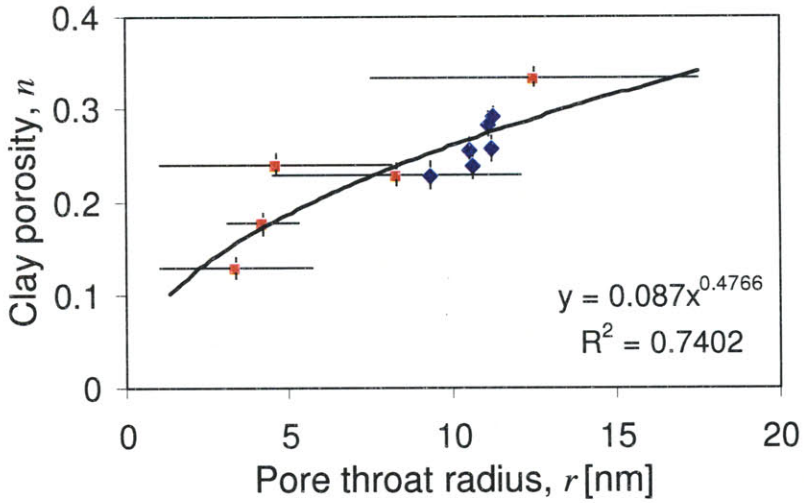

Figure 9-5: Mean clay porosity n, determined from nanoindentation scaling analysis versus pore throat radius, r, from poromercury intrusion (Tab. 7.3) for the GeoGenome Shales (red squares) and Woodford Shales (navy diamonds). The power law fit (black line) is given by the displayed equation. Uncertainties for experimental data represent plus and minus one standard deviation.

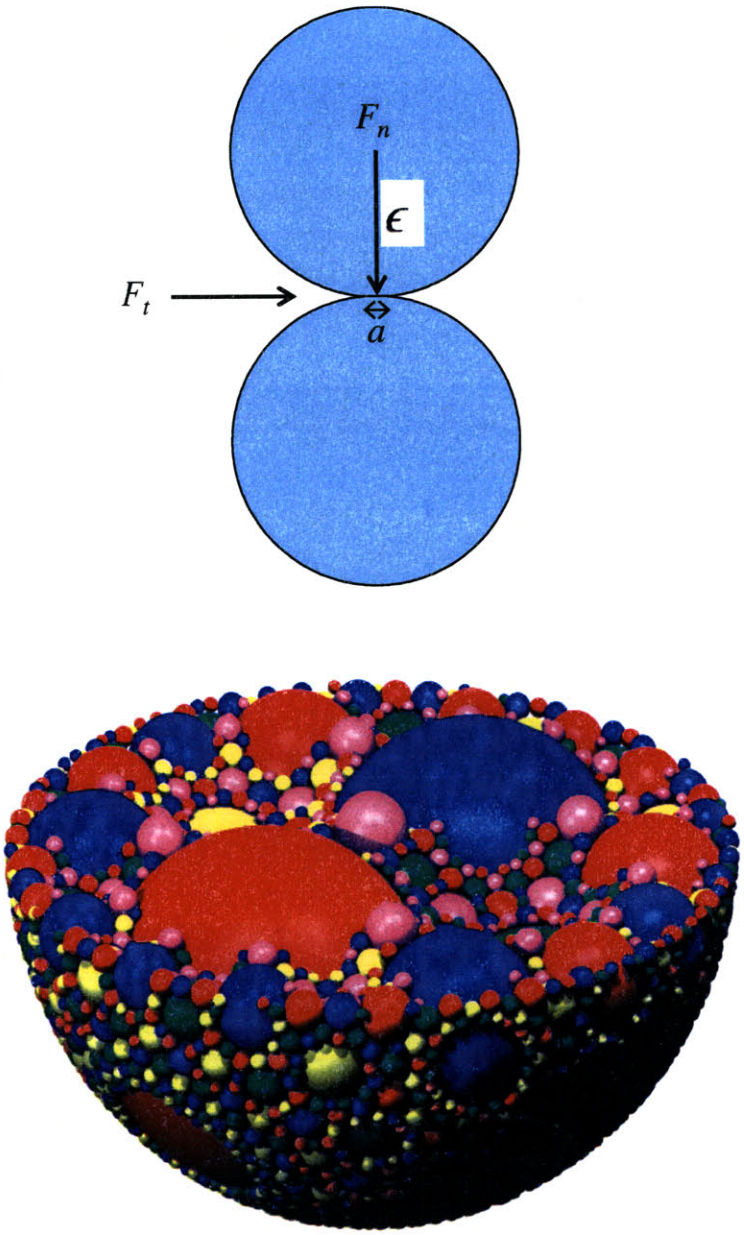

Figure 9-6: Top: Cartoon suggesting the use of a distorted base dimension system for the frictional contact problem. The normal length scale, ϵ, is much larger than the tangential length scale, a. Bottom: A cartoon of the Apollonian packing, from [20].

unit outward normal $\underline{n}$, and $T_n = F_n/A_s = \underline{n} \cdot (\boldsymbol{\sigma} \cdot \underline{n})$ is the normal stress acting on the same surface (with A_s being the contact surface). Then Amontons' Laws may be expressed through the friction coefficient μ:

$$\mu = \frac{|F_t|}{F_n} \tag{9.11}$$

Dimensional analysis in an extended base dimension system provides a way to link the friction coefficient to length dimensions. Consider an extended $L_n L_t MT$ base dimension system [97], where L_n stands for the length dimension measured in the normal direction, and L_t for the length dimension in the plane of contact of the two surfaces, such that the dimension function of any quantity Q can be expressed as:

$$[Q] = L_n^{\alpha} L_t^{\beta} M^{\gamma} T^{\delta} \tag{9.12}$$

This extended dimension system is useful for the contact problem where the magnitude of the length corresponding to the normal dimension is much larger than the magnitude of the length corresponding to the contact area, i.e. the lengths represent a distored system as seen in Figure 9-6 where the length scale associated with the normal direction, $\epsilon << a$, the length scale associated with the contact area and the tangential force. In this extended base dimension system, forces F_t and F_n have the following dimension functions:

$$[F_t] = L_t M T^{-2} \tag{9.13a}$$

$$[F_n] = L_n M T^{-2} \tag{9.13b}$$

and the friction coefficient:

$$[\mu] = \frac{[T_t]}{[T_n]} = \frac{L_t}{L_n} \tag{9.14}$$

Eqs. (9.5) and (9.6) give asymptotic relationships defined by the fractal dimension D, giving the number of all spheres $N(\epsilon)$, the sum of perimeters $s(\epsilon)$, the sum of surface area $p(\epsilon)$, and the volume of spheres $v(\epsilon)$ of all spheres in the packing with radii larger than ϵ. The perimeter of a sphere is measured along any circle, $s = 2\pi\epsilon$, whose normal goes through the center of the sphere and therefore in an extended base dimension system depends only on L_n, without

requiring a tangential measure:

$$[s] = L_n \tag{9.15}$$

In return, the surface area of a sphere corresponds exactly to the tangential area measurement with dimension L_t along tangent planes, given the dimension of surface area p:

$$[p] = L_t^2 \tag{9.16}$$

Substituting these dimensional considerations in the dimension function of the friction coefficient, Eq. (9.14), gives:

$$[\mu] = \frac{L_t}{L_n} = \frac{[p]^{1/2}}{[s]} \tag{9.17}$$

Finally, using the fractal scaling relations, Eqs. (9.6b) and (9.6a) in the previous relations, Eq. (9.17), yields the following asymptotic scaling relation for the friction coefficient:

$$\mu \sim \frac{\sqrt{p(\epsilon)}}{s(\epsilon)} \sim \frac{\sqrt{\epsilon^{2-D}}}{\epsilon^{1-D}} = \epsilon^{D/2} \tag{9.18}$$

The goal of this analysis is to provide a link between packing in porous composites and the friction coefficient. The development of the fractal friction scaling, Eq. (9.18) is based on the packing of solid particles, while the fractal dimension was previously calculated by considering porosity and pore throat radii. A generalized pore-solid fractal model, representative of a composite containing solids, pores, and a porous composite, features symmetry of fractal scalings and identical fractal dimensions for pore and solid size relations [146] [1]. This justifies a combination of the fractal friction coefficient scaling, Eq. (9.18) and the fractal porosity scaling, Eq. (9.8), yielding:

$$\mu \sim \left(n^{\frac{1}{3-D}}\right)^{D/2} = n^{\gamma};\ \gamma = \frac{D}{6-2D} \tag{9.19}$$

Eq. (9.19) provides the means to determine the fractal dimension D from the friction coefficient. For the experimental determination, the friction coefficient $\mu = \tan\varphi$ is calculated

[1] Although Perrier et al. [146] showed the pore-solid fractal model to be a generalized case of pore fractal models or solid fractal models, in those special cases, fractal symmetry may not exist between pore sizes and solid sizes when a cutoff on fractal scaling exists.

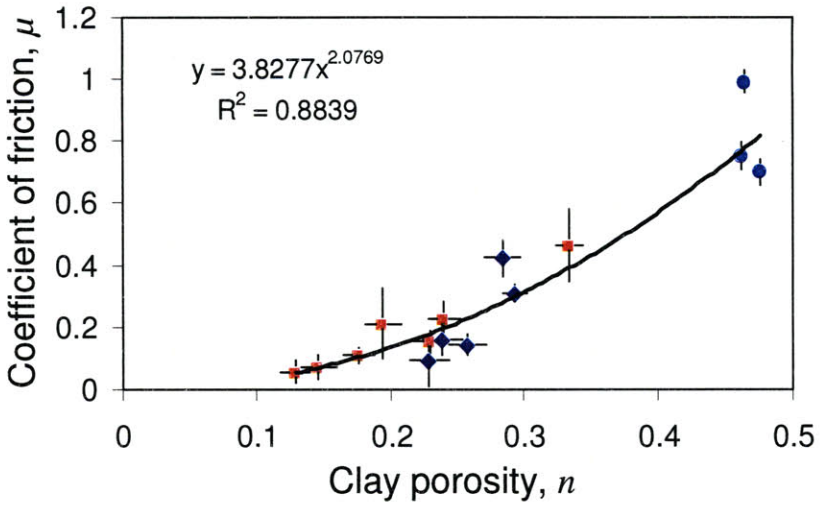

Figure 9-7: Scaling of Mohr-Coulomb friction coefficient μ (determined from experimental data with the internal cone, Eq. 9.20) versus clay porosity, $n = 1 - \eta$ for the GeoGenome Shales (red squares), Woodford Shales (navy diamonds) and Boston Blue Clay samples (light blue circles). The power law fit (black line) is given by the displayed equation. Uncertainties for experimental data represent plus and minus one standard deviation.

from the internal cone (Eq. (5.40)):

$$\sin\varphi = \sqrt{\frac{3\alpha^2}{3-\alpha^2}} \tag{9.20}$$

The power law fit is shown in Figure 9-7. The experimental fit is $\mu \sim n^{2.0769}$; thus:

$$D = \frac{6\gamma}{2\gamma+1} = 2.418 \tag{9.21}$$

This fractal dimension correlates well with $D = 2.523$ determined from the porosity–pore throat radius scaling (Fig. 9-5). It thus seems that the 'apparent' friction coefficient of the clay particles within the elementary building block exhibits fractality, and that this fractal dimension is not far from the fractal dimension of the perfect Apollonian packing, seen in Figure 9-6 (bottom), for which $D = 2.474$.

9.3.4 Fractal Packings and the Origin of Frictional Scaling in Shale

The good correlation between the fractal dimension of a perfect Apollonian packing and the fractal dimensions estimated for the packing in shales implies that the porous clay in shale can come close to a perfect packing. That is, during the slow sedimentary deposition process and subsequent mechanical and chemical diagenesis of shale materials, the packing of clay minerals asymptotically tends towards the densest possible packing. In such a perfect packing, with zero porosity, the solid clay in shale is frictionless. Such a perfect material likely does not exist in nature, however, as there must be a cutoff on minimum particle and pore size, at least at the scale of atoms and individual molecules. The presence of porosity can then be viewed as an imperfect space-filling porosity which introduces frictional behavior in accordance with contemporary views on the origin of friction such as those provided by Müser et al. [140] or Gerde and Marder [78].

The fractal scaling functions thus provide an opportunity to quantitatively link theories about the origin of frictional behavior with experimental observations. The power law scaling relationship with the Mohr-Coulomb coefficient of friction, derived from the fractal space-filling packing and given in Eq. (9.19), can be translated into another useful form. Making use of the internal cone, Eq. (9.20) and the fact that packing density $\eta = 1 - n$, gives:

$$\sin^{-1}\left(\sqrt{\frac{3\alpha_s^2}{3-\alpha_s^2}}\right) = \tan^{-1}\left(3.8277\,(1-\eta)^{2.0769}\right) \tag{9.22}$$

where α_s is the Drucker-Prager friction coefficient. The cohesion, defined as a function of friction coefficient α_s and the constant contact hardness h_s in Eq. (7.6) may also be calculated using the result of Eq. (9.22). Eq. (9.22) may be solved numerically, and compared with the empirical scaling given by Eq. (8.2) and first seen in Figure 7-20. Figure 9-8 recalls that data and empirical scaling, along with a numerical solution of Eq. (9.22). The translation of the fractal power law scaling for friction, Eq. (9.19), into $\alpha_s - \eta$ space fits the experimental data well, and recovers the general shape of the empirical scaling, justifying that functional form and the use of that model relationship. In turn, the cohesion scaling generated using the fractal scaling for α_s corresponds well to the cohesion scaling generated from the empirical relationship for α_s.

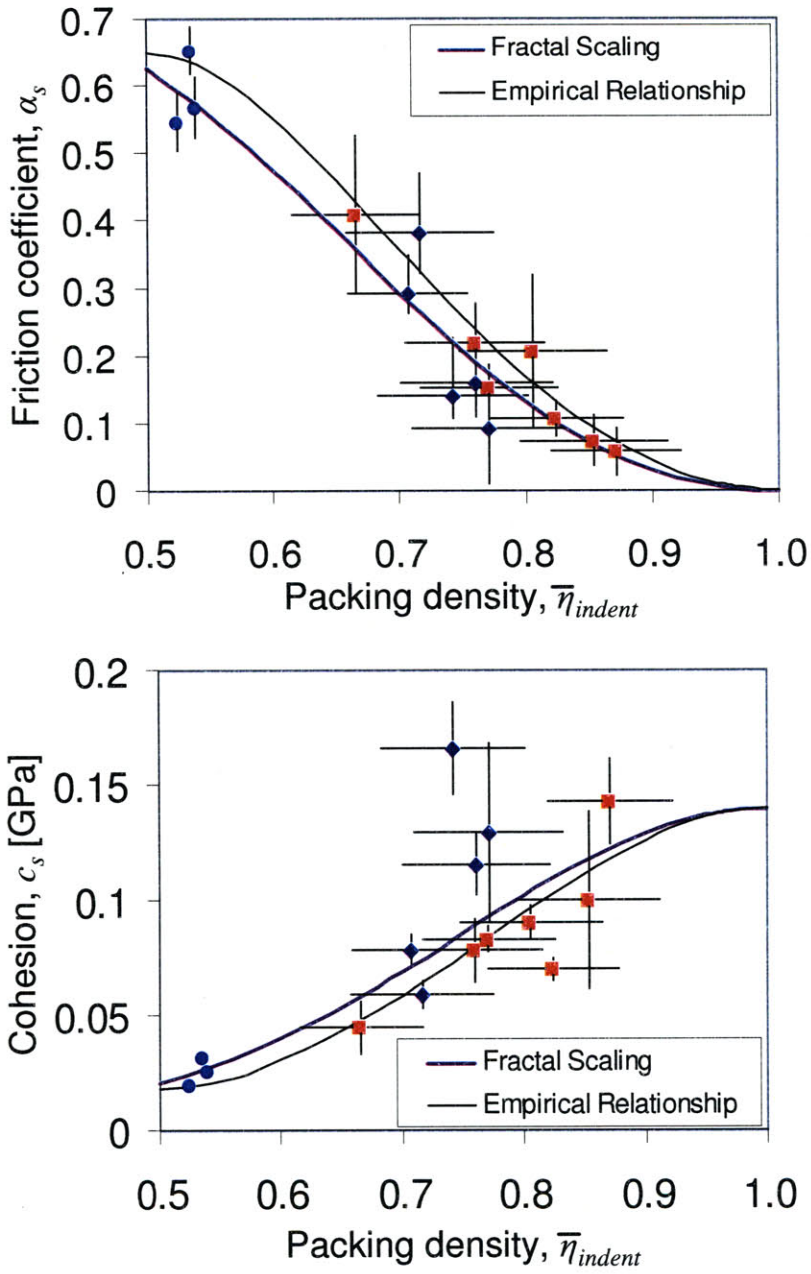

Figure 9-8: Scaling between the Drucker-Prager friction coefficient and clay packing density and cohesion and clay packing density, recalled from Figure 7-20. The fractal scaling relationship for friction coefficient α_s, Eq. (9.22) is very similar to the empirical scaling relationship, Eq. (8.2), presented earlier. Likewise, the related values for for cohesion c_s, using the fractal scaling or the empirical relationship for α_s, are very similar. Included are data from the GeoGenome shales (red squares), Woodford shales (navy diamonds), and Boston Blue Clay samples (light blue circles). Uncertainties represent two standard deviations.

9.4 Chapter Summary

This chapter has explored the physical origins of the elementary building block model of shale. An attempt to reconcile the various pieces of visual evidence, along with the measurements of mechanical behavior by nanoindentation, suggests that the elementary building block is a solid, polycrystal group of clay particles rather than a single clay particle. Moreover, despite the visual observations from SEM images of a platelet structure of clay particles, a body of other evidence begins to mount that suggests the mechanical behavior of the porous clay composite has a mechanical morphology which may be represented by spheres. This spherical representation highlights the importance of the randomness of contact between aggregations of individual clay particles.

Comparison with previously reported values for the elastic properties of clay minerals also gives support to an understanding of the elementary building block as a solid agglomeration of individual clay minerals. Reported stiffness of individual clay minerals demonstrates their intrinsic anisotropy, but the values are much higher than those obtained through nanoindentation testing or back-calculation from macroscopic measurements. Instead, comparing quasi-isotropic stiffnesses from nanoindentation and back-calculation with previously reported isotropic stiffness values for groups of clay minerals in shale gives a very close match. However, the elementary building block model retains intrinsic elastic anisotropy associated with the stiffnessess of individual clay minerals. This feature will permit a better match of model predictions to experimental data.

Finally, the origin of cohesive frictional behavior in the elementary building block was explored. Possibilities for the origin of cohesion, and contemporary views at the origin of frictional behavior were introduced, and seen to be closely linked with packing density and pore sizes, helping to explain the scaling of these properties within the solid elementary building block. Finally, a fractal scaling analysis of the results demonstrated that the elementary building block in shale materials possesses fractal properties, with a fractal dimension close to that of the perfect Apollonian packing. This scaling, linked with the slow deposition history and diagenesis processes, suggests that a perfectly packed shale material would exhibit frictionless behavior, although such a state is never reached in nature. Instead, the fractal scaling analysis provides a quantitative link between the contemporary theories on the origin of frictional behavior,

which depend on the development of spaces between solid contact surfaces, and the packing and porosity of the porous clay in shale.

Improving the understanding of physical phenomena at the heart of the elementary building block model provides additional support for the experimental observations used to the define the model. As a result, the elementary building block model can be used with confidence as a basis for micromechanical modeling of the elasticity and strength behavior of shale. These models, reviewed and implemented in the next chapter, will permit comparisons with macroscopic data that can help to further validate the properties of the elementary building block model.

Chapter 10

Modeling Applications of the Elementary Building Block

The goal of this thesis is to understand the macroscopic diversity in mechanical properties of shale materials by assessing microstructure and material invariant properties as the link between material composition and engineering properties. The development of the elementary building block model in Chapter 8 was made possible through analysis of the experimental results presented in Chapters 6 and 7; this model includes information about the sought material invariant properties and their link with the microstructure of the porous clay in shale. With the physical origins of this model explored and understood in the previous chapter, the model of the elementary building block can be employed with confidence in micromechanics models. These models predict the macroscopic mechanical behavior of shale and provide the final link between material composition and engineering properties.

This chapter reviews and applies state-of-the-art multiscale homogenization modeling applications, for poroelastic properties and for strength behavior, based on the model of the elementary building block of shale. Comparing the model predictions with macroscopic experimental data permits validation of these homogenization models. In turn, validation of the macroscopic predictions provides validation for the model of the elementary building block itself.

Recalling once more the multiscale thought model for the structure of shale, Figure 10-

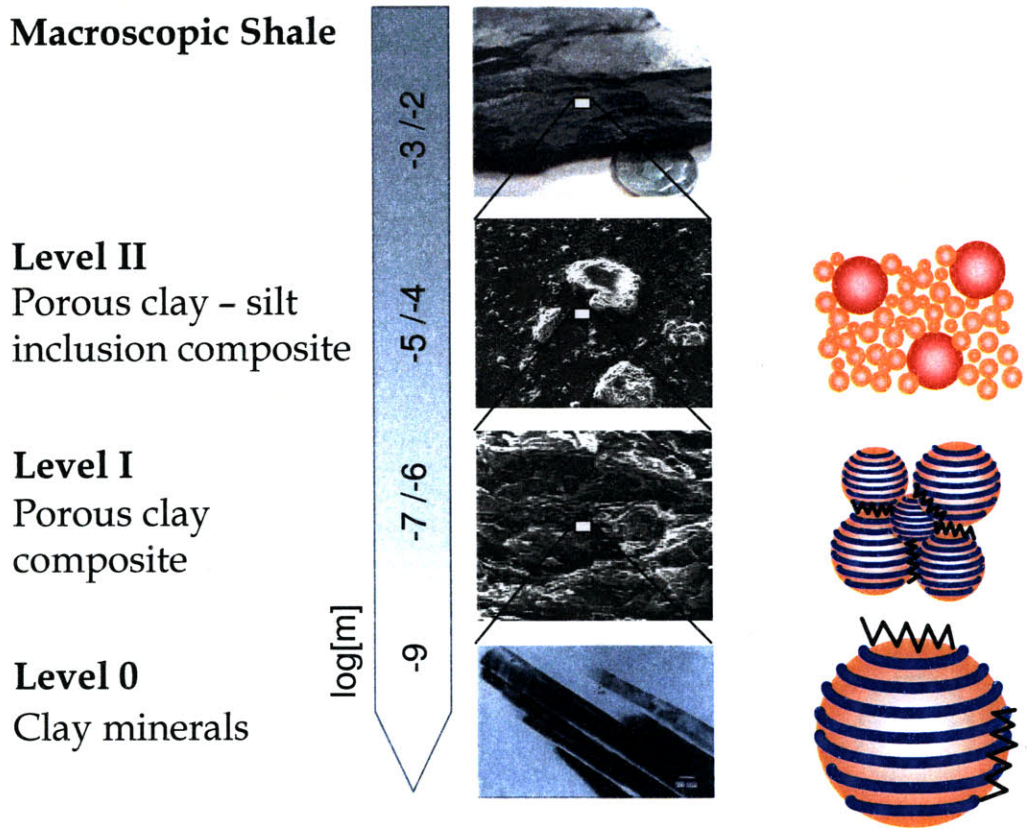

Figure 10-1: The multiscale thought model for shale, repeated from Fig. 2-1, and Fig. 8-5, with cartoon depictions of the elementary building block model at Level '0', the elementary building blocks working together to form the porous clay composite at Level '1,' and the addition of silt inclusions at Level '2.' Adapted from [145].

1 includes cartoon depictions of the situation at each level. The model of the elementary building block enters at Level '0.' Many of these elementary building blocks come together to form the porous clay composite at Level '1.' Finally, at Level '2,' the porous clay composite is mixed with the silt inclusions to form the porous clay - silt inclusion composite. Multiscale homogenization approaches follow this sequence, building up from Level '0' to Level '1', and then from Level '1' to Level '2.' These approaches lead to predicted properties of macroscopic shale (i.e. laboratory bench scales), which may be compared to experimental data.

10.1 Poroelastic Modeling

Recent work has employed the model of the elementary building block of shale for poroelastic modeling of macroscopic shale [145]. This section reviews that work, with good comparisons of model predictions and macroscopic data helping to validate the definition of the elementary building block.

10.1.1 Level '0' to Level '1' to Level '2'

The poroelastic model considered by Ortega et al. [145] is a multiscale homogenization model, motivated by the multiscale thought model for the structure of shale (Fig. 10-1). Level '0' is represented by the elementary building block model, consisting of granular particles with spherical mechanical mophology and intrinsic transverse isotropy (Sec. 8.3). The five independent stiffness coefficients are given by Eq. (8.1):

$$\begin{aligned} C^s_{11} &= 44.9 \text{ GPa} \\ C^s_{12} &= 21.7 \text{ GPa} \\ C^s_{13} &= 18.1 \text{ GPa} \\ C^s_{33} &= 24.2 \text{ GPa} \\ C^s_{44} &= 3.7 \text{ GPa} \end{aligned} \tag{10.1}$$

Based on the multiscale thought model and the volume fraction parameters associated with each level (Sec. 2.4), homogenization from Level '0' to Level '1' depends on the clay packing density,

while homogenization from Level '1' to Level '2' depends on the inclusion volume fraction.

Level '1' Homogenization

At Level '1', the scale of the porous clay composite, a micromechanics homogenization procedure is used. This procedure was first introduced in Sec. 5.2 to develop the scaling relationships between indentation moduli and packing density (Eq. (5.31)). In that presentation, the pore space was assumed to be drained to match the results of nanoindentation. To account for poroelastic effects, Ortega et al. used microporomechanics derivations [145]. This extension of linear homogenization theory aims to link the strain average $\mathbf{E} = \langle \boldsymbol{\varepsilon}(\underline{x}) \rangle$ with the pore pressure p to the overall stress average $\boldsymbol{\Sigma} = \langle \boldsymbol{\sigma}(\underline{x}) \rangle$ and a change in clay porosity $n - n_0$ [48], analogously to Eq. (5.4):

$$\boldsymbol{\Sigma} = \mathbb{C}^{\text{hom},I} : \mathbf{E} - \boldsymbol{\alpha}^I p \tag{10.2a}$$

$$n - n_0 = \boldsymbol{\alpha}^I : \mathbf{E} + \frac{p}{N^I} \tag{10.2b}$$

where $\mathbb{C}^{\text{hom},I}$ is the homogenized stiffness tensor, $\boldsymbol{\alpha}^I$ is the second-order tensor of Biot pore pressure coefficients, and N^I is the solid Biot modulus of the porous clay composite. The superscript I refers to the scale of the porous clay composite at Level '1.' In this formulation, the pore space is assumed to be saturated.

The goal of microporomechanical modeling is to link the poroelastic properties at Level '1' to the properties of the elementary building block at Level '0'. Theoretical developments advanced by Dormieux et al. [36], [66], [67] provide a means to make this link, analogously to Eq. (5.11):

$$\mathbb{C}^I_{\text{hom}} = \eta \mathbb{C}^s : \langle \mathbb{A} \rangle^s = \mathbb{C}^s : (\mathbb{I} - (1-\eta) \langle \mathbb{A} \rangle^p) \tag{10.3a}$$

$$\boldsymbol{\alpha}^I = (1-\eta)\, \mathbf{1} : \langle \mathbb{A} \rangle^p \tag{10.3b}$$

$$\frac{1}{N^I} = \mathbf{1} : \mathbb{S}^s : \left(\boldsymbol{\alpha}^I - (1-\eta)\, \mathbf{1} \right) \tag{10.3c}$$

where $\mathbb{I}$ is the fourth-order identity tensor, and $\mathbf{1}$ is the second order identity tensor. $\mathbb{C}^s$ and $\mathbb{S}^s$ are the stiffness and compliance of the elementary building block, which may be replaced

by $\mathbb{C}^s_{\text{hom}}$ and $\mathbb{S}^s_{\text{hom}}$ for the case of kerogen-rich shales, and $\langle \mathbb{A} \rangle^s$ and $\langle \mathbb{A} \rangle^p$ are the fourth-order strain concentration tensors averaged over the solid clay phase and pore domain, respectively.

The elementary building block model, with granular microstructure and a spherical mechanical morphology, suggests using the self-consistent scheme with spherical particle shapes to specify the strain concentration tensor. Recalling and combing Eqs. (5.25) and (5.28) the expression is [66], [186]:

$$\langle \mathbb{A} \rangle^\beta = \left(\mathbb{I} + \mathbb{P}^{SC} : \left(\mathbb{C}^\beta - \mathbb{C}^{SC} \right) \right)^{-1} : \left\langle \left(\mathbb{I} + \mathbb{P}^{SC} : \left(\mathbb{C} - \mathbb{C}^{SC} \right) \right)^{-1} \right\rangle^{-1} \tag{10.4}$$

where $\beta = s, p$ for the solid or pore phase, $\mathbb{C}^{SC}$ is the stiffness tensor of the equivalent homogeneous medium, which corresponds to $\mathbb{C}^{SC} = \mathbb{C}^I_{\text{hom}}$, and $\mathbb{P}^{SC}$ is the fourth-order Hill tensor characterizing the interaction between particles. As discussed in Sec. 5.2.3, implementing the Hill tensor can be a challenge, but Ortega et al. [145], based on the work of Hellmich et al. [86], have found success with a numerical implementation.

Level '2' Homogenization

The next step in Ortega et al.'s multiscale micromechanics homogenization model is to predict the poroelastic behavior of the shale composite at Level '2' by combining the results from Level '1' with behavior of the silt inclusions. At this level, one of the material phases which makes up the composite is solid, while the other phase is a porous material, governed by the poroelastic state equations (Eq. (10.3)). These phases occupy the volumes $V^{inc} = f^{inc} V$ and $V^{pc} = \left(1 - f^{inc}\right) V$ for the inclusions and the porous clay composite, respectively.

Homogenization of the composite behavior proceeds by considering a continuous description of the stress field in the heterogeneous medium [66]:

$$\left(\forall \underline{z} \in V\right) \quad \boldsymbol{\sigma}\left(\underline{z}\right) = \mathbb{C}\left(\underline{z}\right) : \boldsymbol{\varepsilon}\left(\underline{z}\right) + \boldsymbol{\sigma}^{\mathbf{T}}\left(\underline{z}\right) \tag{10.5}$$

together with the distributions of elastic properties and eigenstresses:

$$\mathbb{C}\left(\underline{z}\right) = \begin{cases} \mathbb{C}^I_{\text{hom}} & \left(V^{pc}\right) \\ \mathbb{C}^{inc} & \left(V^{inc}\right) \end{cases} \qquad \boldsymbol{\sigma}^{\mathbf{T}}\left(\underline{z}\right) = \begin{cases} -\boldsymbol{\alpha}^I p & \left(V^{pc}\right) \\ \mathbf{0} & \left(V^{inc}\right) \end{cases} \tag{10.6}$$

where $\mathbb{C}^{I}_{\text{hom}}$ is the homogenized stiffness tensor from Level '1' (Eq. 10.3a) and $\boldsymbol{\alpha}^{I}$ is the homogenized second-order tensor of Biot pore pressure coefficients from Level '1' (Eq. 10.3b), which characterize the poroelastic behavior of the clay phase. The stiffness tensor of the inclusion phase, $\mathbb{C}^{inc}$, is assumed isotropic.

Application of micromechanics to Eq. (10.5) gives a macroscopic response:

$$\boldsymbol{\Sigma} = \langle \boldsymbol{\sigma}(\underline{z}) \rangle = \mathbb{C}^{II}_{\text{hom}} : \mathbf{E} + \boldsymbol{\Sigma}^{\mathbf{T}} \tag{10.7}$$

where $\mathbb{C}^{II}_{\text{hom}}$ represents the drained macroscopic stiffness of shale at Level '2'. This stiffness is derived from micromechanics:

$$\mathbb{C}^{II}_{\text{hom}} = \langle \mathbb{C}(\underline{z}) : \mathbb{A}(\underline{z}) \rangle = \mathbb{C}^{I}_{\text{hom}} + f^{inc} \left(\mathbb{C}^{inc} - \mathbb{C}^{I}_{\text{hom}} \right) : \langle \mathbb{A} \rangle^{inc} \tag{10.8}$$

where $\langle \mathbb{A} \rangle^{inc}$ is the strain concentration tensor averaged over the volume of the inclusion phase.

An application of Levin's theorem [121] relates the macroscopic eigenstress, $\boldsymbol{\Sigma}^{\mathbf{T}}$, to the microscopic eigenstress, $\boldsymbol{\sigma}^{\mathbf{T}}(\underline{z})$, by [36], [66], [186]:

$$\boldsymbol{\Sigma}^{\mathbf{T}} = \left\langle \boldsymbol{\sigma}^{\mathbf{T}}(\underline{z}) : \mathbb{A}(\underline{z}) \right\rangle = -\boldsymbol{\alpha}^{II} p \tag{10.9}$$

where $\boldsymbol{\alpha}^{II}$ is the second-order Biot coefficient tensor of the macroscopic composite:

$$\boldsymbol{\alpha}^{II} = \boldsymbol{\alpha}^{I} : \left(\mathbb{I} - f^{inc} \langle \mathbb{A} \rangle^{inc} \right) \tag{10.10}$$

Finally, the poroelastic state equation may be derived [173]:

$$\phi - \phi_0 = \left(1 - f^{inc}\right)(n - n_0) = \boldsymbol{\alpha}^{II} : \mathbf{E} + \frac{P}{N^{II}} \tag{10.11}$$

where N^{II} is the macroscopic solid Biot modulus:

$$\frac{1}{N^{II}} = \frac{1 - f^{inc}}{N^{I}} + f^{inc} \boldsymbol{\alpha}^{I} : \left(\mathbb{C}^{inc} - \mathbb{C}^{I}_{\text{hom}} \right)^{-1} : \boldsymbol{\alpha}^{I} : \left(\mathbb{I} - \overline{\mathbb{A}}^{inc} \right) \tag{10.12}$$

Determining an expression of the strain concentration tensor, $\langle \mathbb{A} \rangle^{inc}$, for Level '2' again requires a choice of micromechanical model. The self-consistent scheme is again a good choice, considering the granular nature of the composite and the fact that the volume fraction of inclusions in shale can be high enough that a matrix-inclusion type model would be inappropriate. Similar to Eq. (10.4), the self-consistent scheme gives an expression for $\langle \mathbb{A} \rangle^{inc}$:

$$\langle \mathbb{A} \rangle^{inc} = \left(\mathbb{I} + \mathbb{P}^{SC} : \left(\mathbb{C}^{\beta} - \mathbb{C}^{SC} \right) \right)^{-1} : \left\langle \left(\mathbb{I} + \mathbb{P}^{SC} : \left(\mathbb{C} - \mathbb{C}^{SC} \right) \right)^{-1} \right\rangle^{-1} \tag{10.13}$$

where $\mathbb{C}^{SC} = \mathbb{C}^{II}_{\text{hom}}$ at this level and where the expression for $\mathbb{C}$ is given by Eq. (10.6).

The model gives access to the full poroelastic behavior of the Level '2' composite. It will prove useful to develop a special case, the undrained properties of the porous composite. This is achieved by considering the mass content $m^{II} = \phi \rho^{fl}(p)$ together with a linear state equation of the fluid density as a function of the fluid pressure [47], [48]:

$$\rho^{fl} = \rho_0^{fl} \left(1 + \frac{p}{k^{fl}} \right) \tag{10.14}$$

where ρ_0^{fl} is the reference fluid density and k^{fl} the fluid bulk modulus. The substitution of Eq. (10.14) in the drained form of the poroelastic state equations, i.e. Eqs. (10.7) and (10.11), yields the classical form of Biot's poroelasticity state equations:

$$\boldsymbol{\Sigma} = \mathbb{C}^{II,un}_{\text{hom}} : \left(\mathbf{E} - \mathbf{B}^{II} \frac{(m - m_0)^{II}}{\rho_0^{fl}} \right) \tag{10.15a}$$

$$\frac{(m - m_0)^{II}}{\rho_0^{fl}} = \boldsymbol{\alpha}^{II} : \mathbf{E} + \frac{p}{\mathcal{M}^{II}} \tag{10.15b}$$

where $\mathbb{C}^{II,un}_{\text{hom}}$ is the undrained stiffness tensor, $\mathbf{B}^{II}$ is the second-order tensor of Skempton coefficients, and $\mathcal{M}^{II}$ is the overall Biot modulus, where all quantities are representative of Level '2.' These quantities are given by:

$$\mathbb{C}^{II,un}_{\text{hom}} = \mathbb{C}^{II}_{\text{hom}} + (\mathcal{M} \boldsymbol{\alpha} \otimes \boldsymbol{\alpha})^{II} \tag{10.16a}$$

$$\mathbf{B}^{II} = \mathcal{M}^{II} \mathbb{S}^{II,un}_{\text{hom}} : \boldsymbol{\alpha}^{II} \tag{10.16b}$$

$$\frac{1}{\mathcal{M}^{II}} = \frac{1}{N^{II}} + \frac{\phi_0^{II}}{k^{fl}} \tag{10.16c}$$

with $\phi_0^{II} = \varphi_0 \left(1 - f^{inc}\right)$ at Level '2.'

10.1.2 Validation with Macroscopic Data

With Ortega et al.'s model now developed, the authors validated their multiscale homogenization model by comparing model predictions to experimental values from macroscopic elasticity tests. As the model of the elementary building block of shale is a foundation for the multiscale homogenization model, a validation of the overall homogenization model implies as well a validation of the elementary building block model. The macroscopic measurements are introduced first, followed by a comparison between predictions and experimental values.

Ultrasonic Pulse Velocity Measurements

Since the pioneering work of Kaarsberg [108], researchers have been using ultrasonic wave propogation techniques to assess the elastic content of shale materials at the scale of a few centimeters [94], [103], [107], [181], [183]. In general, the UPV technique consists of coupling a transmitting and receiving transducer to the ends of a cylindrical shale sample which is held at some confining pressure, and sending a pulse through the sample. The travel time for compressional (P) and shear (S) waves are measured, and translated into velocities through knowledge of the distance between transducers. Typical frequencies for these tests are in the megahertz range, giving characteristic wavelengths in the millimeter range. From a poromechanics perspective, the standard UPV test can be considered as an undrained test because there is not enough time for pore pressure resulting from the pulse to dissipate.

For a transversely isotropic material, characterized by five independent stiffness coefficients, five independent velocity measurements are required. Recall that axis of symmetry in shale (the $x3$-direction) is normal to the observed bedding direction (the $x1$-direction). The first two measurements are V_{P1} and V_{P3}, which are the velocities of the pure longitudinal mode (P-waves) propogating in directions parallel and normal to the axis of symmetry, respectively. The next two measurements are V_{S1} and V_{S3}, which are the velocities of the pure shear mode (S-waves) polarized in directions parallel and normal to the axis of symmetry, respectively. A final UPV measurement is required, but a selection of this particular independent measurement is not as obvious as the first four. The geophysics community has settled on propogating a

quasi-longitudinal or quasi-shear wave, measured at 45° from the axis of symmetry.

The inversion of elasticity constants from UPV measurements on transversely isotropic media is achieved through the following relations [9]:

$$\begin{aligned}
C_{11}^{UPV} &= \rho V_{P1}^2 \\
C_{33}^{UPV} &= \rho V_{P3}^2 \\
C_{66}^{UPV} &= \frac{1}{2}\left(C_{11}^{UPV} - C_{12}^{UPV}\right) = \rho V_{S1}^2 \\
C_{44}^{UPV} &= \rho V_{S3}^2 \\
C_{13}^{UPV} &= -C_{44} + \alpha\sqrt{\left(C_{11} + C_{44} - 2\rho V_{45}^2\right)\left(C_{33} + C_{44} - 2\rho V_{45}^2\right)}
\end{aligned}$$

where ρ is the bulk density of the sample, and where $\alpha = +1$ for a quasi-longitudinal (qP) or $\alpha = -1$ for a quasi-shear wave measured at 45° from the axis of symmetry.

Macroscopic Data from Literature

Ortega et al.'s comprehensive literature review [145] identified macroscopic data that provided the appropriate mineralogy information as well as an assessment of all five independent stiffness coefficients. These data, presented in Table 10.1, were not used in any way for development and calibration of the model, making this an appropriate dataset for validation. To make the comparison, the multiscale model for shale elasticity is implemented with the appropriate volume fraction parameters as model inputs. Model outputs are predictions of the undrained stiffness coefficients, to make the comparison with undrained UPV measurements.

Figure 10-2 displays the comparison between predicted and experimental stiffness values for all shales in this validation data set. In Figure 10-2, the horizontal error bars represent the range of predicted stiffness values given the two different input sets of clay packing density and inclusion volume fraction estimates: left-most predictions were calculated using η, f^{inc} estimates from mineralogy and bulk density data, while the right-most predictions were calculated using η, f^{inc} estimates from mineralogy and porosity data (recall Eqs. (2.20) and (2.22)). The vertical error bars correspond to the range of reported UPV stiffness values due to varying confining pressure conditions. The solid data points represent the mean values of these ranges in model predictions and in experimental measurements.

		CRE	KIM	JUR	3492	3506	3525	3536	3564	108/111	MUD
Reference		[107]	[94]	[94]	[103]	[103]	[103]	[103]	[103]	[62]	[56]
Mineralogy (1),(2)	Inc.	73	41	42	69	35	35	31	52	59	33
	Clay	27	59	58	17	53	55	59	38	41	65
	Kao.	5	22	0	4	14	23	14	6	25	15
	I./S.	19	35	58	9	17	8	10	15	16	45
	Other	4	2	0	4	22	24	35	17	0	5
Porosity, ϕ		11	3	11	10	16	8	14	7	15	21
Density, ρ(3)		2.42	-	-	2.43	2.44	2.38	2.44	2.41	2.38	2.20
Volume Fractions(4)	$\eta_{\min}$	53	96	84	38	76	71	66	67	65	62
	$\eta_{\max}$	69	-	-	64	76	88	80	86	71	72
	$f^{inc}_{\min}$	58	39	36	61	33	31	26	48	48	23
	$f^{inc}_{\max}$	64	-	-	72	34	36	30	54	50	26
Elastic Constants(5) (Level II)	Press.	0.1	5	5	1.5	1.5	1.5	1.5	1.5	10	5
	C_{11}	34.3	48.4	33.4	28.8	28.0	23.7	31.8	26.9	31.8	20.0
	C_{12}	13.1	14.4	14.2	7.4	10.6	6.5	8.2	8.3	13.0	6.8
	C_{13}	10.7	16.4	14.8	3.8	3.5	4.5	4.7	3.4	17.8	7.6
	C_{33}	22.7	27.3	22.5	19.9	21.8	19.6	19.3	19.0	24.7	13.0
	C_{44}	5.4	7.8	5.0	9.3	6.9	8.1	5.6	8.6	7.1	3.0
	Press.	-	80	80	13	13	13	13	13	40	60
	C_{11}	-	56.2	46.1	34.0	31.5	27.8	33.8	31.1	35.5	27.0
	C_{12}	-	18.4	17.5	10.6	10.9	7.0	9.8	9.9	13.5	9.5
	C_{13}	-	20.5	18.5	6.9	4.4	5.8	8.0	3.8	16.5	16.2
	C_{33}	-	36.4	32.9	26.5	26.1	25.3	21.9	23.7	29.5	18.0
	C_{44}	-	10.3	8.8	10.4	8.5	9.8	6.0	9.6	8.9	4.5

Table 10.1: Properties of the macroscopic data set at Level '2', as summarized by Ortega et al. [145].

(1) Mineralogy in mass percents. Inc. = inclusion, Kaol. = kaolinite, I./S. = Illite/Smectite. Other = chlorite, glauconite, biotite.

(2) Mineralogy for specimens 3492 to 3564 is specified in volume percents. 10-14 percent of solid volume was specified as 'Other' without distinction between clay or non-clay mineral.

(3) Density in grams per cubic centimeter.

(4) Minimum volume fractions were calculated using mineralogy and bulk density information. Maximum volume fractions were calculated using mineralogy and MIP porosity information.

(5) Press. refers to confining pressure used for testing, except for shale 108/111, which refers to differential pressure. Pressure in MPa, Elastic constants in GPa.

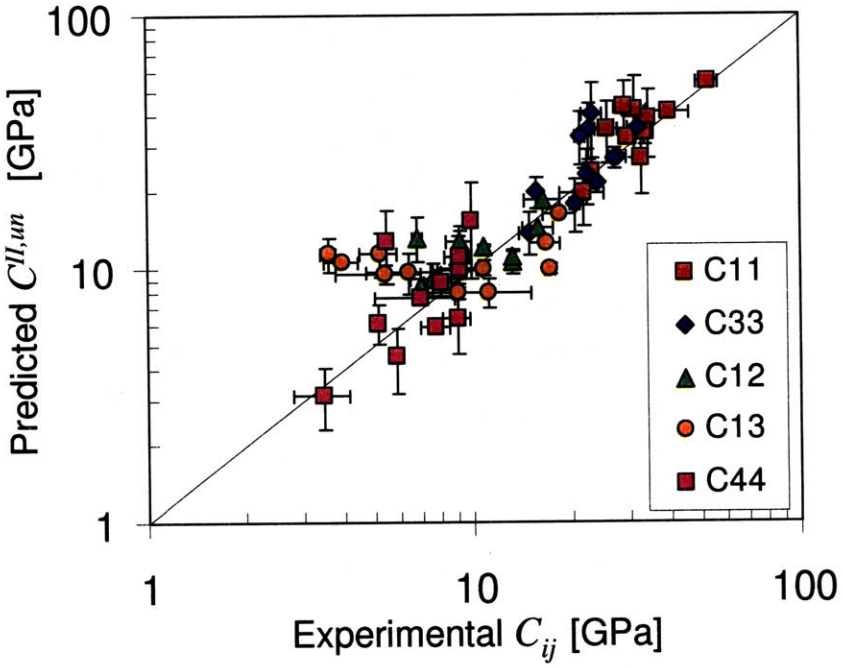

Figure 10-2: Comparison between the undrained stiffness coefficients predicted by Ortega et al.'s multiscale poroelastic model and the undrained stiffness coefficients obtained from UPV tests. Experimental uncertainties represent the variability of UPV stiffness as a function of confining pressure, while prediction uncertainties represent the variability as a result of variability in the input volume fraction parameters. From [145].

Overall, the correlation coefficient between the macroscopic model predictions and experiments is $r^2 = 0.83$. The worst results are for the stiffness coefficient C_{13}, but this is not surprising given that the experimental determination of C_{13} is generally recognized to suffer from higher uncertainties than the other coefficients because of difficulties in performing the experiment and in inversion of elastic properties from UPV measurements. In general, the good comparisons between predicted and measured macroscopic stiffness values, presented in Figure 10-2, form a strong argument in favor of the predictive capabilities of Ortega et al.'s microporomechanical model. More importantly, these results help to validate the morphology and elastic properties of the elementary building block of the porous clay in shale.

10.2 Strength Modeling

With the absence, until now, of the appropriate physical understanding of shale and its strength behavior, many attempts have been made to make empirical predictions of shale strength. The many limitations of these predictions may be overcome by considering a new strength homogenization approach based on the model of the elementary building block of shale.

10.2.1 Empirical Models

A review of many of the publically available empirical relationships for a variety of sedimentary rocks was recently presented by Chang et al. [35], identifying the current state-of-the-art in shale strength prediction. The empirical relationships available in the open literature typically depend on one of three parameters; the interval transit time, Δt (measured directly, the inverse of the P-wave velocity, $\Delta t \propto V_p^{-1}$), the Young's modulus, E, or the overall porosity, ϕ. Eq. (10.17) (proposed by Horsrud [96]), Eq. (10.18) (proposed by Horsrud [96]), and Eq. (10.19) (proposed by Lashkaripour and Dusseault [116]) are identified by Chang et al. [35] as the examples of each type that are applicable to the widest variety of shales.

$$C_0^{\Delta t} = 1.35\,(304.8/\Delta t)^{2.6} \tag{10.17}$$

$$C_0^{E} = 7.22E^{0.712} \tag{10.18}$$

$$C_0^{\phi} = 1.001\phi^{-1.143} \tag{10.19}$$

Macroscopic Strength Data

Although the unconfined compressive strength of rocks is a commonly reported parameter, datasets that provide both strength data and the appropriate data to calculate the two volume fraction parameters identified by the multiscale thought model for the structure of shale, clay packing density and inclusion volume fraction, are not often available. Strength data is not yet provided by the research sponsors for the GeoGenome shales, and was not complete at the time of this publication for the Woodford shales. Comparisons may be made, however with triaxial compression data from the highly compressed resedimented Boston Blue Clay [2].

A literature search revealed two appropriate data sets for comparison. One data set is from the Ph.D. dissertation of D. Jizba at Stanford University [106], who considered mechanical properties of a range of sandstones and shales from the Travis Peak formation in East Texas. The Jizba data includes porosity and clay volume fraction data, which allows calculation of inclusion volume fraction and clay packing density, as well as the results from confined uniaxial compression tests. The strength data may be reduced to give the UCS and a Mohr-Coulomb friction angle. Another data set is from Horsrud et al. [95], who considered mechanical properties of a range of shales from the North Sea. The Horsrud et al. data, like the Jizba data, includes porosity and clay volume fraction data. The Horsrud et al. strength data is given in terms of the UCS and a Mohr-Coulomb friction angle. All of the data labeled by Jizba as "shaley sandstones and shales" were considered. All of the data from Horsurd et al. was considered except for three samples which gave clay packing densities less than the percolation threshold $\eta_0 = 0.5$. Table 10.2 summarizes the macroscopic strength data for the resedimented Boston Blue Clay, the Jizba data, and the Horsrud et al. data.

Application and Limitations of Emprical Strength Relationships

The empirical equations for the unconfined compressive strength of shale, Eqs. (10.17) through (10.19) give predictions which can be compared with experimental data. Table 10.3 summarizes the required input parameters, experimental strength values, and empirical predictions. Table

Sample	η	f^{inc}	C_0 (MPa)	ϕ^{M-C}
Boston Blue Clay				
2 MPa	0.51	0.11	0.58	31
4 MPa	0.54	0.12	1.1	30
6 MPa	0.56	0.12	1.7	30
8 MPa	0.57	0.12	2.3	30
10 MPa	0.59	0.13	2.7	29
Jizba				
9763	0.76	0.75	44	39
6853	0.83	0.64	36	38
7053	0.86	0.57	29	29
9898	0.92	0.55	31	36
10151	0.91	0.43	20	41
8675	0.90	0.38	26	32
6275	0.92	0.32	33	27
Horsrud et al.				
B	0.54	0.11	8.2	50
D	0.52	0.29	13	51
E	0.54	0.33	8	51
H	0.84	0.38	27	58
I	0.70	0.44	22.5	53
J	0.79	0.30	13	60
K	0.94	0.49	77.5	

Table 10.2: Macroscopic strength data for the highly compressed resedimented Boston Blue Clay [2] and literature data from Jizba [106] and Horsrurd et al. [95] .

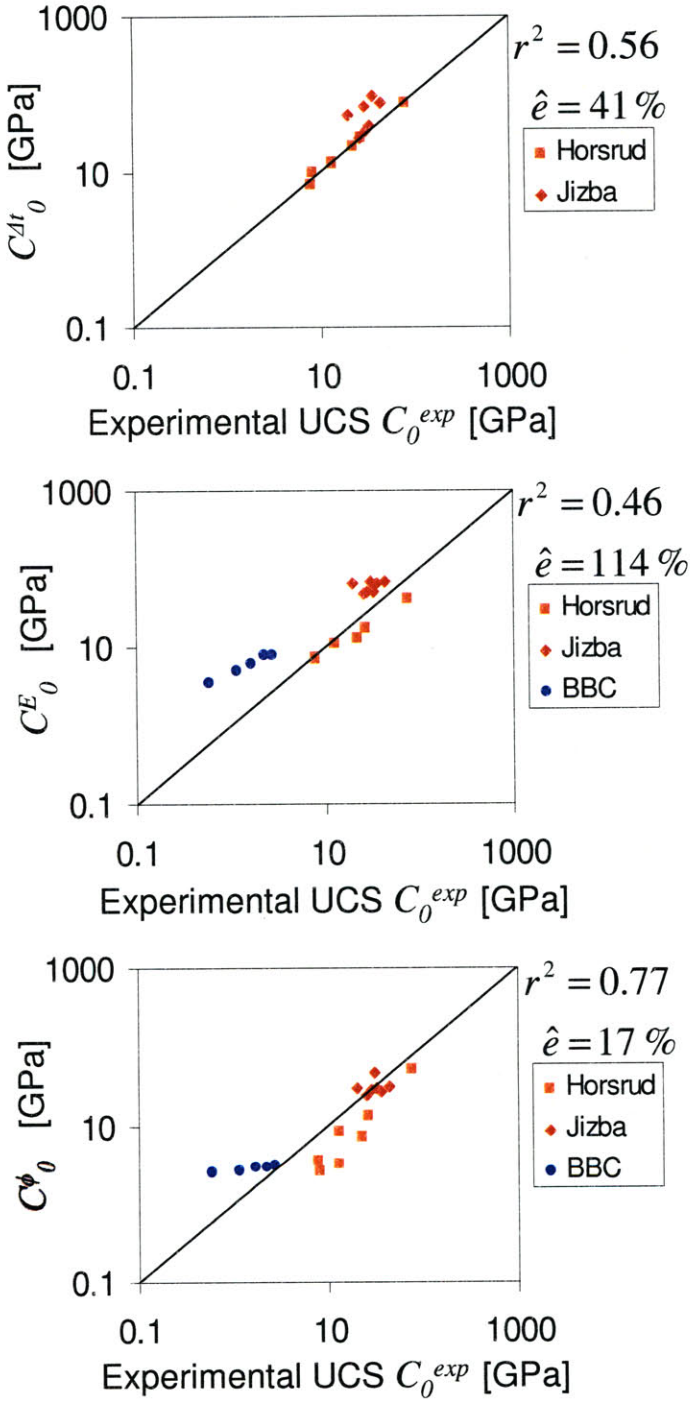

Figure 10-3: Comparison of empirical relationships for unconfined compressive strength of shale, using the same data set as in Figure 10-7. Top: using Eq. (10.17) (proposed by Horsrud [96]) for Δt. Middle: using Eq. (10.18) (proposed by Horsrud [96]) for E. Bottom: using Eq. (10.19) (proposed by Lashkaripour and Dusseault [116]) for ϕ.

Sample	Δt	E	ϕ	C_0^{exp}	$C_0^{\Delta t}$	C_0^E	C_0^ϕ
Boston Blue Clay							
2 MPa	n.a.	0.37	0.43	0.58	n.a.	3.6	2.6
4 MPa	n.a.	0.64	0.41	1.1	n.a.	5.3	2.8
6 MPa	n.a.	0.86	0.38	1.7	n.a.	6.5	3.0
8 MPa	n.a.	1.20	0.38	2.3	n.a.	8.2	3.1
10 MPa	n.a.	1.19	0.36	2.8	n.a.	8.2	3.2
Jizba							
9763	64	25	0.05	44	77	71	32
6853	59	23	0.05	36	96	67	28
7053	66	16	0.05	29	71	52	29
9898	87	25	0.03	31	35	71	49
10151	73	24	0.05	20	55	69	31
8675	95	15	0.06	26	28	50	26
6275	82	17	0.05	33	41	54	31
Horsrud et al.							
B	139	1	0.41	8	10	7	3
D	127	1.9	0.34	13	13	11	3
E	160	1.1	0.31	8	7	8	4
H	95	3.8	0.10	27	28	19	14
I	103	2.4	0.17	23	22	13	8
J	124	2	0.15	13	14	12	9
K	63	12.2	0.03	78	80	43	55
Summary Statistics							
$\widehat{e}$					45	117	17
e_s					66	155	99
r^2					0.56	0.46	0.77

Table 10.3: Data related to the predictions of unconfined compressive strength (in MPa) using empirical relationships. Data from the highly compressed resedimented Boston Blue Clay [2] and literature data from Jizba [106] and Horsrud et al. [95] are considered. The transit time, Δt, has units of s, the Young's modulus, E, has units of MPa, and the porosity, ϕ is dimensionless. Experimental unconfined compressive strength is given by C_0^{exp}, while predictions using Eq. (10.17) are given by $C_0^{\Delta t}$, predictions using Eq. (10.18) are given by C_0^E, and predictions using Eq. (10.19) are given by C_0^ϕ. The mean relative error and standard deviation of relative error (expressed as percentages) for each set of predictions are also included, as are values of the coefficient of determination.

10.3 also provides summary statistics. The mean and standard deviations of relative errors are calculated by:

$$\widehat{e} = \frac{1}{n}\sum e_i = \frac{1}{n}\sum \frac{C_0^{II} - C_0^{\exp}}{C_0^{\exp}} \tag{10.20a}$$

$$e_s = \sqrt{\frac{1}{n-1}\sum (e_i - \widehat{e})^2} \tag{10.20b}$$

Figure 10-3 provides log-log plots comparing experimental and predicted values for the unconfined compressive strength. Of the three empirical relations, the one that depends on porosity, Eq. (10.19), is clearly the best when applied to all three datasets.

The results of empirical models as shown in Figure 10-3 and Table 10.3 illustrate a variety of limitations commonly found in empirical models. First among these is matching the range of calibrated values with the range of predicted values - empirical relationships may work well for the dataset they are calibrated with, but not as well for other data. In particular, the empirical relations for Δt and for E proposed by Horsrud [96] seem to predict well the Horsrud et al. data, but do not do as good a job for the Jizba or Boston Blue Clay data.

All three single-parameter models have over-simplified the complex mechanical behavior of shale. Given our physical understanding of the material, and the isolation of volume fraction parameters as the vital input parameters, it is not surprising that the best empirical relation for unconfined compressive strength depends on porosity. In fact, the clay packing density and inclusion volume fraction allow calculation of the porosity, using Eq. (2.21). The empirical relation for porosity, however, is unable to discriminate between inclusion-rich shales and inclusion-light shales. While the empirical relations as a function of transit time interval, Δt, (or its inverse, P-wave velocity) and Young's modulus, E, do not perform as well, these measurements are the easiest to make in the field, so it is easy to understand the allure of these relationships. However, shale materials are transversely isotropic in elasticity, so only one stiffness measurement is not enough to give a good description of the material. In all cases, single-parameter empirical strength relationships attempt to do too much with too little, and an additional parameter is required.

In addition, the empirical relationships considered in Eqs. (10.17), (10.18), and (10.19) can only be used to predict the uniaxial compressive strength, but give no information about

the complete strength domain of the material and give very little insight into the physical behavior of the material. For example, the good correlation of predictions from the porosity relationship, Eq. (10.19) suggests that porosity is a driving factor in the strength behavior, but it does not deliver any information about a percolation threshold, or about the kinds of mechanical interfaces between inclusions and the porous clay composite. A new approach is clearly required.

10.2.2 Multiscale Micromechanics Strength Homogenization

While applications of elastic and poroelastic homogenization techniques have become well understood and accepted in the past decade or two, similar methods for strength behavior represent an active area of research. Gathier [77] has recently developed a preliminary multiscale homogenization model applicable to shale materials. As with the poroelastic homogenization model, the properties of the elementary building block of shale form a foundation for Gathier's strength homogenization model, which is reviewed here.

A new application of Gathier's model is made to compare predictions with experimental shale strength data available in the open literature, as well as strength data for Boston Blue Clay samples. Analogously to the elasticity model, validation of the multiscale strength homogenization model implies a validation of the morphology and elastic properties of the elementary building block of the porous clay in shale.

Gathier's strength homogenization model proceeds in a multi-step process, motivated like Ortega et al.'s poroelastic model by the multiscale thought model for the structure of shale (Fig. 10-1). Following this approach, homogenization between Level '0' and Level '1' depends on the clay packing density and properties of the elementary building block. Homogenization between Level '1' and Level '2' depends on the inclusion volume fraction and homogenized properties of the Level '1' composite.

Level '1' Strength Homogenization

First, recall the results of the Linear Comparison Composite (LCC) strength homogenization approach applied by Gathier [77] (Eqs. (5.84) and (5.85)) for homogenization between Level '0'

and Level '1':

$$\frac{\left(\Sigma_m - \Sigma_0^{\text{hom},I}\right)^2}{\left(A^{\text{hom},I}\right)^2} + \frac{\left(\Sigma_d/\sqrt{2}\right)^2}{\left(B^{\text{hom},I}\right)^2} = 1 \tag{10.21}$$

and

$$\left(\frac{A^{\text{hom},I}}{c_s}\right)^2 = \frac{\eta^2 \mathcal{K}_I \left(\eta - \alpha_s^2 \mathcal{K}_I\right)}{\left(\eta - 2\alpha_s^2 \mathcal{K}_I\right)^2} \tag{10.22a}$$

$$\left(\frac{B^{\text{hom},I}}{c_s}\right)^2 = \frac{\eta \mathcal{M}_I \left(\eta - \alpha_s^2 \mathcal{K}_I\right)}{\eta - 2\alpha_s^2 \mathcal{K}_I} \tag{10.22b}$$

$$\frac{\Sigma_0^{\text{hom},I}}{c_s} = \frac{\eta \alpha_s \mathcal{K}_I}{2\mathcal{K}_I \alpha_s^2 - \eta} \tag{10.22c}$$

where $\Sigma_m = \text{tr}\left(\boldsymbol{\Sigma}\right)$ is the mean stress and $\Sigma_d = \sqrt{\mathbf{s} : \mathbf{s}}$ with $\mathbf{s} = \boldsymbol{\Sigma} - \frac{1}{3}\Sigma_m \mathbf{1}$ is the mean deviatoric stress, $\mathcal{M}_I$ and $\mathcal{K}_I$ are morphology factors, α_s and c_s are cohesive frictional strength properties of the solid, and η is the packing density of the composite material.

The results of nanoindentation experiments have shown that the cohesive-frictional strength behavior of the elementary building block at Level '0' also scale with packing density. Recalling Eqs. (8.2) and (8.3):

$$\alpha_s = \frac{13}{12}\left(2 - 2\overline{\eta}\right)^2 + \frac{13}{30}\left(2 - 2\overline{\eta}\right)^5 \tag{10.23a}$$

$$c_s = \frac{h_s}{A} \times \left(\frac{1}{1 + B\alpha_s + \left(C\alpha_s\right)^3 + \left(D\alpha_s\right)^{10}}\right) \tag{10.23b}$$

with $A = 4.76438$, $B = 2.5934$, $C = 2.1860$, and $D = 1.6777$. In addition, considering a granular microstructure with a spherical mechanical morphology confirms the choice to specify the morphology factors using the self consistent scheme, recalling Eqs. (5.86) and (5.87):

$$\mathcal{K}_{sc} = \mathcal{K}_I\left(\frac{\kappa}{\mu} = \frac{1}{\alpha_s^2}, \eta\right) = \frac{4\eta \mathcal{M}_{sc}}{4\alpha_s^2 \mathcal{M}_{sc} + 3\left(1 - \eta\right)} \tag{10.24}$$

$$\begin{aligned}\mathcal{M}_{sc} = \mathcal{M}\left(\frac{\kappa}{\mu} = \frac{1}{\alpha_s^2}, \eta\right) &= \frac{1}{2} - \frac{5}{4}\left(1 - \eta\right) - \frac{3}{16\alpha_s^2}\left(2 + \eta\right) \\ &+ \frac{1}{16\alpha_s^2}\sqrt{144\left(\alpha_s^4 - \alpha_s^2\right) - 480\alpha_s^4\eta + 400\alpha_s^4\eta^2 + 408\alpha_s^2\eta - 120\alpha_s^2\eta^2 + 9\left(2 + \eta\right)^2}\end{aligned} \tag{10.25}$$

Consequently, the strength domain of the porous clay composite at Level '1' in the multiscale thought model for the structure of shale can be predicted based only on the clay packing density of that shale. Moreover, as a result of the scaling of the friction coefficient with packing density, Gathier showed that the homogenized strength domain is always an ellipse [77].

Level '2' Strength Homogenization

Gathier's next step is to predict the homogenized strength behavior at Level '2' in the multiscale thought model for the structure of shale by considering the effect of the silt inclusions [77]. A first look at the problem assumes rigid silt inclusions, with an unbounded strength domain. This assumption is reasonable because both the elastic moduli and the strength of quartz and feldspar inclusions are expected to be much greater than the mechanical properties of the porous clay. In other words, the silt inclusions are expected to bear stress, but are expected to fail at much greater stress levels than porous clay. One major unknown in the strength homogenization of shale is the interface condition between the porous clay and the silt inclusions. In order to gain initial insights into the problem, Gathier [77] considered two limit cases; slippery interfaces which transmit normal stresses but no shear stresses between the porous clay and the inclusions, and perfectly adherent interfaces which transmit the full magnitude of normal and shear stresses. These limit interface conditions are modeled in the micromechanical morphology factors.

The overall approach proceeds in a similar fashion to the Level '0' to Level '1' strength homogenization as presented in Sec. 5.3.3; the Linear Comparison Composite technique is employed once more in the same four steps, this time adapted for homogenization with rigid inclusions.

Step 1: Strain Energy Function of the Shale Composite

The first step is to calculate the strain rate energy function $\mathcal{W}_0(\mathbf{D})$. Consider the Level '2' *rev* subjected to a regular strain rate boundary ($\underline{v} = \mathbf{D} \cdot \underline{x}$). The linear comparison composite is composed of the porous clay phase (V_{pc}) and rigid inclusions (V_{inc}), so that the heterogenous stress distribution in the two phases reads as:

$$\boldsymbol{\sigma}(\underline{x}) = \mathbb{C}(\underline{x}) : \mathbf{d}(\underline{x}) + \boldsymbol{\tau}(\underline{x}) \tag{10.26}$$

where $\mathbb{C}(\underline{x})$ and $\boldsymbol{\tau}(\underline{x})$ are respectively the stiffness and the eigenstress whose spatial distributions within the *rev* are given by:

$$\mathbb{C}(\underline{x}) = \begin{cases} \mathbb{C}_{pc} = (3\kappa_{pc}\mathbb{J} + 2\mu_{pc}\mathbb{K}) & (V_{pc}) \\ \infty & (V_{inc}) \end{cases} ; \boldsymbol{\tau}(\underline{x}) = \begin{cases} \boldsymbol{\tau}_{pc} = \tau_{pc}\mathbf{1} & (V_{pc}) \\ 0 & (V_{inc}) \end{cases} \tag{10.27}$$

where $\mathbb{C}_{pc}$ and $\boldsymbol{\tau}_{pc}$ are respectively the stiffness tensor and the prestress of the porous clay phase in the Linear Comparison Composite. Note that the Linear Comparison Composite (LCC) at Level '2' is a priori independent of the LCC at Level '1'; what matters is the final strength criterion for the porous clay. In order to avoid any confusion, we notate the input stiffness and the input prestress in Eq. (10.27) by $\mathbb{C}_{pc}$ and $\boldsymbol{\tau}_{pc}$ and not by $\mathbb{C}^{\text{hom},I}$ and $\mathbf{T}^{I}$ given by Eq. (5.68).

Linear micromechanics as applied to a solid (with prestress) and rigid inclusions is used to derive the macroscopic stress state equation:

$$\boldsymbol{\Sigma} = \mathbb{C}^{\text{hom},II} : \mathbf{D} + \mathbf{T}^{II} \tag{10.28}$$

where $\mathbb{C}^{\text{hom},II}$ and $\mathbf{T}^{II}$ are respectively the Level '2' homogenized stiffness tensor and the Level '2' macroscopic prestress:

$$\mathbb{C}^{\text{hom},II} = \langle \mathbb{C}(\underline{x}) : \mathbb{A}(\underline{x}) \rangle = 3\kappa^{II}\mathbb{J} + 2\mu^{II}\mathbb{K} \tag{10.29a}$$

$$\mathbf{T}^{II} = \langle \boldsymbol{\tau}(\underline{x}) : \mathbb{A}(\underline{x}) \rangle = T_m^{II}\mathbf{1} = \tau_{pc}\mathbf{1} \tag{10.29b}$$

By analogy with Eq. (5.69), the homogenized moduli $\kappa^{\text{hom}} = \kappa^{II}$ and $\mu^{\text{hom}} = \mu^{II}$ are in the form:

$$\kappa^{II} = \mu_{pc}\mathcal{K}_{II}\left(\frac{\kappa_{pc}}{\mu_{pc}}, f_{inc}\right) \tag{10.30a}$$

$$\mu^{II} = \mu_{pc}\mathcal{M}_{II}\left(\frac{\kappa_{pc}}{\mu_{pc}}, f_{inc}\right) \tag{10.30b}$$

where $\mathcal{K}_{II}$ and $\mathcal{M}_{II}$ are solid-inclusion morphology factors to be specified that account for the granular morphology, the interface condition (perfect adherence, slippery imperfect interface),

and the inclusion volume fraction f_{inc}.

For the shale composite, the strain rate energy function $\mathcal{W}_0(\mathbf{D})$ reads in the isotropic case, similar to Eq. (5.70):

$$\begin{aligned} \mathcal{W}_0(D_v, D_d) &= \frac{1}{2}\kappa^{II} D_v^2 + \mu^{II} D_d^2 + T_m^{II} D_v \\ &= \frac{1}{2}\mu_{pc}\mathcal{K}_{II} D_v^2 + \mu_{pc}\mathcal{M}_{II} D_d^2 + \tau_{pc} D_v \end{aligned} \tag{10.31}$$

where $D_v = \mathrm{tr}(\mathbf{D})$ and $D_d = \sqrt{\boldsymbol{\Delta} : \boldsymbol{\Delta}}$ with $\boldsymbol{\Delta} = \mathbf{D} - \frac{1}{3} D_v \mathbf{1}$.

Step 2: Determine the $\mathcal{V}$ Function for the Porous Clay Composite Phase

The second step consists of determining the $\mathcal{V}$ function (Eq. (5.61)) for the porous clay phase ($\mathcal{V} = 0$ for rigid inclusions):

$$\mathcal{V}_{pc} = \underset{\mathbf{d}}{\mathrm{stat}} \left\{ \pi_{pc}(\mathbf{d}) - \omega_{pc}(\mathbf{d}) \right\} \tag{10.32}$$

The function $\pi_{pc}(\mathbf{d})$ of the porous clay phase is given by Eq. (5.82), which we recall:

$$\pi_{pc}(\mathbf{d}) = \widetilde{\Pi}^{\mathrm{hom},I}(\mathbf{D} \to \mathbf{d}) = S_0^I d_v + \sqrt{(A^I d_v)^2 + 2(B^I d_d)^2} \tag{10.33}$$

where S_0^{pc}, A^{pc}, B^{pc} are the Level I homogenization results (Eq. 5.85):

$$A^{pc} = A^{\mathrm{hom},I};\ B^{pc} = B^{\mathrm{hom},I};\ S_0^{pc} = \Sigma_0^{\mathrm{hom},I} \tag{10.34}$$

The strain rate energy function of the porous clay solid phase is analogous to Eq. (5.71):

$$\omega_{pc}(\mathbf{d}) = \frac{1}{2}\kappa_{pc} d_v^2 + \mu_{pc} d_d^2 + \tau_{pc} d_v \tag{10.35}$$

The strength criterion for the porous clay phase is elliptical. Applying the stationarity

condition to the $\mathcal{V}_{pc}$ function defined by Eqs. (10.32), (10.33), and (10.34) yields:

$$\frac{\partial \mathcal{V}_{pc}}{\partial d_v} = 0 \Rightarrow \kappa_{pc} d_v + \tau_{pc} = S_0^{pc} + \frac{(A^{pc})^2 d_v}{\sqrt{(A^{pc} d_v)^2 + \left(\sqrt{2} B^{pc} d_d\right)^2}} \tag{10.36a}$$

$$\frac{\partial \mathcal{V}_{pc}}{\partial d_d} = 0 \Rightarrow 2\mu_{pc} d_d = \frac{2\,(B^{pc})^2 d_d}{\sqrt{(A^{pc} d_v)^2 + \left(\sqrt{2} B^{pc} d_d\right)^2}} \tag{10.36b}$$

A prestress is used to ensure positive values of κ_{pc} and μ_{pc}, letting:

$$\tau_{pc} = S_0^{pc} \tag{10.37a}$$

$$\kappa_{pc} = \frac{(A^{pc})^2}{\sqrt{(A^{pc} d_v)^2 + \left(\sqrt{2} B^{pc} d_d\right)^2}} \tag{10.37b}$$

$$\mu_{pc} = \frac{(B^{pc})^2}{\sqrt{(A^{pc} d_v)^2 + \left(\sqrt{2} B^{pc} d_d\right)^2}} \tag{10.37c}$$

These relations ensure not only that κ_{pc} and μ_{pc} remain positive, but also, akin to Eq. (5.74) require that:

$$\frac{\kappa_{pc}}{\mu_{pc}} = \left(\frac{A^{pc}}{B^{pc}}\right)^2 = const. \tag{10.38}$$

The expression for $\mathcal{V}_{pc}$ thus becomes:

$$\mathcal{V}_{pc}\,(X < 0) = \frac{1}{2}\frac{\left(B^I\right)^2}{\mu_{pc}} \tag{10.39}$$

Step 3: Use Stationarity of $\widetilde{\Pi}^{\text{hom}}$

The next step is to use the stationarity of $\widetilde{\Pi}^{\text{hom}}$ to derive the homogenized strength criterion for the shale composite at Level '2'. Eq. (10.37a) fixes the value of τ_{pc}, which allows for a simplified expression as compared to the hyperbolic case considered at Level '1'. As a result, the stationary condition depends only on μ_{pc} as the sole degree of freedom:

$$\frac{\partial \widetilde{\Pi}^{\text{hom}}}{\partial \mu_{pc}} = \frac{1}{2}\mathcal{K}_{II} D_v^2 + \mathcal{M}_{II} D_d^2 - (1 - f_{inc})\frac{(B^{pc})^2}{2\left(\mu_{pc}\right)^2} = 0 \tag{10.40}$$

A substitution of expressions derived from Eq. (10.28):

$$\begin{aligned} D_v &= \frac{1}{\kappa^{II}}\left(\Sigma_m - \tau_{pc}\right) \\ D_d &= \frac{1}{2\mu^{II}}\Sigma_d \end{aligned}$$

in Eq. (10.40) leads to the sought strength criterion:

$$\frac{\left(\Sigma_m - \Sigma_0^{II}\right)^2}{\left(A^{II}\right)^2} + \frac{\left(\Sigma_d/\sqrt{2}\right)^2}{\left(B^{II}\right)^2} = 1 \tag{10.41}$$

where:

$$\left(A^{II}\right)^2 = \left(B^{pc}\right)^2 \mathcal{K}_{II}\left(1 - f_{inc}\right) \tag{10.42a}$$

$$\left(B^{II}\right)^2 = \left(B^{pc}\right)^2 \mathcal{M}_{II}\left(1 - f_{inc}\right) \tag{10.42b}$$

$$\Sigma_0^{II} = S_0^{pc} = \Sigma_0^{\mathrm{hom},I} \tag{10.42c}$$

Since $\left(B^{pc}\right)^2 > 0$ based on the scaling of cohesive-frictional behavior at Level '0,' then $\left(B^{II}\right)^2 > 0$. This inequality implies that strength domain of the Level '2' composite is always an ellipse.

Finally, combining Level '1' and Level '2' homogenization results, i.e. Eq. (10.22) with Eq. (10.42), yields the following expressions for the ellipse parameters:

$$\left(\frac{A^{II}}{c_s}\right)^2 = \frac{\eta\left(\eta - \alpha_s^2\mathcal{K}_I\right)\mathcal{M}_I}{\eta - 2\alpha_s^2\mathcal{K}_I}\left(1 - f_{inc}\right)\mathcal{K}_{II} \tag{10.43a}$$

$$\left(\frac{B^{II}}{c_s}\right)^2 = \frac{\eta\left(\eta - \alpha_s^2\mathcal{K}_I\right)\mathcal{M}_I}{\eta - 2\alpha_s^2\mathcal{K}_I}\left(1 - f_{inc}\right)\mathcal{M}_{II} \tag{10.43b}$$

$$\frac{\Sigma_0^{\mathrm{hom}}}{c_s} = -\frac{\alpha_s\eta\mathcal{K}_I}{\eta - 2\alpha_s^2\mathcal{K}_I} \tag{10.43c}$$

In these expressions, α_s and c_s are also functions of the clay packing density, η, as given by Eq. (10.23).

Step 4: Specify Solid-Inclusion Morphology Factors

The final step is to specify the Level '2' solid-inclusion morphology factors $(\mathcal{K}_{II}, \mathcal{M}_{II})$ which depend on the morphology and on the interface conditions. The inclusion volume fractions in

the GeoGenome shales range between 0.16 and 0.63 (Tab. 2.6), with the higher values residing well beyond the range where a matrix-inclusion type of representation would be appropriate. Instead, the self-consistent scheme, is considered once more. The nature of the interfaces as Level '2' is not well-understood, however, so two limit cases are employed.

The first limit case assumes perfectly adherent interfaces between porous clay and the rigid inclusions with unbounded strength domains. In this case, the solid-inclusion morphology factors read [40], [13]:

$$\begin{aligned}\mathcal{K}_{II}^{sc,A} = \quad & \frac{1}{18}\frac{1}{(1-f_{inc})(1-2f_{inc})}((18+15f_{inc}^2-42f_{inc})\beta+4f_{inc}(3-f_{inc}) \\ & ...+f_{inc}\sqrt{9\left(5f_{inc}-2\right)^2\beta^2-24\left(f_{inc}+2\right)\left(5f_{inc}-3\right)\beta+16\left(f_{inc}-3\right)^2}\ )\end{aligned} \tag{10.44}$$

$$\begin{aligned}\mathcal{M}_{II}^{sc,A} = \quad & \frac{1}{24}\frac{1}{1-2f_{inc}}((15f_{inc}-6)\beta+(12-4f_{inc}) \\ & ...+\sqrt{9\left(5f_{inc}-2\right)^2\beta^2-24\left(f_{inc}+2\right)\left(5f_{inc}-3\right)\beta+16\left(f_{inc}-3\right)^2}\ )\end{aligned} \tag{10.45}$$

where f_{inc} is the volume fraction of the rigid inclusions with perfect interface adherence and where β is the ratio κ_{pc}/μ_{pc}. The simplifying assumption of rigid inclusions places an analytical limitation on the volume fraction, $f_{inc} < 0.5$.

The second limit case assumes that the interfaces between inclusions and porous clay permit free tangential slips, without transmission of shear stresses. In this case, the solid-inclusion morphology factors read [40], [13]:

$$\begin{aligned}\mathcal{K}_{II}^{sc,L} = \quad & \frac{1}{18}\frac{1}{(1-f_{inc})(2-3f_{inc})}((3(8f_{inc}^2-23f_{inc}+12))\beta+8\,f_{inc}(3-2f_{inc}) \\ & ...+f_{inc}\sqrt{9\left(8f_{inc}-5\right)^2\beta^2+\left(720-1392f_{inc}+528f_{inc}^2\right)\beta+64\left(2f_{inc}-3\right)^2}\ )\end{aligned} \tag{10.46}$$

$$\begin{aligned}\mathcal{K}_{II}^{sc,L} = \quad & \frac{1}{24}\frac{1}{2-3f_{inc}}((24-16f_{inc})-(15-24f_{inc})\beta \\ & ...\ +\sqrt{9\left(8f_{inc}-5\right)^2\beta^2+\left(720-1392f_{inc}+528f_{inc}^2\right)\beta+64\left(2f_{inc}-3\right)^2}\ )\end{aligned} \tag{10.47}$$

where f_{inc} is the volume fraction of the rigid inclusions with slippery boundary conditions and where β is the ratio κ_{pc}/μ_{pc}. The simplifying assumption of rigid inclusions places a less stringent limitation on the volume fraction, $f_{inc} < 2/3$.

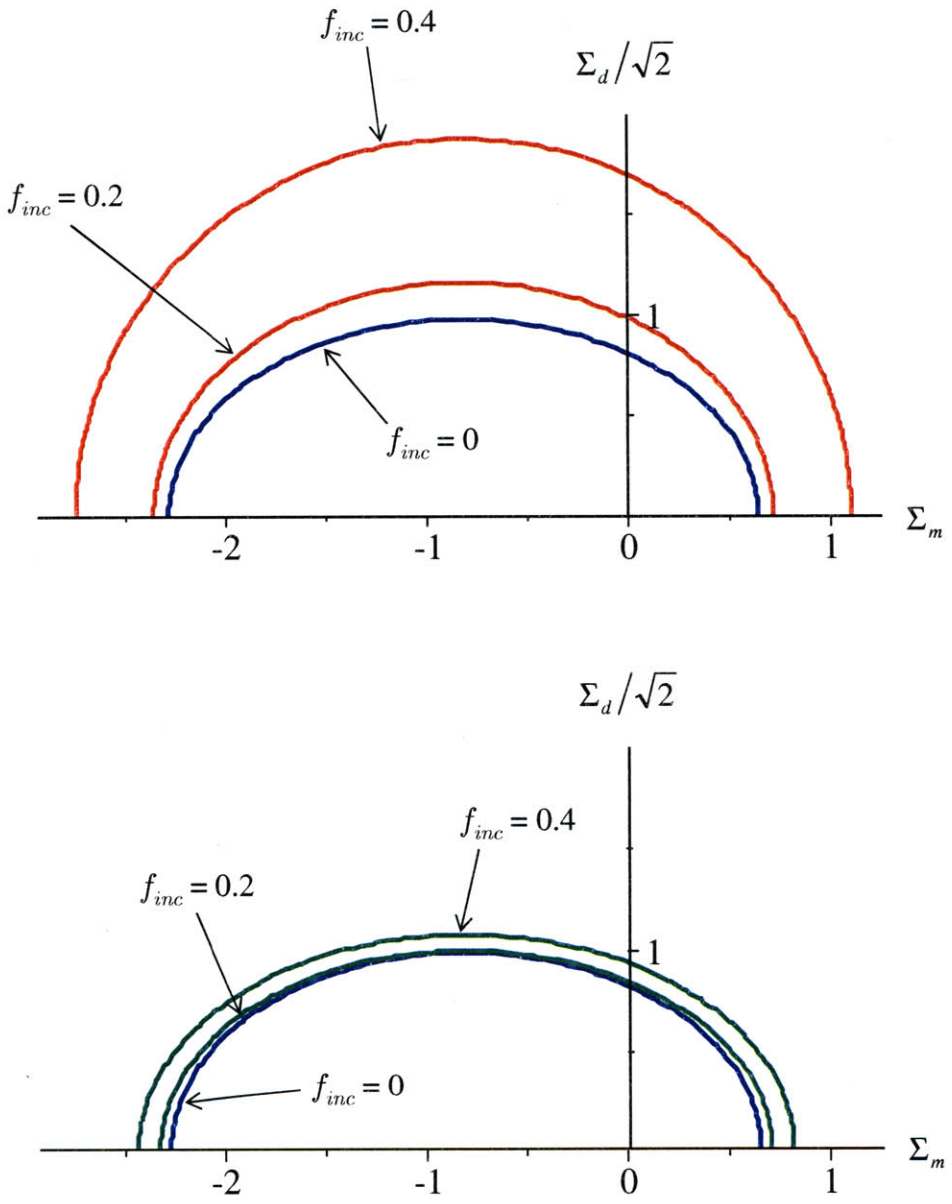

Figure 10-4: Influence of perfectly adherent (top) and perfectly slippery (bottom) rigid inclusions on the homogenized strength domain at Level '2.' Clay packing density is fixed at $\eta = 0.70$. From [77].

Predicted Strength Domains

All the elements are in place to develop predicted strength domains. Figure 10-4 shows example elliptical strength domains obtained by Gathier [77]. For the adherent interface condition, as seen in Fig. 10-4 (top), the addition of rigid inclusions enlarges the strength domain dramatically. For the slippery interface condition, however, the addition of rigid inclusions has a minor effect on the homogenized strength domain.

Predicting the Unconfined Compressive Strength of the Shale Composite

The most commonly reported strength parameter for shale materials is the unconfined compressive strength (UCS). A primary reason for the popularity of this value is that the experiment is simple to perform. Typically, a cylindrical sample is loaded between two end platens until failure; the UCS is the stress applied when failure occurs. The UCS for the shale composite at Level '2,' C_0^{II}, may be determined as a function of clay packing density and inclusion volume fraction by considering the state of stress at failure for uniaxial compression:

$$\boldsymbol{\sigma} = \begin{bmatrix} 0 & 0 & 0 \\ 0 & 0 & 0 \\ 0 & 0 & C_0^{II} \end{bmatrix} \tag{10.48}$$

which gives:

$$\Sigma_m = \sqrt{J_2} = \frac{C_0^{II}}{3} \tag{10.49}$$

In other words, the UCS is defined as a straight line in the $-\frac{1}{3}\Sigma_m \times \sqrt{J_2}$ plane.

Substitution in Eq. (10.41) allows derivation of an explicit solution for the UCS of the shale composite at Level '2' as a function of clay packing density η and inclusion volume fraction f_{inc}:

$$C_0^{II} = -\frac{2\left(B^{II}\right)^2 \Sigma_0^{II} - \sqrt{4\left(A^{II}\right)^2\left(B^{II}\right)^4 + 2\left(A^{II}\right)^4\left(B^{II}\right)^2 - 2\left(A^{II}\right)^2\left(B^{II}\right)^2\left(\Sigma_0^{II}\right)^2}}{2\left(B^{II}\right)^2 + \left(A^{II}\right)^2} \tag{10.50}$$

where the parameters A^{II}, B^{II}, and Σ_0^{II} are defined by Eq. (10.43).

10.2.3 Parametric Study of the Model

Figure 10-5 highlights the differences between the predictions of UCS for the slippery and adherent interface conditions by plotting the results for both interface conditions on the same axes. When comparing the UCS model results as functions of clay packing density as in Figure 10-5 (top), the interface condition appears to be a second order effect. In other words, the clay packing density is the dominant parameter driving the modeled UCS results, followed in importance by inclusion volume fraction, and then by interface conditions. Comparison of the interface effects in terms of model UCS as functions of inclusion volume fraction, as in Figure 10-5 (bottom) tells a slightly different story. First, the variation in model limits on the inclusion volume fractions with the differing interface conditions is especially apparent. The assumption of rigid inclusions with unbounded strength domains, in conjunction with the considered strength homogenization approach and self consistent scheme, limit the inclusion volume fraction of inclusions with adherent interfaces to $f_{inc} < 0.5$, while the limit on volume fraction of inclusions with slippery interfaces is $f_{inc} < 2/3$. Consideration of slippery interfaces permits modeling of shales with higher inclusion volume fractions.

The predicted UCS tends toward infinity as the inclusion volume fraction increases towards its limit value for each interface condition. As a result, modeling inclusions with adherent interfaces, with all other parameters equal, leads to higher predictions of homogenized strength than modeling inclusions with slippery interfaces. The difference becomes more important for both higher clay packing densities and higher inclusion volume fractions.

10.2.4 Comparison with Macroscopic Data

With Gathier's strength homogenization model able to give predictions of the unconfined compressive strength of shale materials (Eq. (10.50)) based on knowedge of their clay packing density and inclusion volume fractions, comparisons can be made to the macroscopic strength data presented in Table 10.2.

Validation of Predictions - Slippery or Adherent Inclusion Interfaces?

A first check on the strength homogenization model consists of overlaying the experimental macroscopic UCS data on the range of UCS values that are possible through prediction. Figure

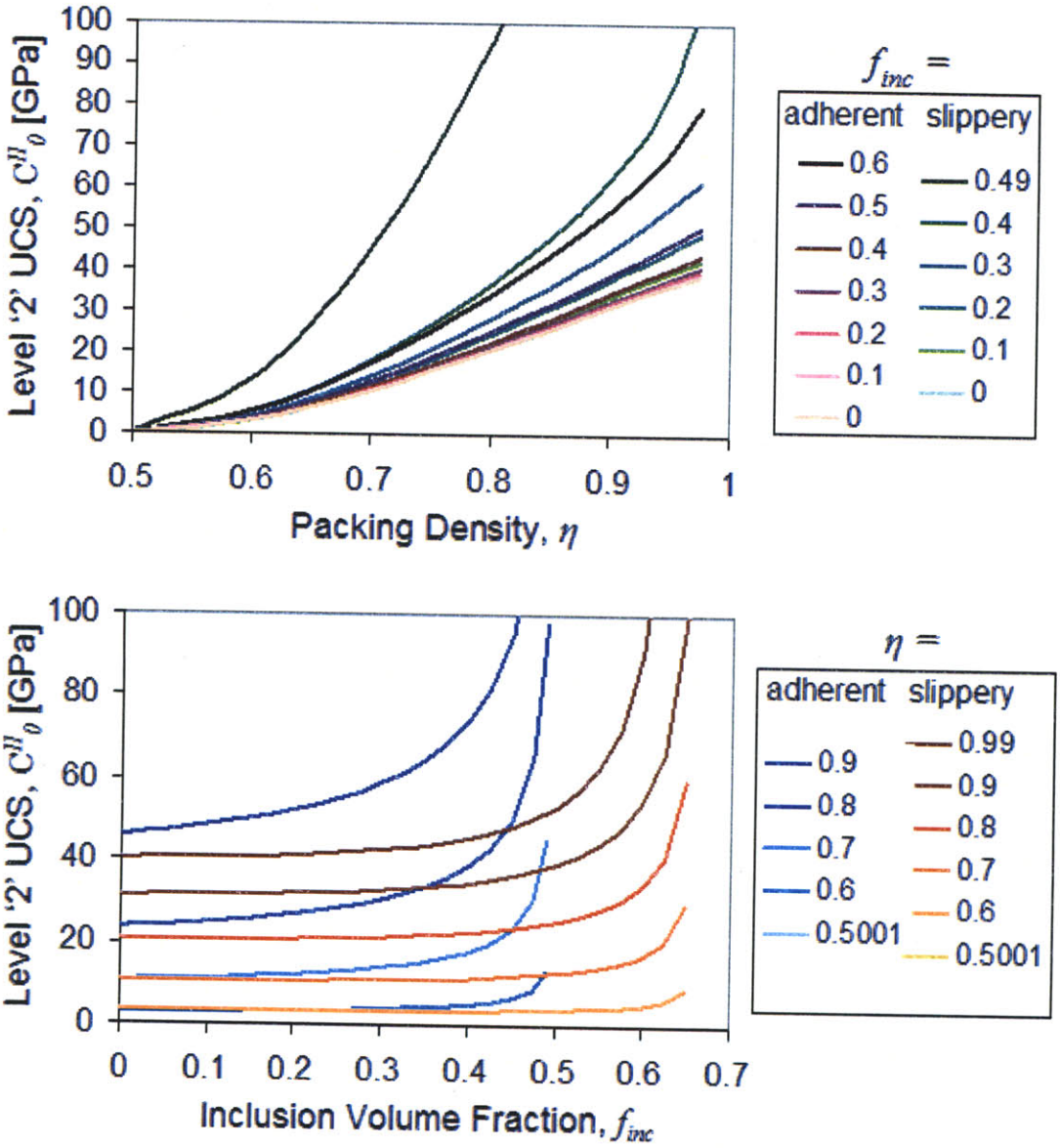

Figure 10-5: Comparisons of scaling of UCS at Level '2', C_0^{II}, for adherent and slippery inclusion interfaces. Top: UCS scales with clay packing density, η. Bottom: UCS scales with inclusion volume fraction, f_{inc}.

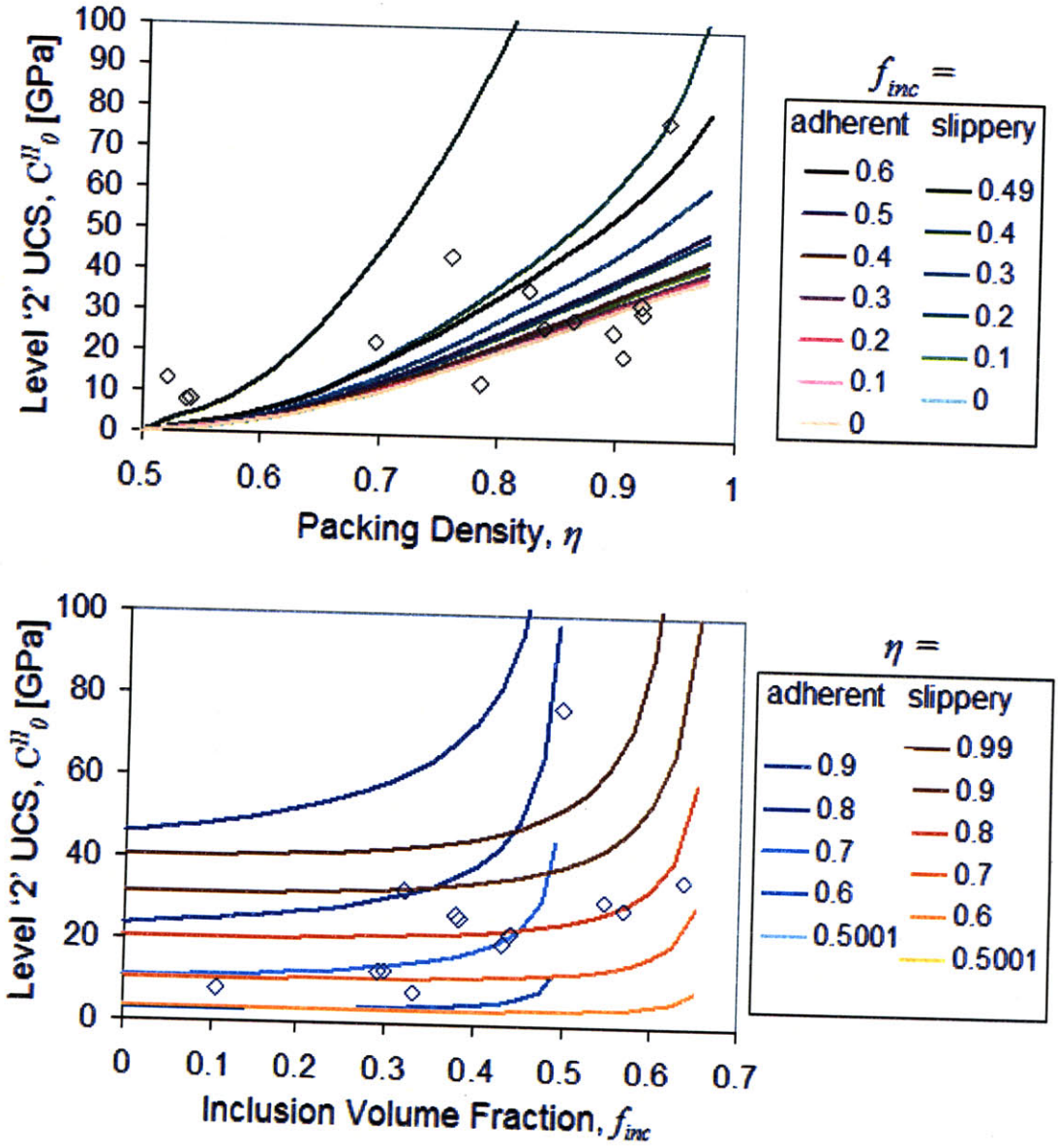

Figure 10-6: Comparisons of scaling of UCS at Level '2', C_0^{II}, for adherent and slippery inclusion interfaces. Top: UCS scales with clay packing density, η. Bottom: UCS scales with inclusion volume fraction, f_{inc}. Same figure as Fig. 10-5, but with experimental data (diamonds) from [106] and [95]. The range of possible model predictions generally overlay the experimental data points.

10-6 (top) displays UCS strength vs. clay packing density, η, for both the slippery and adherent interface assumptions. Figure 10-6 (bottom) displays UCS strength vs. inclusion volume fraction, f_{inc}, for both interface assumptions. Experimental data appears to fall within the appropriate ranges in both plots. There are some experimental data points, however, that have inclusion volume fractions greater than 0.5. These cases, given the assumption of rigid inclusions with unbounded strength domains, can only be modeled using the assumption of slippery interfaces.

A more detailed validation of the predictive model is made by comparing experimental macroscopic strength data with the model predictions. The inclusion volume fraction and clay packing density data for each shale were inputs for Eqs. (10.50), (10.43), considering both slippery and adherent inclusion interfaces, to obtain predictions of macroscopic UCS. Table 10.4 presents the results, comparing the experimental UCS data with the model predictions for slippery and adherent inclusion interfaces. Analogously to the predictions with the empirical strength relationships, mean and standard deviation of the relative errors are calculated by Eq. (10.20) and are also displayed in Table 10.4, along with the coefficient of determination, r^2. Samples with inclusion volume fractions greater than 0.5 can only be modeled with the assumptions of slippery interfaces. The comparison between macroscopic data and model predictions is shown graphically in Figure 10-7. Figure 10-7 (top) displays a log-log plot of predicted UCS strength vs. experimental UCS strength for the case of slippery interfaces. Figure 10-7 (bottom) is similar, but gives results for predictions in the case of adherent interfaces.

Overall, the physical, micromechanics-based strength homogenization model, featuring only two shale-specific input parameters, performs remarkably well when comparing predictions of unconfined compressive strength to experimental results. Qualitatively, this good comparison is evident in Figure 10-7; while there is some scatter in the data, the model apparently captures trends over more than 2 orders of magnitude in unconfined compressive strengths. Visual inspection of Figure 10-7 does not immediately suggest a particular advantage between the slippery interface assumption and the adherent interface assumption.

Quantitatively, the statistical comparisons presented in Table 10.4 give results that initially appear to be mixed. The mean relative error is less than 9 percent for the slippery interface case, and as expected, the slippery interface case tends to underpredict the unconfined compressive

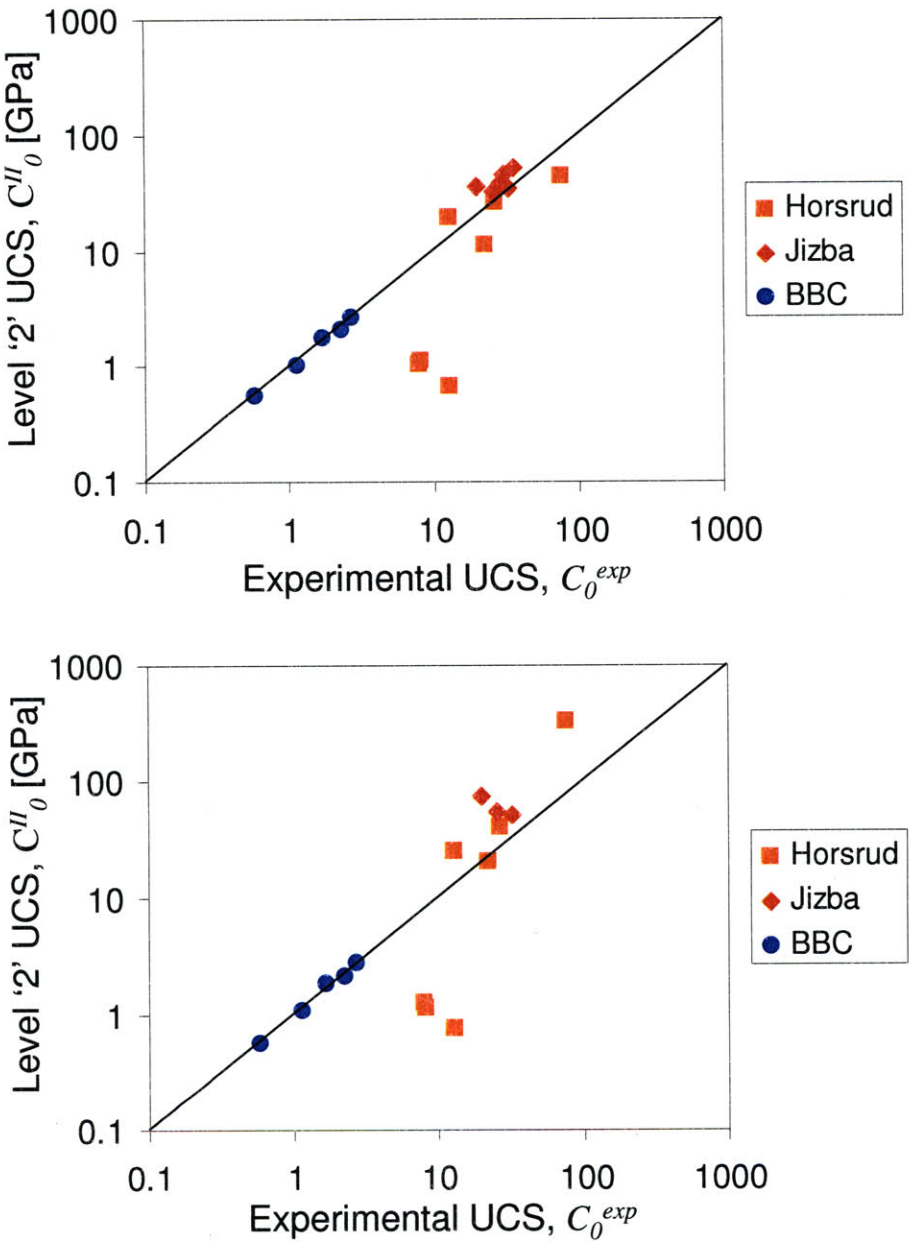

Figure 10-7: Comparison of predicted macroscopic UCS, C_0^{II} vs. experimental UCS, $C_0^{\exp}$ for the Boston Blue Clay samples, as well as data from the literature [106], [95] for the case of slippery inclusion interfaces (top) and adherent inclusion interfaces (bottom).

Sample	C_0^{exp}	$C_0^{II,\text{ slippery}}$	$C_0^{II,\text{ adherent}}$
Boston Blue Clay			
2 MPa	0.58	0.57	0.58
4 MPa	1.1	1.1	1.1
6 MPa	1.7	1.8	1.7
8 MPa	2.3	2.1	2.2
10 MPa	2.8	2.7	2.9
Jizba			
9763	44	N.A.	N.A.
6853	36	53	N.A.
7053	29	40	N.A.
9898	31	47	N.A.
10151	20	36	76
8675	26	34	57
6275	33	35	53
Horsrud et al.			
B	8.2	1.1	1.2
D	13	0.69	0.80
E	8	1.1	1.3
H	27	27	42
I	22.5	12	21
J	13	20	26
K	77.5	45	336
Summary Statistics			
$\widehat{e}$		-3.1	46
e_s		51	123
r^2		0.64	0.87

Table 10.4: Macroscopic unconfined compressive strength (in MPA) for the highly compressed resedimented Boston Blue Clay [2] and literature data from Jizba [106] and Horsrurd et al. [95], compared with the model predictions for both slippery and adherent inclusion interface conditions. The mean relative error and standard deviation of relative error for each set of predicitions are also included, as are values of the coefficient of determination.

strength. The mean relative error for the adherent interface case is much worse, with a value of more than 45 percent. The adherent interface case, on average, tends to overpredict the unconfined compressive strength. Under- and over-predictions support the assertion that the perfectly slippery and perfectly adherent interfaces represent limit cases for the actual interfacial behavior.

The adherent interface predictions, when compared to the experimental data, have a higher coefficient of determination, $r^2 = 0.88$ than the slippery interface predictions, with $r^2 = 0.60$. At first glance, this might suggest that the adherent interface predictions are better, as coefficient of determination can be understood as a measure of the linearity of a relationship between two datasets. More precisely, however, the higher coefficient of determination for the adherent interface model, in conjunction with the higher mean relative error, indicates that the adherent interface model gives a more consistent overprediction of UCS. Conversely, the slippery interface model is less consistent in its underprediction of UCS.

Comparison with Empirical Relationships

Gathier's multiscale strength homogenization model offers improvement over the empirical models in every respect. First, the development of the elementary building block model, a foundation for the multiscale strength homogenization model, was made based on a very wide variety of shale materials, a broader spectrum of composition and mechanical properties. As a result, the model is better suited to the range of actual shale materials than the empirical models. Second, Gathier's model is a two-parameter model, permitting refinement over the single parameter empirical models, i.e. distinguishing between inclusion-light and inclusion-rich shales. Third, the multiscale strength homogenization model is able to go beyond the UCS and predict the entire macroscopic strength domain of a particular shale material, as demonstrated in Figure 10-4.

By overcoming the limitations of empirical strength predictions, Gathier's strength homogenization model with slippery inclusion interfaces, which is based on the model of the elementary building block of shale, gives a smaller mean relative error than any of the empirical strength relationships for the considered macroscopic data.

10.2.5 Multiscale Strength Homogenization Model Limitations and Suggestions for Improvement

Although Gathier's multiscale strength homogenization model is impressive, it contains several simplifying assumptions and related model limitations. The results of the strength homogenization model, in terms of predicted strength domains, predictions of uniaxial compressive strength, and comparison with macroscopic strength data, help to provide insight regarding these limitations. Exploration of the model leads to identification of possibilities for improvement of the strength homogenization model.

One limitation of the multiscale strength homogenization model is that it assumes rigid inclusions with unbounded strength domains. Failure of macroscopic shale is not expected to take place within the inclusions because they are much stronger than the porous clay phase. On the other hand, assuming that the inclusions have unbounded strength domains leads to the model limits on inclusion volume fraction when using the self-consistent scheme. As the inclusion volume fraction approaches these limits, the strength behavior tends asymptotically to the unbounded strength domain of the inclusions. In terms of the unconfined compressive strength, as the inclusion volume fraction approaches the model limits, UCS tends asymptotically to infinity. These tendencies are unrealistic. A possible refinement to the model could be made by considering a large but finite strength domain for the inclusions.

Another limitation of the multiscale strength homogenization model is the use of the perfectly slippery or perfectly adherent inclusion interface conditions. A model case which considers some measure of a degree of adherence, which could transition between perfectly slippery and perfectly adherent interface conditions is likely to be the most realistic case. In other words, it seems plausible that the interface between the porous clay composite and the inclusion is capable of transmitting some amount of shear stress. This shear transfer may will be related to the mineralogy of clays, quartz, and related surface chemistry effects, and warrants futher investigation.

A final limitation of the multiscale strength homogenization model is that the predicted strength domains and uniaxial compressive strengths are isotropic, while anisotropic strength behavior for shale materials has been reported [63], [99], [134]. For laboratory sized specimens, this effect may be smaller for shales than for other layered rocks [99]. The proposed model

neglects anisotropic effects for two reasons. First, model values for the friction angle and cohesion of the elementary clay building block are obtained from nanoindentation, which only tested the materials in orthogonal directions coinciding with the bedding planes and deposition directions. The macroscopic strength observations, on the other hand, suggest that strength is similar in orthogonal directions coinciding with the bedding planes, but is reduced for intermediate loading angles. Nanoindentations were not performed on surfaces of intermediate angles, so there is not yet any experimental basis for considering strength anisotropy at the scale of Level '0' or Level '1.' The second reason for neglecting strength anisotropy is that the root of such behavior may actually come at larger scales. An intuitive rationale for smaller strengths at intermediate loading angles is that shear failure is activated on weaker bedding planes, rather than through the bulk material. Such an explanation, however, would imply that the origin of strength anisotropy is more closely aligned with joints and fractures within large rock masses, rather than the scope of "intact" rock considered as the macroscopic scale in this study. With this idea in mind, one potential way to incorporate strength anisotropy models would be to use the multiscale strength homogenization model presented in this study to define the strength parameters in orthogonal directions, and use strength anisotropy models to predict the strength reduction at intermediate loading angles.

10.3 Chapter Summary

This chapter has reviewed and applied multiscale homogenization models for predicting the poroelastic and strength behavior of shale materials at a macroscopic, lab-bench scale. Both homogenization models are based on the model of the elementary building block of shale. A review of Ortega et al.'s [145] successful poroelastic modeling efforts provided additional validation for the spherical representation of mechanical morphology and the elastic content of the elementary building block model. In addition, a review and new implementation of Gathier's [77] preliminary strength modeling proved extremely intriguing. This strength homogenization model predicts unconfined compressive strengths well, even outperforming empirical relationships available in the open literature for a wide variety of shale samples. This modeling implementation provides excellent validation for the strength behavior of the elementary building

block.

The validation of the elementary building block through multiscale homogenization modeling closes this part discussing the elementary building block. The model of the elementary building block of shale summarizes the material invariant properties and scaling relationships that are common to all shale materials. The elementary building block model represents a departure from a more traditional understanding of the morphology and properties of clay minerals in shale. Still, a closer examination of the model and of experimental observations revealed likely physical origins for the properties of the elementary building block. This goal of this thesis, to understand the macroscopic diversity of the mechanical behavior of shale through an assessment of microstructure and material invariant properties, has been fulfilled.

Part V

CONCLUSIONS

Chapter 11

Summary of Results and Future Perspectives

The overall research goal of this thesis was to understand the macroscopic diversity of shale materials by assessing microstructure and material invariant properties of shale materials as the link between material composition and engineering performance. This chapter presents a summary of this understanding, as obtained through a comprehensive implementation and analysis of nanoindentation experiments on shale materials. Based on the findings and contributions, some limitations and future research suggestions are proposed.

11.1 Summary of Main Findings

This study revealed the following scientific findings about the microstructure and material invariant properties of shale materials, which represent the link between material composition and engineering performance:

- The solid phase of porous clay in shale, the dominating load bearing phase of the material, has intrinsically anisotropic, material invariant elastic properties which do not depend on the clay mineralogy and composition. The transversely isotropic elastic behavior is defined by five independent stiffness coefficients: C^s_{11} = 44.9 GPa, C^s_{12} = 21.7 GPa, C^s_{13} = 18.1 GPa, C^s_{33} = 24.2 GPa, and C^s_{44} = 3.7 GPa. Nanoindentation experiments

identify two snapshots of this behavior, giving indentation moduli of $m_{1,s} = 26.3$ GPa and $m_{3,s} = 14.9$ GPa.

- The solid phase of the porous clay in shale has cohesive-frictional strength behavior. This behavior is not a function of the clay mineralogy, but does depend on the average clay packing density of the porous clay composite to which the solid belongs, as given by Eqs. (7.4) and (7.3):

$$\begin{aligned} \alpha_s &= \frac{13}{12}(2-2\overline{\eta})^2 + \frac{13}{30}(2-2\overline{\eta})^5 \\ c_s &= \frac{h_s}{A} \times \left(\frac{1}{1 + B\alpha_s + (C\alpha_s)^3 + (D\alpha_s)^{10}} \right) \end{aligned}$$

with $A = 4.76438$, $B = 2.5934$, $C = 2.1860$, and $D = 1.6777$. The scaling behavior of friction and cohesion is well represented by fractal scaling of solid and pore sizes in the composite, corresponding to contemporary views of friction that require small spaces between solid surfaces to develop friction. Cohesion and friction come together to define a material invariant contact stiffness for the solid phase of porous clay in shale, $h_s = 0.62$ GPa.

- The porous clay in shale has a nanogranular structure, with a spherical representation of mechanical morphology, characterized by an observed packing density percolation threshold of $\eta_0 = 0.5$. The material properties of the porous clay composite vary only with the clay packing density, η. As a result, single-parameter micromechanical models can be used to predict the full mechanical behavior of the porous clay composite.

- Packing density of the porous clay in shale is not constant in a given sample, but is instead characterized by a distribution of possible packing densities. These distributions, roughly Gaussian, are analogous to pore size distributions, but are obtained through analysis of mechanical measurements. The packing density distributions resulting from testing normal to the bedding direction and parallel to the bedding direction tend to overlap for each shale sample. This observation suggests that the spherical representation of mechanical morphology, with no preferential orientation of particle or pore space, is appropriate.

- A model of the elementary building block of shale summarizes the mechanical and morphological characterization of the solid phase in the porous clay composite. The model reconciles various visual and mechanical observations of morphology, comparisons to previously reported elastic properties of clay minerals, and the observation that solid strength properties vary with packing density. These observations come together to imply that the elementary building block represents an effective solid consisting of a polycrystal group of clay minerals, rather than a single clay mineral.

- The elementary building block may be successfully employed as a basis for microporomechanics homogenization schemes to predict the macroscopic elastic and strength behavior of shale materials.

11.2 Research Contributions

Reaching the scientific findings required development, refinement, and implementation of experimental and analytical methods:

- Minimum surface roughness criteria for repeatable application of the grid indentation technique on a natural heterogeneous composite were developed, based on results from cement paste, a model material. A surface preparation procedure was developed for shale materials, giving surface roughnesses which satisfy the developed criteria.

- The implementation of the grid indentation for shale materials required careful consideration of the scale separability conditions to isolate material phase properties at the sought scale. Appropriate grid indentation parameters were developed and selected to probe the mechanical behavior of the porous clay composite, and another set of parameters were selected to probe the mechanical behavior of locally densely packed areas of porous clay.

- The implementation of the $M - H - \eta$ scaling approach provides a means to identify the packing density distributions in a given shale material, as well as the cohesive-frictional strength behavior of the solid phase of a porous composite material. The packing density distributions are analogous and related to pore size distributions, but are obtained mechanically, and suffer from fewer difficulties in experimental technique and interpretation

than intrusion porosimetry measurements.

- Linking observations about the frictional behavior of clay materials to fractal scalings of particle packing and pore sizes opens a new avenue for investigating the origin of frictional behavior in granular materials.

11.3 Industrial Benefits

The elementary building block model is used as a foundation for multiscale micromechanical modeling to predict the poroelastic and strength behavior of macroscopic (lab-bench scale) shale. The good performance of these two-parameter models as a function of volume fractions, clay packing density η and inclusion volume fraction f_{inc}, illustrates the engineering importance of these findings. Prediction of strength properties, for example, can replace the need to retrieve expensive core samples and perform a series of time consuming triaxial experiments in order to define the strength domain of a particular shale sample.

For seismic exploration, new understanding of the nano-scale origin of macroscopic poroelastic measurements may drive more accurate interpretations of seismic logging data. In particular, a careful combination of poroelastic modeling and strength modeling could provide a direct link between seismic data and strength behavior of shales.

11.4 Current Limitations and Future Perspectives

Some limitations of the approaches and results presented in this thesis must be noted. These limitations and other considerations motivate possible directions for future research, which are grouped into four overall themes.

First, recall assumptions about nanoindentation and related analysis techniques. For example, the interpretation of the strength parameters from indentation hardness depended on a yield design formulation, but yield design approaches cannot capture physical phenomena such as non-associative flow, so they may not be the most representative of the actual behavior. Still, yield design approaches represent a good first tool for analysis. Similarly, it was assumed that pile-up and sink-in phenomena during nanoindentation of shale have a negligible

effect on the measured behavior. This may not be the case, but the estimation of contact area remains an otherwise difficult problem to solve. Finally, nanoindentation was considered to be a drained test, so any flow effects relating to permeability, or time-dependent behavior relating to viscoelasticity and creep were not considered. Thus, the model of the elementary building block does not incorporate these phenomena, and they may also have a small effect on the measurement of elastic and strength properties from nanoindentation. Further refinements to, or validation of, the properties of the elementary building block model could be made by investigating these effects.

Second, additional questions remain about the physical origin of the properties of the elementary building block. While the elementary building block model is nicely understood as an effective particle consisting of a group of agglomerated clay minerals, no model exists yet to firmly link the mechanical properties of the clay minerals (both elastic and cohesive-frictional strength parameters) to the mechanical properties of the elementary building block. Atomistic, molecular dynamics simulations may help to resolve this issue, because direct measurements to obtain further information are not on the horizon. Such simulations may require, and also help to provide, a better understanding of the interfacial behavior within and outside the elementary building block. Moreover, a closer examination of the origin of fractal scaling, associated with a tendency towards perfect packings, could provide a fruitful avenue for future research. It is probably the case that the slow deposition and diagenetic processes which form shale from sedimented clay particles give rise to the importance of packing on the mechanical behavior of shale.

Third, there are some unresolved issues surrounding the use of micromechanical modeling with the elementary building block. In particular, limitations persist in strength homogenization modeling that upscales towards macroscopic properties. Many of these limitations were first discussed in the context of the strength homogenization model, including the assumption of rigid silt inclusions with unbounded strength domains, and the two limit cases of interfacial behavior between the porous clay composite and the silt inclusions. Further modeling work and additional comparisons with macroscopic data, including clues about experimental macroscopic strength domains, will help to resolve these issues. Such resolution should lead to additional insights into the mechanical behavior of shale and improve the predictive capa-

bilities of multiscale micromechanics models. In addition, fracture behavior of the material has yet to be considered in the context of the model of the elementary building block. Given the close relationship between elasticity and fracture, the intrinsic anisotropy in elasticity may well explain the tendency for shales to fracture along preferential directions associated with the bedding planes. Finally, the chemomechanics of shale materials have not been studied at all in the context of the model of the elementary building block. Such an investigation may be of considerable importance to the petroleum engineering industry to understand the chemical effects of various drilling fluids on the mechanical behaviors of shale.

Lastly, the overall success of this study, despite these limitations, suggests that similar approaches to experimental microporomechanics may prove useful for other natural and synthetic porous, nanogranular composites. Understanding of cement pastes has benefited from similarly comprehensive experimental campaigns, while first steps have been taken for bone and sandstone materials. Further work on sandstones and carbonates, combined with the knowledge from this study, would encompass the great majority of sedimentary rock materials.

The results, analysis, and discussion presented in this thesis have provided a significant step, in a new direction, towards an improved understanding of the mechanical behavior of shale. Future research on shale will serve to strengthen and solidify this new understanding of microstructure and material invariant properties as the link between a diversity in macroscopic behavior and material composition.

Bibliography

[1] Aadnoy, B.S, & Ong, S. (2003) 'Introduction to special issue on Borehole Stability.' *Journal of Petroleum Science and Engineering* **38** (3-4): 79-82.

[2] Abdulhadi, N. Personal Communication, March 18, 2008.

[3] Abousleiman, Y., Tran, M., Hoang, S., Bobko, C., Ortega, J.A., & Ulm, F.-J. (2007) 'Geomechanics field and lab characterization of Woodford shale: The next gas play.' *SPE Annual Technical Conference and Exhibition, 11-14 November, 2007, Anaheim, CA.* SPE 110120.

[4] Abousleiman, Y. Personal Communication: Presentation for GeoGeonome Industry Consortium, May 31, 2007, Houston, TX.

[5] Aleksandrov, K.S. & Ryzhova, T.V. (1961) 'Elastic properties of rock-forming minerals II. Layered silicates.' *Bull. Acad. Scie. USSR, Geophys. Ser. English translation* **12**: 1165-1168.

[6] Ang, A., & Tang., W. (1975) *Probability Concepts in Engineering Planning and Design - Volume I: Basic Principles.* Wiley. New York, NY.

[7] Antonangeli, D., Krish, M., Fiquet, G., Badro, J., Farber, D.L., Bossak, A., & Merkel, S. (2005) 'Aggregate and single-crystalline elasticity of hcp cobalt at high pressure.' *Physics Review B* **72**: 134303-1 - 134303-7.

[8] ASTM D-4404-84 (2004). 'Standard test method of determination of pore volume and pore volume distribution of soil and rock by mercury intrusion porosimetry.' West Conshohocken, PA.

[9] Auld, B.A. (1990) *Acoustic Fields and Waves in Solids.* Robert E Kreiger Publishing Company, Malabar.

[10] Aylmore, L.A.G. & Quirk, J.P. (1960) 'Domain or turbostratic structure of clays.' *Nature* **197**: 1046-1048.

[11] Bailey, W.A. (1961) *Effects of Salt on the Shear Strength of Boston Blue Clay.* S.B. Thesis, Department of Civil and Sanitary Engineering, MIT, Cambridge, MA.

[12] Barthélémy, J.-F. & Dormeiux, L. (2003) 'Determination of the macroscopic strength criterion of a porous medium by nonlinear homogenization.' *Comptes Rendus Mecanique* **331** (4): 271-276.

[13] Barthélémy, J.-F. (2005) *Approche micromécanique de la rupture et de la fissuration dans les géomatériaux.* PhD Thesis, Ecole National des Ponts et Chaussées, Champs-sur-Marne, France.

[14] Berge, P.A., & Berryman, J.G. (1995) 'Realizability of negative pore compressibility in poroelastic composites.' *Journal of Applied Mechanics.* **62**: 1053-1062.

[15] Bjorlykke, K. (1998) 'Clay mineral diagenesis in sedimentary basins - a key to the prediction of rock properties. Examples from the North Sea Basin.' *Clay Minerals* **33**: 15-34.

[16] Blatt, H., Middleton, G., and Murray, R. (1980) *Origins of Sedimentary Rocks, Second Edition.* Prentice-Hall, Englewood Cliffs, NJ. 332-405.

[17] Bobko, C. & Ulm, F.-J. (2008) 'The nano-mechanical morphology of shale.' *Mechanics of Materials* **40**: 318-337.

[18] Bobji, M.S., & Biswas, S.K. (1999). 'Deconvolution of hardness from data obtained from nanoindentation of rough surfaces.' *Journal of Material Research* **14** (6): 2259-2268.

[19] Borges, L.A., Zouain, N. & Huespe, A.E. (1996) 'A nonlinear optimization procedure for limit analysis.' *European Journal of Mechanics A - Solids* **15** (3): 487-512.

[20] Borkovec, M., de Paris, W. & Peikert, R. (1994) 'The fractal dimension of the Appolonian sphere packing.' *Fractals* **2** (4): 521-526.

[21] Borodich, F.M. (1989) 'Hertz contact problems for an anisotropic physically nonlinear elastic medium.' *Problemy Prochnosti* **12**: 47-53 (in Russian, English translation in *Strength of Materials* **21**: 1668-1676).

[22] Borodich, F.M. (1998) *Similarity methods in Hertz contact problems and their relations with the Meyer hardness test.* Glasgow, Glasgow Caledonian University: 1-45.

[23] Borodich, F.M., Keer. L.M. & Korach, C.S. (2003). 'Analytical study of fundamental nanoindentation test relations for indenters of non-ideal shapes' *Nanotechnology* **14**: 803-808

[24] Borodich, F. M. & Keer, L. M. (2004) 'Evaluation of elastic modulus of materials by adhesive (no-slip) nano-indentation.' *Proceedings of the Royal Society of London* **A 460**: 507-514.

[25] Bowden, F.P. & Tabor, D. (2001, c1954). *The Friction and Lubrication of Solids.* Oxford classic texts in the physical sciences, Clarendon Press, Oxford, UK.

[26] Brinell, J.A. (1901) 'Mémoire sur les épreuves à billes en acier.' *Congrès International des Méthodes d'Essai des Matériaux de Construction, Vol. 2*, Paris 83-94.

[27] Brune, D.A. & Bicerano, J. (2002) 'Micromechanics of nanocomposites: comparison of tensile and compressive elastic moduli, and prediction of effects of incomplete exfoliation and imperfect alignment on modulus.' *Polymer* **43**: 369-387.

[28] Bryant, W.R., Bennett, R.H., Burkett, P.J., & Rack, F.R. (1991) 'Microfabric and physical properties characteristics of a consolidated clay section: ODP Site 697, Weddell Sea.' In: Bennett, R.H., Bryant, W.R., & Hulbert, M.H. (eds) *Microstructure of Fine-Grained Sediments: From Mud to Shale.* Springer-Verlag, New York.

[29] Buchalter, B.J. & Bradley, R.M., (1994) Orientational order in amorphous packings of ellipsoids. *Europhysics Letters* **26** (3), 159-164.

[30] Buckingham, E. (1914) 'On physically similar systems; illustrations of the use of dimensional equations.' *Phys. Rev.* **4**, 345-376.

[31] Bulychev, S.I., Alekhin, V.P., Shorshorov, M.K., Ternovskii, A.P & Shnyrev, G.D. (1975). 'Determination of Young's modulus according to indentation diagram.' *Zavodskaya Laboratoria* (Transl: Industrial Laboratory) **41**: 1137.

[32] Castagna, J.P., Batzle, M.L., & Eastwood, R.L. (1985) 'Relationship between compressional-wave and shear-wave velocities in clastic silicate rocks.' *Geophysics* **50** (4): 571-581.

[33] Cariou, S., (2006) *The Effect of the Packing Density on the Indentation Hardness of Cohesive-Frictional Porous Materials.* S.M. Thesis, Department of Civil and Environmental Engineering, MIT, Cambridge, MA.

[34] Cariou, S., Ulm, F.-J., & Dormieux, L. (2008) 'Hardness-packing density scaling relations for cohesive-frictional porous materials.' *Journal of the Mechanics and Physics of Solids* **56** (3): 924-952.

[35] Chang, C., Zoback, M. D., & Khaksar, A. (2006) 'Emprical relations between rock strength and properties in sedimentary rocks.' *Journal of Petroleum Science and Engineering* **51**: 223-237.

[36] Chateau, X. & Dormieux, L. (2002) 'Micromechanics of saturated and unsaturated porous media.' *International Journal of Analytical and Numerical Methods in Geomechanics* **26**: 1231-1243.

[37] Chen, B., & Evans, J.R.G. (2006) 'Elastic moduli of clay platelets.' *Scripta Materiala* **54**: 1581-1585.

[38] Cheng, Y.-T., & Cheng, C.-M. (2004). 'Scaling, dimensional analysis and indentation measurements.' *Mater. Sci. Eng.*, **R. 44**: 91–149.

[39] Chitkara, N.R. & Butt, M.A. (1992). 'Numerical construction of axisymmetric slip-line fields for indentation of thick blocks by rigid conical indenters and friction at the tool-metal interface.' *International Journal of Mechanical Sciences* **34** (11): 849-862.

[40] Christensen, R.M., & Lo, K.H. (1979). 'Solutions for effect shear properties in three phase sphere and cylinder models.' *Journal of the Mechanics and Physics of Solids* **27** (4): 315-330.

[41] Coehlo, D., Thovert, J.-F. & Adler, P.M. (1997) 'Geometrical and transport properties of random packings of spheres and aspherical particles.' *Physical Review E* **55** (2): 1959-1978.

[42] Colmenares, L.B. & Zoback, M.D. (2002) 'A statistical evaluation of intact rock failure criteria constrained by polyaxial test data for five different rocks.' *International Journal of Rock Mechanics and Mining Sciences* **39**: 695-729.

[43] Constantinides, G., Ulm, F.-J., & Van Vliet, K. (2003). 'On the use of nanoindentation for cementitious materials', *Materials and Structures* 36 (257): 191-196.

[44] Constantinides, G. (2006) *Invariant Mechanical Properties of Calcium-Silicate-Hydrates (C-S-H) in Cement-Based Materials: Instrumented Nanoindentation and Microporomechanical Modeling.* Ph.D. Thesis, Department of Civil and Environmental Engineering, MIT, Cambridge, MA.

[45] Constantinides, G., Ravi Chandran, K.S., Ulm, F.-J. & Van Vliet, K.J. (2006) 'Grid indentation analysis of composite microstructure and mechanics: Principles and validation' *Mat. Sc. Eng. A 430*(1-2) 189-202.

[46] Constantinides, G., and Ulm, F.-J. (2007) 'The nanogranular nature of C-S-H.' *Journal of the Mechanics and Physics of Solids*, 55 (1): 64–90.

[47] Coussy, O. (1995) *Mechanics of Porous Media.* Wiley, Chichester, UK.

[48] Coussy, O. (2004) *Poromechanics.* Wiley, Chichester, UK.

[49] Coussy, O. & Ulm, F.-J. (2004) *Mechanics and Durability of Solids, Vol. I: Solid Mechanics.* Prentice Hall, Upper Saddle River, NJ.

[50] CSM Instruments SA (2004) *Nanohardness Test Users Manual.* Peseux, Switzerland.

[51] Delafargue, A. (2004) *Material Invariant Properties of Shales: Nanoindentation and Microporoelastic Analysis.* S.M. Thesis, Department of Civil and Environmental Engineering, MIT, Cambridge, MA.

[52] Delafargue, A., & Ulm, F.-J. (2004) 'Explicit approximations of the indentation modulus of elastically orthotropic solids for conical indenters.' *International Journal of Solids and Structures* **41**: 7351-7360.

[53] DeJong, M.J. and Ulm, F.-J. (2007) 'The nanogranular behavior of C-S-H at elevated temperatures (up to 700C).' *Cement and Concrete Research* **37**: 1–12.

[54] Delesse, M. (1847) 'Procédé mécanique pour déterminer la composition des roches.' *Comptes Rendus de l'Académie des Sciences* **25**: 544-547.

[55] Deniau, I., Derenne, S., Beaucaire, C., Pitsch, H., & Largeau, C. (2001) 'Morphological and chemical features of a kerogen from the underground Mol laboratory (Boom Clay Formation, Oligocene, Belgium): structure, source organisms and formation pathways.' *Organic Geochemisty* **32**: 1343-1356.

[56] Dewhurst, D. N. & Siggins, A. F. (2006) 'Impact of fabric, microcracks and stress field on shale anisotropy.' *Geophysics Journal International* **165**: 135-148.

[57] Diamond, S. (2000) 'Mercury porosimetry: An inappropriate method of the measurement of pore size distributions in cement-based materials.' *Cement and Concrete Research* **30**: 1517-1525.

[58] Diamond, S. & Dolch, W.L. (1972) 'Generalized log-normal distribution of pore sizes in Hydrated Cement Paste.' *Journal of Colloid and Interface Science* **38** (1): 234-244.

[59] Dao, M., Chollacoop, N.,Van Vliet, K.J.,Venkatesh, T.A. & Suresh, S. (2001) 'Computational modeling of the forward and reverse problems in instrumented sharp indentation.' *Acta Materialia* **49** (19): 3899-3918.

[60] Desrues, J. (2002) 'Limitations du choix de l'angle de frottement pour le critère de plasticité de Drucker-Prager.' *Revue Française de Génie Civil* **6**: 853-862.

[61] Doerner, M.F. & Nix, W.D. (1986) 'A method for interpreting the data from depth-sensing indentation instruments.' *Journal of Materials Research* **1**: 601-609.

[62] Domnesteanu, P., McCann, C., & Sothcott, J. (2002) 'Velocity anisotropy and attenuation of shale in under- and overpressured conditions.' *Geophysical Prospecting* **50**: 487-503.

[63] Donath, F. (1961) 'Experimental study of shear failure in anisotropic rocks.' *GSA Bulletin* **72** (6): 985-989.

[64] Donev, A., Cisse, I., Sachs, D., Variano, E.A., Stillinger, F.H., Connelly, R., Torquato, S. & Chaikin, P.M. (2004) 'Improving the density of jammed disordered packings using ellipsoids.' *Nature* **303**: 990-993.

[65] Donnely, E., Baker S.P., Boskey, A.L., & van der Meulen, M.C.H. (2006). 'Effects of surface roughness and maximum load on the mechanical properties of cancellous bone measured by nanoindentation.' *J. Biomed. Mater. Res. A.* **77** (2): 426-435.

[66] Dormieux, L., Kondo, D., & Ulm, F.-J. (2006) *Microporomechanics.* Wiley, Chichester, UK.

[67] Dormieux, L., Molinari, A. & Kondo, D. (2002) 'Micromechanical approach to the behavior of poroelastic materials.' *Journal of the Mechanics and Physics of Solids* **50**: 2203-2231.

[68] Dusseault, M. (1994) 'Analysis of borehole stability.' In: *Computer Methods and Advances in Geomechanics*, H.J. Siriwardane & M.M. Zaman, Eds. Balkema, Rotterdam.

[69] Draege, A., Jakobsen, M., Johansen, T. A. (2006) 'Rock physics modelling of shale diagenesis.' *Petroleum Geoscience* **12**: 49-57.

[70] Eshelby, J.D. (1957) 'The determination of the elastic field of an ellipsoidal inclusion, and related problems.' *Proceedings of the Royal Society of London. Series A, Mathematical and Physical Sciences* **A241**: 376-396.

[71] Ewy, R.T. (1999) 'Wellbore-stability predictions by use of a modified Lade criterion.' *SPE Drilling and Completion* **14** (2): 85-91.

[72] Fritsch, A., Dormieux, L., Hellmich, C. & Sanahuja, J. (2007) 'Micromechanics of crystal interfaces in polycrystalline solid phases of porous media: fundamentals and application to strength of hydroxyapatite biomaterials.' *J. Mater. Sci.* **42**: 8824-8837.

[73] Galin, L.A. (1953). *Contact Problems in the Theory of Elasticity.* Gostekhizdat, Moscow.

[74] Ganneau, F.P. (2004). *From Nanohardness to Strength Properties of Cohesive-Frictional Materials - Application to Shale Materials.* S.M. Thesis, Department of Civil Engineering, MIT, Cambridge, MA.

[75] Ganneau, F.P., Constantinides, G., and Ulm, F.-J. (2006). 'Dual-indentation technique for the assessment of strength properties of cohesive-frictional materials.' *International Journal of Solids and Structures* **43** (4): 1727-1745.

[76] Gao, J., Luedtke, W.D., Gourdon, D., Ruths, M., Israelachvili, J.N. & Landman, U. (2004) 'Frictional forces and Amontons' Law: from the molecular to the macroscopic scale.' *J. Phys. Chem. B* **108**: 3410-3425.

[77] Gathier, B. (2008) *Multiscale Strength Homogenization - Application to Nanoindentation.* S.M. Thesis, Department of Civil and Environmental Engineering, MIT, Cambridge, MA.

[78] Gerde, E. & Marder, M. (2001) 'Friction and fracture.' *Nature* **413**: 285-288.

[79] Germaine, J.T. (1982) *Development of the Direction Shear Cell for Measuring Cross-Anisotropic Clay Properties.* Sc.D. Thesis, Department of Civil Engineering, MIT, Cambridge, MA.

[80] Giannakopoulos, A.E. & Suresh, S. (1999) 'Determination of elastoplastic properties by instrumented sharp indentation.' *Scripta Materialia* **40** (10): 1191–1198.

[81] Gillaizeau, B., Derenne, S., Largeau, C., Berkaloff, C. & Rousseau, B. (1996) 'Source organisms and formation pathway of the kerogen of the Göynük Oil Shale (Oligocene, Turkey) as revealed by electron microscopy, spectroscopy and pyrolysis.' *Organic Geochemistry* **24** (6/7): 671-679.

[82] Gologanu, M., Leblond, J.-B., Perrin, G. & Devaux, J. (1997) 'Recent extensions of Gurson's model for porous ductile metals.' In: *Continuum Micromechanics* P. Suquet, ed. Springer-Verlag, Wein, 61-130.

[83] Gurson, A.L. (1977) 'Continuum theory of ductile rupture by void nucleation and growth. Part I. Yield criteria and flow rules for porous ductile media.' *Journal of Engineering: Materials and Technology, Trans. ASME* **99**: 2-15.

[84] Grau, P., Ullner, Ch., and Behncke, H.-H. (1997) 'Uncertainty of Depth Sensing Hardness.' *Materialprüfung*, **39** (9): 362-367.

[85] Hay, J.C., Bolshakov, A. & Pharr, G.M. (1999) 'A critical examination of the fundamental relations used in the analysis of nanoindentation data. *Journal of Materials Research* **14** (6): 2296-2305.

[86] Hellmich, C., Barthélémy, J.-F. & Dormeiux, L. (2004) 'Mineral-collagen interactions in elasticity of bone ultrastructure - a continuum micromechanics approach.' *European Journal of Mechanics A - Solids* **23**: 783-810.

[87] Hellmich, C. & Ulm, F.-J. (2005) 'Drained and undrained poroelastic properties of healthy and pathological bone: a poro-mecromechanics investigation.' *Transport in Porous Media* **58**: 243-268.

[88] He, G., Muser, M.H. & Robbins, M.O. (1999) 'Adsorbed layers and the origin of static friction.' *Science* **284** (5420): 1650-1652.

[89] Herrmann, H.J., Mahmoodi Baram, R. & Wackenhut, M. (2003) 'Searching for the perfect packing.' *Physica A: Statistical Mechanics and its Applications* **330** (1-2): 77-82.

[90] Hershey, A.V. (1954) 'The elasticity of an isotropic aggregate of anisotropic cubic crystals.' *Journal of Applied Mechanics* **21**: 236-240.

[91] Hertz, H. (1896) *Miscellaneous papers.* Macmillan, London.

[92] Hill, R. (1967) 'The essential structure of constitutive laws for metal composites and polycrystals.' *Journal of the Mechanics and Physics of Solids* **15**: 79-95.

[93] Hornby, B., Schwartz, L., & Hudson, J. (1994) 'Anisotropic effective medium modeling of the elastic properties of shales.' *Geophysics* **59** (10): 1570-1583.

[94] Hornby, B. (1998) 'Experimental laboratory determination of the dynamic elastic properties of wet, drained shales.' *Journal of Geophysical Research* **103** (B12): 29945-29964.

[95] Horsrud, P., Sonstebo, E.F., & Boe, R. (1998) 'Mechanical and Petrophysical Properties of North Sea Shales.' *International Journal of Rock Mechanics and Mining Sciences* **35** 8: 1009-1020.

[96] Horsrud, P. (2001) 'Estimating mechanical properties of shale from empirical correlations.' *SPE Drill. Complet.* **16**: 68-73.

[97] Huntley, H.E. (1967) *Dimensional Analysis.* Dover, New York.

[98] Hysitron, Inc. (2001) *Triboindenter Users Manual*, Minneapolis, MN.

[99] Ibanez, W.D. & Kronenberg, A.K. (1993) 'Experimental deformation of shale: Mechanical properties and microstructural indicators of mechanisms.' *International Journal of Rock Mechanics, Mineral Science & Geomechanics Abstracts* **30** (7): 723-734.

[100] Ingles, O.G. (1962) 'Bonding forces in soils - Part 3.' *Proc. of the first Conference of the Australian Road Research Board, Vol. 1.* pp. 1025-1047.

[101] ISO-14577-1 (2002). 'Metallic materials - Instrumented indentation test for hardness and materials parameters - Part 1: Test Method' Geneva, Switzerland.

[102] International Society for Rock Mechanics, Commisson on Standardization of Laboratory and Field Tests (1981) 'Suggested methods for geophysical logging of boreholes.' *International Journal of Rock Mechanics, Mineral Science & Geomechanics Abstracts* **18**: 67-84.

[103] Jakobsen, M. & Johansen T.A. (2000) 'Anisotropic approximations for mudrocks: A seismic laboratory study.' *Geophysics* **65** (6): 1711-1725.

[104] Johnson, K.L. (1985) *Contact Mechanics.* Cambridge University Press, Cambridge, UK.

[105] Johnston, J.E. & Christensen, N.I. (1995) 'Seismic anisotropy of shales.' *Journal of Geophysical Research* **100** (B4): 5991-6003.

[106] Jizba, D.L. (1991) *Mechanical and Acoustical Properties of Sandstones and Shales.* Ph.D. Thesis, Department of Geophysics, Stanford University, Palo Alto, CA.

[107] Jones, L.E.A. & Wang, H.F. (1981) 'Ultrasonic velocities in Cretaceous shales from the Williston basin.' *Geophysics* **46**: 288–297.

[108] Kaarsberg, E.A. (1959) 'Introductory studies of natural and artificial argillaceous aggregates by sound-propagation and X-ray diffraction methods.' *Journal of Geology* **67**: 447-472.

[109] Katahara, K.W. (1996) 'Clay mineral elastic properties.' *SEG Expanded Abstracts* **15** (1): 1691-1694.

[110] Kenney, T.C. (1964) 'Sea-level movements and the geologic histories of the postglacial marine soils at Boston, Nicolet, Ottawa and Oslo.' *Géotechnique* **14** (3): 203-230.

[111] Kim, J.-U., Lee, J.-J., Lee, Y.-H., Jang, J., & Kown, D. (2006) 'Surface roughness effect in instrumented indentation: A simple contact depth model and its verification.' *Journal of Materials Research* **21** (12): 2975-2978.

[112] Kröner, E. (1958) 'Berechnung der elastischen Konstanten des Vielkristalls aus den Konstanted des Einkristalls.' *Zeitschrift für Physick* **151**: 504-518

[113] Kruyt, N.P. (2003) 'Contact forces in anisotropic frictional granular materials.' *International Journal of Solids & Structures* **40**: 3537-3556.

[114] Ladd, C.C., Bovee, R.B., Edgers, L., & Rixner, J.J. (1971) *Consolidated-Undrained Plane Strain Shear Tests on Boston Blue Clay.* Research Report R71-13, No. 273, Department of Civil Engineering, MIT, Cambridge, MA.

[115] Larsson, P.-L., Giannakopoulos, A., Soderlund, E., Rowcliffe, D., & Vestergaard., R. (1996) 'Analysis of Berkovich indentation.' *International Journal of Solids and Structures* **33** (2): 221-248.

[116] Laskaripour, G.R. & Dusseault, M.B. (1993) 'A statistical study on shale properties; relationship among principal shale properties.' *Proc. Conference on Probabilistic Methods in Geotechnical Engineering*, Canberra, Australia, 195-200.

[117] Laws, N. (1985) 'A note on penny-shaped cracks in transversely isotropic materials.' *Mechanics of Materials* **4**: 209-212.

[118] Leblond, J.-B. (2003) *Mécanique de la rupture fragile et ductile.* Etudes en mécanique des matériaux et des structures, Hermes Science, Paris, France.

[119] Lee, S.Y., Hyder, L.K. & Alley, P.D. (1991) 'Microstructural and Mineralogical Characterization of Selected Shales in Support of Nuclear Waste Repository Studies.' In: Bennett, R.H., Bryant, W.R., & Hulbert, M.H. (eds) *Microstructure of Fine-Grained Sediments: From Mud to Shale.* Springer-Verlag, New York.

[120] Lemaitre, A. (2002) 'Origin of a repose angle: kinetics of rearrangement for granular materials.' *Physical Review Letters* **89** (6): 064303.

[121] Levin, V.M. (1967) 'Thermal expansion coefficients of heterogeneous materials.' *Mekhanika Tverdogo Tela* **3** (1): 88-94. english translation: *Mechanics of Solids* **2**: 58-61.

[122] Limpert, E., Stahel, W. A. & Abbt, M. (2001) 'Log-normal distributions across the sciences: Keys and clues.' *BioScience.* **51** (5): 341-352

[123] Lockett, F. (1963) 'Indentation of a rigid plastic material by a conical indenter.' *Journal of the Mechanics and Physics of Solids* **11**: 345-355.

[124] Lonardelli, I., Wenk, H.-R., & Ren, Y. (2007) 'Preferred orientation and elastic anisotropy in shales.' *Geophysics* **72** (2): D33-D40.

[125] Love, A.E.H. (1929) 'The stress produced in a semi-infinite solid by pressure on part of the boundary.' *Philosophical Transactions of the Royal Society of London. Series A, Mathematical and Physical Sciences.* **228**: 377-420.

[126] Love, A.E.H. (1939) 'Boussinesq's problem for a rigid cone.' *The Quarterly Journal of Mathematics* **10**: 161-175.

[127] Lubliner, J. (1990) *Plasticity Theory.* Macmillan, New York.

[128] Mahmoodi Baram, R. & Herrmann, H.J. (2004) 'Self-similar space-filling packings in three dimensions.' *Fractals* **12** (3): 293-301.

[129] Mahmoodi Baram, R., Herrmann, H.J., & Rivier, N. (2004) 'Space-filling bearings in three dimensions.' *Physical Review Letters* **92** (4): 044301-1–044301-4.

[130] Manevitch, O.L. & Rutledge, G.C. (2004) 'Elastic properties of a single lamella of montmorillonite by molecular dynamics simulation.' *Journal of Physical Chemistry B* **108**: 1428-1435.

[131] Marion, D., Nur, A., Yin, H., & Han, D. (1992) 'Compressional velocity and porosity in sand-clay mixtures.' *Geophysics* **57** (4): 554-563.

[132] The MathWorks, Inc. (2006) 'Optimization toolbox for MATLAB, fmincon function.' Online manual, http://www.mathworks.com.

[133] Mavko, G., Mukerji, T., & Dvorkin, J. (1998) *The Rock Physics Handbook.* Cambridge University Press, Cambridge, UK.

[134] McLamore, R. & Gray, K.E. (1967) 'The mechanical behaviour of anisotropic sedimentary rocks.' ASME Journal of Engineering and Industry **89**: 62–76.

[135] McLane, M. (1995) *Sedimentology.* Oxford University Press, New York.

[136] Mendenhall, W. & Sincich, T. (1995) *Statistics for Engineering and the Sciences, 4th Ed.* Prentice Hall, Upper Saddle River, NJ.

[137] Miller, M., Bobko, C., Vandamme, M, & Ulm, F.-J. (2008). 'Surface roughness criteria for cement paste nanoindentation.' *Cement and Concrete Research* **38**: 467-476.

[138] Mitchell, J. & Soga, K. (2005). *Fundamentals of Soil Behavior, 3rd ed.* Wiley, New York.

[139] Mori, T. & Tanaka, K. (1973) 'Average stress in matrix and average elastic energy of materials with misfitting inclusions.' *Acta Metallurgica* **21**(5): 571-574.

[140] Müser, M.H., Wenning, L. & Robbins, M.O. (2001) 'Simple microscopic theory of Amonton's laws for static friction.' *Physical Review Letters* **86** (7): 1295-1298.

[141] Oda, M. (1977). 'Co-ordination number and its relation to the shear strength of granular material.' *Soils and Foundations* **17** (2): 29-42.

[142] Oliver, W.C. & Pharr, G.M. (1992). 'An improved technique for determining hardness and elastic modulus using load and displacement sensing indentation experiments.' *Journal of Materials Research* **7** (6): 1564–1583.

[143] Oliver, W.C., Pharr, G.M., 2004. Measurement of hardness and elastic modulus by instrumented indentation: Advances in understanding and refinements to methodology. *Journal of Materials Research* **19** (1): 3-20.

[144] Onoda, G. Y. & Liniger, E.G. (1990) 'Random loose packings of uniform spheres and the dilatancy onset.' *Physical Review Letters* **64** (22): 2727-2730.

[145] Ortega, J.A., Ulm, F.-J. & Abousleiman, Y. (2007) 'The effect of the nanogranular nature of shale on their poroelastic behavior.' *Acta Geotechnica* **2**: 155-182.

[146] Perrier, E.M.A., Bird, N. & Rieu, M. (1999) 'Generalizing the fractal model of soil structure: the pore-solid fractal approach.' *Geoderma* **88**: 137-164.

[147] Perriot, A., & Barthel, E. (2004) 'Elastic contact to a coated half-space: Effective elastic modulus and real penetration.' *Journal of Materials Research* **19** (2): 600-608.

[148] Ponte Castañeda, P. (1992) 'New variational principles in plasticity and their application to composite materials.' *Journal of the Mechanics and Physics of Solids* **40**: 1757-1788.

[149] Ponte Castañeda, P. (1996) 'Exact second-order estimates for the effective mechanical properties of nonlinear composite materials.' *Journal of the Mechanics and Physics of Solids* **44**: 827-862.

[150] Ponte Castañeda, P. (2002) 'Second-order homogenization estimates for non-linear composites incorporating field fluctuations. I. Theory.' *Journal of the Mechanics and Physics of Solids* **50**: 737-757.

[151] Radlinski, A.P., Ioannidis, M.A., Hinde, A.L., Hainbuchner, M., Baron, M., Rauch, H., & Kline, S.R. (2004) 'Angstrom-to-millimeter characterization of sedimentary rock microstructure.' *Journal of Colloid and Interface Science* **274**: 607-612.

[152] Roux, J.-N. (2000) 'Geometric origin of mechanical properties of granular materials.' *Physical Review E* **61** (6): 6802-6836.

[153] Salençon, J. (1990) 'An introduction to the yield design theory and its applications to soil mechanics.' *European Journal of Mechanics - A/Solids* **9** (5): 477-500.

[154] Sanahuja, J., Dormiuex, L, & Chanvillard, G. (2007) 'Modelling elasticity of a hydrating cement paste.' *Cement and Concrete Research* **37**: 1427-1439.

[155] Santagata, M.C. (1998) *Factors Affecting the Initial Stiffness and Stiffness Degradation of Cohesive Soils.* Ph.D. Thesis, Department of Civil and Environmental Engineering, MIT, Cambridge, MA.

[156] Savage, W.Z., & Braddock, W.A. (1991) 'A model for hydrostatic consolidation of Pierre shale.' *International Journal of Rock Mechanics and Mining Sciences* **28** (5): 345-354.

[157] Sayers, C.M. (1994) 'The elastic anisotropy of shales.' *Journal of Geophysical Research* **99** (B1): 767-774.

[158] Sayers, C.M. (1999) 'Stress-dependent seismic anisotropy of shales.' *Geophysics* **64** (1): 93-98.

[159] Schwiger, H.F. (1994) 'On the use of Drucker-Prager failure criteria for earth pressure problems.' *Computer and Geotechnics* **16**: 223-246.

[160] Seo, Y.-S., Ichikawa, Y., & Kawamura, K. (1999) 'Stress-strain response of rock-forming minerals by molecular dynamics simulation.' *Materials Science Research International* **5** (1): 13-20.

[161] Sheng, N., Boyce, M.C., Parks, D.M., Rutledge, G.C., Abes, J.I., & Cohen, R.E. (2004) 'Multiscale micromechanical modeling of polymer/clay nanocomposites and the effective clay particle.' *Polymer* **45**: 487-506.

[162] Sherwood, J.D. & Van Damme, H. (1994) 'Nonlinear compaction of an assembly of highly deformable platelike particles.' *Physical Review E* **50** (5): 3834-3843.

[163] Sherwood, J.D. (1997) 'Packing of spheroids in three-dimensional space by random sequential addition.' *Journal of Physics A - Mathematical and General* **30** (24): L839-L843.

[164] Shi, D., Brown, P.W. & Ma W. (1991) 'Lognormal simulation of pore size distributions in cementious materials.' *Journal of the American Ceramic Society* **74** (8): 1861-1867.

[165] Sneddon, I.N. (1965) 'The relation between load and penetration in the axisymmetric Boussinesq problem for a punch of arbitrary profile.' *International Journal of Engineering Science* **3** (1): 47-57.

[166] Sneddon, I.N. (1977) *Applications of Integral Transforms in the Theory of Elasticity.* Springer Verlag, Wien-New York.

[167] Stillwell, N.A., & Tabor, D. (1961) 'Elastic recovery of conical indentations.' *Proceedings of Physical Society* **78**: 169-179.

[168] Tabor, D. (1948) 'A simple theory of static and dynamic hardness.' *Proceedings of the Royal Society of London* **192A**: 247-274.

[169] Thomsen, L. (1995) 'Elastic anisotropy due to aligned cracks in porous rock.' *Geophysical Prospecting* **43**: 805-829.

[170] Thomsen, L. (2001) 'Seismic anisotropy' *Geophysics* **66** (1): 40-41.

[171] Trillat, M. & Pastor, J. 'Limit analysis and Gurson's model.' *European Journal of Mechanics and Solids* **24**: 800-819.

[172] Ulm, F.-J., Constantinides, G., Delafargue, A., Abousleiman, Y., Ewy, R., Duranti, L., & McCarty, D.K. (2005) 'Material invariant poromechanics properties of shales.' In: Abousleiman, Y., Cheng, A.H.-D., Ulm, F.-J. (Eds.) *Poromechanics III. Bio centennial (1905-2005)*, A.A. Balkema Publishers, London, 637-644

[173] Ulm, F.-J., Delafargue, A., & Constantinides, G. (2005) 'Experimental Microporomechanics.' In: Dormieux, L. & Ulm, F.-J. (eds) *Applied Micromechanics of Porous Materials.* CISM Lecture Notes, No. 580, Springer, Vienna, pp. 207-288.

[174] Ulm, F.-J. & Abousleiman, Y. (2006) 'The nanogranular nature of shale.' *Acta Geotechnica* **1**: 77-88.

[175] Ulm, F.-J., Vandamme, M., Bobko, C., Ortega, J.A., Tai, K. & Ortiz, C. (2007) 'Statistical indentation techniques for hydrated nanocomposites: Concrete, bone, and shale.' *Journal of the American Ceramic Society* **90** (9): 2677-2692.

[176] Urbakh, M., Klafter, J., Gourdon, D. & Israelachvili, J. (2004) 'The nonlinear nature of friction.' *Nature* **430**: 525-528.

[177] Vandamme, M. (2008) *The Nanogranular Origin of Concrete Creep: A Nanoindentation Investigation of Microstructure and Fundamental Properties of Calcium-Silicate-Hydrates.* PhD Thesis, Department of Civil and Environmental Engineering, MIT, Cambridge, MA

[178] Van Damme, H. (2008) Personal Communication, March 14, 2008.

[179] Vanorio, T., Prasad, M., & Nur, A. (2003) 'Elastic properties of dry clay mineral aggregates suspensions and sandstones.' *Geophysics Journal International* **155**: 319-326.

[180] Vaughan, M.T. & Guggenheim, S. (1986) 'Elasticity of muscovite and its relationship to crystal structure.' *Journal of Geophysical Research* **91** (B5): 4657-4664.

[181] Vernik, L. & Nur, A. (1992) 'Ultrasonic velocity and anisotropy of hydrocarbon source rocks.' *Geophysics* **57** (5): 727-735.

[182] Vlassak, J.J. & Nix, W.D. (1993) 'Indentation modulus of elastically anisotropic half spaces.' *Phil. Mag. A* **67** (5): 1045-1056.

[183] Wang, Z. (2002) 'Seismic anisotropy in sedimentary rocks, part 2: Laboratory data.' *Geophysics* **67** (5): 1423-1440.

[184] Wang, Z., Wang, H, & Cates, M.E. (2001) 'Effective elastic properties of solid clays.' *Geophysics* **66** (2): 428-440.

[185] Zaoui, A. (1997) 'Structural morphology and constitutive behavior of microheterogeneous materials.' In: P. Suquet (ed.) *Continuum Micromechanics.* Spring, Vienna, pp. 291-347.

[186] Zaoui, A. (2002) 'Continuum micromechanics: survey.' *Journal of Engineering Mechanics (ASCE)* **128**(8): 808-816.